AN ABSTRACT OF THE DISSERTATION OF

Atul Chhotray for the degree of Doctor of Philosophy in Physics presented on July 11, 2017.

Title: Radiative Acceleration and Emission from Relativistic Outflows

Abstract approved: _____

Davide Lazzati

Outflowing streams of matter or jets are a common phenomenon in the observed universe. The most extreme and powerful jets are relativistic, i.e., they travel at speeds comparable to the speed light. Gamma Ray-Bursts (GRBs) and Active Galactic Nuclei (AGNs) are two sources of these relativistic jets. In this work I will explore the role played by advected radiation – the radiation internal to the jet itself – in modifying the jet dynamics and creating the observed radiation spectrum. First, I present a Monte Carlo code designed to simulate the spectrum formed in a scattering dominated photon-lepton plasma. I demonstrate that non-thermal features in the emitted spectrum can arise from the interaction of thermal populations of photons and leptons, initially at different temperatures. I find the existence of a correlation between the spectral parameters that suggests the presence of this mechanism in cosmic sources, for example, in prompt spectra of GRBs. These simulations, however, do not account for the dynamical coupling between the radiation and matter within the jet, which is expected for outflows from both GRBs and AGNs. In the second part of this dissertation, I show how radiation regulates the dynamical properties (such as structure, acceleration) of jets. I use a custom-made dynamic Monte Carlo code to study radiation (Compton scattering) driven expansion and acceleration in unexplored evolutionary stages of GRB jets. My results uncover new regimes of jet evolution and allow me to obtain analytical estimates to better parameterize the jet dynamics in analytical and semi-analytical studies. In addition, I explore radiative acceleration and deceleration as mechanisms to produce two-component structured AGN jets. I find that this radiation-driven regulatory mechanism plays a crucial role in explaining the puzzling observation of high-energy emission from misaligned AGN jets.

©Copyright by Atul Chhotray
July 11, 2017
All Rights Reserved

Radiative Acceleration and Emission from Relativistic Outflows

by

Atul Chhotray

A DISSERTATION

submitted to

Oregon State University

in partial fulfillment of
the requirements for the
degree of

Doctor of Philosophy

Presented July 11, 2017
Commencement June 2018

Doctor of Philosophy dissertation of Atul Chhotray presented on July 11, 2017

APPROVED:

Major Professor, representing Physics

Chair of the Department of Physics

Dean of the Graduate School

I understand that my dissertation will become part of the permanent collection of Oregon State University libraries. My signature below authorizes release of my dissertation to any reader upon request.

Atul Chhotray, Author

ACKNOWLEDGEMENTS

First and foremost, I would like to express my sincerest appreciation and gratitude towards Professor Davide Lazzati for being the best advisor and mentor that any graduate student can have. Under his guidance I have 'Lorentz transformed' into a proficient programmer, an independent researcher and a better physicist.

I would like to thank Professor Gabriele Ghisellini for inviting and accommodating me at INAF, Merate, Italy. I have been fortunate to have several insightful discussions with him about high–energy astrophysics. I would also like to express my thanks towards graduate students and friends at Merate for making me feel at home.

In Oregon, at the physics department, I would like to thank the chair Professor Heidi Schellman for her advice and guidance during my time at OSU. A huge thanks goes to Clarissa Amundsen and Kelly Carter for being the most wonderful coordinators (and for their chocolate stash!). I thank fellow astro–graduate students, Christopher Mauney and Tyler Parsotan for innumerable stimulating discussions and for being excellent officemates. I also thank Professor Randall Milstein for not overloading his astronomy TAs (like me)!

I wish to express my gratitude towards all my dear friends at NC State. In particular, I would like to thank Rhonda Bennett for being the most lovely friend and an amazing coordinator. And thank you Kory Green, for being a wonderful friend, getting me into racquetball and supporting Liverpool with me!

Last but not the least, this section would be incomplete without thanking and appreciating my family, especially, the person without whom none of this would have been possible – my mother. She instilled in me the values vital for a PhD – hard work and perseverance. I offer my sincerest thanks to Mishra sir in Delhi, for being the most amazing and engaging teacher during my school years. I cannot express enough appreciation and gratitude towards Vicky mama & Mukta mami, and Sabbi aunty, who supported and cheered me throughout the entire PhD, and made me feel at home away from home (in the United States).

CONTRIBUTION OF AUTHORS

Professor Davide Lazzati contributed to research ideas, coding, several discussions, and manuscript revisions for 'Gamma-Ray Burst Spectra and Spectra Correlations from Sub-Photospheric Comptonization' and 'Dynamic Monte Carlo Simulations of Radiatively Accelerated GRB Fireballs'. Professor Lazzati also contributed to discussions and assisted in revising the manuscript, 'On radiative acceleration in spine-sheath structured blazar jets'.
Professor Gabrielle Ghisellini contributed to research ideas, discussions, and helped revise the manuscript, 'On radiative acceleration in spine-sheath structured blazar jets'.
Francesco Nappo contributed to the manuscript titled, 'On radiative acceleration in spine-sheath structured blazar jets' through coding, obtaining results, discussions and provided writing assistance.
Om Sharan Salafia contributed a figure and discussions to the manuscript, 'On radiative acceleration in spine-sheath structured blazar jets'.
Professor Fabrizio Tavecchio also contributed ideas and discussions to the manuscript, 'On radiative acceleration in spine-sheath structured blazar jets', and assisted in its revision.

TABLE OF CONTENTS

TABLE OF CONTENTS (Continued)

TABLE OF CONTENTS (Continued)

TABLE OF CONTENTS (Continued)

TABLE OF CONTENTS (Continued)

LIST OF FIGURES

LIST OF FIGURES (Continued)

LIST OF FIGURES (Continued)

RADIATIVE ACCELERATION AND EMISSION FROM RELATIVISTIC OUTFLOWS

1 INTRODUCTION

Ejection of matter from astrophysical objects is a commonly occurring phenomenon in astrophysics (Livio 1999). These ejections of matter, also referred to as jets, come in a variety of sizes and occur at a range of speeds. Sub-relativistic outflows have been discovered in several objects such as, Herbig-Haro objects (Reipurth and Bally 2001; also see Figs. 1.1, 1.2 and 1.3), line–driven winds (Castor et al. 1975) and continuum driven winds (Smith and Owocki 2006) from stars (see Fig. 1.4). Relativistic outflows or jets have been observed from several compact progenitors, for example, Active Galactic Nuclei (AGNs) (see Figs. 1.5 and 1.6), X-ray binaries, black hole transients and Gamma-Ray Bursts (GRBs). In this work, we will focus upon relativistic outflows and emission occurring in GRBs and AGNs, but first, we begin by discussing their properties.

1.1 Gamma-Ray Bursts

1.11 Introduction

Gamma-**R**ay **B**ursts (or GRBs) are bursts of high-energy electromagnetic radiation (high energy X-rays and γ rays) (for a review see Piran 2004; Kumar and Zhang 2015). Due to the inability of high–energy radiation to penetrate the Earth's atmosphere (fortunately for us), these radiations can only be detected by detectors onboard high altitude balloons or space based satellites. As a result GRBs were first detected serendipitously about five decades ago by VELA - a group of satellites launched by the US to monitor compliance of the Nuclear Test Ban Treaty by the USSR. However, the discovery of GRBs was not made public until 1973 (Klebesadel et al. 1973). Since the public disclosure, there have been several observational (due to state of the art, space based satellite observations) and theoretical advances in our understanding of the physics behind GRBs. For a detailed overview of the advances see reviews by Piran (2004) and Kumar and Zhang (2015).
The GRB community has adopted the following naming convention to identify individual GRBs: each burst is assigned a unique identifier depending upon the date that it is

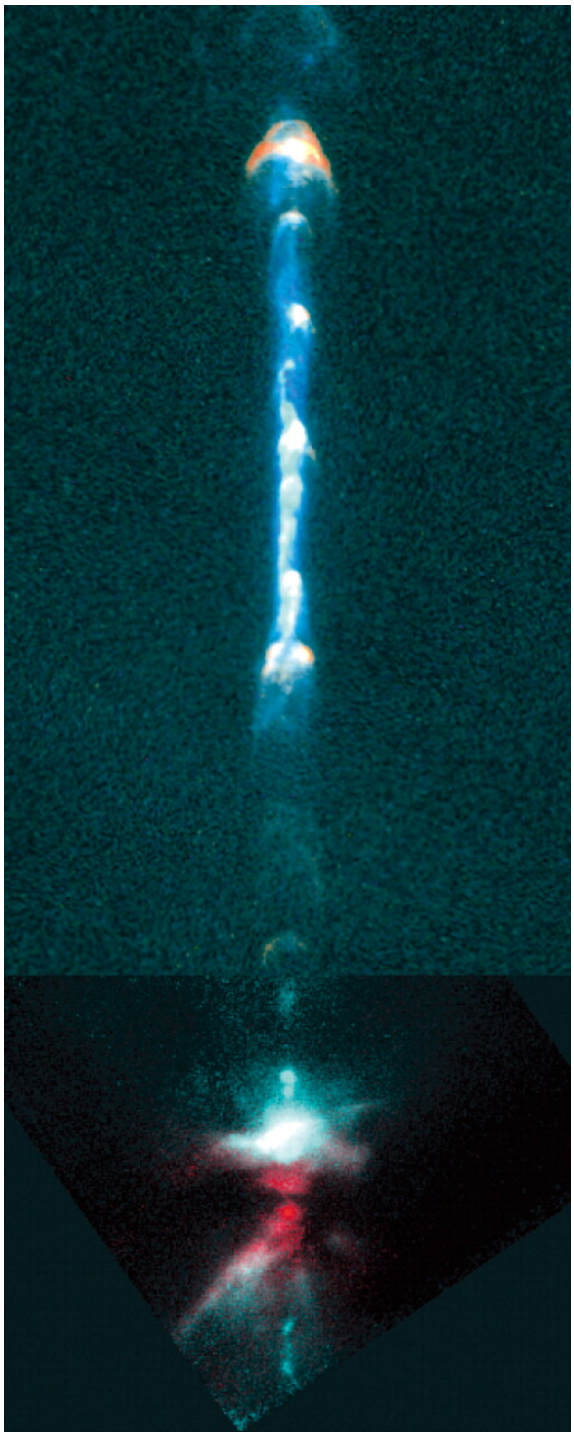

FIGURE 1.1: An outflow from Herbig-Haro object HH 111 imaged by the Hubble Space Telescope in the optical and infrared bands. Image adapted from Reipurth and Bally (2001).

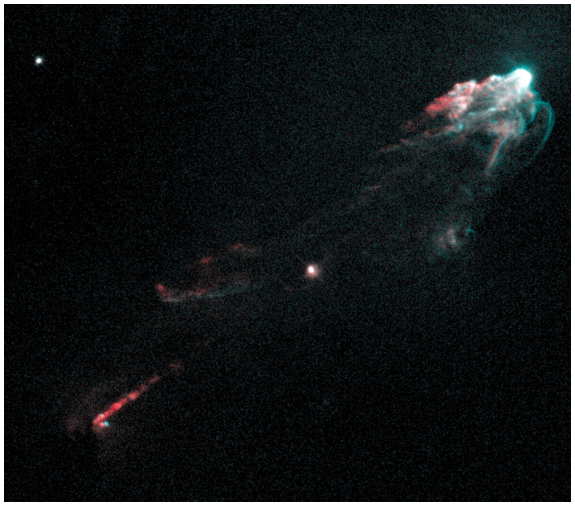

FIGURE 1.2: An image of Herbig Haro object HH 1 with bow shock and jet, courtesy the Hubble Space Telescope. The red and blue colors represent [SII] and Hα emissions respectively. Image adapted from Reipurth and Bally (2001).

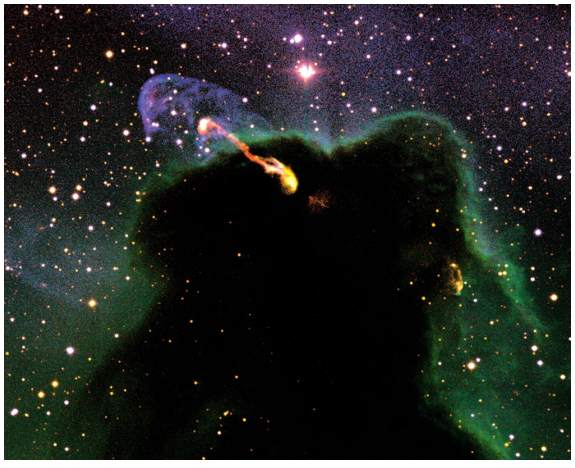

FIGURE 1.3: The HH 47 outflow observed by the ESO New technology Telescope. [SII] emission is in red, Hydrogen emission in green, and [OIII] emission in blue. Image adapted from Reipurth and Bally (2001).

FIGURE 1.4: Stellar winds from the massive Wolf-Rayet star (WR 124) (bright dot in the center) have created a nebula surrounding the star (measuring 6 light years across). Details of the nebula creation process are still not understood and are being investigated. Image adapted from *https://goo.gl/ZWNz1Q*.

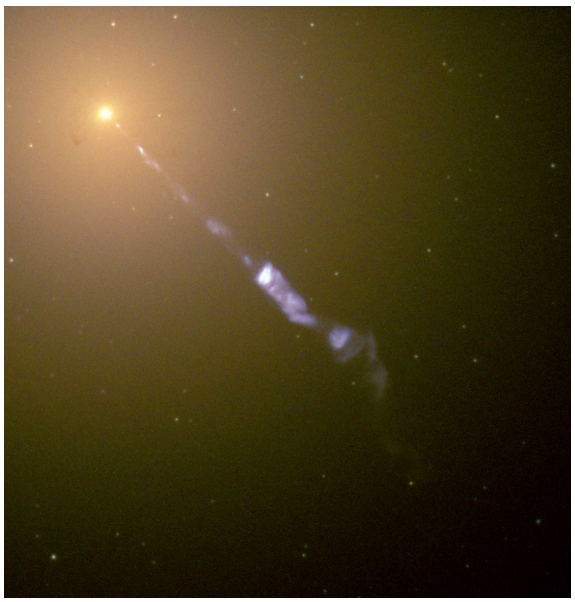

FIGURE 1.5: The image shows M87, a giant elliptical galaxy (producing the yellow glow) with a relativistic jet (blue color) emerging from it. The jet spans $\sim$ 5,000 light-years at optical wavelengths (and $\sim$ 100,000 light years at radio wavelengths). The jet is created by a black hole two billion times as massive as our sun. This image was taken by Hubble Space Telescope in optical and infrared light and has been adapted from *https://goo.gl/Bw7Efv*.

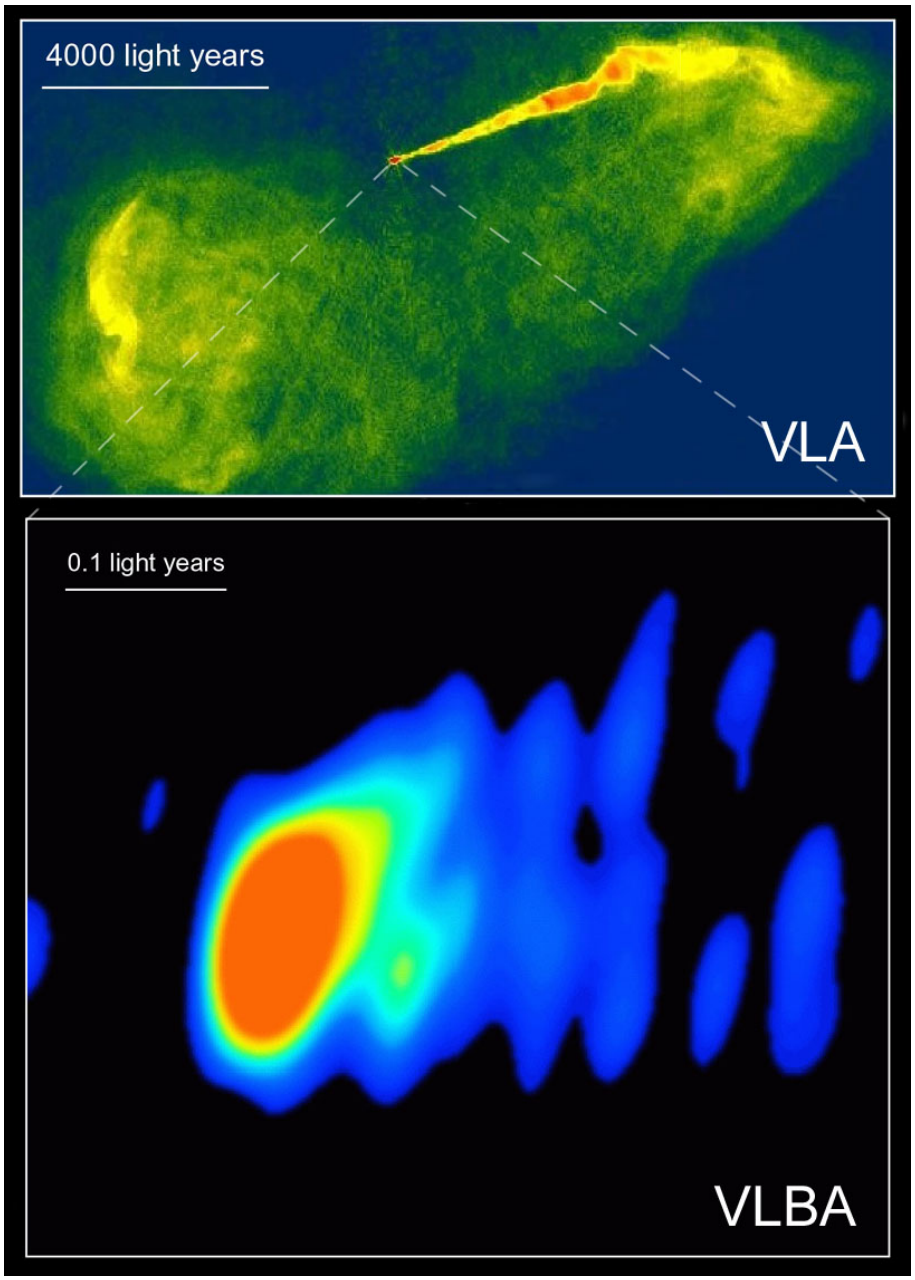

FIGURE 1.6: The M87 galaxy seen at radio frequencies. The image in the top panel (taken by the Very Large Array) shows that the relativistic jet emerges from the galaxy and spans thousands of light years. The bottom panel image (taken by VLBA - Very Large Baseline Array) enlarges the region close to the galaxy's center (harboring the black hole) where the jet is formed and collimated into a narrow beam. Image adapted from *https://goo.gl/VQAmsr*.

detected with the format YYMMDD. As an example a GRB detected on Dec 31, 2015 would be identified as GRB 151231. A letter is suffixed to YYMMDD if multiple detections occur on the same day, with the earliest detection assigned the letter A, the next detection B and so on. In this introduction we detail the fundamental properties of GRBs that will be most beneficial to our understanding of GRB jets and their emission.

1.12 GRB Classification and Progenitors

The burst of gamma rays from GRBs typically lasts for a few seconds. According to the time interval during which 90% of the GRB flux (referred to as T_{90}) is collected by the detector, GRBs can be divided into two distinct classes (Piran 2004; Qin et al. 2013; Kumar and Zhang 2015) -

- Short GRBs (SGRBs): $T_{90} < 2$ seconds
- Long GRBs (LGRBs): $T_{90} \geq 2$ seconds

Fig. 1.7 shows the T_{90} distributions of short and long GRBs as detected by several GRB missions over the past few decades. A majority of the missions confirm the bimodal T_{90} distribution of GRBs. This classification scheme was the primary motivation behind the idea that these two classes have different progenitors. There is strong evidence that LGRBs result from the core–collapse of massive stars - also referred to as the collapsar scenario. This evidence includes the association of several long GRBs with Type Ic supernovae (as a consequence, Wolf-Rayet stars are considered a LGRB progenitor candidate) or supernovae like bump in the afterglow lightcurve (see Woosley and Bloom 2006; Hjorth and Bloom 2011). The detection of most long GRBs in galaxies that are actively forming stars (most of these are irregular galaxies, but some are spirals) and in particular, the brightest regions of these host galaxies (Fruchter et al. 2006) further corroborates the collapsar origin of LGRBs. The progenitors of SGRBs are believed to be compact object mergers (neutron star–neutron star or neutron star–black hole mergers). The non-detection of supernovae with SGRBs is consistent with this belief (Berger 2014). The merger origin is supported by SGRB detections in both early and late-type galaxies with older stellar populations

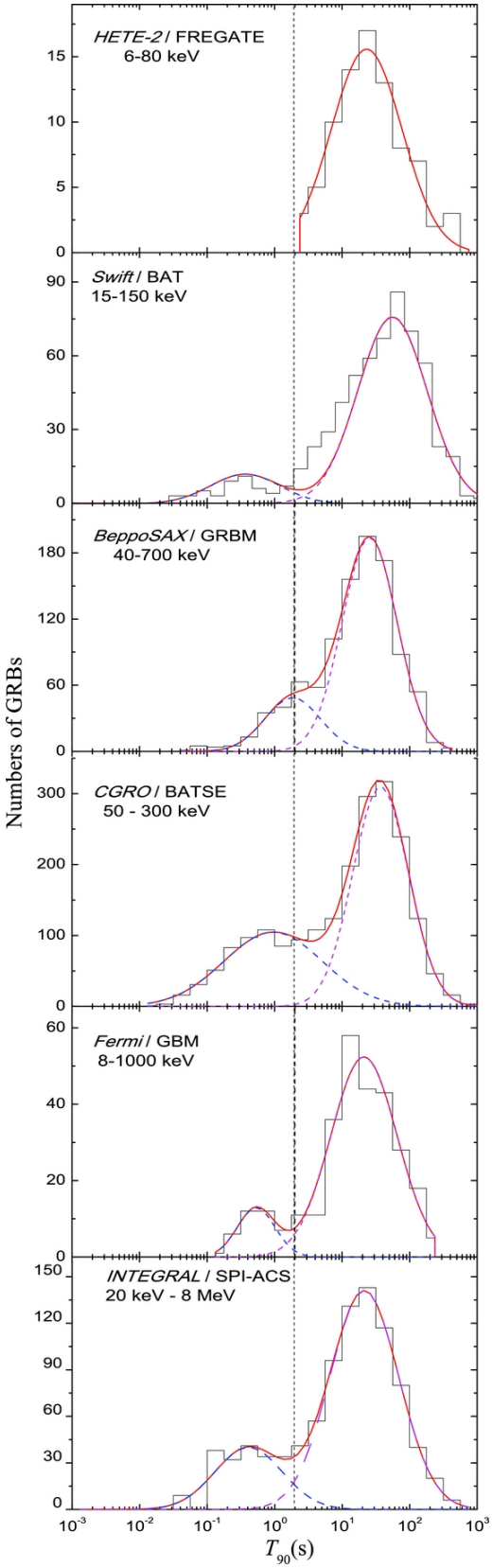

FIGURE 1.7: T_{90} distribution for several GRB missions. Image adapted from Qin et al. (2013).

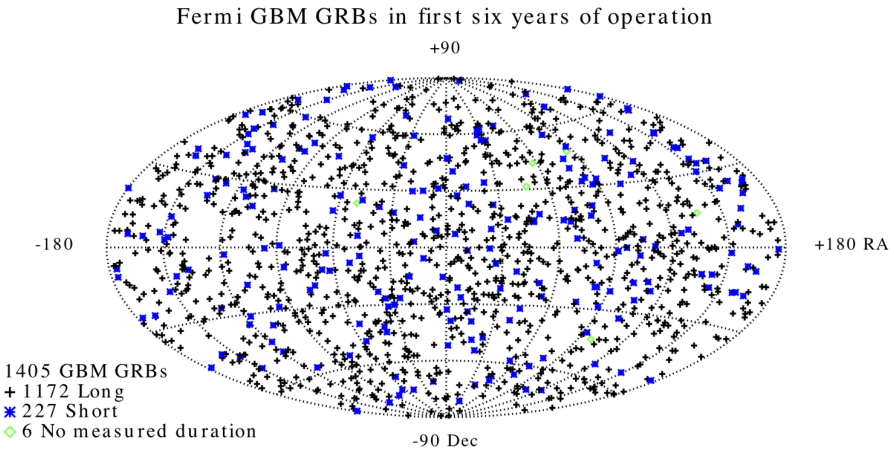

FIGURE 1.8: All sky distribution for 1405 GRBs detected by the *Fermi* mission. Note that the bursts are distributed isotropically across the entire sky and not concentrated along any particular direction. Image adapted from *https://fermi.gsfc.nasa.gov/science/eteu/grbs/*.

(and low star-formation rates) (see Berger 2014). Older stellar population increases the chances of a binary merger encounter between two compact objects. Another factor which supports the merger origin is the detection of SGRBs at significantly larger radial offsets from their host galaxies than long GRBs. This is an indication of natal kicks imparted to compact objects (Berger 2011).

1.13 Distance and Luminosity

Before the 1990s, satellites detecting high–energy radiation were not sensitive enough to pinpoint the exact locations of GRBs. As a result the distances to the source could not be determined, and the measured flux could not be used to obtain a luminosity for the burst's source. This led to the existence of two schools of thought based upon how far away the bursts were located in space. Supporters of the galactic origin model claimed that GRBs occurred within the Milky-Way (our own galaxy), whereas the other group argued for the cosmological or extra-galactic origin of GRBs. The launch of CGRO (Compton–Gamma Ray Observatory) and subsequent detection of GRBs isotropically across the sky decided the argument in favor of the cosmological origin theory (if GRBs were galactic in origin, then they would be preferentially distributed within the galactic plane which is anisotropic). The exact distance scale, however, was revealed only in the

late 90s when another satellite, BeppoSAX, pinpointed for the first time the location of a GRB down to few arc–minutes (Costa et al. 1997) . This enabled ground based observatories to conduct a multi–wavelength search for a counterpart to the burst within the pinpointed region, and led to the discovery of a transient afterglow in the optical regime. These multi–wavelength afterglows are crucial (and the only method) for determining the redshift and thus, the distance to the host–galaxy harboring the GRB. Fig. 1.8 depicts the sky locations of GRBs detected by *Fermi* during the first six years of its operation. It clearly shows the GRB distribution to be isotropic and further supports the view that GRBs are cosmological in origin.

Once the distance to the bursts is determined, the measured flux can be used to calculate the luminosity. For several bursts with known redshifts, the isotropic equivalent luminosity (luminosity of the source assuming the entire energy is radiated isotropically) of GRBs lies between $L_{\rm iso} \sim 10^{48} - 10^{53}$ ergs/s, which makes them the brightest electromagnetic explosions in the universe (only the Big-Bang was more powerful an explosion than GRBs). Being the brightest, they are also one of universe's farthest detected objects (redshift $z \sim 9.4$). Detected by Swift satellite, the remarkably luminous GRB 080319B (Racusin et al. 2008; Bloom et al. 2009) holds the record for the farthest object that (redshift $z \sim 0.937$, i.e., this event that actually happened 7.5 billion years ago) could have been seen with the naked eye.

1.14 Lightcurves, Spectra and Timescales

The radiation spectrum detected by the space based satellites (e.g., BATSE, Swift, *Fermi*) is primarily a non–thermal power law spectrum both at the high and low energies and these power laws are smoothly joined together at the peak energy. A phenomenological fit to the GRB spectra was first made by Band et al. (1993) and since then, the Band function has been used by astrophysicists to model prompt spectra from GRBs. The Band function has three free parameters to fit the spectra. These parameters are: 1) Peak Energy ($E_{\rm peak}$) is the energy at which the spectrum peaks, 2) the low energy power law index (α) which determines the slope of the low energy tail, and 3) the high energy index β which determines the high energy tail's slope. Fig. 1.9 shows the peak energy

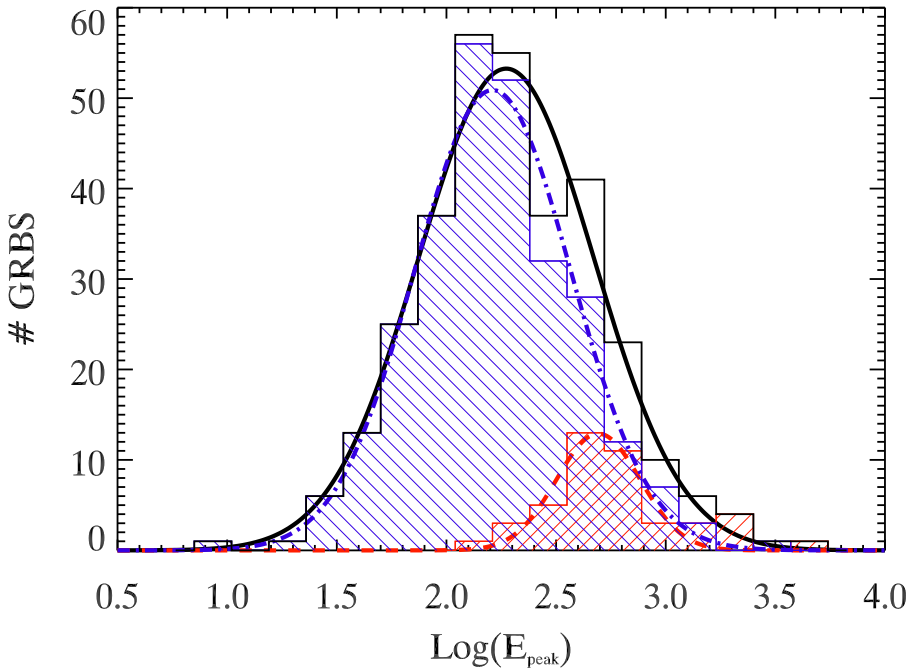

FIGURE 1.9: E_{peak} distribution for a sample of GRBs detected by *Fermi*/*GBM*. The solid line shows the Gaussian fit. The hatched blue and red histograms depict the distributions of 274 LGRBs and 44 short GRBs, respectively. Image adapted from Nava et al. (2011).

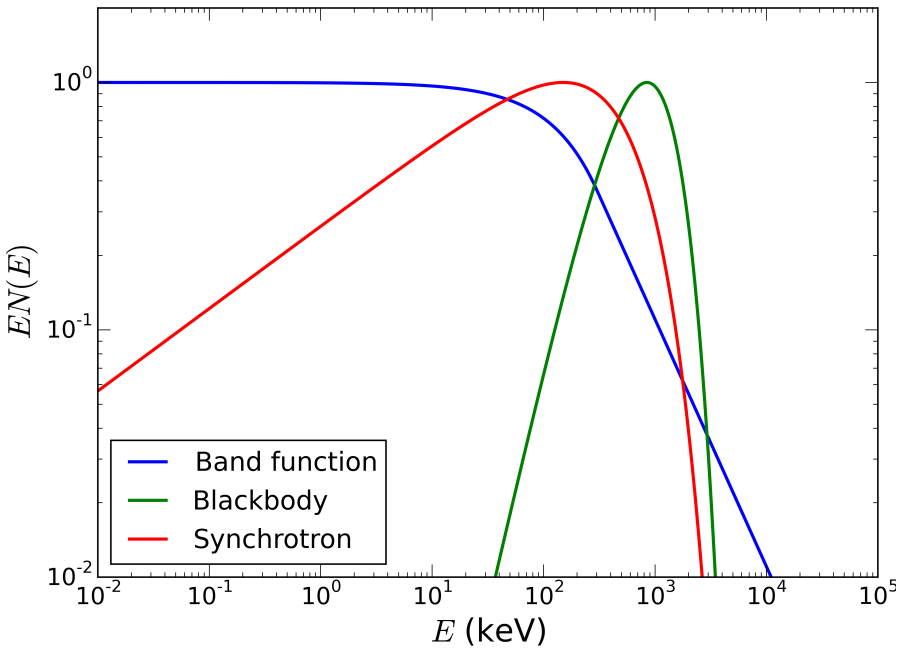

FIGURE 1.10: The flux $F(E)$ for several spectra is depicted in the figure for comparison. As can be seen both the blackbody and the slow cooling synchrotron spectra are not a good match for the typical GRB Band spectrum.

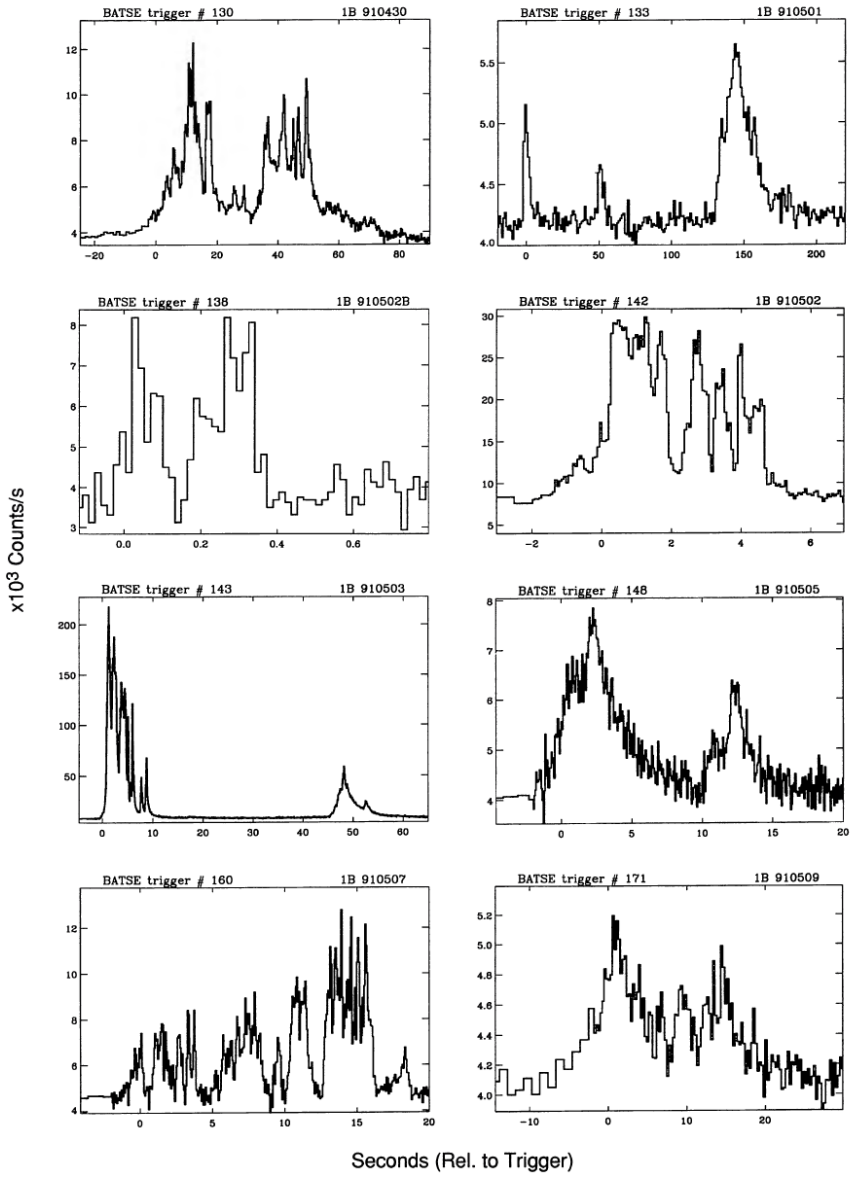

FIGURE 1.11: A sample of BATSE lightcurves showing photon counts of GRBs detected from April 30, 1991 to May 9, 1991 along with the trigger number and time of the bursts relative to the trigger. Figure adapted from Fishman et al. (1994).

distributions of a selected sample of GRBs detected by *Fermi/GBM*. Fig. 1.10 shows a typical non–thermal GRB spectrum (along with a blackbody and synchrotron spectrum for comparison) constructed with the typical values of Band function parameters, i.e., $\alpha \sim -1$, $\beta \sim -2.2$ and $E_{\rm peak} \sim 100$ keV (Nava et al. 2011; also see Fig. 1.9). It should be noted that although most GRB spectra are non–thermal in nature, the spectra from some GRBs fit the thermal spectrum. We discuss the GRB spectra and their origin in greater detail later in § 1.18 and Chapter 2.

As can be seen from Fig. 1.11, the GRB light–curves are highly variable and irregular (in the past it was said that no two GRBs are alike and that statement still holds true today!). As found by Nakar and Piran (2002), the common LGRB variability timescale is ~ 10 ms.

1.15 Compactness Problem

As discussed in in § 1.13 and 1.14, GRBs are bursts of high–energy radiation, located at cosmological distances and have small variability time–scales. It was realized that these observations were physically incompatible with the existing models. In this section we will outline the incompatibility problem and how relativistic motion can resolve it.

To explore the problem heuristically, let us assume a GRB with typical parameters, i.e., situated at cosmological distances, having a luminosity of $L \sim 10^{53}$ ergs/s, an average photon energy $e_\gamma \sim 300$ keV, and with the minimum variability time–scale $t_{\rm var} \sim 10$ ms. Using the luminosity, time–scale, and average photon energy we can calculate the average photon number from such as typical GRB as -

$$N_\gamma = \frac{L t_{\rm var}}{e_\gamma} \sim \frac{10^{53} \times 10^{-2}}{300 \times 10^3 \times 1.6 \times 10^{-12}} \sim 10^{57}. \tag{1.1}$$

As the GRB lightcurve varies on a time–scale of a few milliseconds, this implies that the cause of the variability, which can propagate at most the speed of light, must be able to influence a significant part of the radiation producing source. This provides an upper constraint on the source size -

$$R_{\rm source} \leq c t_{\rm var} \sim 3 \times 10^8 \text{ cm}. \tag{1.2}$$

The source size is about half the Earth's radius, implying that the source is extremely compact. Photons detected from GRBs have energy exceeding MeVs, which is large enough

that pair–production becomes important (even with the majority of photons having lesser energies). Thus, the opacity $\tau_{\gamma\gamma}$ of the photons produced at the source to $\gamma\gamma$ annihilation or e^-e^+ creation is -

$$\tau_{\gamma\gamma} = f n_\gamma \sigma_T R_{\rm source}, \tag{1.3}$$

where f is the fraction of photons that can produce pairs, $n_\gamma = \frac{3N_\gamma}{4\pi R^3_{\rm source}}$ is the photon density and σ_T is the Thomson cross–section. The opacity can be expressed in terms of typical GRB parameters as -

$$\tau_{\gamma\gamma} \sim \frac{N_\gamma}{4\pi R^3/3}\sigma_T R_{\rm source} \sim \frac{3L\sigma_T}{4\pi c^2 t_{\rm var} e_\gamma} \sim 10^{14} \gg 1 \tag{1.4}$$

Eq. 1.4 reveals that the pair-production opacity is extremely large, implying that the high-energy radiation (especially photons having energies exceeding MeV) within the volume will produce copious amounts of e^-e^+ pairs. The increased lepton density will increase the photon opacity to Compton scattering and cause thermalization. While the photon and leptons thermalize, the adiabatic expansion of the plasma causes the temperature to drop. Once the temperature drops below the pair-production temperature threshold ($\sim$ few keVs) none of the escaping photons will have energies exceeding the pair-production threshold and the emerging spectra should be thermal. However, both these arguments are in contrast to the detected high-energy radiation (up to GeVs) and non-thermal spectrum (see § 1.14). Thus, the extreme compactness of the source leads to a disagreement between the theoretical spectra and the observations, which is the GRB compactness problem.

Goodman (1986) and Paczynski (1986) realized that the compactness problem could be resolved if the source was not static but moving relativistically with respect to the observer. By invoking relativistic motion, the observed parameters in the lab frame would be different from the parameters measured in the comoving frame or the rest frame of the burst. As the observed radiation is being emitted by a moving source, the average photon energy in the comoving frame would be reduced to $e'_\gamma = e_\gamma/\Gamma$ due to the Doppler effect. If the source was traveling towards us (the observer) at a Lorentz factor Γ, relativistic beaming reduces the luminosity to $L'_\gamma = L_\gamma/\Gamma^4$. Since GRB spectra have a non-thermal high energy tail (with a power law index β), the fraction of photons energetic enough to produce pairs drops to $f e'^{-2\beta}_\gamma$. Thus, the flux in the comoving frame becomes $f\,(e_\gamma/\Gamma)^{-2\beta}$. Furthermore, due to arrival time effect and relativistic time–dilation, the photon emission times $t'_{\rm var} = \Gamma^2 \times t_{\rm var}$

are much larger (and also the size of the source). As a consequence, eq. 1.4 in the comoving frame becomes -

$$\tau_{\gamma\gamma} = n'_{\gamma}\sigma_T R'_{\rm source} \sim \frac{3fL\sigma_T}{4\pi c^2 t_{\rm var} e_\gamma} \times \frac{1}{\Gamma^{4+2\beta}}. \quad (1.5)$$

For $\Gamma \geq 300$ the obtained opacity is of the order of unity and as a result pair-production is not a problem in the comoving frame. The process of $\gamma\gamma \rightarrow e^- e^+$ is an event and the laws of relativity demand that if any event cannot occur in one reference frame, then it will not be seen to occur in any other frame. As a result, pairs will not be produced and observed in any reference frame. This lack of pairs prevents the radiation from thermalizing and a non–thermal spectrum can thus be produced and detected. Thus, relativistic motion of the source resolves the GRB compactness problem. Significant observational evidence supports the idea of a relativistic jet in GRBs, such as radio scintillation (Frail et al. 1997; Frail et al. 2001) and achromatic breaks in the afterglow light curves (Curran et al. 2007).

1.16 Relativistic Motion and GRB Fireball Model

In the previous section (§ 1.15) it was shown that relativistic motion is necessary to reasonably explain several GRB observables. However, it raises the additional important question of how the motion becomes relativistic in the first place. Several prior works have associated the origin of relativistic motion to compact objects (Blandford and Znajek 1977). It has been proposed that jets can be accelerated by magnetic fields (Komissarov 2011; McKinney 2006) and/or by radiation (Zampieri et al. 2003; Madau and Thompson 2000). However, how GRB jets attain relativistic speeds and what is the underlying acceleration mechanism are still under investigation (Kumar and Zhang 2015). Both magnetic acceleration and radiation have been proposed as the driving mechanisms for GRBs (see Drenkhahn and Spruit 2002; Lyutikov et al. 2003; Zampieri et al. 2003). Hereon we will focus on radiation as the mechanism driving the acceleration of GRB jets.

The first model to explain important GRB properties and which employed radiative acceleration was the fireball model. The idea of the fireball was advocated by Cavallo and Rees (1978) to explain the phenomenon of GRBs. Created by depositing a large amount of energy onto matter confined to a small volume, a sufficiently dense fireball will be optically thick ($\tau \gg 1$) to its own radiation. This radiation can drive the acceleration and

ultra-relativistic expansion of the fireball if the radiation energy density exceeds the fireball's rest mass energy density. Thus, the fireball model resolved the GRB compactness problem by employing radiation as a mechanism to drive the radiation-matter mixture to ultra-relativistic speeds (Paczynski 1986; Goodman 1986).

To understand the dynamics of fireball evolution, let us consider a fireball created by depositing an amount of energy E into a small volume characterized by a radius R_0. We assume that this energy is deposited in the form of thermal or internal energy. As per the above discussion, the fireball works by converting this energy into bulk kinematic motion. If the amount of matter contained inside this volume is M, then the final Lorentz factor η attained when this entire energy is converted into bulk kinetic energy is -

$$\eta = \frac{E}{Mc^2}. \tag{1.6}$$

This is also the maximum Lorentz factor attained by the fireball. We note that for this bulk motion to be relativistic, $E >> Mc^2$ or the initial radiation energy density must exceed the rest mass energy of the fireball.

Radiation-Dominated and Optically Thick Phase

To characterize the dynamics of the fireball as it accelerates and expands, we require the velocity of expansion or the bulk Lorentz factor Γ, its radius R, and the comoving temperature T'. Note that the idea of temperature is well defined only in the comoving frame of the fireball (i.e., the frame moving along with the fireball which only observes adiabatic expansion and no bulk motion). All comoving quantities will be denoted with a prime, unlike those in the lab frame.

To obtain a mathematical relationship between the physical quantities which describe the fireball dynamics, let us consider the fireball when it has expanded to a radius R and attained a Lorentz factor Γ. An adiabatically expanding fireball satisfies -

$$T'V'^{\gamma-1} = \text{constant}, \tag{1.7}$$

where the adiabatic index is given by γ and equals $4/3$ for a relativistically expanding gas (such as a gas composed of photons or relativistically moving particles). In the comoving

frame, an observer would see the fireball expanding spherically with the volume growing proportionally to R'^3. Using eq. 1.7, we obtain -

$$T' \propto \frac{1}{R'}. \tag{1.8}$$

As Γ and R are measured in the lab frame, we need to Lorentz transform between lab and comoving frames to connect them with comoving quantities (such as T'). By employing the principle of conservation of energy at the initial and final points of evolution we can write -

$$E = \Gamma_f (E'_{f,\gamma} + E'_{f,\mathrm{matter}}) \tag{1.9}$$

where $E'_{f,\gamma}$ and $E'_{f,\mathrm{matter}}$ denote the energy in radiation and matter respectively, and Γ_f denotes the Lorentz factor at the final point. Lorentz transformations give us the lab frame volume V in terms of the comoving frame volume V' as -

$$V = \frac{V'}{\Gamma}. \tag{1.10}$$

Using eqs. 1.7 & 1.10, the comoving temperature can be expressed in terms of the lab frame quantities as -

$$T' \propto \frac{1}{(\Gamma V)^{1/3}}. \tag{1.11}$$

During the radiation-dominated phase $E'_{f,\gamma} \gg E'_{i,\mathrm{matter}}$ and since radiation energy density grows as T^4, eq. 1.9 can be rewritten as -

$$\frac{E}{\Gamma} \propto \mathrm{a T'^4_f V'_f}, \tag{1.12}$$

where a is the radiation constant, T'_f is the comoving temperature, and V'_f is the comoving volume at the final point. Since the initial injected energy E is constant, the expression can be further simplified to -

$$\Gamma^{2/3} \propto V^{1/3} \propto R^{2/3} \Delta R, \tag{1.13}$$

which gives us

$$\Gamma \propto R \tag{1.14}$$

Therefore, an optically thick, radiation-dominated fireball's dynamical evolution can be specified by the following proportionality relation -

$$\Gamma \propto R \propto \frac{1}{T'}. \tag{1.15}$$

Eq. 1.15 can also be obtained via alternate methods (see Meszaros et al. 1993; Piran 2004; Kumar and Zhang 2015).

Matter-Dominated and Optically Thick Phase

If the fireball remains opaque to photons, it will continue to accelerate and convert internal energy into bulk motion. As the total internal energy of the fireball is constant and finite, at some point during the evolution all that energy will be converted into bulk kinetic motion. Thereafter, as radiation is unable to further accelerate the fireball the acceleration saturates, and as a result, the maximal Lorentz factor is achieved at saturation. Assuming that the fireball remains in the radiation-dominated phase up to this point, the characteristic radius where saturation occurs is called the saturation radius and can be obtained as -

$$R_{\rm sat} = \frac{\eta}{\Gamma_0} R_0 = \eta R_0. \tag{1.16}$$

where Γ_0 is the fireball bulk Lorentz factor at the initial radius R_0 (which equals unity if the fireball is assumed to start from rest).

Optically Thin Phase and Photospheres

All fireballs will eventually become optically thin, i.e., when $\tau \sim$ unity. At this point radiation will decouple from the fireball and escape. As a fireball devoid of photons cannot be radiatively accelerated, the Lorentz factor will saturate and its terminal value depends upon whether the fireball has achieved saturation or not. The characteristic radius where radiation and matter decouple is referred to as the photospheric radius (denoted by R_{ph}) and is traditionally computed at $\tau \sim 1$.

Fireball evolutionary dynamics depend upon the ratio of photospheric to saturation radius, which can be used as a proxy for the fireball opacity. If the fireball becomes transparent before reaching $R_{\rm sat}$, it stops accelerating and coasts at the terminal Lorentz factor ($\Gamma_{\rm term}$) achieved at the photosphere $\Gamma_{\rm term} = \Gamma_{\rm ph}$, which is less that η. In the other case $R_{\rm ph}/R_{\rm sat} \geq 1$, the conversion of internal energy to bulk motion is complete and $\Gamma_{\rm term} = \eta$. The Lorentz factor evolution of an expanding fireball can thus be summarized by the following equation

-

$$\Gamma_{\rm term} = \begin{cases} \Gamma_{\rm ph} = \eta \frac{R_{\rm ph}}{R_{\rm sat}}, & {\rm for} \frac{\rm R_{ph}}{\rm R_{sat}} < 1 \\ \eta, & {\rm for} \frac{\rm R_{ph}}{\rm R_{sat}} \geq 1 \end{cases} \tag{1.17}$$

Fireball Geometry

We can see from eq. 1.17 that the dynamical evolution of the Lorentz factor depends upon the ratio $R_{\rm ph}/R_{\rm sat}$. As the volumes in the comoving and the lab frame are connected by the bulk Lorentz factor Γ (see eq. 1.10), any change in the kinematic evolution will affect the dynamical evolution of the fireball volume and thus, its geometry.

In the lab frame, the particles move in radially outward directions and are geometrically distributed in a shell of width ΔR, the size of which is of the order of the initial fireball radius R_0 (Meszaros et al. 1993; Piran 2004). As the particles move at relativistic speeds, the speed difference between slowest and the fastest particles is extremely small and the width of the shell does not change appreciably. However, an appreciable change in the width occurs after the fireball covers a large enough distance (or travels for a long enough time such that the separation between the fastest and the slowest particles becomes comparable to the size of the shell). If the radial velocity spread between the fastest and slowest particles is $\Delta v = c - v$, then the separation between these after time t is $\Delta R(t) = \Delta v t$ (which would be the width of the shell at time t). This shell width can be further expressed as -

$$\Delta R(t) \sim \Delta v t \sim \frac{\Delta v R(t)}{c} \sim \frac{R(t)}{\Gamma^2} \tag{1.18}$$

Let the radius equal R_b when the width of fireball shell starts to appreciably evolve and deviate from the constant width R_0. From eq. 1.18, it can be seen that $R_b > R_{sat}$ and occurs when the fireball is no longer radiation-dominated. Using eq. 1.18, for $\Delta R(t) > R_0$, R_b equals $\eta^2 R_0$. As a result, the lab frame width evolves as -

$$\Delta R \sim \begin{cases} R_0, & {\rm for}\ R < R_b \\ R/\Gamma^2, & {\rm for}\ R \geq R_b \end{cases} \tag{1.19}$$

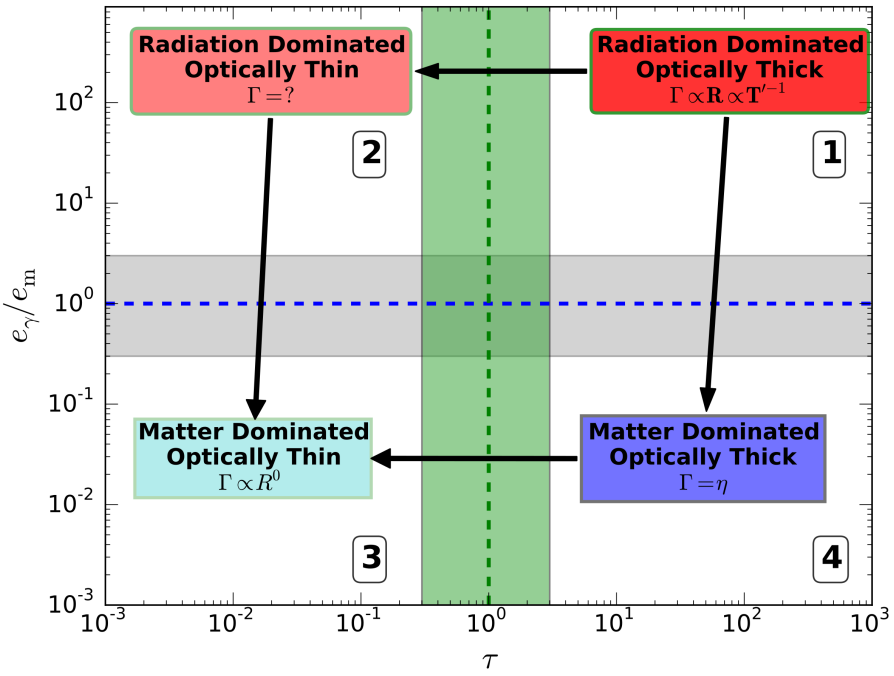

FIGURE 1.12: Diagram illustrating the phase space evolution of a GRB fireball based on the fireball model. The y axis depicts the ratio of radiation to matter energy density and the x-axis plots the opacity. In the phase space diagram, GRB fireballs begin their evolution in quadrant 1 ($\tau \gg 1, e_\gamma/e_m \gg 1$) and end it in quadrant 3 ($\tau \ll 1, e_\gamma/e_m \ll 1$). The arrows show possible evolutionary paths of fireballs. The shaded regions near $\tau \sim 1$ and $e_\gamma/e_m \sim 1$ represent transition zones or regions where fireball evolution has not been well studied.

It is instructive to look at the width evolution in the comoving frame also. Using eq. 1.10, the shell width in the comoving frame can be expressed as -

$$\Delta R' \sim \begin{cases} \Gamma R_0, & \text{for } R < R_{\rm sat} \\ \eta R_0, & \text{for } R_{\rm sat} \leq R < R_{\rm b} \\ R/\eta, & \text{for } R \geq R_{\rm b} \end{cases} \tag{1.20}$$

1.17 GRB Phase Diagram and Unexplored Phase Space

In the previous sections we outlined different evolutionary paths for GRB fireballs. The fireball's evolution depends on its initial energy density and opacity, and the effect of both these parameters can be mathematically represented by the ratio of the characteristic radii, i.e., $R_{\rm ph}/R_{\rm sat}$. The information presented in the previous sections can be summarized in

the form of a GRB phase space diagram (see Fig. 1.12). The diagram plots the ratio of radiation to matter energy density (e_γ/e_m) on the y-axis and the opacity of the fireball on the x axis. We divide the diagram into four regions (or quadrants), similar to the quadrant division in the Cartesian coordinate system. The evolutionary trajectories are also presented on the diagram and they depend upon the path taken by the fireball to reach the matter-dominated, optically thin phase.

As we will discuss in detail in Chapter 3, there are several zones and regions in the phase space that cannot be explored analytically (for example the Lorentz factor evolution during the optically thin regime). In the same chapter, we will also present our Monte Carlo code which we can use to study fireball evolution thorughout the entire phase space.

1.18 Prompt Emission Mechanisms

As outlined in § 1.14, the mechanism behind the prompt emission of GRBs is still unknown and under investigation. Just like the driving mechanism of the relativistic jet is either magnetic or radiation (or scattering) driven, the primary emission mechanisms that aim to reproduce the observed prompt emission can be divided into two classes which we discuss in the next two sections.

Synchrotron Emission

Synchrotron radiation is produced by relativistically moving charged particles under the influence of magnetic fields (Rybicki and Lightman 1986). The fact that magnetic fields are ubiquitous in astrophysical environments (especially jet producing ones), GRB prompt spectra are non-thermal, and GRB afterglow (the multi-wavelength radiation emission occurring after the prompt emission phase) spectra can be well explained with synchrotron models, makes synchrotron radiation a very attractive emission mechanism for explaining prompt GRB emission. As a result, synchrotron has been the mechanism of choice for the GRB community and a significant amount of work exists to convince people of its validity (see reviews by Kumar and Zhang 2015; Pe'er 2015; Pe'er and Ryde 2016).

However, there are several observational properties of the prompt emission that the synchrotron model is unable to address. One such property is the inability of synchrotron

models to explain the observed low energy slope for most GRBs ($\alpha \sim -1$). The observed slopes are much steeper than the slopes synchrotron can produce ($\alpha \sim -2/3$ or $-3/2$). This problem is well known in the GRB community as the 'Synchrotron line of death' (Preece et al. 1998). Fig. 1.10 plots the spectra of GRB and also synchrotron emission, and it can be clearly seen that they are inconsistent with each other. Synchrotron models also fail to explain several correlations that have been observed in the data (without invoking additional assumptions, e.g., see Zhang and Mészáros 2002). These include the Amati (Amati, L. et al. 2002) and the Yonetoku (Yonetoku et al. 2004) correlations. In addition, the synchrotron models requires significant fine tuning of parameters (such as magnetic field strength, Lorentz factor etc.) in order to reproduce the observed clustering of peak energies in GRBs (Brainerd 1998; Preece et al. 2000).

Photospheric Emission

Due to severe difficulties encountered by the synchrotron emission mechanism the other model that is gaining popularity is the photospheric model. As outlined in § 1.16, the photosphere is the radius at which the GRB plasma / fireball becomes transparent to radiation. Unlike the synchrotron mechanism which occurs primarily in the optically thin regime, photospheric emission is produced when the fireball/jet transitions from optically thick regime to transparency. The radiation released during this process is expected to be thermalized, unless no energy injection occurred at moderate to low opacity (we shall discuss the impact of such injections on GRB spectra in greater detail in Chapter 2). It is important to note that thermal GRB spectra have been detected but they are rare (most spectra are non-thermal as has been outlined in detail in § 1.14). However, observations indicate that brighter GRBs and GRBs for which spectra can be time-resolved exhibit a thermal component. So the non-detection of a thermal component can be attributed to the fact that the photon counts are too low. As discussed in § 1.16, photospheric emission occurs naturally because of fireball (or jet) evolution. The same works that invoked relativistic motion in GRBs also predicted quasi-thermal emission detections (Goodman 1986) from these sources due to light aberration effects (Pe'er 2015).

Fig. 1.10 plots a normalized typical Band function as well as the Planck or Blackbody distribution. It is clear that these two are not in agreement with the Band function due

to the broadness of the Band spectrum. However, there are several ways to broaden the thermal spectrum, one of which is the light aberration effect mentioned earlier. Another broadening process is geometrical broadening (Lundman et al. 2013) where the on-axis jet photons are detected at different (higher) energies as compared to photons emitted off-axis. As a result, due to more scatterings/adiabatic losses experienced by off-axis photons as well as reduced Doppler boosts, these lower energy photons flatten the low energy part of the thermal spectrum and broaden the blackbody spectrum as a whole.

Sub-photospheric dissipation or dissipation of bulk kinetic energy into thermal energy below the photosphere is another promising mechanism that can broaden a thermal spectrum into a non-thermal one. Sub-photospheric Comptonization, i.e., inverse Compton scattering of photons by energized leptons, has been investigated as the energy transfer mechanism from matter to radiation in several prior works (Giannios 2006; Pe'er et al. 2006). These works were able to show spectral broadening of the thermal spectrum and reproduced the Band function's high-energy spectral slopes. However, these works were unable to replicate the low energy spectral index and assumed that leptons always remain thermally distributed. In Chapter 2, we discuss our Monte Carlo simulations that self–consistently evolve photon and lepton populations to investigate sub-photospheric dissipation (Chhotray and Lazzati 2015). We show that a dissipation event leads to disequilibrium between leptons and photons, and that transient non-thermal spectra can arise during the process of equilibrium restoration. We obtain the low energy spectral index α from our simulations and discuss the unexpected spectral correlations that emerge from our results. Thus, sub-photospheric dissipation remains a viable model for producing GRB prompt emission.

At the present stage, neither synchrotron nor the photospheric mechanism can take the title of *the radiation mechanism* responsible for prompt emission. Recently, several works have focused on the study of spectral width (a measurement of broadness of the observed spectra) and its evolution as a tool to evaluate if the width of GRB spectra are in agreement with synchrotron spectral widths. Axelsson and Borgonovo (2015) & Yu et al. (2016) analyzed unfolded empirical GRB spectral width and reached the conclusion that synchrotron widths are unable to explain the observed width of a large fraction of GRBs. To the contrary, results from Burgess (2017) suggest that synchrotron is still a viable emission mechanism if a physical model is directly fitted to GRB data, rather than to empirical

data. The results have not been too conclusive and, therefore, the prompt GRB radiation mechanism is still an open problem seeking a solution.

1.2 AGNs

1.21 Introduction

Active-**G**alactic **N**ucleus (or AGN, with the plural AGNs for Active Galactic Nuclei) refers to the nuclear region of a galaxy having energetic activity that cannot be directly associated with stars. This leads to an increased luminosity of the nuclear region as compared to regular galaxies. The nuclei of such active galaxies have been detected across multiple wavelengths of the electromagnetic spectrum - from radio to gamma-rays (Beckmann and Shrader 2012). Although all AGNs may not necessarily emit across all wavelengths, all have been observed to emit in X-rays (Elvis et al. 1978; Peterson 1997; Beckmann and Shrader 2012). Strong evidence suggests that the central / nuclear regions of all galaxies harbor a super–massive black hole – several orders of magnitude more massive than the sun. It is currently believed that this extra activity in the nuclei of active galaxies is powered by accretion of matter onto this super–massive black hole leading to the AGN phenomenon.

AGNs have several sub-classes primarily because of the manner in which each of the sub-classes were first historically discovered. In the next section we shall discuss these sub-classes and the observational differences between them. We will then outline how these sub-classes can be unified under the AGN umbrella.

1.22 AGN Classification

The diversity shown by AGNs is phenomenal. For example, the central black hole masses range from $10^6 M_\odot$ to $10^{10} M_\odot$, the bolometric luminosities vary from 10^{41-48} ergs s^{-1}, some AGN spectra show strong emission features whereas others don't. Such diversity and the detection of AGNs across several wavebands initially led to the labeling of the sub-classes as different objects. The various AGN sub-classes were discovered individually

and no connections were established between these different sub-classes until recently. We will now discuss these sub-classes and their observational features before unifying them under the AGN black–hole paradigm.

Seyfert Galaxies

The class of active galaxies which we refer to as Seyferts were first detected by Edward Fath and Vesto Slipher in 1908 (Peterson 1997). Seyfert galaxies are named after Carl Seyfert who noted that these galaxies have star–like bright cores with high–excitation nuclear emission lines (Seyfert 1943). They are different from non–active galaxies due to the presence of an active core - which is bright and point like (and thus unresolved). The brightness of the core is comparable to the brightness of the rest of the galaxy. The characteristic feature that aids in identification of Seyfert galaxies is that their cores emit strong, high–ionized narrow emission lines (unlike stars which show strong absorption lines as well). Seyfert galaxies were further classified into two primary categories based upon the presence (Type I Seyfert) or absence (Type II Seyfert) of broad emission lines (Khachikian and Weedman 1974). However, several Seyfert spectra display intermediate and borderline features and they have been further classified according to their Balmer line characteristics (Osterbrock 1977; Osterbrock 1981). Today, Seyfert galaxies are classified as lower–luminosity AGNs (Schmidt and Green 1983). A better understanding about why they are classified as lower–luminosity objects will emerge in the follwing section.

Quasars

With the advent of radio astronomy in the 1950s, several all-sky radio surveys were conducted which led to the discovery of objects actively producing radio waves. This led to the compilation of several catalogs of radio sources (e.g., Edge et al. 1959 - the Cambridge all-sky catalog) containing information about radio sources emitting at particular frequencies and fluxes. Several objects in the catalog appeared, optically, as point like sources (similar to stars), however, their spectra revealed strong emissions and broad spectral lines at wavelengths not seen before (unlike stellar spectra). Fig. 1.13 shows a composite optical/UV spectra of several quasars detected in the Sloan Digital Sky Survey (SDSS) - where

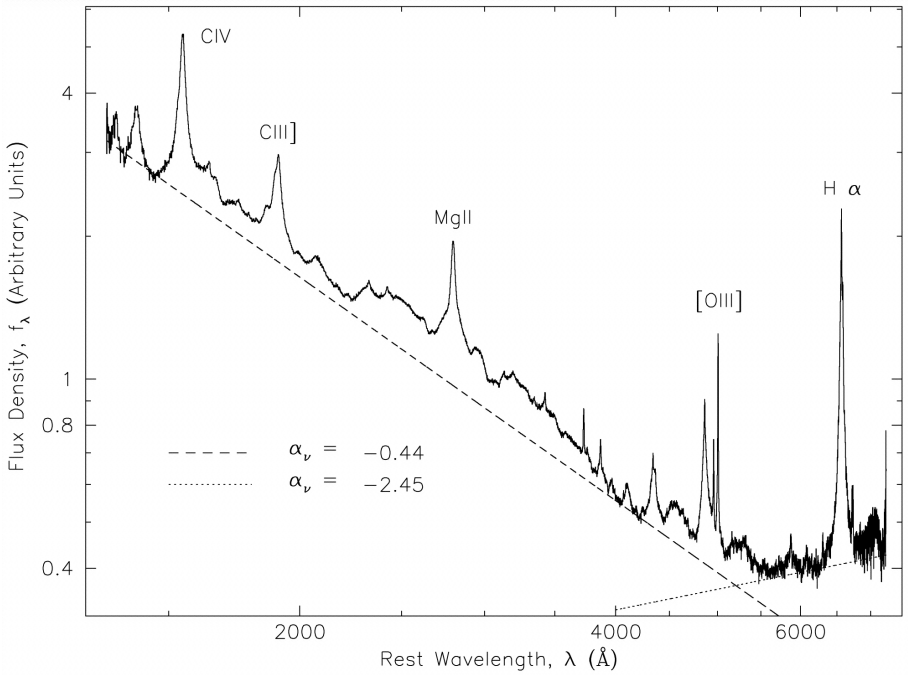

FIGURE 1.13: Composite quasar spectrum generated using the geometric mean of the input spectra from quasars in the Sloan Digital Sky Survey (SDSS). Figure adapted from Vanden Berk et al. 2001.

broad lines (as well as narrow ones) are visible. They were also observed to be bluer than stars. As the nature of these star like radio sources was not understood, they were called '**qua**si-stell**a**r **r**adio sources', which was later shortened to quasar.
Schmidt (1963) was the first to realize that the optical spectra detected from the radio source 3C 273 could be explained from the lines of known elements if the emission occurred at $z = 0.158$. This was one of the largest redshifts detected at that time and much larger than for Seyferts. Because of the large distance involved, the 3C 273 luminosity exceeded those of bright spirals by a factor of 100 (3C 273 is still the brightest known optical quasar). As summarized in Schmidt (1969), quasars have the following properties –

- Star like objects detectable at radio frequencies
- Large redshifts (redshifts ≥ 0.1 were considered large in the 1960s)
- Variability in continuum flux
- Large UV flux / bluer in comparison to stars and inactive galaxies
- Broad emission lines

Though the first quasars were found via all sky radio surveys, it was soon realized that quasars could be detected without radio localizations. Being optically bluer, UV rich and variable in comparison to stars, quasars were also detected in the optical / UV wavelengths. This led to the discovery of several quasar-like objects many of which were *radio–quiet*. These objects were called QSOs or Quasi-stellar Objects due to the non-detection of an associated radio source. The criteria for a QSO to be labeled radio–quiet is that the radio flux from such an object should be less than ten times its optical flux (Peterson 1997; Beckmann and Shrader 2012). In the current literature, the terms QSO and quasar are used interchangeably.

Radio Galaxies

Optical observations of several radio sources (identified by all-sky radio surveys) associated them with galaxies, which are now called radio galaxies. The radio emission from these

galaxies is produced by synchrotron radiation. Radio galaxies can be morphologically divided into two categories, 1) extended components (which can be resolved) and 2) compact (where the source is unresolved).

The extended component morphology displays two lobes of emission symmetric to the galaxy (or the central quasar) which can extend to Mpc scale. The extended component is optically thin to synchrotron emission and also displays steep spectra (see Peterson 1997). Extended sources can sometimes also show jets, that appear to originate at the central compact region and then extend to produce the lobes (Bridle and Perley 1984). Within the extended component morphological class, Fanaroff and Riley (1974) proposed a further division based on the radio luminosity of the sources. FR I extended radio sources exhibit lower luminosities, with brightness decreasing towards the edges. FR II sources, however, are more luminous and display limb–brightening.

For the compact component morphology type, the emission appears to be generated from a point source, such as the position of the optical quasar. The compact source is not considered to be optically thin to its synchrotron emission and displays a flat spectrum (Peterson 1997).

Optical studies of radio galaxy cores show that they are similar to Seyfert cores. As a result, radio galaxies producing broad emission lines (optical/UV spectrum) are called broad line radio galaxies (BLRG). In contrast, if a radio galaxy core emits narrow emission lines then the radio galaxy harboring that core will be referred to as a narrow line radio galaxy (NLRG) (Beckmann and Shrader 2012). Radio galaxies are generally found to be giant, massive elliptical galaxies.

Low–Luminosity AGNs

Low–luminosity AGNs fall into the category of objects that have a bolometric luminosity in the range $10^{37} < L_{\rm bolo} < 10^{40}$ erg s^{-1} (Beckmann and Shrader 2012). These AGNs fill the gap that separates Seyferts and objects like Sgr A (corresponding to the location of the radio source at the Milky way's center, strongly believed to be associated with a supermassive black hole).

First identified by Heckman (1980), LINERs or Low–Ionization Nuclear Emission–Line Regions belong to this category. LINERs are characterized by strong emission lines and

faint core luminosities. They differ from Seyfert 2 as they exhibit strong low–ionization lines. LINER galaxies seem to be younger and their X-ray spectra are dominated by starburst emission unlike those associated with AGN cores (Beckmann and Shrader 2012).

Blazars

Blazars are a sub-class of AGNs characterized by rapid variability (in some cases even IDV or intra-day variability, i.e., with spectral variations occurring in a span of hours). This variability has been observed in radio and optical wavelengths (Wagner and Witzel 1995). They are now known to be active across almost the entire electromagnetic spectrum - from radio to very high energy gamma-rays (and even in the TeV regime) (Abdo et al. 2009a). Blazars were found and initially classified based on their optical variability. However, observations at non–optical wavelengths (e.g., radio and X-ray) were also able to discover several objects, which turned out to be blazars when viewed through telescopes (due to rapid optical variability). Blazars that were first identified in such a manner (i.e., discovered in radio and X–rays), were labelled under the categories of radio–selected and X–ray selected blazars, respectively. In order to improve blazar classification scheme and make it independent of the particular wavelength at which they are first discovered, blazars are now distinguished based upon their entire spectra or SED (spectral energy distribution). Historically, blazars were first divided into two categories depending upon their optical spectra - BL Lacertae objects (BL Lac objects) and Flat Spectrum Radio Quasars (FSRQ). BL Lacertae objects display all characteristics of blazars with the exception that their optical spectra are generally featureless or lack strong emission lines. Due to their rapid optical variability, they were discovered in 1929 (Hoffmeister 1929) but were erroneously identified as variable stars. As a result of this misidentification these blazars were incorrectly christened as BL Lacertae objects or BL Lac objects for short. It took several years for these BL Lacs to be associated with radio sources (Schmitt 1968) and recognized as extragalactic objects (Oke and Gunn 1974). Recently, by using the spectra of bright BL Lacs, Stocke et al. (2011) have shown that they do possess weak lines. Due to the difficulty in obtaining line spectra from a featureless continuum, only the redshifts of the brightest and nearest BL Lacs have been measured. As a consequence, only a few BL Lacs beyond $z = 0.5$ are known (Beckmann and Shrader 2012). Depending upon where the SEDs of BL

Lacs peak, those that have dominant X–ray emissions (relative to radio) are called 'high–frequency peaked BL Lacs' (HBL) and conversely, those that peak in the radio frequencies are termed 'low–frequency peaked BL Lacs' (LBL).

The other blazar category is the category of Flat Spectrum Radio Quasars or FSRQ. FSRQ are differentiated from BL Lacs by the strength of their emission lines, i.e., the equivalent width of the emission lines of FSRQ exceeds 5 Å. This category is further sub–divided into Optically Violent Variables (OVVs) that show strong optical variability and Highly Polarized Quasars (HPV) - which also show strong polarized continua. Due to stronger line emissions, FSRQ have been found to a redshift ~ 2, but not beyond (Beckmann and Shrader 2012).

1.23 AGN structure

Based upon decades of research since the discovery of the very first AGNs, the following are thought to be the basic structural components of an AGN. I will now discuss these components in some detail.

Super–massive Black Hole (SMBH)

A brief mention of the existence of a super–massive black hole was made in § 1.21. Based upon the extreme luminosity, compactness, and time–variability arguments, the idea that accreting black holes can possibly drive the AGN phenomenon was presented several decades ago (Salpeter 1964; Zel'dovich 1964; Lynden-Bell 1969). There is now strong evidence that super–massive black holes are present in the centers of most (if not all) galaxies. There are several methods by which central black hole masses can be estimated, e.g., the virial / reverberation mapping method (requires measuring the spectral widths of broad lines close to the black hole), the $M - \sigma$ correlation method (using this tight empirical relation between the mass of the black hole and the stellar velocity dispersion of the galactic bulge, see Peterson 2014 for details). It is currently believed that black holes at the centers of galaxies have masses between $10^6 M_\odot$ and $10^{10} M_\odot$ (Ghisellini 2013).

Accretion Disc

The super–massive black hole at the center of the galaxy will naturally attract mass (such as gas, dust, and stars) towards it. Most of the in–falling matter accretes with some angular momentum leading to the formation of an accretion disc. It is well known that accretion onto compact objects is the most efficient process to convert gravitational potential energy into other forms of energy, such as radiation (Frank et al. 2002). This is the only process efficient enough to power AGNs (Salpeter 1964; Zel'dovich 1964; Lynden-Bell 1969). Emission from the accretion disc typically peaks around the UV wavelengths (Ghisellini 2013) and is likely responsible for the increased UV emission from AGNs (which is the reason why AGNs are bluer than stars and galaxies).

X-ray corona

As stated in § 1.21, X-ray emission is a characteristic feature of AGNs. The accretion disc is unable to reach high enough temperatures to produce X-ray emission (which in some cases extends to several hundred keVs). The X-ray corona is believed to be a region located above the accretion disc and also significantly hotter than the disc (Ghisellini 2013).

Broad Line Region (BLR)

As we continue to move radially outward from the central black hole we encounter the Broad Line Region (BLR) harboring the sources of broad emission lines. Due to variability detected in the broad emission lines but not in the narrow lines, broad lines are now thought to be emitted from a region that lies closer to the black hole (which does not emit any narrow lines) (see Beckmann and Shrader 2012).

The line intensities and ionization states of the broad lines have been used to infer that, in general, BLRs have temperatures $\sim 10^4$ K and densities $\sim 10^9$ cm^{-3} (Beckmann and Shrader 2012; Ghisellini 2013). Temperatures of $\sim 10^4$ K can produce spectral broadening of ~ 10 km/s. However, the width of the broad lines indicates velocities between $10^3 - 10^4$ km/s (see Fig. 1.13). Thus, the detected broadening must be attributed to bulk-motion of the sources in the BLR and suggests that this region lies close to the black hole. The reasons for this bulk–motion are at present not understood (Beckmann and Shrader 2012).

Using the reverberation mapping technique, the BLR has been estimated to be located at a distance of $0.01 - 1$ parsec (Beckmann and Shrader 2012) from the SMBH.

Torus

Located at several parsec from the black hole is a toroidal clumpy structure composed of dust (Beckmann and Shrader 2012; Ghisellini 2013) known as the torus. It lies beyond the accretion disc and the BLR. The torus plays the key role of obscuring radiation and thus unifying radio–quiet AGNs (see § 1.24; Beckmann and Shrader 2012; Ghisellini 2013).

Narrow Line Region (NLR)

This region is thought to produce the narrow forbidden emission lines that are seen in all AGNs (see Fig. 1.13), and is distinct from the Broad Line Region (see § 1.23). Using the line intensities and ionization states of the observed emission lines, the typical values of density and temperature of the NLR are estimated to be $\sim 10^{3-5}$ cm^{-3} and $\sim 10^4$ K, respectively. The line widths indicate typical velocities of $\sim 400 - 500$ km/s.
NLR can currently be resolved in the nearest Seyferts and exhibits a biconical morphological structure, which can be attributed to the collimating action of the torus (Kraemer et al. 2008). It is estimated that the NLR is located $10^2 - 10^4$ parsecs (Beckmann and Shrader 2012) from the galactic center.

Jets

As discussed in § 1.22, jets or outflows have been detected in AGNs since the 1950s. One example of a jet from an elliptical galaxy is the M87 jet (see Figs. 1.5 & 1.6). Size of radio jets range from hundreds of parsecs to several Mpc. Several AGN jets are also known to be relativistic and show apparent superluminal motion. Due to their relativistic nature, the appearance of and emission from such jets is modified due to relativistic considerations (as has been discussed in § 1.15), especially if the jets are aligned with our line of sight.
Only 10% of all AGNs are associated with jets. The process of jet creation and the composition of jets is not known (Beckmann and Shrader 2012).

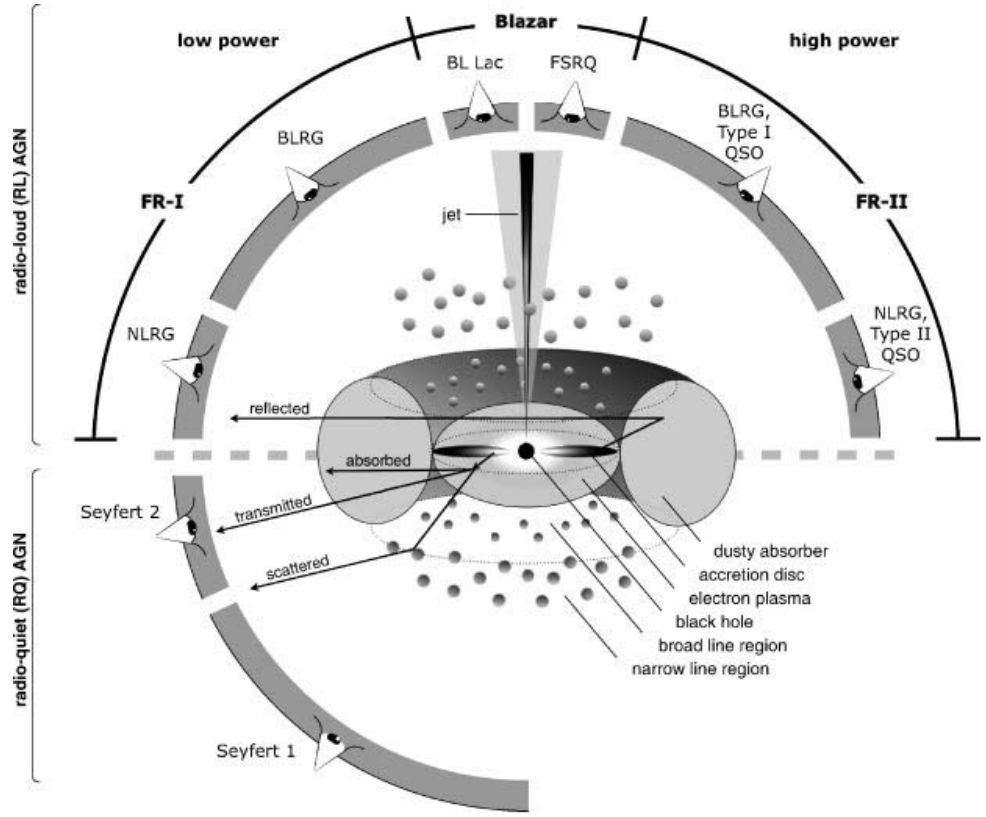

FIGURE 1.14: Cartoon diagram representing the unification of AGN phenomena. The diagram illustrates the idea that AGNs are powered by a supermassive black hole located in the galactic center and the type of AGN we observe depends upon the viewing angle, the occurrence of a jet, and the power of the central engine. Image adapted from Beckmann and Shrader (2012).

1.24 AGN Unification

In § 1.22, we have outlined the observational characteristics of several objects belonging to the class of AGNs. Now we discuss the black hole paradigm of AGNs which unifies AGN diversity by explaining the variation in observed properties due to orientation effects and few free parameters.

Fig. 1.14 is a cartoon diagram that depicts the AGN unification scheme. We begin the unification by first providing an explanation for why Type 2 Seyferts lack broad emission lines. The Seyfert unification idea is based on the assumption that all Seyfert galaxies

emit both broad and narrow emission lines, but we do not observe broad lines from some Seyferts due to our relative orientation. The broad emission lines are emitted by the BLR, which is located closer to the central black hole than the dusty torus (see Fig. 1.14 and § 1.23). The narrow lines, visible in all Seyferts, originate from the narrow line region, which lies outside the torus and thus cannot be obscured by it. If a galaxy is viewed from the side (see Fig. 1.14) such that the torus obscures the BLR, only the narrow emission lines will be detected. Such a galaxy will lack broad lines and will be classified as a Type 2 Seyfert. However, if the same galaxy is observed from a direction away from the torus, such that the torus in unable to obscure the BLR, both broad and narrow emission lines will be detected. As a result the same galaxy (which was earlier classified as Seyfert 2) will now be classified as a Type 1 Seyfert. In the case of Type 2 Seyferts, the broad lines could still be detected indirectly if these lines were scattered by electron plasma in the region surrounding the torus. As post-scattered radiation is polarized, detection of these polarized broad lines in Type 2 Seyferts would provide evidence for this scheme. Polarized broad line emissions were first detected by Antonucci and Miller (1985) in the spectra of NGC 1068, a Type 2 Seyfert galaxy.

The Seyfert unification scheme based on obscuration is insufficient to explain the phenomena of radio emission and therefore, a separate unification scheme was proposed to unify radio–quiet and radio–loud AGNs. Seyfert galaxies (which have now been unified as the same object viewed from different vantage points) are known to be weak radio emitters and are devoid of jets (Lal et al. 2011). As a result, Seyferts along with LINERs are placed in the radio–quiet AGN category. As noted in § 1.22, radio galaxies also display narrow and broad line features. BLRGs and NLRGs can be unified in the manner similar to Seyferts, with the torus obscuring the BLR for NLRGs (also see Fig. 1.14). Unifying the radio–loud AGNs require additional assumptions and parameters. The first assumption which is partly observationally motivated (also discussed in § 1.22) is that radio–loud AGNs are associated with jet phenomena - which is related to the central black hole activity. The Fanaroff–Riley extended radio source classification can be combined into a single class if the black holes powering these jets are low–powered (FR I) or high–powered (FR II). Furthermore, the beaming emission from jets can be used to explain the difference in the spectra observed for compact and extended radio galaxy morphologies. If the jet is point-

ing at us its emission is beamed (it would appear brighter) and we observe a flat spectra (similar to compact component spectra - see § 1.22) whereas, if the jets are misaligned or not pointing at us we would observe the object at its intrinsic luminosity and detect a steeper spectral slope (similar to extended morphology spectra in § 1.22).

Emissions from the jet have also been used to explain the short variability time-scale observed in blazars. Relativistic beaming makes the spectra flat (as the names of FSRQ suggests) and thus the slope of the spectra can be used as an indicator of the viewing angle between the jet and the observer. Beaming also makes the variability time scale smaller due to relativistic effects. Doppler boosting and beaming can also explain the very high–energy emissions from BL Lacs and FSRQ. The beamed emission from BL Lac jets is also thought to be responsible for its characteristic featureless continuum spectra. The enhanced jet luminosity can effectively overpower and hide the line spectra making it harder to detect. This is consistent with the idea that only the nearest or intrinsically brightest BL Lacs have strong enough spectral lines that could be seen on top of the jet emission.

We have thus outlined some unification schemes and the importance of jets to those schemes. We would like to point out that the above unification schemes are still a work in progress as there are several unresolved issues. Moreover, there exist alternate unification schemes that invoke additional parameters such as black hole spin. These can be found in Beckmann and Shrader (2012).

1.25 Structured Jets

As discussed in § 1.24, jets play a crucial role in the emissions produced from blazars. The large bulk Lorentz factor associated with these jets is crucial for overcoming the compactness problem (suppressing pair–production) and is responsible for the observed high–energy emissions. The process of relativistic beaming causes a dramatic increase in the flux observed from jetted sources.

In comparison, misaligned AGNs (or MAGNs) are AGNs that do not have their jets pointed towards us. The term misaligned implies that the jet points in a direction which is not aligned with our line of sight. Due to the misalignment of the jet, there is no amplification of the observed flux or Doppler boosting and hence, these objects are not expected

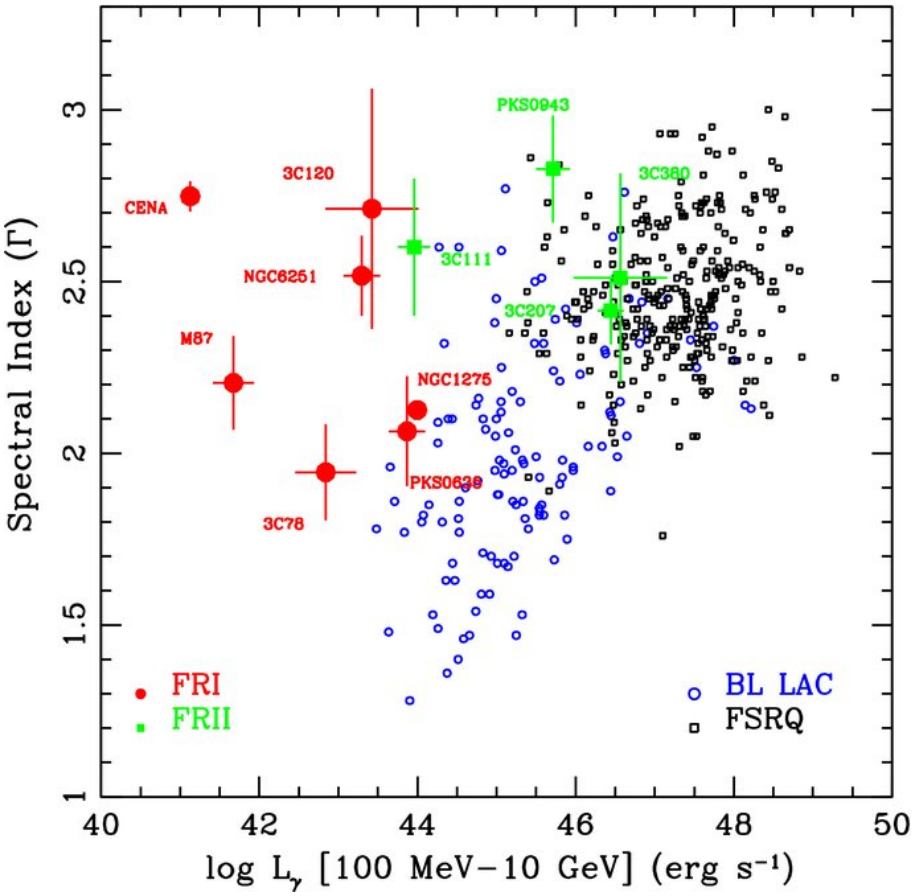

FIGURE 1.15: Spectral slopes of various gamma-ray sources detected in the *Fermi* sample plotted against the gamma-ray luminosity (100 MeV to 10 GeV). Image adapted from Abdo et al. (2009b)

to be detected in high–energy wavebands. These MAGNs would include FR-I and FR-II type radio galaxies. However, the LAT (Large Area Telescope) onboard *Fermi* surprisingly detected GeV photons from several misaligned AGNs (in particular radio galaxies) (Abdo et al. 2009b; Neronov et al. 2010; Abdo et al. 2010; Grandi 2012). Fig. 1.15 plots the slopes of spectra obtained from several *Fermi* sources against their gamma-ray luminosities, and shows that several radio galaxies are gamma-ray emitters. The existence of MAGNs is in agreement with AGN unification models, where radio–galaxies are considered as de–beamed blazars, with jets pointing away from us. However, what is puzzling is the fact that we still detect high–energy photons from these radio galaxies even though their jets are not pointed at us.

The Lorentz factor obtained from detailed analysis of the SED of several radio galaxies is ~ 3 (Migliori et al. 2011; Abdo et al. 2009b), which is lower than typical BL Lac values. This points to the fact that these radio galaxies have slower jets which might be visible at comparatively larger viewing angles. To explain these slow jets, models have been proposed such as decelerating jets (Georganopoulos and Kazanas 2003a) and the spine–layer structured jet (Ghisellini et al. 2005). The simplest of these complex structured jet models is a two component model called the spine–sheath jet or the spine–layer jet. The spine–layer jet morphology is supported by radio and optical observations (Laing 1996; Swain et al. 1998; Attridge et al. 1999), and by simulations (Rossi et al. 2008).

Additional evidence for (at least) two-zone structured jets emerges from limb brightening morphology. VLBI radio mapping of the galaxy Markarian 501 by Giroletti et al. (2004) shows significant limb brightening features. Giroletti et al. (2004) associate these features to a velocity structure within the jet, with the slower outer layers encapsulating the faster moving inner region. Several other studies confirm the existence of limb brightening features in many AGN jets, e.g, TeV blazars (Piner and Edwards 2014; Piner and Edwards 2004), BL Lacs (Giroletti et al. 2006). The idea of structured jets is strengthened further by the detection of decelerating spines in TeV emitting BL Lacs (Edwards and Piner 2002; Piner and Edwards 2004; Piner et al. 2008; Piner et al. 2010) due to radiative interactions between the sub–structures.

By invoking two jet components traveling at different velocities, the spine–layer structured jet can explain the GeV emission from radio galaxies at large viewing angles (due to the

slower outer layer) and the phenomenon of limb brightening. In the spine–layer morphology, deceleration of the jet components can occur due to radiative feedback (Compton rocket effect - Odell 1981) between the spine and the layer.

In Chapter 4, we will discuss how radiative feedback between the spine and the layer can lead to a scenario where the layer travels at just the right velocity to produce the observed GeV emission.

GAMMA-RAY BURST SPECTRA AND SPECTRAL CORRELATIONS FROM SUB–PHOTOSPHERIC COMPTONIZATION

Atul Chhotray, Davide Lazzati

Journal: The Astrophysical Journal
Address of Journal:
NOAO/AURA
950 N. Cherry Ave.
Tucson, AZ 85719
Issue Manuscript Appears in: Issue 802 (April 1, 2015), Pages 132-143,

2 GAMMA-RAY BURST SPECTRA AND SPECTRAL CORRELATIONS FROM SUB-PHOTOSPHERIC COMPTONIZATION

2.1 Abstract

One of the most important unresolved issues in gamma-ray burst physics is the origin of the prompt gamma-ray spectrum. Its general non-thermal character and the softness in the X-ray band remain unexplained. We tackle these issues by performing Monte Carlo simulations of radiation-matter interactions in a scattering dominated photon-lepton plasma. The plasma – initially in equilibrium – is driven to non-equilibrium conditions by a sudden energy injection in the lepton population, mimicking the effect of a shock wave or the dissipation of magnetic energy. Equilibrium restoration occurs due to energy exchange between the photons and leptons. While the initial and final equilibrium spectra are thermal, the transitional photon spectra are characterized by non-thermal features such as power-law tails, high energy bumps, and multiple components. Such non-thermal features are observed at infinity if the dissipation occurs at small to moderate optical depths, and the spectrum is released before thermalization is complete. We model the synthetic spectra with a Band function and show that the resulting spectral parameters are similar to observations for a frequency range of 2-3 orders of magnitude around the peak. In addition, our model predicts correlations between the low-frequency photon index and the peak frequency as well as between the low- and high-frequency indices. We explore baryon and pair dominated fireballs and reach the conclusion that baryonic fireballs are a better model for explaining the observed features of gamma-ray burst spectra.

2.2 Introduction

The radiation mechanism that produces the bulk of the prompt emission of Gamma-Ray Bursts (GRBs) is still a matter of open debate (e.g. Mastichiadis and Kazanas 2009; Medvedev et al. 2009; Ryde and Pe'er 2009; Asano et al. 2010; Ghisellini 2010; Lazzati and Begelman 2010; Daigne et al. 2011; Massaro and Grindlay 2011; Resmi and Zhang 2012; Hascoët et al. 2013; Crumley and Kumar 2013). Among the many proposed possibilities, the synchrotron shock model (SSM) and the photospheric model (PhM) have recently gathered most of the attention (Rees and Meszaros 1994; Rees and Mészáros 2005; Piran

1999; Lloyd and Petrosian 2000; Mészáros and Rees 2000; Giannios 2006; Pe'er et al. 2006; Bošnjak et al. 2009; Lazzati et al. 2009; Beloborodov 2010; Mizuta et al. 2011; Nagakura et al. 2011). Within the SSM, the bulk of the prompt radiation is produced by synchrotron from a non-thermal population of electrons gyrating around a strong, locally-generated magnetic field. The non-thermal leptons are produced either by trans-relativistic internal shocks (the SSM proper, Rees and Meszaros 1994) or by magnetic reconnection in a Poynting flux dominated outflow (e.g. the ICMART model, Zhang and Yan 2011). The SSM naturally accounts for the broad, non-thermal nature of the spectrum. However, it has difficulties in accounting for bursts with particularly steep low-frequency slopes (Preece et al. 1998; Ghisellini et al. 2000) and has limited predictive power, since the radiation properties are tied to poorly constrained quantities such as the lepton's energy distribution, the ad-hoc equipartition parameters, and the ejection history of shells from the central engine.

The PhM does not specify a radiation mechanism, assuming instead that the burst radiation is produced in the optically thick part of the outflow and advected out, its spectrum being the result of the strain between mechanisms that tend to bring radiation and plasma in thermal equilibrium and mechanisms that can bring them out of balance (e.g., Beloborodov 2013). The PhM has been shown to be able to reproduce ensemble properties of the GRB population, such as the debated Amati correlation, the Golenetskii correlation, and the recently discovered correlation between the burst energetics and the Lorentz factor of the outflow (Amati, L. et al. 2002; Amati 2006; Liang et al. 2010; Fan et al. 2012; Ghirlanda et al. 2012; Lazzati et al. 2013; López-Cámara et al. 2014). However, it is not yet understood how the broad-band nature of the prompt spectrum, spanning many orders of magnitude in frequency, is produced. In a hot, dissipationless flow, only the adiabatic cooling of the plasma would work as a mechanism to break equilibrium, and the GRB outflow would work as a miniature big bang, the entrained radiation maintaining a Planck spectrum. In a cold, dissipationless outflow, lepton scattering dominates the radiation-matter interaction producing a Wien spectrum (Rybicki and Lightman 1986). Outflows from GRB progenitors are, however, far from dissipationless. Hydrodynamic outflows are continuously shocked out to large radii (Lazzati et al. 2009), and Poynting-dominated outflows suffer dissipation through magnetic reconnection (Giannios and Spruit 2006). Ei-

ther way, even if thermal equilibrium is reached at some point in the outflow, it is likely that such equilibrium is broken by a sudden release of energy in the lepton population or altered by a slow and continuous (or episodic) injection of energy. The effects of such energy injection on the photospheric spectrum are profound (e.g., Giannios 2006; Pe'er et al. 2006; Beloborodov 2010; Lazzati and Begelman 2010). In addition, the interaction between different parts of the outflow in a stratified flow alter the thermal spectra into a non-thermal, highly polarized spectrum (Ito et al. 2013; Ito et al. 2014; Lundman et al. 2013).

In this paper we investigate the evolution of the radiation spectrum following the sudden injection of energy in the lepton population of a plasma, assuming that the radiation and leptons interact via Compton scattering and pair processes. We use a Monte Carlo (MC) method that evolves simultaneously the photon and lepton populations by performing inelastic scattering between photons and leptons in both the non-relativistic and the relativistic (Klein-Nishina) regimes. The code also accounts for e^-e^+ annihilation (pair annihilation henceforth) and e^-e^+ pair production from photon-photon collisions (pair production henceforth). We focus on transient features that can be observed if the episode(s) of energy injection in the leptons occur at small or moderate optical depths ($\tau < 1000$).

This manuscript is organized as follows. In Section 2 we describe the physics and the methods of the MC code, in Section 3 we show our results and in Section 4 we discuss the results and compare them to previous findings.

2.3 Methodology

2.31 Step 1: Particle Generation

As a first task, the code generates a user-defined number of leptons and photons. Their energies follow a distribution that can be either of thermal equilibrium (Wien for the photons and Maxwell-Jüttner for the leptons) or any other user-specified distribution. After initializing the photon and lepton distributions, our code performs the following steps iteratively.

2.32 Step 2: Particle/Process selection

To initiate either a scattering or a pair event we need to select two particles[1] - which we obtain by randomly selecting a pair from our generated distributions. Depending upon the particles selected, Compton scattering (if a photon and a lepton is chosen), pair annihilation (if an e^- or e^+ is chosen) or pair production (if two photons are chosen) is performed or another pair is re-selected if any other combination occurs. After the selection, the code proceeds with the following calculations:

1. Incident angle generation (θ) using the appropriate relativistic scattering rates, under the assumption that both leptons and photons are isotropically distributed.
2. Lorentz boost to the necessary reference frames (details explained in successive sections) from the lab frame.
3. Event probability computations from total cross section (σ) calculations.
4. Scattering angle generation from differential cross section ($\frac{d\sigma}{d\Omega}$).
5. Lorentz boost from the necessary frame back to the lab frame.

In the following sub-sections we discuss each of the three possible processes in detail

Process 1: Compton Scattering

As the choice of reference frame is arbitrary, in the lab frame we can assume that the lepton is traveling along the x-axis and the photon is incident upon the lepton in the xy plane without any loss of generality. The angle of incidence $\theta_{\gamma e}$ between the chosen photon-lepton pair is generated by a probability distribution $P_{\gamma e}$:

$$P_{\gamma e}(\beta_e, \theta_{\gamma e}) \propto \sin\theta_{\gamma e}(1 - \beta_e \cos\theta_{\gamma e}) \tag{2.1}$$

where $\beta_e = v_e/c$, is the ratio of lepton speed to the speed of light.
To simulate the scattering event the code Lorentz transforms to the lepton frame (that we

[1] Note that here particle can mean both a lepton or a photon.

call the co-moving frame). The probability that the chosen photon-lepton pair interacts depends on the incident photon energy in the co-moving frame. As Compton scattering becomes less efficient at higher energies, photons having energies comparable to or greater than the lepton's rest mass energy are less likely to scatter. Using Monte Carlo sampling we determine if scattering occurs or not. This is done by generating a random number and comparing it to the ratio of the Klein-Nishina cross section $\sigma_{\gamma e}$ to the Thomson cross section, which we use as a reference value. We proceed with the scattering event if $\sigma_{\gamma e}/\sigma_T \geq s_1$ where s_1 is a random number. If the condition is not satisfied, the code returns to step 2. If instead the condition is satisfied and the scattering occurs, the code generates the polar scattering angle θ'_s in accordance with the Klein-Nishina differential cross-section formula

$$\frac{d\sigma_{\gamma e}}{d\Omega} = \frac{r_0^2}{2}\frac{E_s'^2}{E'^2}\left(\frac{E'}{E'_s} + \frac{E'_s}{E'} - \sin^2\theta'_s\right) \tag{2.2}$$

where r_0 is the classical radius of an electron, E' and E'_s are the energies of the incident and scattered photon respectively (e.g. Blumenthal and Gould 1970; Longair 2011; Rybicki and Lightman 1986). The energy transfer equation connecting E' with E'_s is the Compton equation (e.g. Blumenthal and Gould 1970; Longair 2011; Rybicki and Lightman 1986)

$$E'_s = \frac{E'}{1 + \frac{E'}{m_e c^2}(1 - \cos\theta'_s)}. \tag{2.3}$$

(Note here that θ'_s is the angle that the scattered photon makes with the direction of propagation of the incident photon in the co-moving frame. Hence equations (2.2) and (2.3) hold true only in the lepton frame). Finally, the azimuthal angle ϕ'_s is generated randomly between zero and 2π. Thus, we now have the four momenta of the scattered particles in the co-moving frame.

Process 2: Pair Production / Photon Annihilation

If the particle selection process selects two photons then the pair production/photon annihilation channel is chosen. The code computes the angle of incidence $\theta_{\gamma\gamma}$ between the chosen photons by using the probability distribution $P_{\gamma\gamma}$:

$$P_{\gamma\gamma}(\theta_{\gamma\gamma}) \propto \sin\theta_{\gamma\gamma}(1 - \cos\theta_{\gamma\gamma}). \tag{2.4}$$

To ensure that the photon pair has enough energy to lead to a pair production event the code checks the energy of the photon/s in the zero momentum frame. The zero momentum frame photon energy E'_o can be computed given the incident photon energies E_1, E_2 and the incident angle as

$$E'_o = \sqrt{E_1 E_2}\sin(\theta_{\gamma\gamma}/2). \tag{2.5}$$

(Gould and Schréder 1967). If $E'_o < m_e c^2$ the colliding photon pair is not energetic energy to produce an $e^- e^+$ pair, hence the code jumps to step 2 for a new particle pair selection. Due to the energy dependence of cross-section $\sigma_{\gamma\gamma}$, even photons exceeding the energy threshold might not produce pairs. To make this determination, we again use the Thomson cross section as a reference and determine if the photon annihilation takes place by randomly drawing one number s_2, obtaining $\sigma_{\gamma\gamma}$ by boosting to the center of momentum frame and evaluating if $\sigma_{\gamma\gamma}/\sigma_T \geq s_2$. If the inequality holds true, the code proceeds with the pair production calculation. Otherwise, it is abandoned and the code returns to step 2.

Once the photons succeed in producing leptons, the polar scattering angle θ'_s of the newly born e^- is computed from the pair annihilation differential cross section as given by

$$\frac{d\sigma_{\gamma\gamma}}{d\Omega} = \frac{r_0^2 \pi}{2} b \left(\frac{m_e c^2}{E'_o}\right)^2 \frac{1 - b^4 \cos^4\theta'_s + 2\left(\frac{m_e c^2}{E'_o}\right)^2 b^2 \sin^2\theta'_s}{\left(1 - b^2\cos^2\theta'_s\right)^2}. \tag{2.6}$$

(see Jauch and Rohrlich 1980, p.300) where $b = \sqrt{1 - \left(\frac{m_e c^2}{E'_o}\right)^2}$. A random azimuthal angle $\phi'_s \in [0, 2\pi)$ is assigned to the e^-. Note that Lorentz transformation to the zero momentum frame is necessary because equation (2.6) is frame dependent. Utilizing conservation laws, the four momenta of the e^+ can be determined.

Process 3: Pair Annihilation/ Photon Production

The pair annihilation channel is chosen if the random particle selection constitutes an $e^- e^+$ pair. As with the other channels, we first determine the incident angle θ_{ee} (subscript $_{ee}$ stands for lepton pair annihilation) between the pair by computing the probability distribution of scattering as given by

$$P_{ee}(\beta_{e^-}, \beta_{e^+}, \theta_{ee}) \propto \sin\theta_{ee} f_{kin} \tag{2.7}$$

where f_{kin} as obtained from (Coppi & Blandford 1990) is given by:

$$f_{kin} = \sqrt{\beta_{e^-}^2 + \beta_{e^+}^2 - \beta_{e^-}^2\beta_{e^+}^2 \sin^2\theta_{ee} - 2\beta_{e^-}\beta_{e^+}\cos\theta_{ee}}. \tag{2.8}$$

Here $\beta_e = \frac{v_e}{c}$ i.e. the ratio of lepton speed to the speed of light. The code transforms all quantities to the rest frame of the electron to calculate the the total cross section σ_{ee} as (Jauch and Rohrlich 1980, p.269):

$$\sigma_{ee} = \frac{r_0^2\pi}{\beta'^2}\left[\frac{\left(\gamma' + \frac{1}{\gamma'} + 4\right)\ln\left(\gamma' + \sqrt{\gamma'^2 - 1}\right) - \beta'(\gamma' + 3)}{\gamma'(\gamma' + 1)}\right] \tag{2.9}$$

where $\beta' = v'_{e+}/c$, $\gamma' = \frac{1}{\sqrt{1-\beta'^2}}$ i.e. the e^+ speed and Lorentz factor respectively in the co-moving frame traveling with the e^-. On comparing the σ_{ee}/σ_T with a random number s_3 the code evaluates the occurrence of the annihilation event. If the event fails, the code returns to step 2 to re-select another pair of particles. Following a successful event, the polar scattering angle θ'_s between either of the pair produced photons is generated from the differential cross section (from Jauch and Rohrlich 1980, p.268)

$$\frac{d\sigma_{ee}}{d\Omega} = \frac{r_0^2\pi}{\beta'\gamma' d}\left[\gamma' + 3 - \frac{[1+d]^2}{(1+\gamma')d} - \frac{2(1+\gamma')d}{[1+d]^2}\right] \tag{2.10}$$

where $x = \cos\theta'_s$ and $d = \gamma'(1 - \beta' x)$. As pointed out in the preceding sub-sections, Lorentz transformation to the electron frame is necessary as equation (2.10) is expressed in terms of quantities defined in the electron's co-moving frame. The random azimuthal angle $\phi'_s \in [0, 2\pi)$ is randomly assigned to either photon. Using conservation laws, the four momenta of the pair produced photons can be obtained.

2.33 Step 3: Back to the lab frame

At the end of the event, the code transforms the four momenta of the particles back to the lab frame by employing Lorentz transformations. The loop is repeated until equilibrium is restored i.e. when the particle numbers saturate and distributions become thermal.

2.4 Results

We employ the Monte Carlo code described above to study the evolution of the radiation spectrum in a closed box containing leptons and photons. The simulations are initialized with a Wien radiation spectrum at 10^6 K and a non-equilibrium lepton population, either because leptons and photons are at different temperature or because the leptons energy distribution is non-thermal. This is expected to mimic a scenario in which the leptons and radiation were initially at equilibrium, but the lepton population has been brought out of equilibrium by a sudden energy release. Such energy release may be due to shocks in the fluid (e.g., Rees and Meszaros 1994; Lazzati and Begelman 2010) or by magnetic reconnection in a magnetized outflow (e.g. Giannios and Spruit 2006; McKinney and Uzdensky 2012). As it will be clear at the end, a fundamental parameter that determines the interaction between the photons and leptons is the particle ratio, i.e., the ratio of photon and lepton number densities. In a GRB outflow, such a ratio can be readily estimated.

Let us call E_K the kinetic energy of the outflow carried by particles with non-zero rest mass and E_γ the energy in electromagnetic radiation. We have:

$$\begin{aligned} \frac{E_\gamma}{E_K} &= \frac{N_\gamma h\nu_{\rm pk}}{\left(N_p + \frac{m_e}{m_p}N_{\rm lep}\right)\Gamma m_p c^2} \\ &\simeq 10^{-5}\frac{n_\gamma}{n_p + \frac{n_{\rm lep}}{1836}}\left(\frac{h\nu_{\rm pk}}{1\,{\rm MeV}}\right)\Gamma_2^{-1} \end{aligned} \tag{2.11}$$

By calling $\eta = E_\gamma/(E_\gamma + E_K)$ the radiative efficiency of the outflow, and assuming that matter and radiation are coupled in the optically thick region and occupy the same volume, equation (2.11) can be inverted to yield:

$$\frac{n_\gamma}{n_{\rm lep}} = \begin{cases} 10^5\frac{\eta}{1-\eta}\left(\frac{1\,{\rm MeV}}{h\nu_{pk}}\right)\Gamma_2 & n_{\rm lep} = n_p \\ 50\frac{\eta}{1-\eta}\left(\frac{1\,{\rm MeV}}{h\nu_{pk}}\right)\Gamma_2 & n_{\rm lep} \gg n_p \end{cases} \tag{2.12}$$

where the top line is valid for a non-pair enriched fireball while the bottom line is for a pair-dominated fireball. All values in between are allowed for a partially pair-enriched fireball. Note also that we used the convention $\Gamma_2 = \Gamma/10^2$. GRB fireballs are therefore photon-dominated, even if highly pair-enriched.

We here consider two possible values of the particle ratio. As a representative of pair-enriched plasma, we explore the case $n_\gamma/n_{\rm lep} = 10$. A non-enriched plasma (or photon-rich plasma) is represented by the ratio $n_\gamma/n_{\rm lep} = 1000$. Note that the latter value is not as extreme as the one in equation (2.12). It is, however, technically challenging to simulate any higher value of the particle ratio. To ensure that the statistics of the lepton population is under control, we need to simulate at least 1000 irreducible electrons (electrons that are not possibly annihilated by a positron). For a particle ratio $n_\gamma/n_{\rm lep} = 10^5$, that would require the simulation of 10^8 photons. We believe that the adopted value $n_\gamma/n_{\rm lep} = 1000$ does capture the characteristics of the spectrum emerging from a photon-rich plasma and we will discuss the consequences of higher particle ratios in Section 4.

For each particle ratio, we explore different scenarios in which the accelerated leptons are either thermal (Lazzati and Begelman 2010) or non-thermal (e.g. Giannios 2006; Pe'er et al. 2006; Beloborodov 2010) and we consider the possibility of multiple acceleration events, in which the leptons are re-energized before the equilibrium is reached. Some of these possibilities have been previously explored, in particular the Comptonization from a non-thermal population of electrons (e.g. Pe'er et al. 2006). We do not consider in this study continuous energy injection, in which a stationary equilibrium between photons and electrons is reached, and for which our code is not well suited (e.g. Giannios 2006; Pe'er et al. 2006).

All simulations are run until equilibrium is attained. Here we define equilibrium as the time at which the spectral shape does not change with further collisions and the number of photons and leptons saturate. This is generally much later than the time at which the total energies in leptons and photons approach their asymptotic values, since a very small amount of energy can make a significant difference in the tails of the distribution, which are the interesting aspect of the spectrum for this study. Our simulations do not have a time stamp, since all processes involved are scale free. A time stamp can be added upon deciding on a particle and photon density, rather than a total number as specified in the code. A meaningful comparison with the data can be accomplished by considering that a photon in a relativistic outflow with Thomson opacity τ scatters-off/collides with leptons an average number of times $n_{\rm sc} \simeq \tau$ before being detected by an observer at infinity (e.g. Pe'er et al. 2005). Here we adopt as the Thomson opacity of a medium $\tau = \int n_{lep} \sigma_T ds$

(see Rybicki and Lightman 1986). It is possible therefore to look at our spectra in the following manner: if a shock or a reconnection event dissipates energy in the outflow at a certain optical depth τ, the spectrum observed at infinity is the one derived from our code after τ_{diss} scatterings per photon.

2.41 Photon Rich Plasma

We first explore a photon-rich plasma with $n_\gamma/n_{\rm lep} = 1000$. Three simulations are initialized with an out-of-equilibrium electron population (there are no positrons initially in the plasma) with different initial distributions. We inject identical amounts of total kinetic energy K in all three cases, raising the average kinetic energy of the leptons to 1.365 MeV. This can be considered as a mild energy injection and within the equipartition shock-acceleration scenario this corresponds to either a mildly-relativistic shock or a relativistic shock with a fairly low fraction of energy given to electrons ($\epsilon_e \ll 1$) (e.g. Guetta et al. 2001). In the first simulation, the leptons adopt a Maxwell-Jüttner distribution at $T_e = 6.5 \times 10^9$ K. In the second case the leptons conform to a Maxwellian distribution (at 10^8 K) which is smoothly connected to a non-thermal power law tail $n_e(\gamma) \propto \gamma^{-2.2}$. The third and final simulation explores the scenario of energy dissipation via multiple (10) less energetic injections instead of a single intense injection event.

Thermal Leptons at 6.5×10^9 K

The lepton population in this case is shocked and then thermalizes at 6.5×10^9 K. A similar scenario was explored analytically and with a simplified Monte Carlo code by Lazzati and Begelman (2010).

The results of the simulation are shown in Figure 2.1, where the evolution of the radiation spectrum and of the spectrum of the kinetic energy of the leptons' population are displayed. We first note that the final distributions (blue curves in both panels) are all thermal, as expected for a plasma in equilibrium. Looking at the intermediate spectra in more detail, we notice that the immediate reaction of the radiation spectrum is the formation of a high-frequency non-thermal tail, initially appearing as a new component (for spectra at $\tau_{diss} = 0.001$) and subsequently forming a continuous tail stemming from the thermal

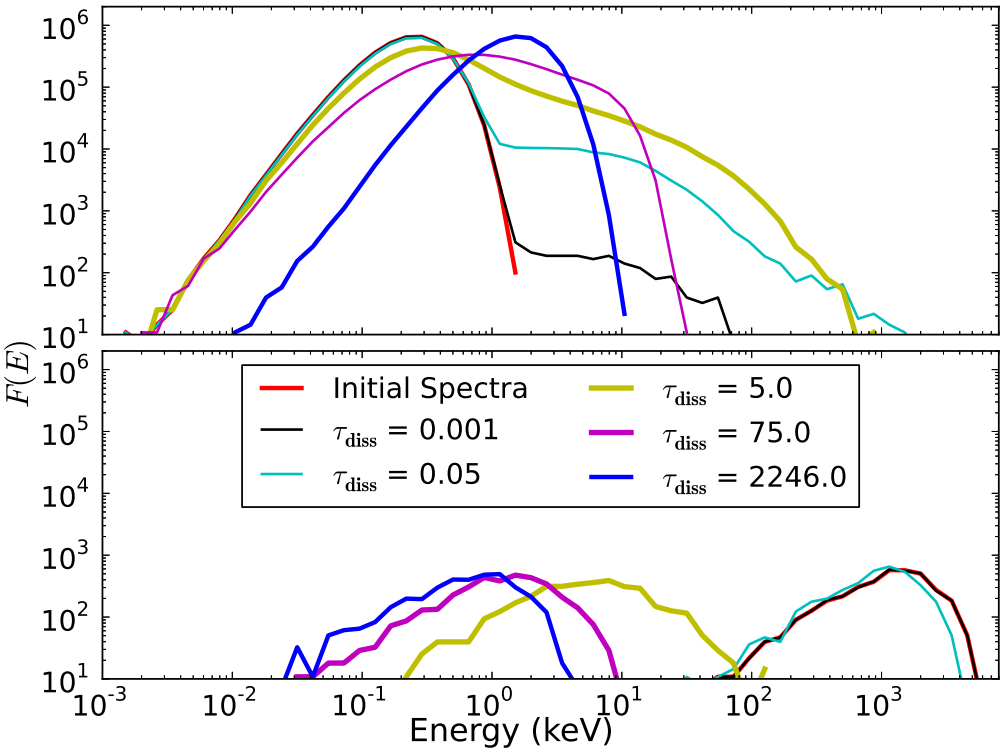

FIGURE 2.1: Radiation spectrum (upper panel) and leptons' kinetic energy distribution (lower panel) at different simulation stages for a photon-rich plasma ($N_\gamma/N_{\rm lep} = 1000$) with a sudden injection of thermal energy in the lepton population (see Sect. 2.41). The legend displays the various optical depths at which if energy was injected, the corresponding color coded spectrum and distribution would be observed.

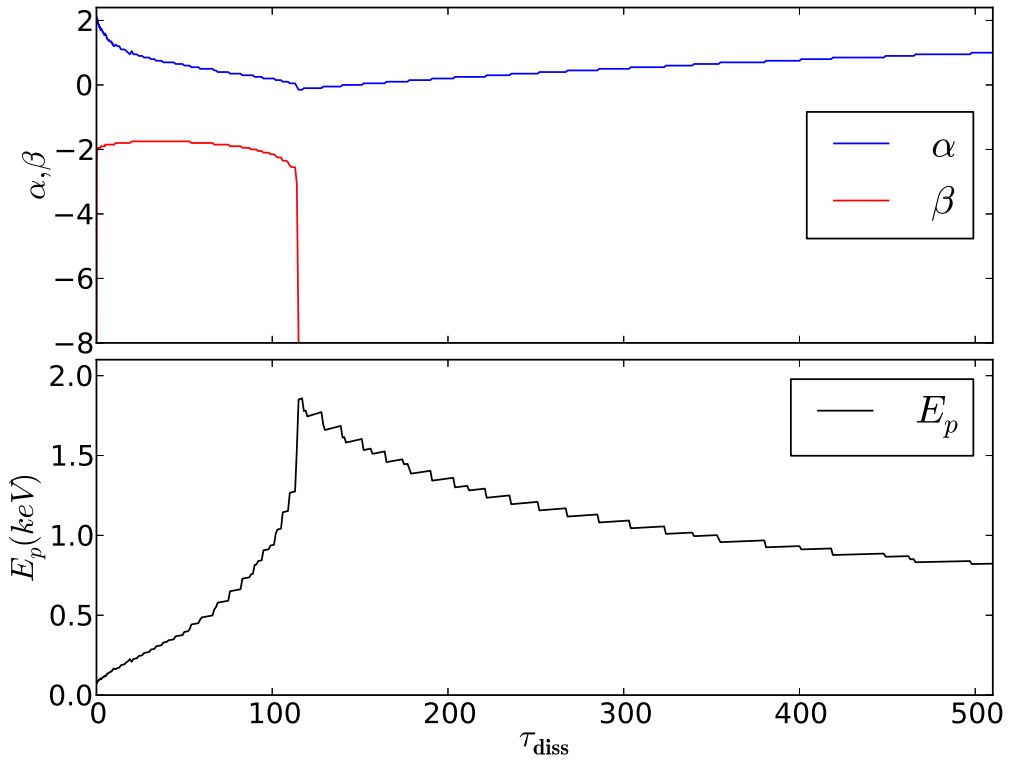

FIGURE 2.2: Evolution of the Band parameters α, β and, E_p of spectra from the simulation shown in Figure 2.1. The x-axis indicates the optical depth of energy injection.

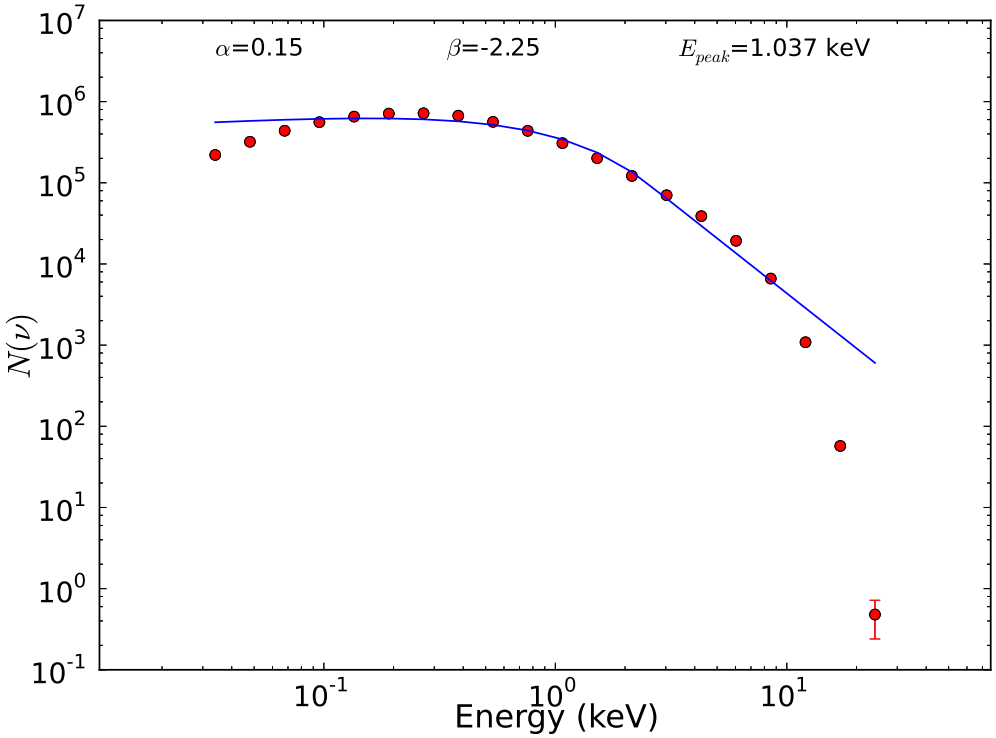

FIGURE 2.3: Fitting of the Band parameters α, β and E_p of spectra from the simulation shown in Figure 2.1 at $\tau_{diss} = 103$.

photon population ($\tau_{diss} = 5$). At a subsequent stage, the low-frequency part of the radiation spectrum is also modified, with the spectral peak migrating to higher frequencies and causing a flattening of the low-frequency component ($\tau_{diss} = 75$). The figure shows that the spectrum takes a very large number of scatterings for equilibrium restoration, especially for frequencies lower than the peak. For energy dissipation at optical depths up to ~ 100 a high-frequency non-thermal tail is observed. A non thermal low-frequency tail is instead observed even for a larger optical depth, up to a few thousand.

In order to quantify our synthetic transient spectra and compare them with observations, we fit them to an analytic model. We adopt the widely used Band function (Band et al. 1993) and fit it to the data over a frequency range of three orders of magnitude. Although the GRB spectra are in most cases more complex than a Band function (e.g. Burgess et al. 2015; Guiriec et al. 2011; Guiriec et al. 2013) this still constitutes a zero-order test that any model should pass. We begin by computing the mean frequency from our data and select neighboring frequencies within 1.5 orders of magnitude around the mean. This data set is binned in frequency and a best-fit Band function is obtained by minimizing the χ^2.

Figure 2.2 shows the evolution of the spectral parameters α, β and E_p for increasing optical depths. We again emphasize that this should not be considered as a time evolution, since the number of scattering is set by the optical depth at which the energy is released in the leptons. A sample fit of the spectrum at $\tau_{diss} = 103$ to the Band function is shown in Figure 2.3. The figure represents a typical case, and shows that the Band model fits well the frequencies around the peak but deviations are observed for the lowest and highest frequencies. We will address this issue further in the discussion. The legend at the top of the figure shows the Band parameters for the fit. An interesting aspect of these simulations is that the low-frequency photon index α and the peak frequency are strongly anti-correlated. This is due to the fact that it is necessary that the peak frequency shifts to higher values for the low-frequency spectrum to change from its thermal equilibrium shape. We also note that the high-energy slope anticipates the low-energy one, the non-thermal features building-up earlier and disappearing faster. We will discuss in more detail these correlations and their implications in Section 4.

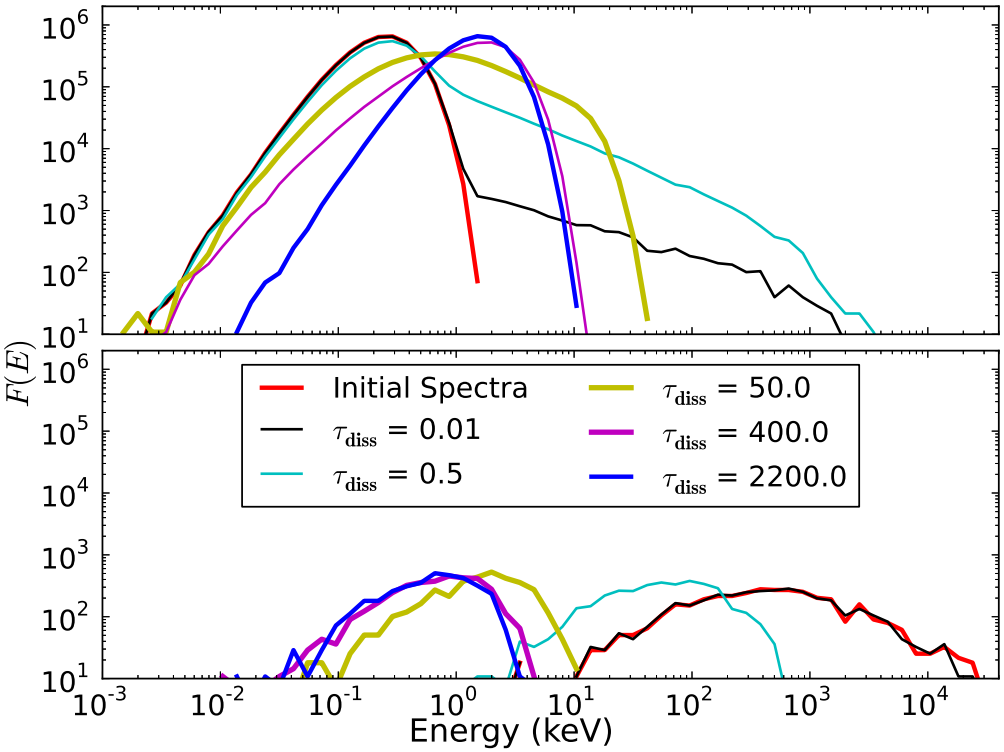

FIGURE 2.4: Color coded photon spectrum (upper panel) and leptons' kinetic energy distribution (lower panel) at different stages for the photon-rich simulation discussed in Section 2.41. The legend displays the various optical depths at which if energy was injected, the corresponding color coded spectrum and distribution would be observed.

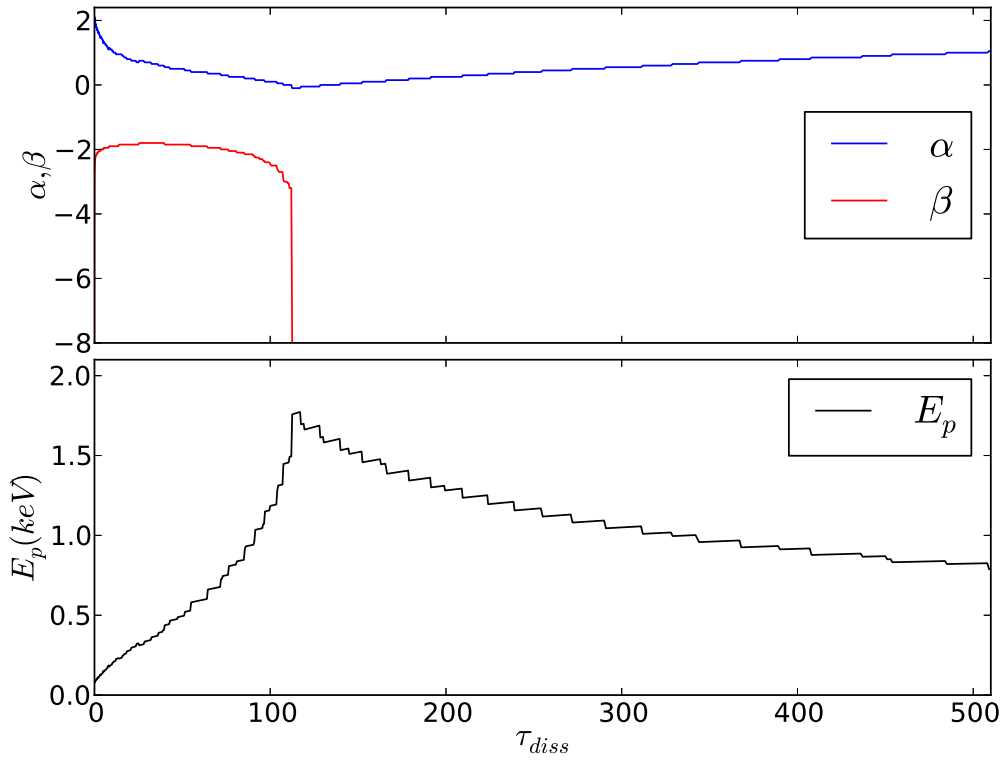

FIGURE 2.5: Evolution of the Band parameters α, β and E_p of spectra from the simulation shown in Figure 2.4. The x-axis indicates the optical depth of energy injection.

Maxwellian leptons at 10^8 K with a power law tail $p = 2.2$

Most models of internal shocks predict the acceleration of non-thermal particles. Comptonization of seed thermal photons by non-thermal leptons has been widely studied in different scenarios and under different assumptions (e.g. Giannios 2006; Pe'er et al. 2005; Pe'er et al. 2006). In this scenario the shock generates a non-thermal lepton distribution characterized by

$$N(E)dE \propto \gamma^{-p} d\gamma \tag{2.13}$$

where γ is the lepton Lorentz factor and $p = 2.2$. The results of the simulation are shown in Figure 2.4, where we present the evolving radiation spectrum and distribution of the kinetic energy of the leptons' population. We notice that the equilibrium photon and lepton distributions (blue curves) are thermal, as expected at equilibrium. We also notice that the spectrum appears non-thermal for a wide range of opacities. Initially a prominent high-energy power-law tail is developed, for a very small opacity (or $\tau_{diss} \sim 0.01$). As the injection opacity increases, the power-law tail is truncated at progressively lower frequencies, the peak frequency shifts to higher values, and a non-thermal tail at low-frequencies develops. The high-frequency tail disappears for $\tau_{diss} \sim 400$, but even larger opacities are required to turn the low-frequency tail back to the scattering-dominated equilibrium spectrum. We fit the Band function to our synthetic spectra and obtain Figure 2.5, which shows the evolution of the spectral parameters α, β and E_p for increasing injection optical depths. We also notice correlations between the spectral parameters α and the peak frequency, as discussed in Section 2.41.

Discrete Multiple Energy Injections

The presence of multiple minor shocks has been emphasized in 2D axisymmetric numerical simulations of jets in collapsars (e.g. Lazzati et al. 2009) and seem to be an even more common feature in 3D simulations (López-Cámara et al. 2013). Hence, to provide a more realistic scenario for the energy injection we explore lepton heating by multiple energy injections mimicking multiple shocks instead of a single more powerful one. The total energy injected into the lepton population is identical to the amount injected in the simulations discussed in Sections 2.41 and 2.41. However, the energy is divided into 10 equal

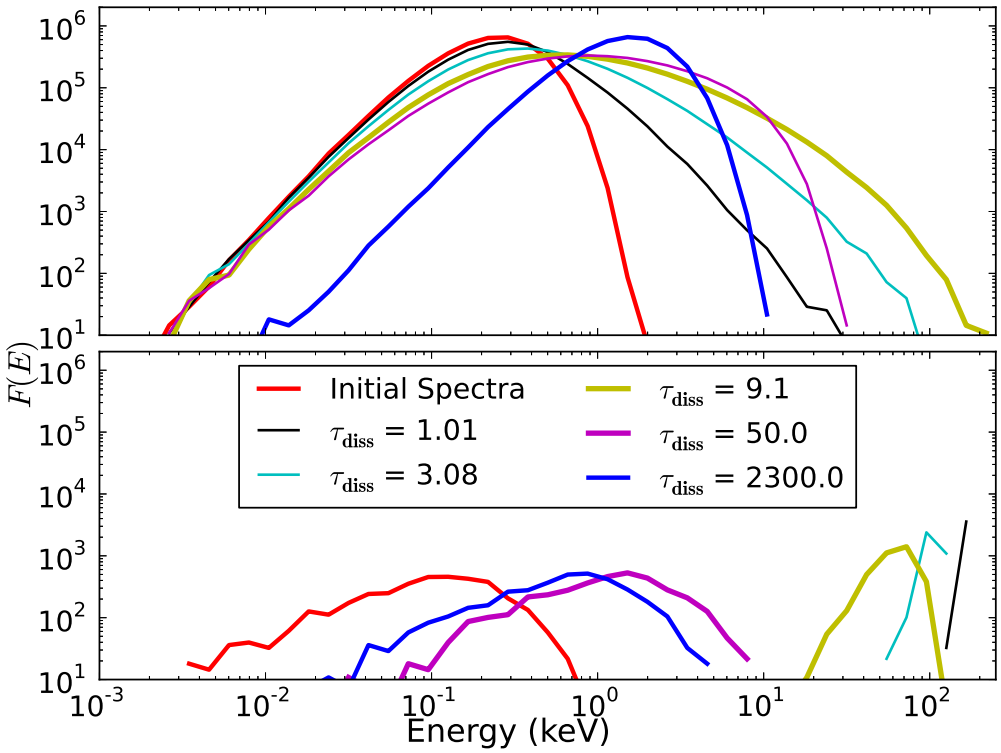

FIGURE 2.6: Photon spectrum (upper panel) and leptons' kinetic energy distribution (lower panel) at different stages of the simulation discussed in Section 2.41. The legend associates the various optical depths of energy injection with the corresponding color coded spectrum and distribution observed.

and discrete partitions with each one being injected and distributed uniformly among the leptons, after every million scatterings.

The results of the MC simulation are shown in Figure 2.6, where the evolving radiation spectrum and the spectrum of the kinetic energy of the leptons' population are displayed. In comparison to Figures 2.1 and 2.4, two differences are apparent for small optical depths. First, the high-frequency tail develops much more slowly. Secondly, the slowly developing tail does not extend to the same high energies and in fact, it never approaches the MeV mark. Neither of these differences is surprising, given that a smaller amount of energy is injected at regular intervals. The results of the Band function fitting are reported in Figure 2.7 and bring to our attention that like previous other simulations, the high-frequency photon index β is the first to respond, and also the first to drop just when the α parameter reaches it's minimum value. Another remarkable aspect of the multiple

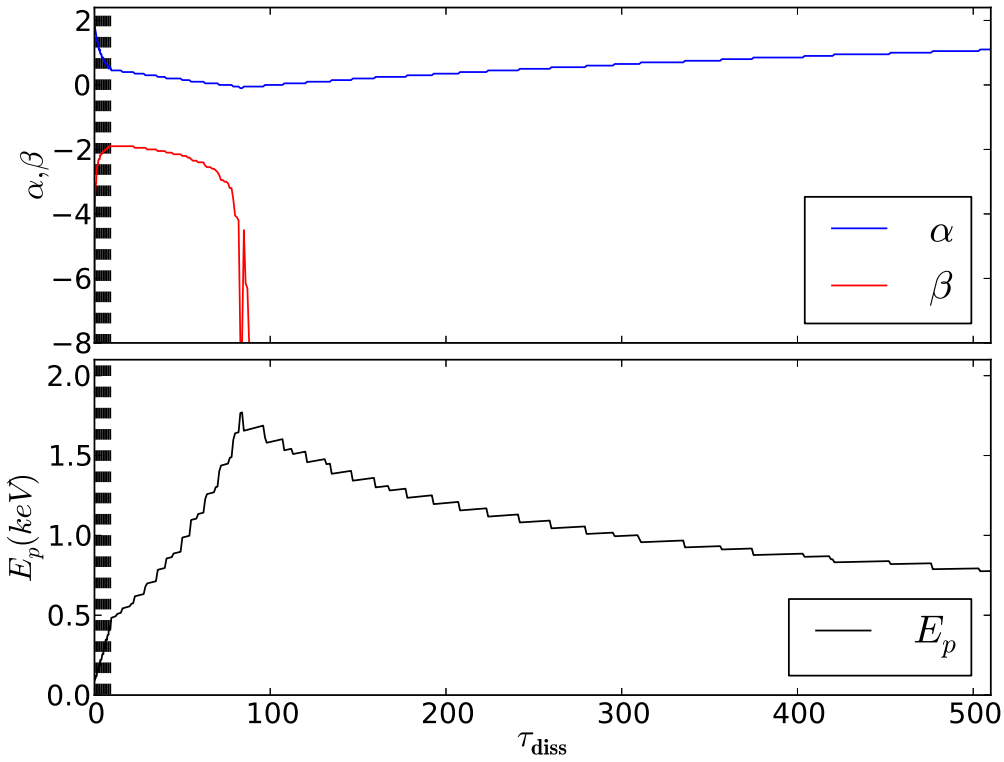

FIGURE 2.7: Evolution of the Band parameters α, β and E_p of spectra from the simulation shown in Figure 2.6. The x-axis displays the opacity at which energy deposition occurred.

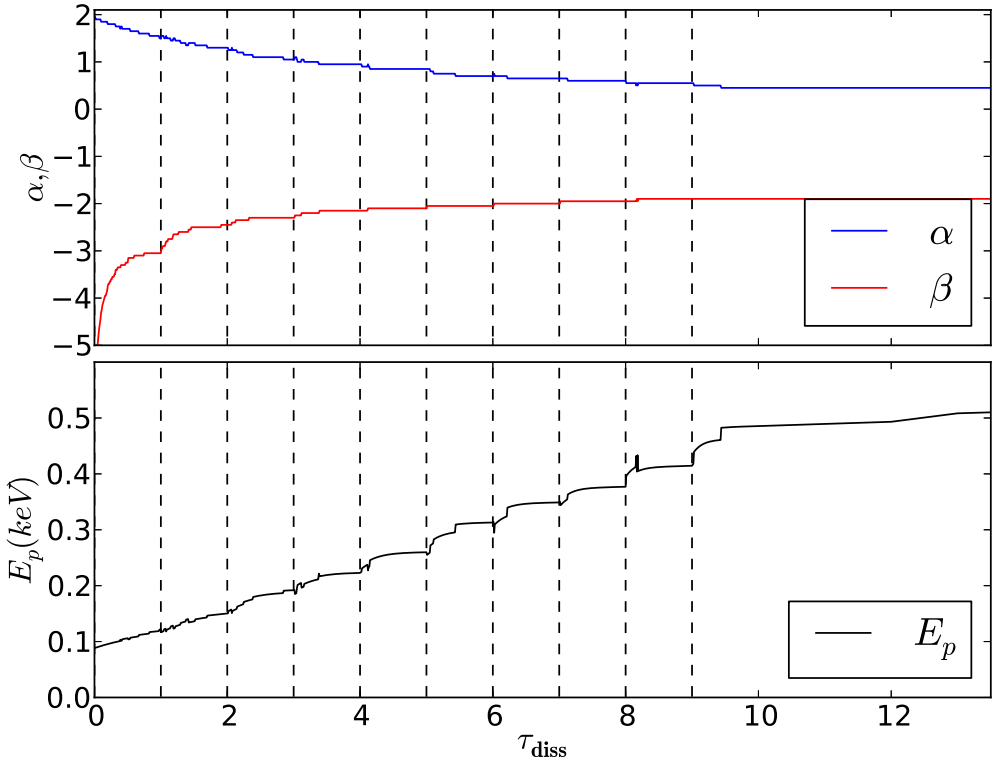

FIGURE 2.8: Magnified version of Figure 2.7 depicting the response of the Band function parameters α, β and E_p to discrete and multiple energy injections, indicated by the broken black vertical lines. The x-axis displays the opacity at which energy deposition occurred.

injection scenario is the immediate reaction of the spectrum to new injections, especially for the high-frequency photon index and the peak frequency (see Figure 2.8).

What is perhaps mostly interesting, rather than the subtle differences among the three scenarios discussed here, is the fact the Band parameters of Figures 2.2, 2.5, and 2.7 show remarkably similar behavior, even though the injection scenarios are very different. In all three cases, injection at low optical depth only produces a high-frequency power-law tail. Injection at moderate optical depths ($\tau_{diss} \sim 10 - 100$) produces a high-frequency power-law tail, a shift in the peak frequency, and a non-thermal low-frequency tail. Injection at high to very high optical depths only results in a non-thermal low-frequency tail (see also Section 4 for a discussion).

2.42 Pair Enriched Plasmas

In this section we investigate plasmas enriched by e^-e^+ pairs, by choosing $n_\gamma/n_{\rm lep} = 10$. GRB plasmas can become pair enriched via energy injection through shocks/magnetic dissipation (Mészáros et al. 2002; Pe'er and Waxman 2004; Rees and Mészáros 2005) and if the peak energy of the resulting distribution exceeds 20 keV (Svensson 1982). The generation of pairs is also evident from the photon and lepton distributions crossing the 511 keV mark as shown in the simulations in Sections 2.41 and 2.41. We assume, as in the previous scenario, that the the pair enriched leptons are impulsively heated by injecting equal amounts of kinetic energy $K/10$ for the first two simulations, albeit with different distribution functions (Maxwellian and Maxwellian plus power law). The third simulation explores the spectral evolution of a pair enriched plasma with an even greater kinetic energy injection. The initial photon count of the plasma N_γ is 1.01×10^5. Being pair-enriched, the total lepton count N_e of the plasma is 1.01×10^4,

$$N_e = N_{e^-} + 2N_{e^+e^-} = 10^2 + 10^4 \tag{2.14}$$

where N_{e^-} are electrons associated with protons and $N_{e^+e^-}$ denotes the number of pairs in the system.

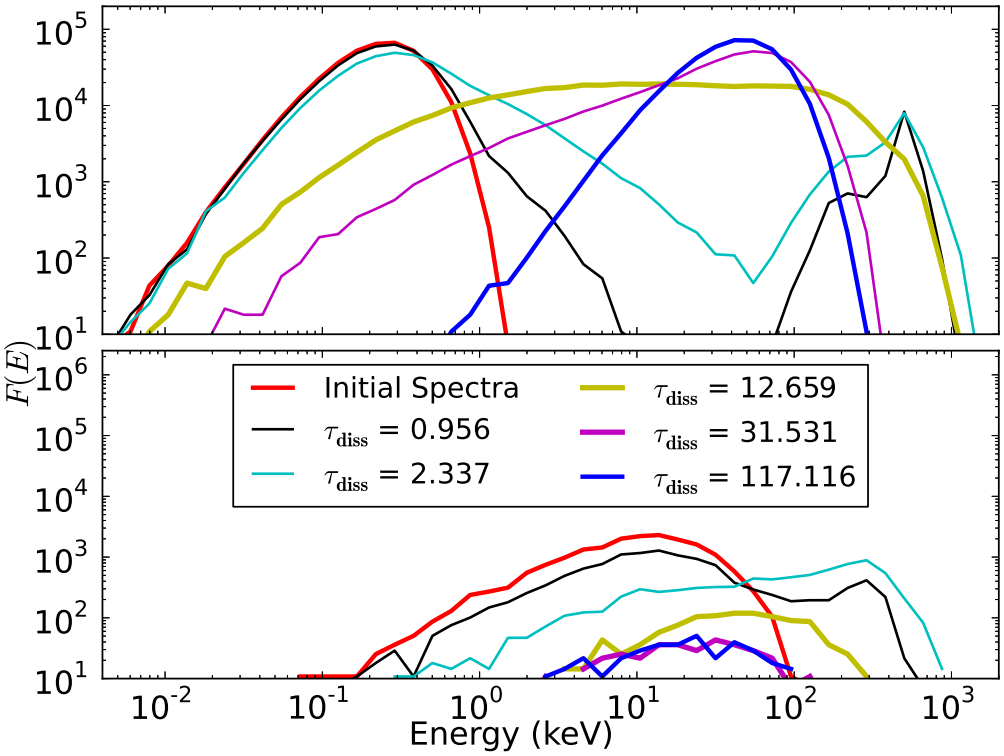

FIGURE 2.9: Photon spectrum (upper panel) and leptons' kinetic energy distribution (lower panel) at different stages of the pair-enriched simulation discussed in Section 2.42. The legend displays the various optical depths at which if energy was injected, the corresponding color coded spectrum and distribution would be observed.

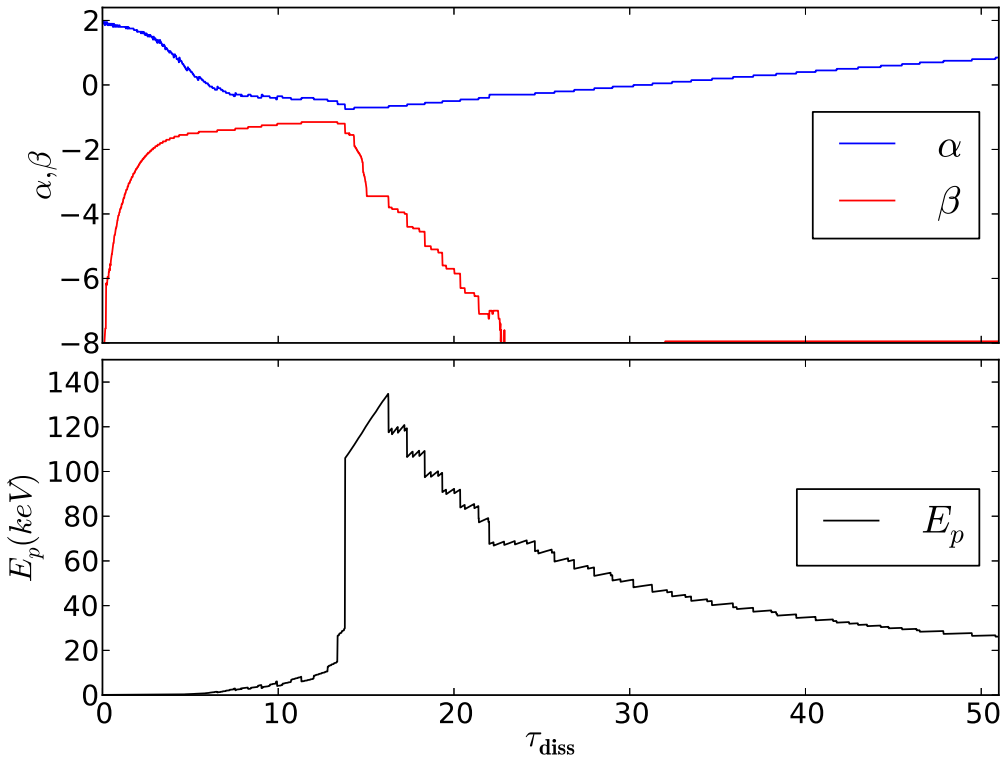

FIGURE 2.10: Evolution of the Band parameters α, β and E_p of spectra from the simulation shown in Figure 2.9 for increasing values of energy-injection optical depths.

Maxwellian leptons

We initiate the simulation with Maxwellian pair-enriched leptons that have been impulsively heated to 10^8 K, thereby taking the population out of equilibrium with the photons. The results of the simulation are displayed in Figure 2.9 with the upper panel depicting the photon spectra and the lower panel illustrating the kinetic energies of the leptons. Firstly, as observed in the section on photon rich plasmas, the final (blue curve) spectra is consistent with the equilibrium Wien distribution. For $\tau_{diss} \sim 1$ a bump is observed to spike near the annihilation line along with a power law tail (black curve). The lepton distribution also displays a two component distribution (black curve in the lower panel). For $\tau_{diss} \sim 2.3$, the power law tail extends farther to high frequencies and merges with the annihilation bump (cyan curve). On increasing the injection opacity to around 13, the low frequency spectrum flattens, the peak frequency increases and the annihilation bump merges completely with the initial Wien distribution (or the remnant of the initial spectrum) creating a non-thermal flattened plateau-like feature (yellow curve). The high-frequency power law tail returns to the equilibrium Wien spectrum much earlier ($\tau_{diss} \leq 32$) than the non-thermal low frequency tail, which requires about ($\tau_{diss} \sim 100$) to form the equilibrium spectrum. We interpret this behavior to the inability of the plasma to support a large population of pairs. As a consequence the pairs quickly annihilate and a large amount of ~ 511 keV photons are injected in the plasma.

The Band parameters obtained by fitting the Band functions to the simulation spectra are plotted in Figure 2.10. We note that for moderate optical depths, $\alpha = -0.75$ and $\beta = -1.15$ which corresponds to an extremely non-thermal spectrum. We also observe from the lower panel of Figure 2.10 that $E_p = 20-40$ keV. Furthermore, an anti-correlation is observed between the Band parameters α and β and between α and E_p.

Maxwellian leptons at 10^8 K with a power law tail

This simulation initializes the lower energy lepton population as thermally distributed at 10^8 K and a higher energy population with a power law tail. However, pair enrichment and constraining the injected kinetic energy to $K/10$ lowers the average kinetic energy per lepton in comparison to the photon-rich plasmas. As a result the leptons are generated

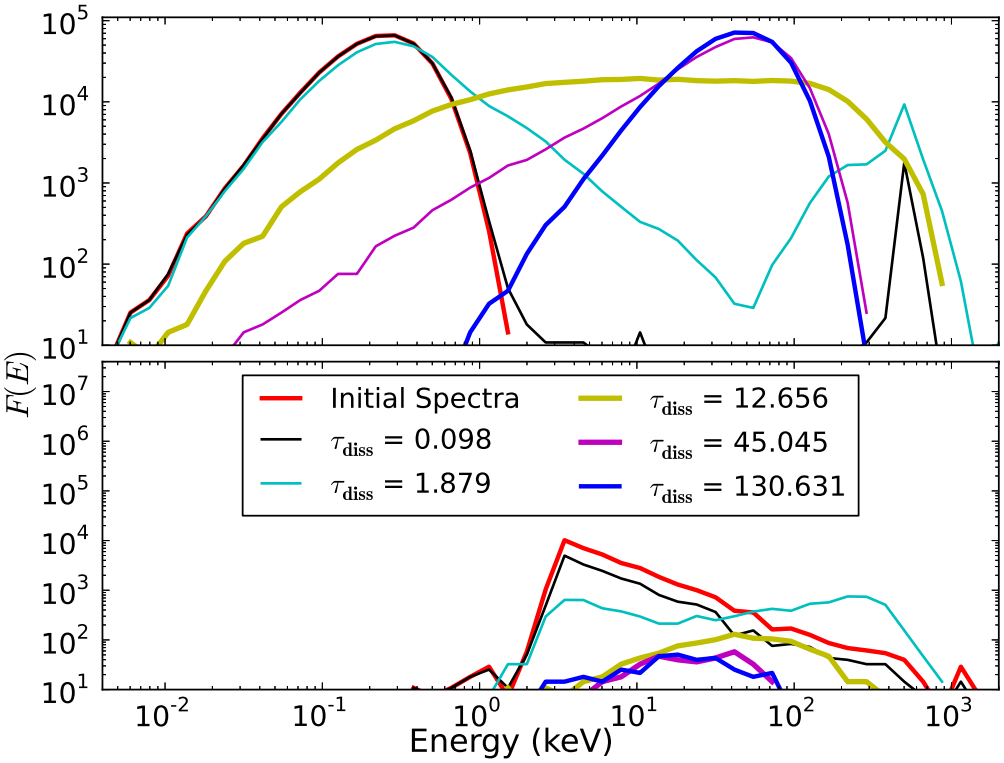

FIGURE 2.11: Photon spectrum (upper panel) and leptons' kinetic energy distribution (lower panel) at different stages of the simulation discussed in Section 2.42. The legend associates the various optical depths of energy injection with the corresponding color coded spectrum and distribution observed.

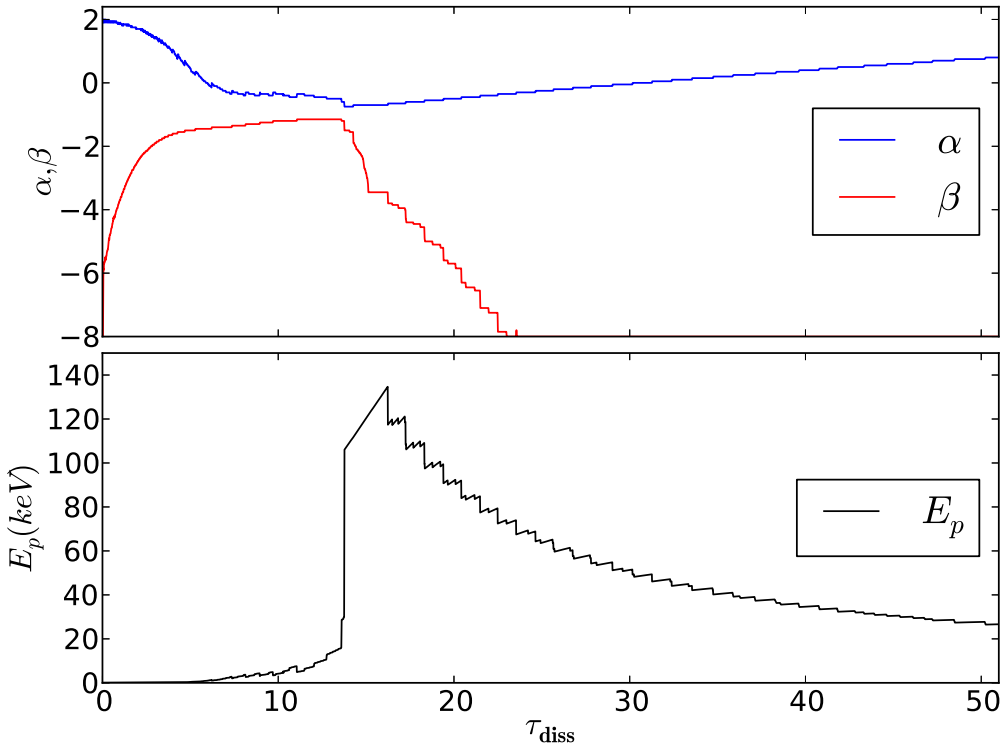

FIGURE 2.12: Evolution of the Band parameters α, β and E_p of spectra from the simulation shown in Figure 2.11. The x-axis displays the opacity at which energy injection occurred.

according to the distribution

$$N(E)dE \propto (\gamma - 1)^{-p} d(\gamma - 1) \tag{2.15}$$

where γ is the lepton's Lorentz factor and $p = 2.2$. The red curve in lower panel of Figure 2.11 displays the initial kinetic energy distribution of the lepton population. Note that the power law tail does not extend to high energies as the tail in Figure 2.4 does. The figure also shows the evolution of the photon spectra and leptons' kinetic energy as equilibrium restoration occurs. For the photons, the initial spectra (red curve) and equilibrium spectrum (blue curve) fit the Wien distribution. As is expected, pair annihilation produces a hump in the vicinity of the 511 keV region. Meanwhile, the photons forming the initial Wien spectrum form a power law tail. Similar to the previous scenario, at around $\tau_{diss} \sim 2$, the power law extends to high frequencies and merges with the growing annihilation hump (cyan curve). We also observe a two component distribution in the lepton panel. By $\tau_{diss} \sim 13$, the two component spectrum transforms into a broad band flat-plateau like spectrum (yellow curve) with the low-frequency spectrum being modified as well. The high frequency spectrum of the magenta curve (for $\tau_{diss} \sim 45$) assumes the exponential cut-off of the Wien spectrum while the low-frequency tail is still prominent. These features make the transient spectra highly non-thermal.

A comparison of Figure 2.9 with Figure 2.11 informs us that the spectra of these two scenarios are quite similar. Consequently, a comparison among Figure 2.10 and Figure 2.12 also exhibits very similar results - including the anti-correlations between α and peak frequency and between α and β.

Maxwellian leptons at 10^8 K with a power law tail $p = 2.2$

This section explores the system when pair enriched leptons are distributed according the Maxwell-Boltzmann distribution at 10^8 K for lower energies whereas the high energy ones form a power-law tail with index $p = 2.2$.

Similar to the previously discussed cases, the photon spectrum fits the Wien spectrum at equilibrium in Figure 2.13. A remarkable difference between Figure 2.13, and between Figures 2.9 and 2.11 is that the high frequency power law tail catches up with the pair-annihilation much earlier ($\tau_{diss} << 0.05$) as depicted by the black curve. Remnants of the

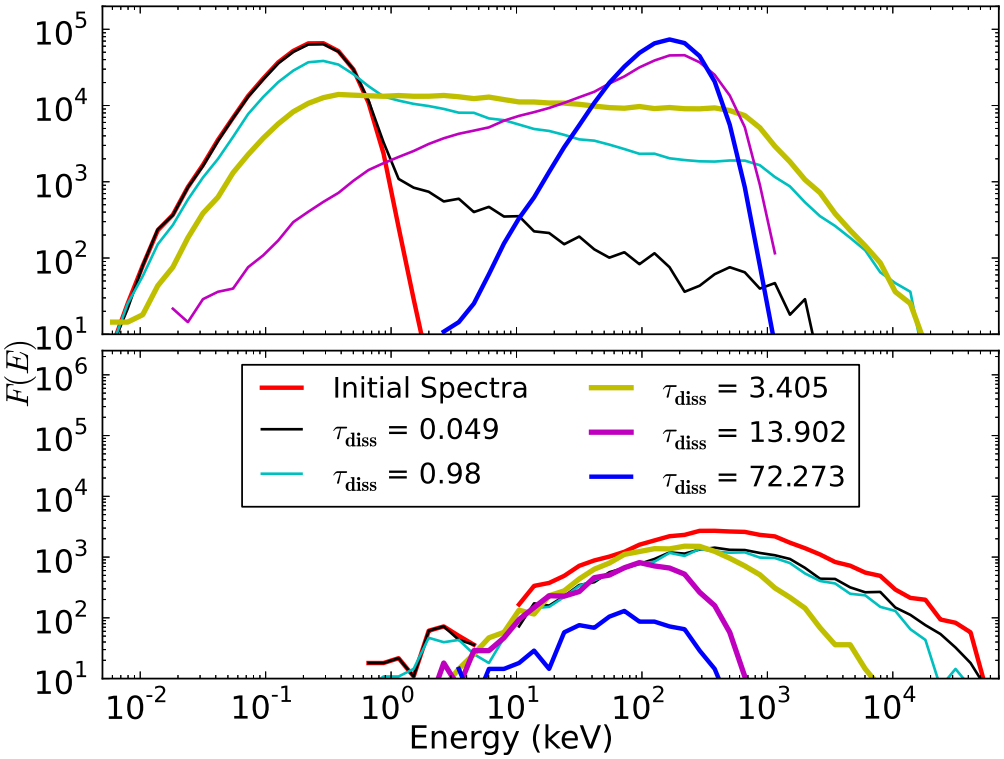

FIGURE 2.13: Photon spectrum (upper panel) and leptons' kinetic energy distribution (lower panel) at different stages of the pair-enriched simulation discussed in Section 2.42. The legend associates the various optical depths of energy injection with the corresponding color coded particle spectrum and distribution.

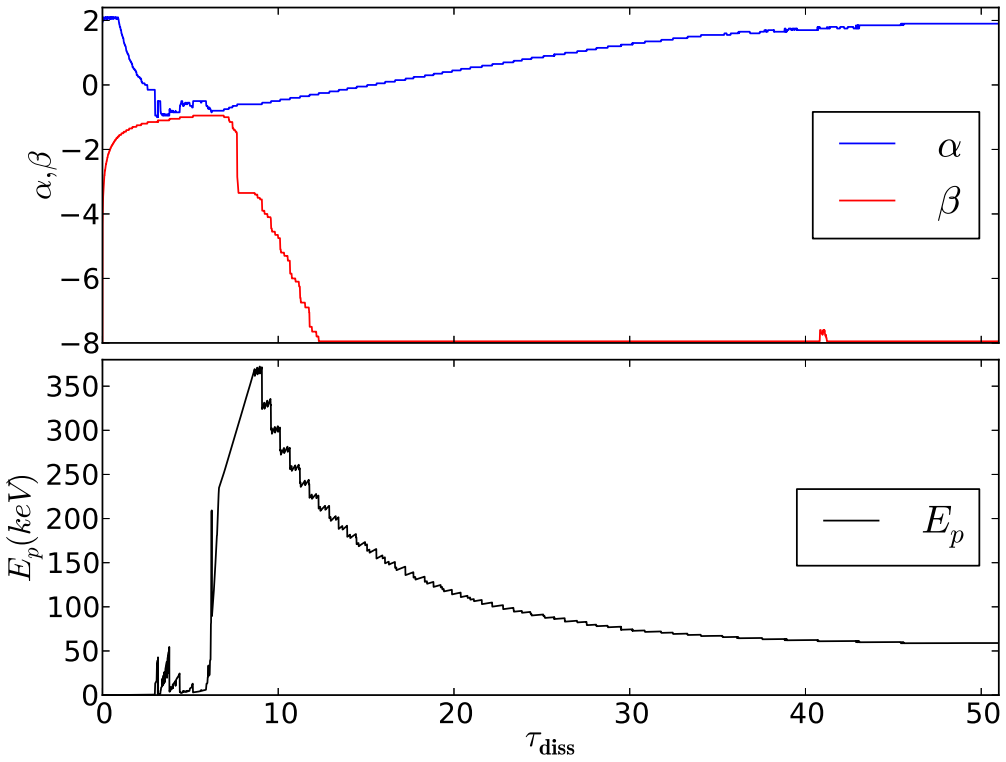

FIGURE 2.14: Evolution of the Band parameters α, β and E_p of spectra from the simulation shown in Figure 2.13 with increasing energy-injection opacity.

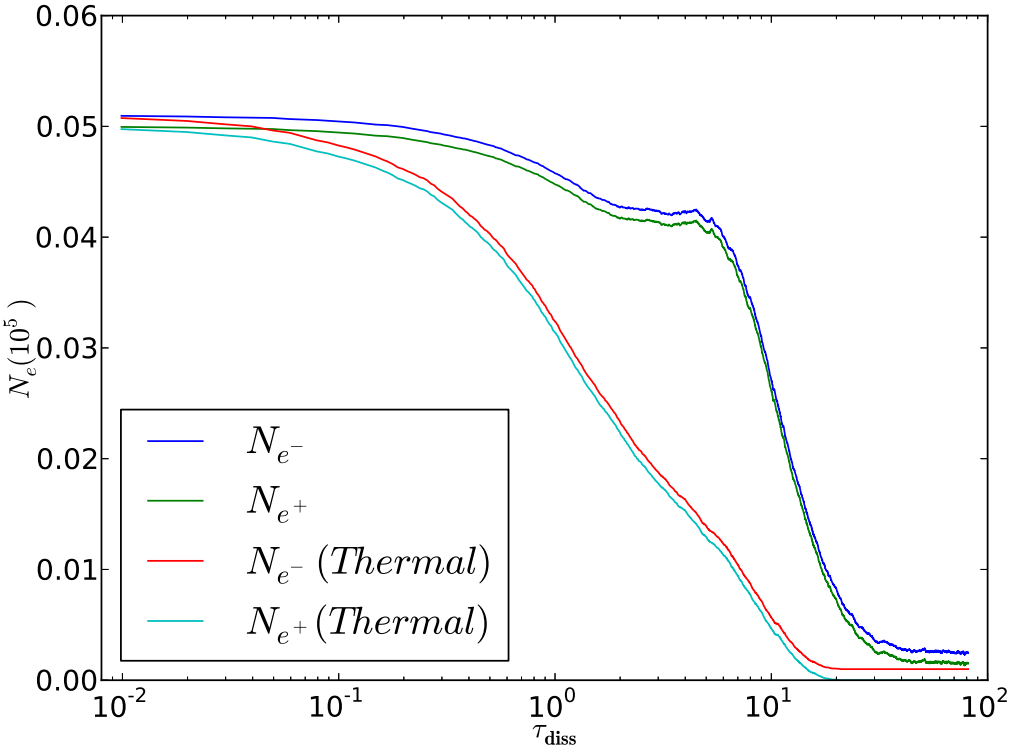

FIGURE 2.15: Evolution of lepton count N_e for the simulations in Section 2.42 (labeled as *Thermal*) and 2.42. Note that the lepton count evolution of the simulations discussed in Sections 2.42 and 2.42 is indistinguishable. The x-axis displays the opacity at which energy injection occurred.

hump are visible in the black and cyan curves. Furthermore, for less than 1 scatterings, the low frequency tail becomes softer than the Wien spectrum (cyan curve). Another important non-thermal feature is the broadband nature of the flattened spectrum (the yellow curve extends over four orders of magnitude in frequency). By about $\tau_{diss} \sim 14$, the truncated high frequency tail approaches the exponential cut-off of the Wien spectrum, whereas the soft low frequency tail still persists.

The best-fit Band function obtained by χ^2 minimization technique, produces highly non-thermal spectral indices (α and β) but the peak frequency as shown in Figure 2.14 is relatively high for GRBs. The lack of smoothness in the α values for moderate optical depths is due to the flatness of the photon spectrum as seen from the yellow curve in Figure 2.13, which occurs in conjunction with the transient saturation phase in the lepton count (see Figure 2.15). Figure 2.15 also displays and compares the lepton count for the simulation in Section 2.42 (the curves labeled as *Thermal*, which are indistinguishable from the pair evolution in Section 2.42). Although the initial lepton content of the plasmas in the three discussed simulations is identical, the plasma with a greater kinetic energy injection can sustain pairs for larger optical depths leading to a much broader and flatter spectrum. For moderate number of scatterings, we obtain $\alpha = -1$ and $\beta = -0.95$. Again, an anti-correlation is found to exist between the parameters α and β and also between α and the peak frequency.

2.5 Summary and Discussion

We present Monte Carlo simulations of Compton scattering, e^-e^+ pair production, and e^-e^+ pair annihilation in GRB fireballs subject to mild to moderate internal dissipation. We explore cases of photon-rich media – as expected in baryonic fireballs – and of pair-dominated media. The leptonic component in our simulations is initially set out of equilibrium by a sudden injection of energy and the spectrum is followed as continuous collisions among photons and leptons restore equilibrium.

We find that non-thermal spectra arise from transient effects. Such spectra could be ad-

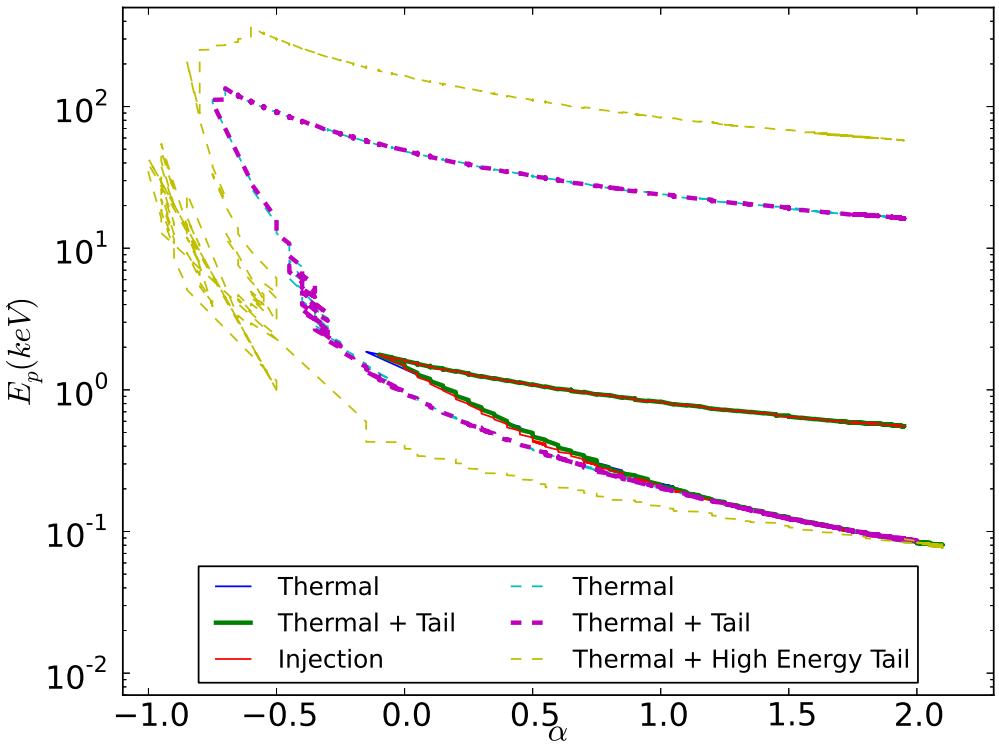

FIGURE 2.16: Plot of Band parameters E_p and α for the various simulations discussed. The solid curves represent photon-rich plasmas ($\frac{N_\gamma}{N_{lep}} = 1000$) whereas the broken curves are indicative of pair-enriched plasmas where ($\frac{N_\gamma}{N_{lep}} = 10$). Note the similarity among the curves and the exhibited anti-correlation.

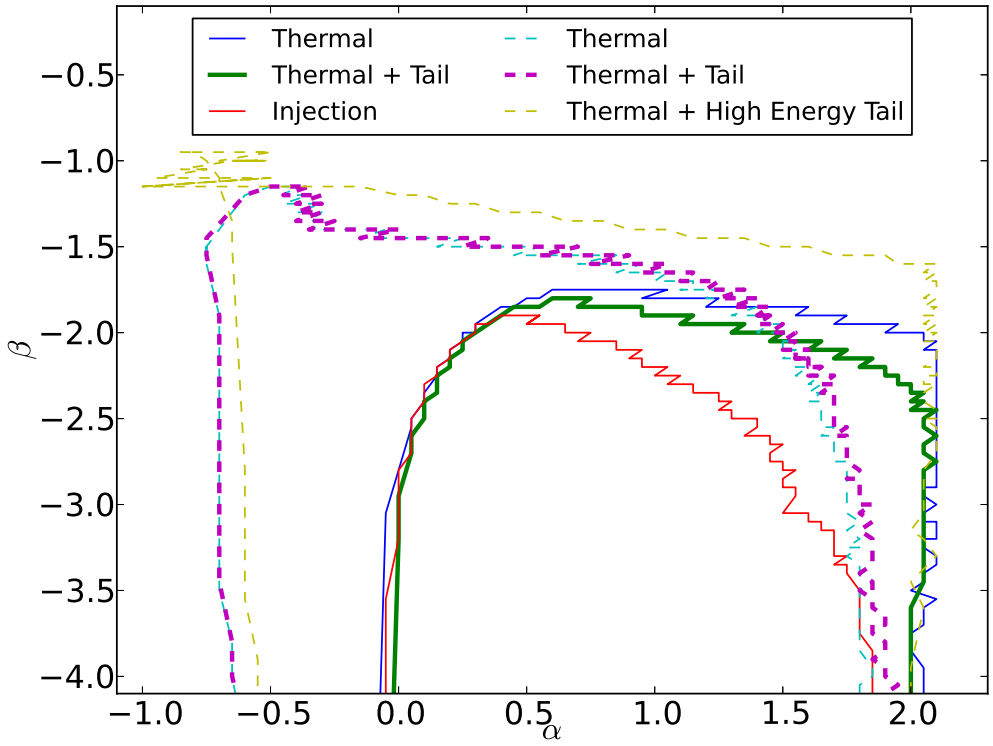

FIGURE 2.17: Plot of Band parameters β and α for the various simulations discussed. The solid curves represent photon-rich plasmas ($\frac{N_\gamma}{N_{lep}} = 1000$) whereas the broken curves are indicative of pair-enriched plasmas where ($\frac{N_\gamma}{N_{lep}} = 10$). Note the complex behavior of the curves, especially the evolution of β.

vected by the expanding fireball and released before equilibrium is reached if the dissipation takes place at optical depths of up to several hundred. We show that the transient spectra can be reasonably fit by a Band function (Band et al. 1993) within a frequency range of 2-3 orders of magnitude around the peak and could therefore explain GRB observations. As suggested by Lazzati and Begelman (2010), non-thermal features can arise even if both the photon and lepton distributions are initially thermal, provided that they are at different temperatures. As a matter of fact, we find that the spectrum emerging from the fireball after a dissipation event at a certain optical depth does not depend strongly on the way in which the energy was deposited in the leptons. For the photon-rich cases, the first reaction of the photon spectrum to a sudden energy injection into the leptons is the formation of a high-frequency power-law, either because non-thermal leptons are present or through the mechanism described in Lazzati and Begelman (2010). If the injection happens at moderate optical depths, the peak frequency of the photon spectrum also shifts to higher frequencies and a non-thermal low-frequency tail appears. If the energy injection occurs at somewhat large optical depths, the high frequency tail disappears and the spectrum presents a cutoff just above the peak. The low-frequency non-thermal tail is however very resilient and only if the dissipation takes place at very large optical depths, the equilibrium Wien spectrum is attained. The pair-enriched simulations show a more complex behavior at low optical depths due to pair processes, however we still observe the low frequency tail's resilient behavior. We show that this phenomenology is rather independent on the details of the energy dissipation process and generated lepton distributions: non-thermal leptons, high-temperature thermal leptons, and multiple discrete injection events all produce similar spectra. For the case of the pair-enriched simulations however, we obtain peak frequencies that are somewhat large in the comoving frame (several hundred keV) making this scenario less interesting for explaining observed burst spectra. However their complex behavior and extreme peak energies offer a tantalizing explanation for the rich diversity observed in peak energies of GRBs (Goldstein et al. 2012) especially when the peak energies $>$ MeV.

The conclusion we can glean from this study is therefore that comptonization of advected seed photons by sub-photospheric dissipation continues to be a viable model to explain the prompt gamma-ray bursts spectrum. Agreement is particularly strong when the dis-

sipation occurs at moderate optical depth (of the order of tens) so that both a high- and a low-frequency tail are produced. Dissipation at too low optical depth would only produce a high-frequency tail, while dissipation at too large optical depth would only produce a low-frequency tail. In a GRB dissipation is likely to occur at all optical depths (e.g. Lazzati et al. 2009). The dissipation events that occur at moderate optical depth would therefore be those mostly affecting the spectrum and giving it its non-thermal appearance. Bursts characterized by a Band spectrum over more than three orders of magnitude of frequency remain however challenging for this model, and other effects need to be invoked to avoid deviations from the pure power-law behavior at very low and high frequencies. Among these effects, some studied in the literature are sub-photospheric, radiation mediated multiple shocks (Keren and Levinson 2014; line of sight effects (Pe'er and Ryde 2011) and high-latitude emissions Deng and Zhang 2014).

2.51 Spectral correlations

Besides finding that the overall shape of the partially Comptonized spectra is qualitatively analogous to what observed in GRBs, we find that this model predicts the existence of two correlations that can be used as a test of its validity. We first notice an anti-correlation between the low-energy photon index α and the peak frequency. The correlation is clearly seen in Figure 2.16, where results from all simulations are shown simultaneously. All simulations start with the same injected photon spectrum, the common point in the lower right of the diagram. The leptons in all three of the photon-rich simulations are energized to identical total kinetic energies K albeit different distribution functions. It is clear that the evolution of all photon-rich simulations is virtually indistinguishable from each other. As more and more scatterings occur, the peak frequency initially grows and the low-frequency slope flattens. At moderate optical depths (~ 100 in all three cases) the peak frequency reaches its maximum, the high frequency tail disappears (shown in the Figure 2.17) and the low-frequency tail begins to thermalize, dragging the peak frequency to slightly lower values. The correlation has two branches, a steeper one for $\tau < 100$ and a flatter one at $\tau > 100$. The second branch corresponds, however, to spectra without a high-frequency tail and is therefore not expected to represent observed GRBs. A similar pattern is followed by the pair-enriched cases, with the main difference that larger peak

frequencies are attained along with softer values for α and β. The evolutionary curves for the pair-enriched cases show complexity due to the presence of pairs especially at low opacities - with the simulation in Section 2.42 showing a greater amount of variability due to its ability to sustain pairs by temporarily balancing the number of pair production and annihilation events (see Figure 2.15).

In addition to the $\alpha - \nu_{\rm pk}$ anti-correlation, we also find hints of an anti-correlation between α and β. This correlation is shown in Figure 2.17 and is much more complex, reflecting the more complex behavior of the high-frequency spectrum with respect to the low-frequency one. In the case of the high-frequency photon-index β, the way in which the energy is injected in the lepton population matters, each simulation producing a different track on the graph.

Comparing these predictions to GRB spectral data is not straightforward, since the correlations should not be strong in observational data. Adding together data from different bursts, the correlations in the observer frame would be diluted by the different bulk Lorentz factors of bursts and by the diversity of the particle ratio, radiation temperature, and dissipation intensity among busts and pulses in a single burst. Still, some degree of correlation has been discussed in the literature, with contradictory conclusions as to its robustness. The $\alpha - \nu_{\rm pk}$ anti-correlation has been discussed in large burst samples (e.g. Amati, L. et al. 2002; Goldstein et al. 2012; Burgess et al. 2015). The α-β anti-correlation has been observed for some bursts (Zhang et al. 2011), however it is not a common feature among GRBs.

Photospheric dissipation models have found it difficult to reproduce low frequency photon index $\alpha \sim -1$ and have been unable to explain the GeV emissions (Zhang et al. 2011). Figure 2.13 displays the emission spectra in the rest frame of the burst and once Lorentz boosted the photons forming the high frequency tail reach GeV energies. For low/moderate opacities, our simulations have consistently reproduced the low-energy photon index $\alpha < 0$ as shown in Figure 2.16 thus providing a possible resolution for the mentioned issues. Our current model is unable to reproduce $\alpha < -1.1$ for the parameter space explored, however additional effects such can modify and further soften the low frequency spectra. Analogous studies of comptonization effects in GRB outflows have been performed in the

past, for example by Giannios (2006) and Pe'er et al. (2006). Our work differs from both of these previous studies in both content and methodology. Giannios (2006) studied with Monte Carlo techniques the formation of the spectrum in magnetized outflows, considering a particular form of dissipation and assuming that the electrons distribution is always thermalized, albeit at an evolving temperature. Pe'er et al. (2006), instead, used a code that solves the kinetic equations for particles and photons, and considered injection of non-thermal particles (as in our Section 2.41) as well as continuous injection of energy in a thermal distribution. None of these previous studies consider impulsive injection of energy in thermal leptons, as discussed here or the case of multiple, discrete injection events. In an attempt to keep our results as general as possible we have performed the calculations in a static medium, rather than in an expanding jet. As long as the opacity at which the dissipation occurs is not too large, this should not be a major limitation, and the advantage is that our results are not limited to a particular prescription for the jet radial evolution. In addition, most of the interesting results (the non-thermal spectra) are obtained for small and moderate values of the optical depth (or, analogously, of the number of scatterings that take place before the radiation is released). It should also be noted that the assumption of an impulsive acceleration of the leptons that does not affect the photon spectra is likely not adequate in a highly opaque medium. A final limitation of this study is that only moderate values of the particle ratio can be explored. This is an inevitable limitation when both the lepton and photon distributions are followed in the scattering process with a Monte Carlo technique. If one of the two significantly outnumbers the other, a very large number of photons (or leptons) are required, making the calculation extremely challenging and would require parallelizing the code. While performing such simulations is important and will eventually become possible, we do not anticipate big phenomenological differences with respect to what we consider here. Even with less electrons, we expect the formation of a high-frequency tail (e.g. Lazzati and Begelman 2010), the subsequent shift of the peak frequency accompanied by a flattening of the low-frequency photon index, and complete thermalization only after many scatterings (i.e., only if the dissipation occurs at a very high optical depth).

Acknowledgments

We thank the anonymous referee for her/his comments leading to improvement and clarity of the manuscript. We thank Paolo Coppi for his advice and insight into the physics of scattering and Gabriele Ghisellini and Dimitrios Giannios for insightful discussions. This work was supported in part by NASA Fermi GI grant NNX12AO74G and NASA Swift GI grant NNX13AO95G.

3 DYNAMIC MONTE CARLO SIMULATIONS OF RADIATIVELY ACCELERATED GRB FIREBALLS

3.1 Abstract

We present a novel Dynamic Monte Carlo code (DynaMo code) which self-consistently simulates the Compton scattering driven dynamic evolution of a plasma. We use the DynaMo code to investigate the time–dependent expansion and acceleration of dissipationless GRB fireballs by varying their initial opacities and baryonic content. We study the opacity and energy density evolution of an initially optically thick, radiation–dominated fireball across its entire phase space - in particular during the $R_{\rm ph} < R_{\rm sat}$ regime. Our results reveal new phases of fireball evolution: a transition phase with a radial extent of several orders of magnitude - the fireball transitions from $\Gamma \propto R$ to $\Gamma \propto R^0$, a post–photopsheric acceleration phase - where fireballs accelerate beyond the photosphere, and a Thomson–dominated acceleration phase - characterized by slow acceleration of optically thick, matter–dominated fireballs due to Thomson scattering. We quantify the new phases by providing analytical expressions of Lorentz factor evolution, which will be useful for deriving jet parameters.

3.2 Introduction

Gamma–Ray Bursts (GRBs henceforth) are intense bursts of high energy radiation (high energy X-rays and γ rays). First detected serendipitously about five decades ago (Klebesadel et al. 1973), today GRBs are regularly detected by space-based satellites and are known to be one of the brightest explosions in the universe ($L \sim 10^{51-52}$ ergs / s) (see Piran 2004). These large luminosities along with small variability time-scales and the emission of high energy gamma rays ($\sim$ 100+ keV) led to the compactness problem in GRBs. The compactness problem was resolved by invoking ultra-relativistic motion

(Paczynski 1986; Goodman 1986) of the emitting source, which has been confirmed by observations (Frail et al. 1997; Frail et al. 2001)

GRBs are thought to be powered by the core-collapse of a massive rotating star (leading to Long GRBs) and the merger of two neutron stars / a neutron star and black hole (resulting in Short GRBs) (see Kumar and Zhang 2015). Although ultra-relativistic jets are invoked to explain GRBs, the mechanism responsible for the jet production from GRB progenitors is not well understood and is under investigation. The two mechanisms that have been proposed to launch and accelerate jets to relativistic speeds are 1) magnetic fields and 2) radiation. Several prior works have studied the driving role of magnetic fields in collimating and accelerating relativistic outflows in astrophysical environments (see for e.g., Blandford and Znajek 1977, McKinney 2006, Komissarov 2011, Tchekhovskoy et al. 2011). Consequently, they have been been proposed as the jet production mechanism in GRBs (Drenkhahn and Spruit 2002; Lyutikov et al. 2003). In this paper we will explore in detail radiation as an alternative mechanism to accelerate (and possibly launch) relativistic outflows.

Radiative acceleration of outflows is a well known astrophysical phenomenon (e.g., continuum and line–driven stellar winds – see Castor et al. 1975; Smith and Owocki 2006). To produce relativistic outflows associated with GRBs and AGNs, radiative acceleration due to external radiation sources has been investigated. Madau and Thompson (2000) studied the radiative acceleration of cold, optically thin plasmas due to external radiation sources. Zampieri et al. (2003) studied radiative acceleration of low density ion-electron plasma by incident transient radiation along with radiation-induced internal electric fields. The above mentioned works have primarily focused on the dynamical evolution of a low-density, optically thin plasma under the influence of radiation sources external to the plasma. In contrast to the earlier studies, one of the first and foremost theoretical models to understand the physics of GRBs was the GRB fireball model, based on a hot, spherically expanding, outflow optically thick to radiation. The fireball model assumes an initially optically thick plasma, with radiation and matter in thermal equilibrium, and the radiation energy density exceeding the rest mass energy density

significantly (Meszaros et al. 1993; Piran 2004). When these conditions are met, radiation pressure due to the trapped photons dominates the outflow (or fireball - we will use these terms interchangeably) evolution leading to an accelerating, ultra-relativistic fireball.

In this article, we will investigate from a micro-physical perspective Comptonization driven acceleration by radiation advected with the outflow. We present our Dynamic Monte Carlo code (DynaMo code) that we have used to self-consistently investigate the scattering induced acceleration, and relativistic expansion of a spherical fireball. This paper is organized as follows: § 3.3 begins with an introduction to the fireball theory (§ 3.31) followed by an overview of the methodology behind the DynaMo code (§ 3.32). In § 3.4 we present and discuss our results, followed by a comparison with the fireball model's theoretical results. In § 3.5, we summarize our work and draw our conclusions.

3.3 Theory and Methodology

3.31 Fireball Theory

The idea of the fireball was first advocated by Cavallo and Rees (1978) to explain the phenomenon of GRBs. Created by depositing a large amount of energy onto matter confined to a small volume, a sufficiently dense fireball will be optically thick ($\tau \gg 1$) to its own radiation. This radiation can drive the acceleration and ultra-relativistic expansion of the fireball if the radiation energy density exceeds the fireball's rest mass energy density. Thus, the fireball model resolved the GRB compactness problem by employing radiation as a mechanism to drive the radiation-matter mixture to ultra-relativistic speeds (Paczynski 1986; Goodman 1986). Radiation to matter energy density and opacity are important factors that govern the evolution of a fireball, and this is graphically represented in Fig. 3.1 by the phase-space diagram. In this diagram, GRB fireballs start optically thick and radiation–dominated in the top–right part of the graph. We refer to this part of the diagram as quadrant 1 (here exponents of both logarithmic axes are positive, analogous to first quadrant in the Cartesian coordinate system where x and y are positive). The fireballs eventually evolve to quadrant 3 (bottom–left portion of Fig. 3.1 where exponents of both

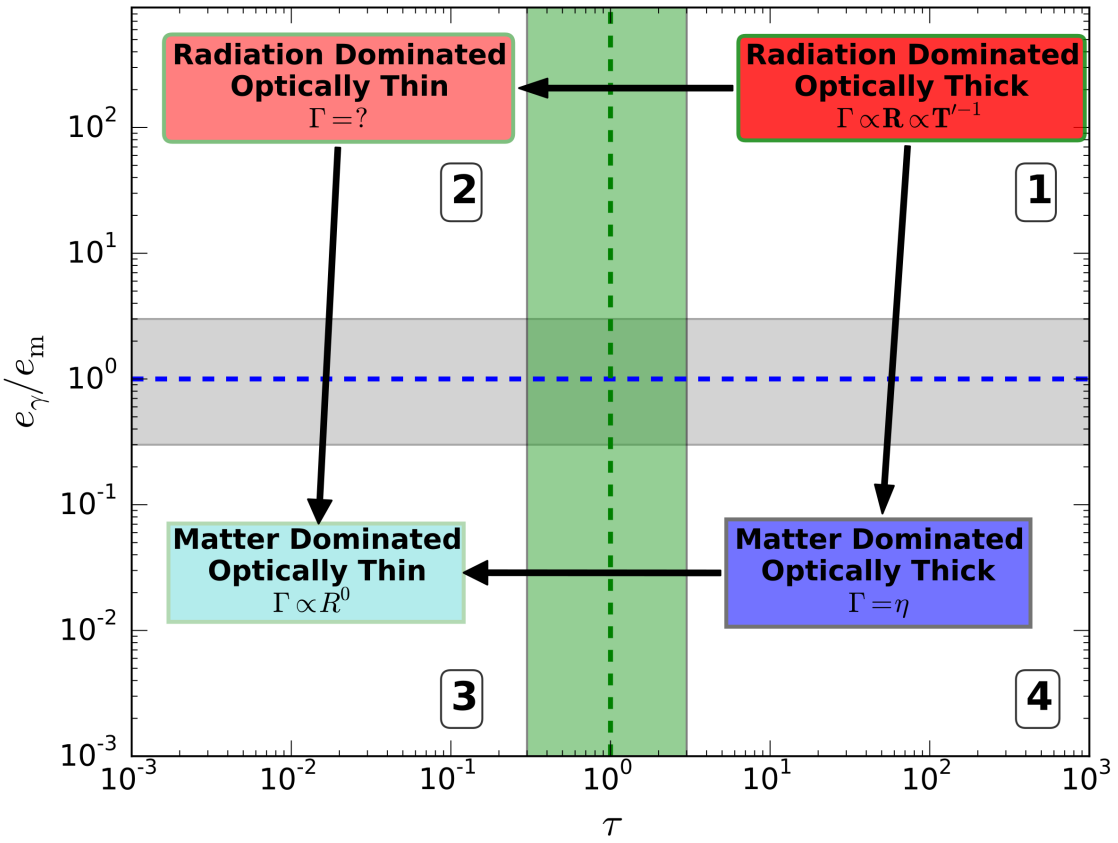

FIGURE 3.1: Diagram illustrating the phase space evolution of a GRB fireball based on the fireball model. The y axis depicts the ratio of radiation to matter energy density and the x-axis plots the opacity. In the phase space diagram, GRB fireballs begin their evolution in quadrant 1 ($\tau \gg 1, e_\gamma/e_\mathrm{m} \gg 1$) and end it in quadrant 3 ($\tau \ll 1, e_\gamma/e_\mathrm{m} \ll 1$). The arrows show possible evolutionary paths of fireballs. The shaded regions near $\tau \sim 1$ and $e_\gamma/e_\mathrm{m} \sim 1$ represent transition zones or regions where fireball evolution has not been well studied.

logarithmic axes are negative, similar to the third quadrant in the Cartesian coordinate system) where they become optically thin and matter–dominated. As we discuss later in this section, the evolutionary trajectory of a fireball as it evolves from quadrant 1 to 3 depends on the fireball's initial parameters.

To parameterize the fireball the most important physical quantities are 1) the total energy E (includes energies of both matter and radiation), 2) its rest mass M, and 3) the initial radius of the fireball R_0 (i.e., fireball evolution begins with bulk Lorentz factor $\Gamma_0 = 1$ at R_0). Radiation-matter interactions transform the fireball's internal energy into bulk kinematic motion. Assuming that the fireball remains highly opaque ($\tau \gg 1$) during expansion, the maximum possible Lorentz factor η attained (using energy conservation) is given by -

$$\eta = \frac{E}{Mc^2}. \tag{3.1}$$

To characterize the evolution (acceleration and expansion) of the fireball plasma, we require the bulk Lorentz factor Γ and the radius R of the fireball. These physical quantities do not evolve independently during the radiation–dominated acceleration phase (quadrant 1 in Fig. 3.1). The mathematical relationship between these quantities and the comoving temperature T' can be obtained using energy, momentum, and entropy conservation, as given by (Meszaros et al. 1993; Piran 2004) –

$$\Gamma \propto R \propto \frac{1}{T'}. \tag{3.2}$$

Piran (1999) has studied an adiabatically expanding fireball with infinite opacity using hydrodynamic equations. The conservation equations for energy, momentum, and number of particles, are as follows:

$$R^2 \rho \Gamma = c' \tag{3.3}$$

$$R^2 e^{\frac{3}{4}} \Gamma = c'' \tag{3.4}$$

$$R^2 \left(\rho + \frac{4e}{3} \right) \Gamma^2 = c''', \tag{3.5}$$

where R denotes the fireball radius, and c', c'' and c''' are constants (see Piran 1999 for an exact definition of the variables used). The boundary conditions for this system are 1) the fireball starts from rest at an initial radius R_0 and 2) as $R \to \infty$ the Lorentz factor equals

η. Using these boundary conditions, the conservation equations can be solved to obtain -

$$R = \frac{R_0 \Gamma (\eta - 1)^{3/2}}{(\eta - \Gamma)^{3/2}}. \tag{3.6}$$

The radiation–dominated acceleration phase can end if 1) the optically thick fireball's radiation energy density becomes comparable to or less than the rest mass energy density (i.e., radiation energy does not dominate matter energy density), and/or 2) radiation escapes at the photopshere due to the expanding plasma's decreasing opacity. In the former case, the trapped photons lose their energy by continually accelerating the plasma to the maximum possible Lorentz factor η (see eq. 3.1). The fireball, thereafter, coasts at η and this new phase is thus termed the saturation or the coasting phase. In the GRB phase space diagram (Fig. 3.1), this evolution is represented by the fireball moving from quadrant 1 to 3 via quadrant 4. Using eq. 3.2, the characteristic radius at which the saturation phase begins can be computed as -

$$R_{\rm sat} = \frac{\eta}{\Gamma_0} R_0 = \eta R_0. \tag{3.7}$$

In the latter case, the photons escape the fireball if the expanding plasma's optical depth does not remain large enough, thereby, bringing an end to the acceleration process. In the phase space diagram, this evolution is represented by the fireball moving from quadrant 1 to 2 and eventually to 3. The characteristic theoretical radius where radiation decouples and escapes the plasma (assumed to occur when the optical depth $\tau \sim 1$) is termed the photospheric radius and is denoted by $R_{\rm ph}$. The absence of radiation causes the driving force to vanish, and as a result the plasma coasts at the Lorentz factor achieved at the photospheric radius.

In the previous paragraphs we outlined different evolutionary paths for GRB fireballs. The fireball's evolution depends on its initial energy density and opacity, and the effect of both these parameters can be mathematically represented by the ratio of the characteristic radii, i.e., $R_{\rm ph}/R_{\rm sat}$. It is important to point out that earlier works have studied extreme regimes of fireball evolution, e.g., the hydrodynamical evolution of a fluid with infinite opacity (Piran 1999). Another well studied scenario is when a radiation–dominated fireball reaches the photosphere and then suddenly loses its radiation (Meszaros et al. 1993; Rees and Mészáros 2005). Earlier works have not studied the realistic scenario where,

due to the expansion and acceleration, the fireball 1) gradually becomes optically thin (evolves from quadrant 1 to 2) and loses photons, and 2) is no longer radiation energy dominated (transitions from quadrant 1 to 4). These transition zones are represented by the highlighted regions in Fig. 3.1. In addition, analytical calculations encounter difficulties in studying fireball evolution for small opacities (e.g., the Lorentz factor evolution is unknown in quadrant 2 – as indicated by the question mark in Fig. 3.1). In § 3.4, we will show and discuss the results of fireball evolution in all regimes and across the transition zones. These results are obtained using our DynaMo code, which we detail in the next section.

3.32 The Code

In this section we detail the methodology behind the DynaMo code, which simulates the Compton scattering driven expansion and evolution of an outflow. The outflow is a scattering dominated plasma composed of photons, leptons (and protons). Figure 3.2 shows a diagrammatic cross-sectional view of the outflow geometry, which is a conical wedge with an opening angle θ_c and encapsulates a section of the fireball's spherical shell. Also shown is a fireball shell as it travels radially outward, expands and becomes optically thin (the differently colored arcs represent the expanding shell at different radial positions and opacities).

For our simulations, we are primarily concerned with the physical quantities in three distinct reference frames -

- **Lab Frame** - The lab or the laboratory frame is the frame at rest with respect to the GRB progenitor producing the outflow or the host galaxy. Any observer at rest in the lab frame observes the jet moving with a bulk Lorentz factor Γ.

- **Jet Frame** - Also known as the comoving frame, this reference frame travels with the GRB outflow at the bulk Lorentz factor Γ. From the perspective of an observer in the lab frame, the jet frame would be in motion along the radial direction (which is along the z direction as depicted in Fig. 3.2). Any physical quantity computed in the jet frame will be primed, e.g., the four–momentum of an electron in the comoving

frame will be denoted as $p'^{\mu}_{e^-}$. This frame is naturally suited for calculating local properties of the fluid/plasma (e.g., comoving temperature T').

- **Particle Frame** - At any given time, the motion of any particle in the plasma will be different from the bulk motion of the jet plasma due to the random thermal motion of the particle. The particle frame is the frame comoving with the lepton (or proton) selected for the scattering (or collision) process (we will discuss the particle interactions in greater depth later in this section). The interaction cross-sections (total and differential) are expressed in terms of physical quantities defined in the frame of the particle involved in the interaction.
  All physical quantities in the particle frame will be double primed, for example, the four–momentum of a photon as observed in the frame of an electron will be denoted by p''^{μ}_{γ}.

Fireball Initialization

The first step of our simulation is the initialization of the GRB fireball with the appropriate parameters. As we simulate a section of a fireball shell encapsulated within a conical wedge, the following parameters need to be specified to initialize the simulation –

- Wedge Opening Angle: $\theta_c = \pi/10^4$ radians.
  To prevent causality violation and unphysical scatterings, it is imperative that the condition $\theta_c \ll 1/\Gamma$ is always satisfied during fireball evolution.
- Initial Bulk Lorentz factor: $\Gamma_0 = 1$
  The GRB fireball initially possesses only internal energy and no bulk kinetic energy.
- Wedge Outer Radius: $r_{\text{outer},0} = 10^8$ cm (Pe'er et al. 2015)
- Wedge Inner Radius: $r_{\text{inner},0} = 8 \times 10^7$ cm
- Particle Initialization:
  - Particle Count: The code can simulate interactions between photons, leptons (electrons) and baryons (protons), and thus requires the number N and type

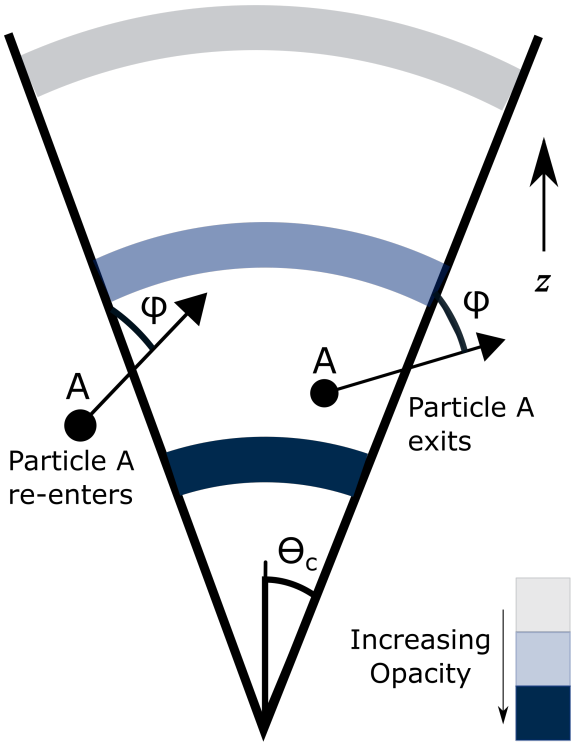

FIGURE 3.2: Diagram depicting the cross-sectional view of the simulated wedge. The colored arcs represent a shell traveling radially outward (along the z direction), expanding and becoming more transparent. Also shown is an implementation of the periodic boundary condition with particle A exiting and re-entering the wedge at an angle φ with the lateral surface.

of particles to be specified. Unless otherwise stated, the total photon count is $N_\gamma = 2800$, and the electron and proton counts are $N_e = N_p = 100$.

- Spatial Distribution: The code synthesizes the specified number N of particles, and uniformly distributes them within the specified inner and outer radii of the wedge.
- Distribution Functions: The user can synthesize particles by supplying the appropriate parameters to the inbuilt energy distribution functions (e.g., comoving temperature T' for thermal distribution, power law index p for non-thermal distribution, the energy for mono-energetic distribution).

  Though the code can accept any temperature value, the simulations shown in this paper start at $T' = 7.7 \times 10^9$ K. At this temperature the electrons are distributed according to a Maxwell Jüttner distribution, the protons adopt a Maxwell Boltzmann distribution, and the photons conform to a Blackbody distribution.

Dynamic Time Step Calculation

As one of the motivations of our code is to track and evolve the plasma and its constituents, it is essential to track the four–momenta and positions of all the particles in the lab frame. In order to dynamically evolve the system a time step is required, and the maximum value of that step is dictated by the mean free times of the photons in the plasma. Let us first consider photon-lepton scatterings. From a physical perspective, all the particles travel in straight lines until a photon-lepton pair scatters, exchanges energy and momenta, and then the particles again travel in straight lines until the next photon-lepton scattering occurs. This time interval between successive photon-lepton scatterings is the collision-free time experienced by all particles in the plasma (we shall refer to this interval as the collision time - $t_{\rm coll}$). Thus, the dynamic time step in our simulation is this collision time. The reader should refer to Appendix A for a detailed calculation of the collision time.
As experienced by a single photon, the infinitesimal opacity of a medium (at rest) as given in Rybicki and Lightman (1986) is –

$$d\tau = n\sigma_T dl, \tag{3.8}$$

where n denotes the number density of the scatterers, σ_T is the Thomson cross section, and dl is the infinitesimal path length traversed by the photon.

Using eq. 3.8 and as shown in detail in Appendix A, the mean free time $t_{\rm mf}$ of the photon is (see eq. 6.2) –

$$t_{\rm mf} = \frac{1}{nc\sigma_T}, \tag{3.9}$$

where $c = 3 \times 10^{10}$ cm/s, is the speed of light. If the scattering medium contains $\rm N_p$ photons, the mean free time $\tau_{\rm Pop}$ for any photon within this population would be given by –

$$t_{\rm Pop} = \frac{1}{\sum_{i=1}^{\rm N_p} nc\sigma_T} = \frac{1}{\sum_{i=1}^{\rm N_p} \left(\frac{1}{t_{\rm mf}}\right)} = \frac{t_{\rm mf}}{\rm N_p}. \tag{3.10}$$

Physically, if the number of photons in a medium increases so should the likelihood of a photon colliding, thereby decreasing the mean free time of the entire population.

Now we shall discuss how the opacity and mean free quantities are modified if the scatterers themselves are in motion. The motion of scatterers introduces a velocity dependence in the opacity. As shown in Appendix A2 and Abramowicz et al. (1991), a single photon immersed in a medium of moving $\rm N_s$ scatterers, experiences an opacity $d\tau$ given by –

$$d\tau = \sum_{j=1}^{\rm N_s} n_j \sigma_T (1 - \beta_j \cos\theta_j) dl, \tag{3.11}$$

where β_j is the speed of the scatterer traveling in the $\rm j^{th}$ direction normalized by the speed of light and θ_j is the angle between the three momenta of the photon and the scatterer.

Let us now consider a plasma having multiple photons interacting with multiple scatterers. As shown in Appendix A2, the mean free time of the entire population is –

$$t_{\rm Pop} = \frac{V}{\sum_i \sum_j \sigma_T (1 - \beta_{\rm j} \cos\theta_{\rm ij}) c} = \frac{1}{\left(\sum_i \left(\sum_j \frac{1}{t_{\rm ij}}\right)\right)} = \frac{1}{\sum_i \left(\frac{1}{t_{\rm i}}\right)}. \tag{3.12}$$

Thus all the particles experience an *average or mean* free time $t_{\rm Pop}$ given by eq. 3.12. We note that this is an average value and therefore the extraction of the real collision time or the actual free travel time between successive scatterings (which is different from the mean free time) requires the use of a Monte Carlo acceptance-rejection algorithm. The probability of one photon scattering between the time interval t and $t + dt$ is proportional to –

$$P(t) \propto e^{\frac{-t}{t_{\rm Pop}}}, \tag{3.13}$$

which we use to obtain the collision time $t_{\rm coll}$ for our simulation.

Particle Selection

The collision time $t_{\rm coll}$ determines the travel time between photon–lepton scatterings. As some photon–lepton pairs are more likely to scatter than others, the code thus needs to account for this likelihood to identify and select the scattering pair.

Intuitively, the photon more likely to scatter will have a smaller free travel time as compared to the other photons. The *mean free* time is a measure of the free travel time for a given photon, and we use each photon's mean free time (eq. 6.15) and Monte Carlo techniques to identify and select the scattering photon. For any given photon, the probability of scattering is inversely proportional to its mean free time. Thus by inverting the mean free time $t_{\rm i}$ (see eq. 6.15) we obtain a number $p_{\rm i}$ proportional to the likelihood for that photon to scatter. For $p_{\rm i}$ to be a probability distribution, we normalize the inverses obtained from all photons, by obtaining the norm A –

$$\mathrm{A} = \sum_{i=1}^{\mathrm{N_p}} p_{\rm i} = \sum_{i=1}^{\mathrm{N_p}} \frac{1}{t_{\rm i}}. \tag{3.14}$$

By normalizing the inverses using A, we create a probability distribution amenable to Monte Carlo techniques. As each photon has a mean free time and an associated scattering probability, it is uniquely represented along the probability distribution by a certain range of values. We generate a uniformly distributed random variable in the interval [0,1) to identify which photon scatters.

The code follows a similar procedure to select the scattering lepton. To generate the probabilities for each lepton, we use the mean free time of interaction of the selected photon with the leptons in the plasma (given by eq. 6.13). As a result, we obtain the inverses $p_{\rm i,j}$ and the new norm $\mathrm{A_i}$-

$$\mathrm{A_i} = \sum_{\mathrm{j}=1}^{\mathrm{N_e}} \mathrm{p_{i,j}} = \sum_{\mathrm{j}=1}^{\mathrm{N_e}} \frac{1}{\mathrm{t_{i,j}}} \tag{3.15}$$

As illustrated by the photon selection process, each normalized probability $\mathrm{p_{i,j}/A_i}$ represents a range of values, thereby, identifying a unique lepton. We generate a uniform random variable in the interval [0,1), and thus identify which lepton among the N_e leptons scatters with the selected photon.

Particle Propagation

Between the scattering/collision events, the particles freely propagate for the duration of the time step. The position of any particle at time t is given by-

$$x^i(t) = x^i(t - t_{\rm coll}) + c\frac{p^i}{p^0}t_{\rm coll} \tag{3.16}$$

where $x^i(t - t_{\rm coll})$ denotes the i^{th} position component of the particle at time $t - t_{\rm coll}$, p^i and p^0 denote respectively the spatial and the zeroth component of the four–momenta of the particle.

Periodic Boundary Condition

As explained in § 3.32, once the time step is determined, the DynaMo code propagates and tracks the particles constituting the GRB fireball. Depending upon their momenta, particles can propagate to positions outside the simulated wedge resulting in the simulation losing particles. The radial thickness of the simulated fireball is determined by the innermost and outermost leptons, and so by the virtue of this definition, matter can never escape the simulated region radially. However, photons in the plasma can and are allowed to escape, as is discussed in § 3.32. However, all particles can also propagate to regions outside the wedge through the lateral surfaces (as shown by particle A in Fig. 3.2). These laterally escaping particles are, in fact, still within the spherical fireball (albeit outside our current simulation) and will influence the evolution of the entire spherical fireball. Just as a particle escapes our simulated wedge to an adjacent region, a particle from an adjacent region can enter via these lateral surfaces. To correctly simulate a spherical fireball the DynaMo code implements a periodic boundary condition scheme to account for particles traveling across lateral boundaries. This scheme implicitly assumes that the total particle count of the fireball is constant. If any particle exits through the lateral surface of the simulated wedge making an angle φ with the exiting surface, then a corresponding particle is inserted through the wedge surface opposite to the exit location, but at the same radius (see Fig. 3.2). The inserted (re-entering) particle makes the same angle φ with the entering surface as the exiting particle made with the exit surface, and possesses the same energy. This scheme is similar to the periodic boundary condition for parallel surfaces (where the

inclination angle between the surfaces is zero) where the particle momentum vectors at exit and entry surfaces are parallel and hence unrotated. As our simulated wedge has inclined surfaces, a lateral surface crossing requires the particle's three momenta be rotated by an angle of $2\theta_c$ (or twice the opening angle of the wedge). It should be noted that energy and total momentum magnitude of the particle remains constant during this scheme's implementation. However, the direction of three momentum does not remain constant.

Compton Scattering

The dynamical energy transfer mechanism in our simulations is Compton / Inverse Compton scattering. Once the particle selection step decides which pair of particles will be scattered, we use the Compton scattering algorithm (Klein–Nishina regime included) discussed in Chhotray and Lazzati (2015) for the scattering event. Post scattering, we have a new four–momenta for both the scattered lepton and photon which we use to calculate a new time step for the next scattering.

Baryon–Lepton Collisions

In general, GRB fireballs are baryon loaded (Meszaros et al. 1993) making them significantly more massive than baryon–deficient fireballs. We wish to explore whether the baryons (protons) in these baryon–loaded fireballs can accelerate and attain relativistic speeds (just like electrons do). We ignore the photon–proton (γp) scatterings because the photon energies have to be comparable to rest mass energy of protons ($\sim$ GeV) for the scattering process to transfer an appreciable amount of energy. To accelerate the protons the DynaMo code accounts for energy transfer between electrons and protons via electron–proton ($e^{-}p$) collisions. To simplify the physics and the collision process, the code does not carry out $e^{-}p$ collisions using the Coulomb cross section, instead it performs elastic collisions between electrons and protons. We note that our goal is to explore if protons can be accelerated to relativistic speeds, and not to simulate the $e^{-}p$ collision process to perfection. As our results demonstrate (see § 3.4), the elastic collisions we use provide a fast and reliable method to mimic the energy transfer that would have occurred during a real collision using Coulomb cross section. Another simplification we make is employing

pseudo protons to mimic the behavior of massive baryons. In order to accelerate protons (which are 1838 times the electron's mass) the code requires around 2000 additional photons for each proton in the plasma. To ensure that the simulations can be completed in a reasonable time frame, we employ pseudo protons of effective mass $m_{\rm eff} = 5m_e$ instead of real protons that are 1838 times more massive. This is similar to the reduced ion-masses employed by multi-dimensional PIC simulations (see Spitkovsky 2008).

The Coulomb cross section for interaction between charged particles (like e^-p interactions) is much larger than the cross section of γe^- interactions. Due to the attractive nature of the forces between these charged particles, there will be many e^-p interactions for every γe^- interaction. In other words, for every Compton scattering event, there will be several elastic e^-p collisions. As a consequence, between successive γe^- scatterings, the code ensures that each electron collides with a proton (for every γe^- scattering the number of e^-p collisions equal the number of e^-p pairs in the system).

To perform this elastic collision, the code begins by randomly selecting one e^-p pair from the plasma. To simulate an e^-p collision and the involved energy transfer, we first Lorentz transform to the proton's reference frame and compute the transformed four–momentum of the incoming electron. To calculate the transferred energies, we move to the center of momentum frame (COM frame) of the system. The advantage of employing this frame is that the collision here is always head on and the net three momenta of the e^-p system, pre and post collision is always zero. We Lorentz transform the four–momenta of the colliding proton and electron to this frame, which completely specifies the pre–collision geometry. To specify the post–collision geometry, we randomly generate the polar angle θ' and the azimuthal angle ϕ' in the COM frame. Now, by employing conservation laws, we can obtain the four–momentum of the proton after collision.

The four–momenta thus obtained in the COM frame is de-boosted to get the momenta in the proton's frame and subsequently, in the lab frame. This provides us with the post–collision momenta of both the proton and the electron in the lab frame. As stated earlier, for every γe^- scattering event, the code collides all the e^-p pairs once, leading to energy and momentum exchange among these particles. As a result, though the photons and the protons do not interact directly, the electrons act as an intermediary for transferring energy between radiation and baryons.

Data Update and Photon Escape Condition

Once the code performs the scattering and collisions, it updates the positions and four–momenta of all particles involved in the simulation. After each time step the code computes the radius of the farthest and nearest lepton from the origin, thereby, determining the fireball's outer and inner radii, respectively. To evaluate if a photon has escaped from the fireball, the code compares the radii of all photons with the fireball's outer radius. If any photon's radius exceeds the outer radius of the fireball, that photon is deemed to have escaped the fireball and is no longer a part of our simulation (it will not be involved in the time-step calculation nor the scattering process). The code runs until all the photons escape and are unable to further accelerate the fireball.

3.4 Results and Discussion

We have performed simulations of Compton scattering induced – radiative acceleration and expansion of a fireball, with and without baryon loading. Figure 3.3 shows the radial evolution of the bulk Lorentz factor of baryon–deficient fireballs for several ratios of $R_{\rm ph}/R_{\rm sat}$ (which serves as a proxy for the opacity). A detailed calculation of $R_{\rm ph}/R_{\rm sat}$ can be found in Appendix E. These results confirm the idea that greater the opacity of a plasma, the greater the terminal Lorentz factor achieved by the plasma due to acceleration by embedded radiation. Alternatively, as opacity indicates the number of scatterings occurring in a medium, these results confirm that an increasing number of scatterings is necessary for a plasma to continue accelerating radiatively by converting its internal energy into bulk motion. The evolution of our simulated fireballs is in strong agreement with the fireball model's proportionality relation $\Gamma \propto R$, during the radiation–dominated acceleration phase. In addition to $\Gamma \propto R$, the simulated fireballs also follow the relation $T' \propto R^{-1}$. The radial evolution of comoving temperature and other code tests can be found in Appendix D.

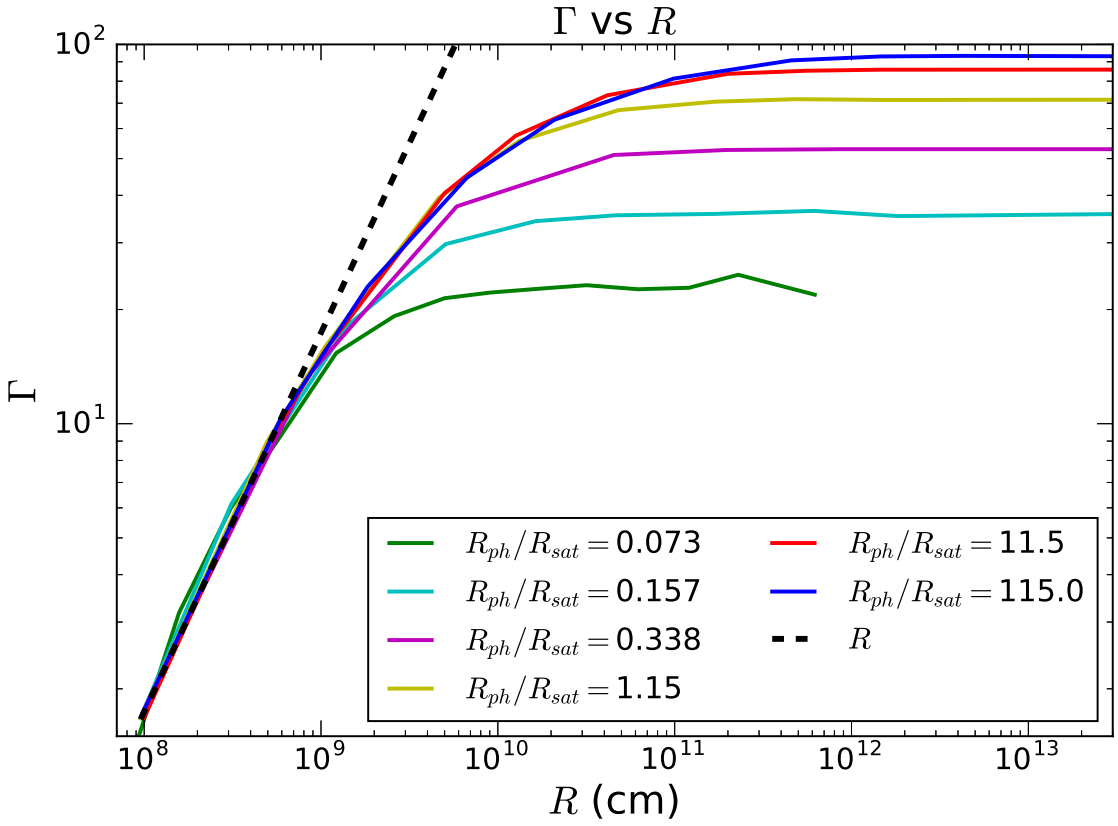

FIGURE 3.3: Evolution of Lorentz factor with radius for fireballs characterized by different initial opacities. The legend displays the $R_{\rm ph}/R_{\rm sat}$ value for each fireball and the corresponding color representing it.

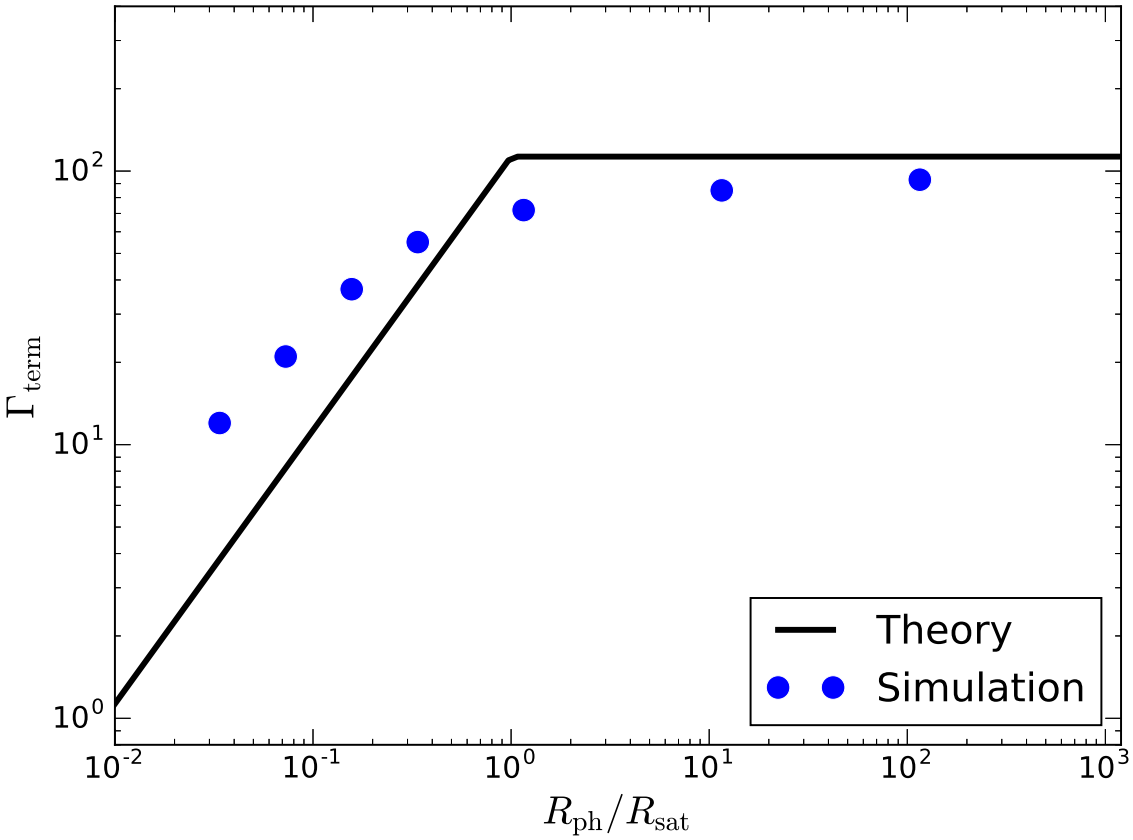

FIGURE 3.4: Theoretical and simulated values of terminal Lorentz factor $\Gamma_{\rm term}$ plotted against different $R_{\rm ph}/R_{\rm sat}$ ratios. The black curve plots the theoretical value of the terminal bulk Lorentz factor (obtained from the fireball model). The blue points represent the results obtained from our DynaMo simulations.

3.41 Transition Regime and Lorentz factor turnover

An interesting and new feature that emerges from Fig. 3.3 is the transition of the simulated Lorentz factors from the $\Gamma \propto R$ (radiation dominated) to $\Gamma \propto R^0$ (matter dominated) regime. As we pointed out in § 3.31, departure from $\Gamma \propto R$ regime occurs because fireball's energy density is no longer dominated by radiation. Further, we note that the magnitude of curvature or turnover of the Lorentz factor (the measure of how rapidly Γ transitions from $\Gamma \propto R$ to $\Gamma \propto R^0$) is opacity dependent. This implies that more opaque fireballs (e.g, blue curve in Fig. 3.3) transition more smoothly and gradually (with larger curvature) as compared to less opaque fireballs (e.g., green curve). A consequence of this gradual transition is an increase in the radial extent of the fireballs' transition zone, which spans several orders of magnitude (it is also larger in extent than the $\Gamma \propto R$ regime).

3.42 Post–Photospheric Acceleration Phase

Figure 3.4 plots the terminal Lorentz factor of several fireballs against their corresponding $R_{\rm ph}/R_{\rm sat}$ values. For a given $R_{\rm ph}/R_{\rm sat}$ ratio, the black curve depicts the theoretically calculated terminal Lorentz factor ($\Gamma_{\rm Th}$). The blue points show the terminal Lorentz factor obtained by DynaMo simulations (let us call them $\Gamma_{\rm Sim}$). For $R_{\rm ph}/R_{\rm sat} < 1$, the fireball model predicts that all radiation escapes at the photoshere and the Lorentz factor saturates, i.e., $\Gamma_{\rm Th} = \Gamma_{\rm ph}$ (see § 3.31 and Appendix E). However, Fig. 3.4 shows that for $R_{\rm ph}/R_{\rm sat} < 1$ simulated Lorentz factors exceed the corresponding theoretical values, i.e., $\Gamma_{\rm Sim} > \Gamma_{\rm Th}$. Physically, this excess represents an acceleration phase occurring *after* the theoretical photosphere.

The reason underlying this excess acceleration lies in the definition of opacity. The opacity of a medium is a probabilistic quantity and can only provide information regarding the probability of escape of a photon (Pe'er 2008). However, the theoretical values (such as the $\Gamma_{\rm Th}$ at the photospheric radius) are calculated assuming that all the photons in the fireball escape at $\tau = 1$ (Rees and Mészáros 2005) and do not account for the opacity's probabilistic nature. By using the particle tracking feature of the DynaMo code we find that even for optically thin fireballs (i.e., $\tau \leq 1$) a fraction of photons are still trapped, which concurs with the probabilistic nature of opacity. These trapped photons (that are

unaccounted for in the fireball model) continue scattering beyond the photosphere and are the reason why $\Gamma_{\rm Sim}$ exceeds $\Gamma_{\rm Th}$. It is interesting to note that the smaller the value of $R_{\rm ph}/R_{\rm sat}$ the larger the discrepancy between simulated and theoretical values. This can be attributed to the fact that the (trapped) radiation energy density is larger for smaller $R_{\rm ph}/R_{\rm sat}$ fireballs, which leads to greater acceleration beyond the photosphere. As $R_{\rm ph}$ grows, the radiation energy density decreases and it becomes harder for less energetic, trapped photons to provide that extra push, causing $\Gamma_{\rm Sim}$ to converge to $\Gamma_{\rm Th}$. On the fireball phase diagram (Fig. 3.1), the post–photospheric acceleration phase occurs during the transition from quadrant 1 to 3 via 2.

3.43 Thompson–Dominated Acceleration Phase

According to the standard fireball model, for $R_{\rm ph}/R_{\rm sat} \geq 1$ the fireball enters the saturation phase and thereafter coasts at η (see § 3.31 and Appendix E). For $R_{\rm ph}/R_{\rm sat} \geq 1$ and in contrast to the results of the post–photospheric acceleration phase, Fig. 3.4 shows that $\Gamma_{\rm Sim} \leq \Gamma_{\rm Th}$. Another interesting observation is that the for increasing $R_{\rm ph}/R_{\rm sat}$ values the discrepancy between simulated and theoretical values is reduced, and $\Gamma_{\rm Sim} \rightarrow \Gamma_{\rm Th} = \eta$ asymptotically. These features can be attributed to the fact that 1) at this stage these fireballs are matter dominated and 2) Comptonization is inefficient for transferring energy from low energy photons to leptons. The matter–dominated fireball phase implies that the average lepton energy is significantly larger than the average photon energy. As seen from the comoving frame, the photon energies are significantly lower than the rest mass energy of electrons and scatterings here occur in the *Thomson regime*. In order to extract the final remnants of the significantly smaller photon energies and reach the maximum allowed Lorentz factor, a large number of (Compton) scatterings are required (Chhotray and Lazzati 2015). Our results show that once fireballs become matter dominated, Comptonization is not efficient in completely converting internal energy into bulk motion. On the phase–space diagram shown in Fig. 3.1, the fireball encounters this phase as it evolves from quadrant 1 to 3, transitioning via quadrant 4. It is this Thomson–dominated phase that is responsible for the gradual fireball acceleration, the gradual Γ turnover (which becomes increasingly smooth for higher opacities) and the large extent of the transition phase. Thus, optically thick fireballs that become matter dominated accelerate gradually,

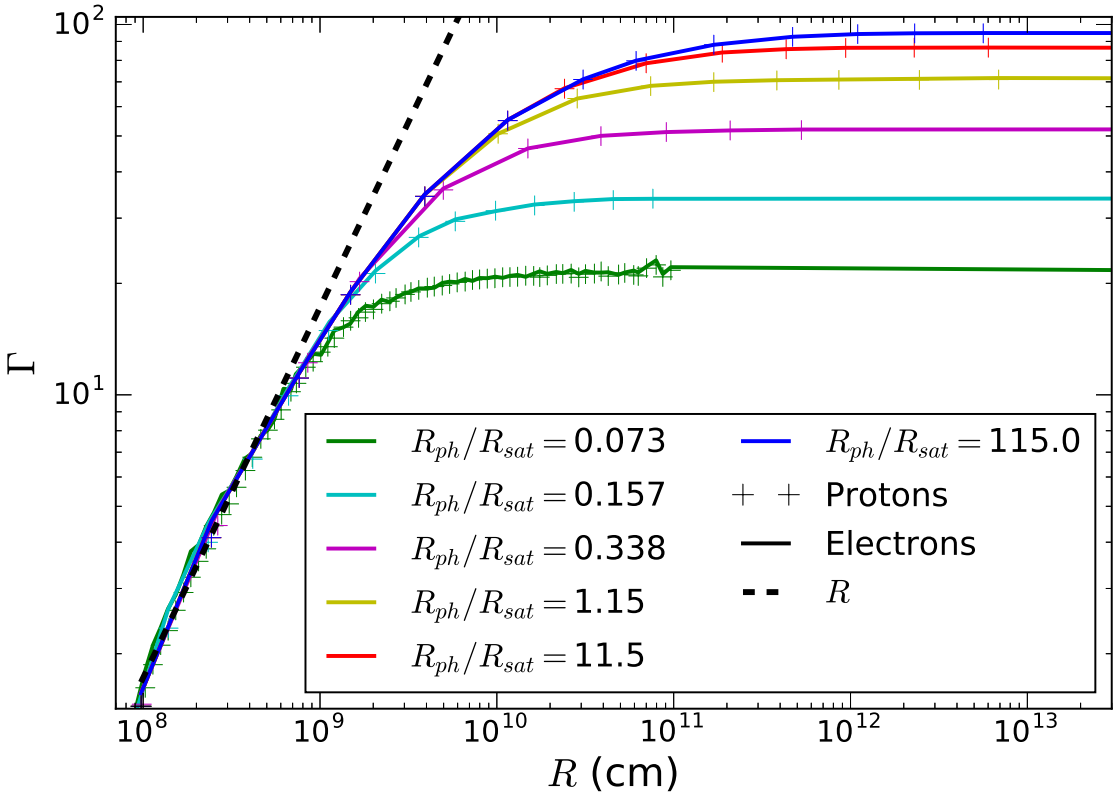

FIGURE 3.5: Same as Fig. 3.3 but with fireballs that are baryon loaded. Also plotted is the Lorentz factor evolution of protons (represented by + markers).

and require extremely large opacities (or an extremely large number of scatterings) to approach η.

3.44 Baryon Loading

Figure 3.5 plots the radially evolving Lorentz factors of baryon–loaded fireballs, with each colored curve corresponding to a unique value of $R_{\rm ph}/R_{\rm sat}$. The fireball evolution is again in strong agreement with the fireball model's proportionality relations (see eq 3.2) during the radiation–dominated acceleration phase. We observe again that fireballs with larger $R_{\rm ph}/R_{\rm sat}$ attain larger Lorentz factors. Thus, both Figs. 3.3 & 3.5 confirm the idea that larger opacity leads to larger acceleration, independently of the fireball's baryonic content. The inclusion of baryons increases the effective mass of the plasma and in comparison to baryon–free plasmas requires more photons for acceleration. This leads to an increase in

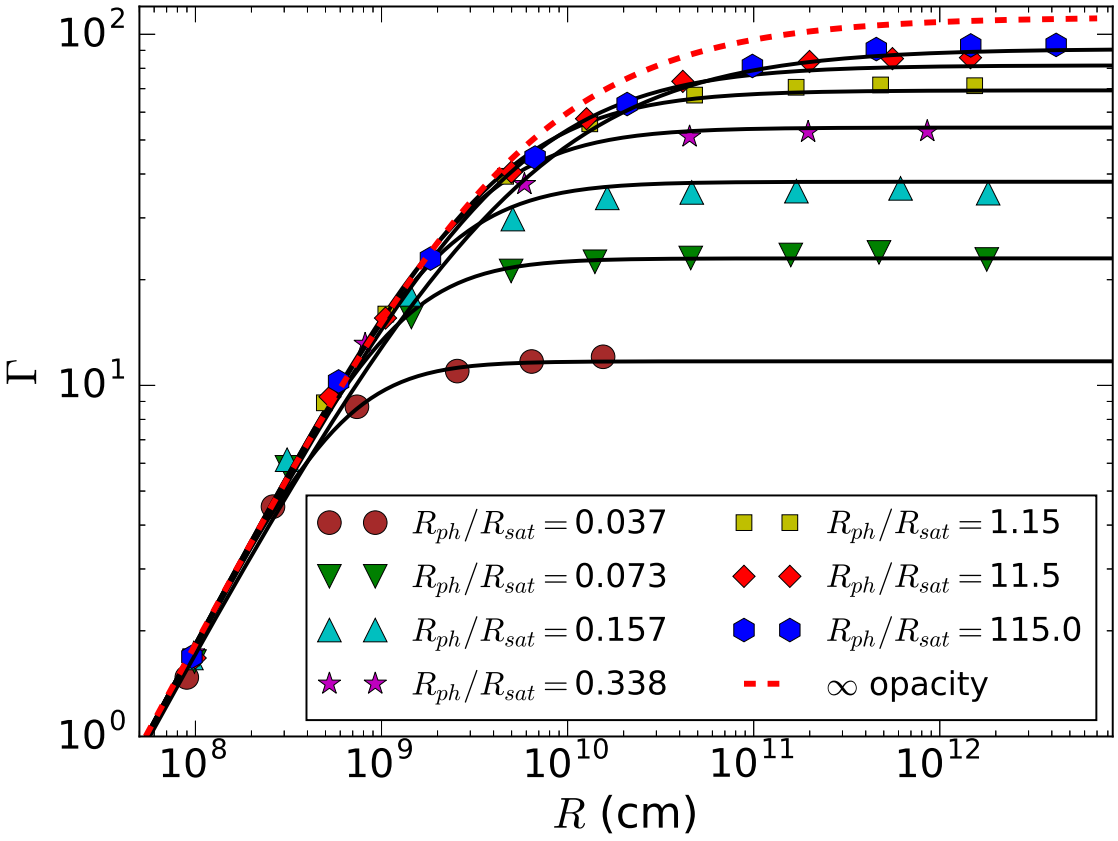

FIGURE 3.6: Lorentz factor evolution with increasing radii of fireballs characterized by different initial opacities. The differently shaped and colored markers plot eq. 3.17, which is obtained by curve fitting (see § 3.45). The solid lines plot the simulation results. The red dashed line is an analytical result (see eq. 3.6) obtained from an infinite opacity fireball (discussed in § 3.31).

.

computational time and memory consumption. Since both baryon–devoid and baryon–loaded plasmas have extremely similar Lorentz factor evolution and terminal values at saturation, we think it is better to simulate just baryon–free fireballs as they require less computational time and resources.

3.45 Expression from curve fitting

In this section, we present and discuss the analytical expressions obtained by fitting the simulated data depicted in Fig. 3.3. Each simulation in Fig. 3.3 is characterized by unique

initial outflow conditions – value of injection radius R_0, maximum possible bulk Lorentz factor η (attained when all internal energy is converted to bulk motion) and the unique parameter σ (a measure of opacity of the plasma; its relation to $R_{\rm ph}/R_{\rm sat}$ is described in detail in Appendix E). The expression we use to model the radial evolution of the Lorentz factor $\Gamma(R)$ is (the expression used has a form similar to Beuermann et al. 1999) –

$$\Gamma(R) = \frac{\Gamma_\infty(\sigma,\eta)}{\left[1+\left(\frac{r_{\rm acc}(\sigma,\eta)}{r}\right)^{s(\sigma)}\right]^{\frac{1}{s(\sigma)}}}, \tag{3.17}$$

which depends primarily on three parameters, which in turn are functions of the initial outflow conditions. These three parameters are –

- $s(\sigma) = 2.53 - 0.1796 \log_{10}\sigma$
- $\Gamma_\infty(\sigma,\eta) = 10^{\left(\log_{10}\eta[1-\exp(-0.43 log_{10}\sigma)]^{3.3}\right)}$
- $r_{\rm acc}(\sigma,\eta,R_0) = 0.54 R_0 \eta$

Fig. 3.6 compares the Lorentz factors calculated from the numerical expression obtained via curve fitting (i.e., eq. 3.17 and depicted by markers) and the simulation results (represented by the solid lines). As the markers and the solid lines show, the numerical and simulated results are in good agreement with each other. The dashed red line is the Lorentz factor calculated from eq. 3.6, which was obtained from the hydrodynamic evolution of an infinite opacity fireball (see § 3.31). The evolution of the red dashed line is very similar to our simulated, optically thickest fireball during the radiation–dominated and transition phases.

3.5 Summary and Conclusions

In this paper, we have studied the bulk kinematic evolution of a radiation–driven GRB fireball via Monte Carlo simulations. We have presented our novel Dynamic Monte Carlo code (DynaMo) code, which we use to self–consistently simulate, the Compton scattering–induced expansion and acceleration of a GRB fireball. Earlier works have studied particular phases of fireball evolution analytically (Meszaros et al. 1993; Piran 1999). The analytical

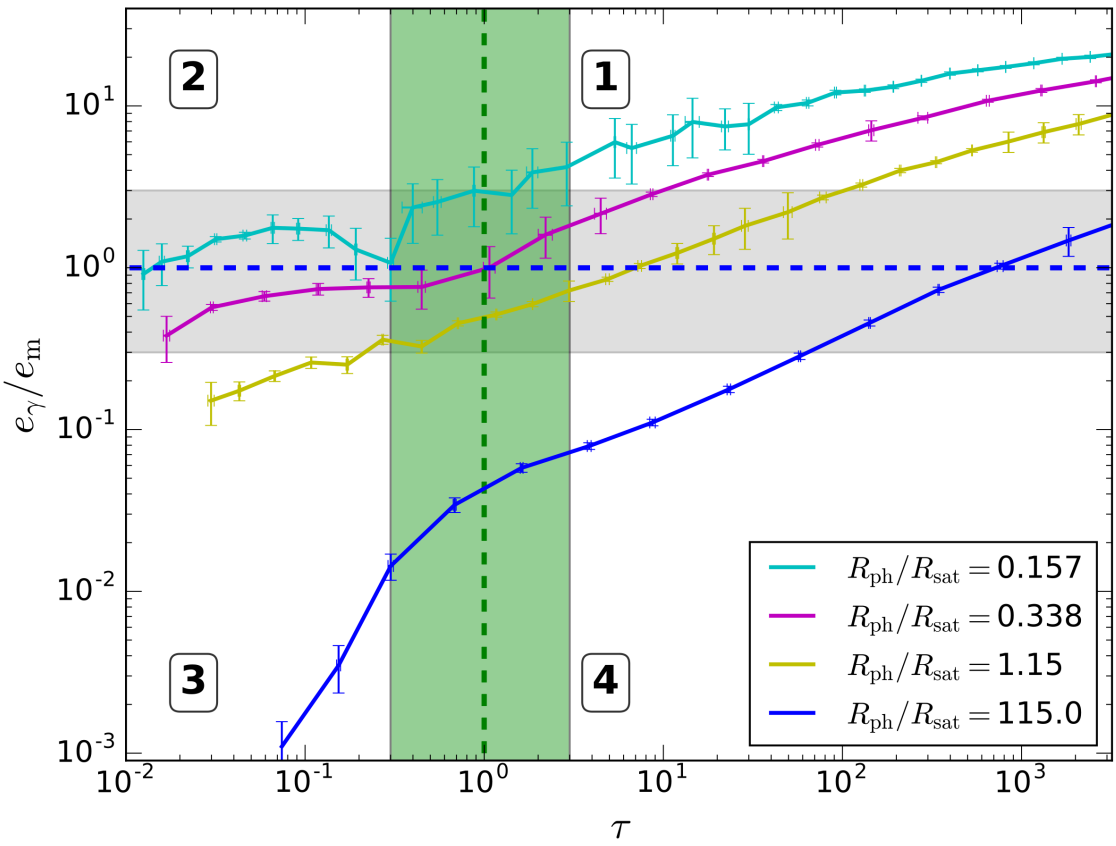

FIGURE 3.7: An updated version of Fig. 3.1 with the DynaMo code's simulation results in context. The differently colored curves represent fireballs starting with different initial opacities. Fireballs that start comparatively optically thin ($R_\mathrm{ph}/R_\mathrm{sat} < 1$) evolve from quadrant 1 to 3 via 2. Comparatively optically thick fireballs ($R_\mathrm{ph}/R_\mathrm{sat} \geq 1$) evolve from quadrant 1 to 3 via quadrant 4. All curves eventually drop because only photons trapped inside the fireball contribute to the radiation energy density e_γ. The Lorentz factor evolution across the entire phase space is given by eq. 3.17.

approximations do not properly address the question of self consistent fireball evolution, especially when 1) the radiation energy density becomes comparable to or less than the fireball's rest mass energy density and/or 2) the fireball becomes optically thin (the case when $R_{\rm ph} < R_{\rm sat}$). Fig. 3.7 is an updated version of the GRB phase space diagram (Fig. 3.1) with the evolution of DynaMo code's simulated fireballs plotted onto the diagram. We have studied fireball evolution across all regimes, including the transition regimes that are the highlighted regions in phase diagrams (see Figs. 3.1 & 3.7). We summarize our results as follows –

- The evolution of a GRB fireball (or any outflow) can be summarized by Fig. 3.7. All radiation–dominated and optically thick GRB fireballs start in the upper–right quadrant (quadrant 1) and evolve towards quadrant 3 (optically thin, matter dominated). Depending on where the fireball originates within quadrant 1, it will enter quadrant 3 via paths through quadrants 2 or 4.

- We have investigated the effect of initial opacity on fireball evolution by simulating several fireballs, each starting with a different initial opacity (as differentiated by the colored curves in Figs. 3.3 and 3.5). Our results are in agreement with the fireball model, as optically thick fireballs achieve higher Lorentz factors, and saturate at larger radii than comparatively thin ones.

- We have also investigated the effects of baryon loading of fireballs on the Lorentz factor evolution, as shown by Fig. 3.5. Our results show identical evolutionary behavior of baryon–deficient and baryon–loaded fireballs (Figs. 3.3 and 3.5 evolve similarly). Being baryon loaded, these fireballs require more photons to accelerate the additional mass and hence require more computational time and resources. Our results strongly suggest that the evolution of baryon–loaded fireballs can be accurately predicted from the significantly faster and less memory intensive, baryon–deficient fireball simulations. This can also be realized with the aid of eq. 3.1, as the mass term in the denominator does not differentiate between baryonic or leptonic mass.

- A remarkable result that can be seen from both Figs. 3.3 and 3.5 is the existence of a transition regime, with an opacity dependent radial extent. Occuring between

the radiation–dominated acceleration phase (where $\Gamma \propto R$) and the phase where the Lorentz factor flattens ($\Gamma \propto R^0$), the transition phase has 1) a significant radial extent (which exceeds the radial extent of $\Gamma \propto R$ phase) and 2) a curvature / turnover radius which gradually increases with increasing opacity. In Fig. 3.7, this regime begins within the highlighted regions, where opacity approaches unity and/or radiation energy no longer dominates the fireball energy density.

- Another unexpected result from our simulations is the discovery of a post–photospheric acceleration phase (see Fig. 3.4) during the previously unexplored $R_{\rm ph} < R_{\rm sat}$ regime. This phase is encountered by the fireball as it travels from quadrant 1 to 3 via 2 (see Fig. 3.7). In this regime, simulated fireballs' terminal Lorentz factors are found to be larger than the theoretical Lorentz factors obtained using the fireball model. In other words, the simulated fireballs continue accelerating beyond the theoretical photosphere. We attribute this post–photospheric acceleration phase to the energetic photons still trapped in the plasma. The particle tracking feature informs us that 1) not all photons escape at the theoretical photosphere (when $\tau \sim 1$) and 2) photons at the these small radii are sufficiently energetic. These trapped, energetic photons continue to scatter and accelerate the fireball beyond the model's theoretical values.

- The final unexpected result is the existence of the Thomson–dominated acceleration phase, detected in the regime $R_{\rm ph} \geq R_{\rm sat}$ (see Fig. 3.4). Conversely to the post–photospheric acceleration phase, this phase is characterized by the theoretical Lorentz factor exceeding the simulated terminal Lorentz factor. On the phase space diagram (Fig. 3.7), this phase arises as the plasma evolves from quadrant 1 to 3 via 4. This phase can be attributed to the fact that in the optically thick and matter-dominated regime, the average energy of matter is greater than the average photon energy. As a result, energy transfer per scattering is low (Thomson scattering) and for Comptonization to transfer significant energy from radiation to matter, a large number of scatterings is required. The Thomson–dominated scattering phase is re-

sponsible for the gradual acceleration and the large transition / gradual turnover phase for fireballs with large $R_{\rm ph} \geq R_{\rm sat}$.

We have shown that radiation can accelerate fireballs beyond the photosphere (post–photospheric acceleration – see § 3.4) and to Lorentz factors larger than previously estimated. A powerful implication of our DynaMo code is that the photosphere cannot be assigned a single value or a radius (and not all radiation escapes at this value), instead it corresponds to a region or volume from where photons gradually escape (Pe'er 2008; Beloborodov 2011; Lazzati 2016). While escaping through this volume, the radiation scatters and accelerates the plasma leading to larger than expected acceleration. Another consequence of our results is the re–definition of saturation radius. The saturation radius defined using eq. 3.7 does not hold true if the energy density is not dominated by radiation. Our results show that at the end of the radiation–dominated acceleration phase, an opaque fireball can still accelerate but only gradually (Thomson–dominated acceleration phase). As a result, the fireball can attain η only for extremely large opacities (or equivalently a large number of scatterings) and at radii significantly larger than the saturation radius (see Fig. 3.4).

We quantify the radial evolution of the Lorentz factor by fitting the simulated data using χ^2 technique. The analytical expression obtained (see eq. 3.17) is parametrized using the fireball's initial opacity. The advantage of this expression is that it can successfully capture the evolution of the GRB fireball across its entire phase space. This includes the transition regimes as well as the fireball evolution in quadrant 2. As an example, by supplying the relevant input parameters (such as the initial opacity) to eq. 3.17, the Lorentz factor at any radius can be obtained for an evolving GRB fireball.

Our simulated fireballs are hot and dense enough that electron–positron pair processes can become important in changing the photon and lepton counts. At the beginning of the fireball evolution the changing particle count only serves to increase the opacity which decreases the escape probability of the photons. As a result, radiation and matter remain in equilibrium as the fireball expands, cools and eventually reaches a temperature where pair processes become unimportant and thus can be ignored. In all our simulations, pairs become irrelevant long before radiation escapes the plasma and thus pair processes are not accounted for.

The results obtained in this paper will be useful for studying photospheric emission from GRBs. Though this paper only focuses on GRB fireballs, the DynaMo code can be used for studying radiative acceleration in relativistic outflows from other astrophysical environments, such as AGNs and microquasars. The DynaMo code's particle tracking feature allows the user to not only obtain the spectrum of the escaping radiation, but also determine when and where the photons escape the outflow. The code can thus produce time–resolved spectra and light curves from GRB fireballs, which will be the subject of future publications.

Acknowledgements

This work made use of NumPy (van der Walt et al. 2011) for computation, and Matplotlib (Hunter 2007) for preparing figures. This work was supported in part by NASA Swift Grant NNX15AG96G.

ON RADIATIVE ACCELERATION IN SPINE–SHEATH STRUCTURED BLAZAR JETS

Atul Chhotray, Francesco Nappo, Gabriele Ghisellini, Om Sharan Salafia, Fabrizio Tavecchio, Davide Lazzati

Journal: Monthly Notices of the Royal Astronomical Society
Address of Journal:
Royal Astronomical Society
Burlington House
Piccadilly
London W1J 0BQ
United Kingdom
Issue Manuscript Appears in: Issue 466 (2017), Pages 3544–3557,

4 ON RADIATIVE ACCELERATION IN SPINE–SHEATH STRUCTURED BLAZAR JETS

4.1 Abstract

It has been proposed that blazar jets are structured, with a fast spine surrounded by a slower sheath or layer. This structured jet model explains some properties of their emission and morphology. Because of their relative motion, the radiation produced by one component is seen amplified by the other, thus enhancing the inverse Compton emission of both. Radiation is emitted anisotropically in the comoving frames, and causes the emitting plasma to recoil. As seen in the observer frame, this corresponds to a deceleration of the fastest component (the spine) and an acceleration of the slower one (the layer). While the deceleration of the spine has already been investigated, here we study for the first time the acceleration of the sheath and find self–consistent velocity profile solutions for both the spine and the sheath while accounting for radiative cooling. We find that the sheath can be accelerated to the velocities required by the observations if its leptons remain energetic in the acceleration region, assumed to be of the order of $\sim$100 Schwarzschild radii, demanding continuous injection of energetic particles in that region.

4.2 Introduction

Relativistic jets in low-power radio–loud active galactic nuclei (AGN) are thought to be structured, namely composed of a fast central part, that we call the spine, and a sheath or a layer surrounding it, moving at a slower speed. There are several arguments that support the structured jet hypothesis. It is very unlikely that the jet plasma moves with a large bulk Lorentz factor Γ ($\sim$ 10–15) inside the jet and with $\Gamma = 1$ just outside it. The velocity of the plasma should decrease gradually across the edge of the jet because of shear viscosity and/or Kelvin–Helmoltz instabilities (e.g., Henri and Pelletier 1991; for a review see Ferrari 1998; see also Bodo et al. 2003). Structured jets could also result from the

acceleration mechanism itself (e.g., McKinney 2006).

Observationally, the emission of high energy γ–ray radiation requires a large bulk Lorentz factor in blazars (i.e., sources whose jets are pointing at us), to avoid suppression by the $\gamma\gamma \rightarrow e^{\pm}$ process. Low-power, TeV emitting BL Lacs require the largest values of Γ among all blazars (Tavecchio et al. 2001; Kino et al. 2002; Katarzyński et al. 2003; Krawczynski et al. 2002; Konopelko et al. 2003; Tavecchio et al. 2010). However, the Large Area Telescope (LAT) onboard the *Fermi* satellite has detected (low-power) radio galaxies at $\sim$ GeV energies (Abdo et al. 2010; Grandi 2012). Their radiation cannot be the de–beamed emission coming from plasma moving with $\Gamma \sim 15$, since the de–beaming would be too strong, making the flux undetectable. The GeV radiation of radio galaxies must be produced by material moving with $\Gamma \sim 3$ (Ghisellini et al. 2005) which is high enough to avoid the $\gamma\gamma$ absorption process but sufficiently small to avoid strong de–beaming of the flux.

Detailed VLBI radio maps of Mkn 501 revealed a *limb brightening* morphology, interpreted as evidence of a slower external flow surrounding a faster spine (Giroletti et al. 2004). Similar results have been obtained for Mkn 421 (Giroletti et al. 2006), 0502+675 and 1722+119 (Piner and Edwards 2014).

In addition to the above evidences for structured AGN jets, there is also mounting evidence for a decelerating spine in TeV BL Lacs, and therefore radial structure. Many TeV BL Lacs are not superluminal sources at the $\sim$pc scale (Edwards and Piner 2002; Piner and Edwards 2004; Piner and Edwards 2014; Piner et al. 2008; Piner et al. 2010) even though they require the highest bulk Lorentz factors in the TeV emitting region (that is in most, but not all, cases located at sub–pc distances from the black hole).

Georganopoulos and Kazanas (2003b) proposed a model in which the jet has a fast inner part and a slower part further out. In their model, the fast base of the jet sees the radiation produced by the slower zone relativistically boosted. Analogously, the slow part of the jet sees the radiation coming from the fast base of the jet relativistically boosted. The radiation energy density seen by both components is amplified with respect to the pure one–zone model.

Ghisellini et al. (2005) proposed a “spine–layer" (or spine–sheath) jet structure with the

two components having different velocities (the spine is faster). As before, each component receives increased amounts of seed photons. In this configuration the fast spine could be decelerated by the Compton rocket effect (Odell 1981), justifying the decelerating jet model of Georganopoulos and Kazanas (2003b). The spine–layer model has been successfully applied to explain the high energy emission of radiogalaxies (M87: Tavecchio and Ghisellini 2008; NGC 1275: Tavecchio and Ghisellini 2014; 3C 66B: Tavecchio and Ghisellini 2009) and slightly misaligned blazars (PKS 0521–36: D'Ammando et al. 2015). It has also been shown to help the production of high energy neutrinos in the relativistic jet of radio–sources (Tavecchio et al. 2014).

In the original model and in the later application to specific sources, the velocity of the layer was a free parameter, and was assumed to be constant. On the other hand, the emitting plasma of the layer, being illuminated by the photons of the spine, emits anisotropically in its comoving frame and thus must recoil. The relative bulk Lorentz factor between the two structures is therefore bound to decrease, limiting the seed amplification effect leading to the extra inverse Compton emission.

In the initial jet zone (where there is no radiative interplay between the spine and the layer), the jet launching mechanism could itself be responsible for accelerating both the spine and the layer (e.g. McKinney 2006). An alternative option is that this launching mechanism is responsible only for the acceleration of the spine, while the layer gets accelerated radiatively. The aim of this paper is to study self-consistently the photon-mediated interaction between the two jet components that move with high relative velocity and thus find out which of the two options is preferred. In particular, we aim to explore and describe the dynamic coupling of the two radial components and to better understand this physical feedback process, as it could be important for relativistic jets in general, including Gamma Ray Bursts (e.g., Rossi et al. 2008; Lazzati and Begelman 2005).

This paper is organized as follows: in § 4.3 we discuss the setup of the model and the assumption made to make it mathematically tractable. In § 4.4 we present and discuss our results, and this is followed by our conclusions in § 4.5. We divide the study in five parts: i) we find the velocity profile of the layer assuming a constant spine velocity, and assuming a fixed energy distribution of the emitting electrons in the spine–layer system; ii) we study the layer motion assuming that the emitting electrons are injected at the

start, and then radiatively cool; iii) we explore the layer's motion for a case where the injected electrons maintain a fixed energy distribution inside a fixed volume (this fixed volume is discussed in greater detail in § 4.31) and cool radiatively once the plasma exits that volume; iv) we self–consistently calculate the motion of the spine and the layer, under their reciprocal radiative influence; and v) we study how the self–consistent motion of the spine–layer system is influenced by electron–positron pair loading.

4.3 Set up of the model

Our model consists of a cylindrical spine–layer structure as shown in Fig. 4.1. This structure is a system of concentric cylinders with the spine being the inner cylindrical structure and the layer surrounds it. We use this model to describe the dynamical evolution of the spine and the layer due to Compton scattering by photons produced by the layer and the spine respectively. The physical quantities of interest for investigating this problem are measured in three different reference frames. These three frames are:

(1) The observer frame K: the quantities measured in this frame are identical to those measured by an observer on Earth, hence we will refer to this frame as the "observer frame". Any quantity measured in this frame will be marked as unprimed.

(2) The layer frame K': This is the frame instantaneously at rest with respect to the layer. It moves with respect to the observer frame at a variable Lorentz factor, denoted by $\Gamma_{\rm L}$. The quantities measured in this frame are marked with a single prime, e.g., $L'_{\rm S}$ is the spine luminosity as observed in the frame instantaneously co-moving with the layer.

(3) The spine frame K'': This frame is co–moving with the spine plasma with a Lorentz factor $\Gamma_{\rm S}$. The quantities measured in this frame are marked with a double prime, e.g., $L''_{\rm L}$ is the layer luminosity as measured in the spine frame.

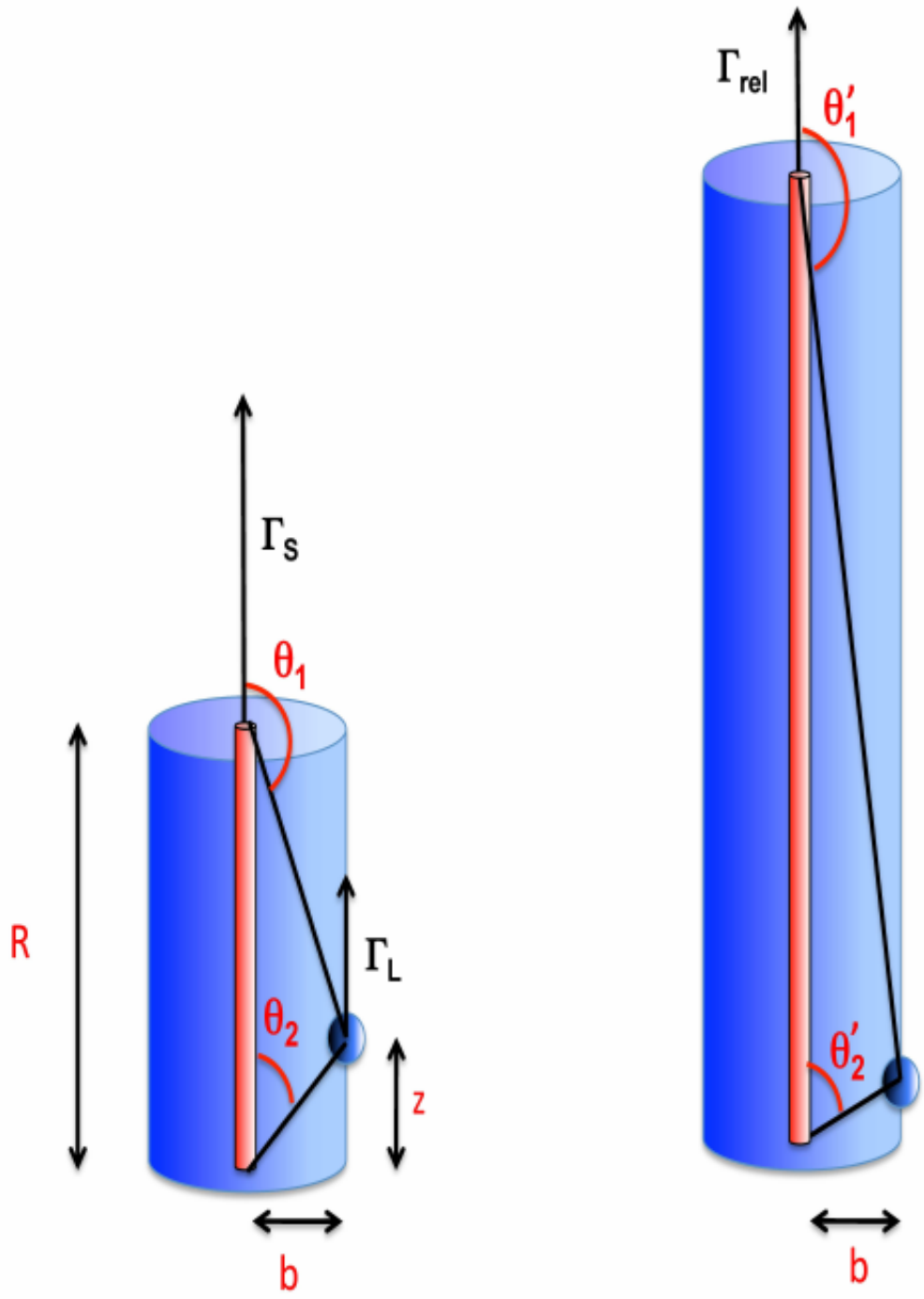

FIGURE 4.1: A cartoon depiction of the cylindrical spine-layer structure with its dimensions. On the left is the spine–layer jet as observed by a distant observer (such as on Earth) with both the layer and the spine in motion with Lorentz factors $\Gamma_{\rm L}$ and $\Gamma_{\rm S}$ respectively. The vertical height or size of the active region is $R \sim 10^{16}$ cm and the radial extent of the layer is $b \sim 10^{15}$ cm. We also show a layer particle at a height z and the corresponding angles subtended at that height by the extremities of the active region. The figure on the right depicts the same structure as observed in the layer frame. For the layer the spine appears to move at a Lorentz factor $\Gamma'_{\rm rel}$ and relativistic effects elongate the vertical size of the active region. The radial width of the system however, is unaffected as it is orthogonal to the direction of motion.

4.31 Assumptions

We simplify the analysis of our spine–layer model by assuming that the spine is uni–dimensional and is in motion with an initial Lorentz factor $\Gamma_{S,0}$ (measured in the observer frame) along the jet–axis direction (referred to as z–axis) as is depicted in the left panel of Fig. 4.1 by the inner cylinder. The layer is the outer cylinder surrounding the spine, has a radius of $b \sim 10^{15}$ cm and, like the spine, travels along the jet axis with an initial Lorentz factor given by $\Gamma_{\rm L,0}$ (subscript L denotes layer which we shall use synonymously with the sheath).

In our model we assume that the both the spine and the layer are 'active' only between two points which are fixed in the observer frame and separated by a distance of $R = 10^{16}$ cm, implying the emitting volume to be fixed in that frame. Such an active region can be a result of a standing shock, where energy dissipation happens between fixed points. Both the spine and the sheath emit radiation isotropically in their respective reference frames, however any other frame would observe the emissions to be beamed. We thus introduce the relativistic Doppler factor (hereafter *beaming* factor) δ as:

$$\delta_{\rm L} = \frac{1}{\Gamma_{\rm L}(1 - \beta_{\rm L}\cos\theta)} \tag{4.1}$$

which is the beaming factor of the radiation produced in the layer frame as seen in the observer frame. θ is the angle between the jet axis and the line of sight as measured in the observer frame.

$$\delta_{\rm S} = \frac{1}{\Gamma_{\rm S}(1 - \beta_{\rm S}\cos\theta)} \tag{4.2}$$

is the beaming factor of the radiation produced in the spine frame as seen in the observer frame, and

$$\delta_{\rm S,L} = \frac{\delta_{\rm S}}{\delta_{\rm L}} \tag{4.3}$$

is the relative beaming factor of the radiation produced in the spine frame and as seen in the layer frame (see also Georganopoulos and Kazanas 2003b; Ghisellini et al. 2005).

The forces resulting from Compton scattering of the layer particles by the spine photons can drive/accelerate the sheath (in this work we consider scattering only within the Thomson regime). As the seed photons of Compton scattering are produced outside the layer, if the scattering particles are hot in K', the scattered radiation is anisotropic also in the layer

co–moving frame, making the layer recoil. For this reason, this interaction is often called *Compton Rocket* (Sikora et al. 1996; Ghisellini and Tavecchio 2010; Vuillaume et al. 2015) and for hotter particles this driving force increases proportionally to their average internal energy $\langle\gamma^2\rangle$.

We assume that the layer particle is free to move in the direction parallel to the jet axis. For simplicity, we assume that the distance between the layer and the jet axis, b, is fixed, despite the presence of a radial radiative force, and thus also along the normal to the jet axis. This can be achieved through the presence of a magnetic field. To analyze the motion of the sheath we consider an infinitesimal part of the sheath at a position z which we treat as an "effective particle". The constituent particles inside the layer are representative of the sheath particles and the sheath can be thought of as composed of a collection of these effective particles (see also §4.33).

The right panel of Fig. 4.1 depicts the structure as viewed in the frame of the sheath. The sheath finds the spine moving at a Lorentz factor $\Gamma_{\rm rel} = \Gamma_{\rm S}\Gamma_{\rm L}(1 - \beta_{\rm S}\beta_{\rm L})$ and due to the aberration of light observes the vertical dimension of the active region to be larger than R. We assume that the observer is located at a viewing angle of $\theta_{\rm view} = 5^{\circ}$.

4.32 Particle distributions and cooling

We assume that the particle distributions $N(\gamma)$ in the spine and the sheath to be a broken power law, with slope p_1 below and p_2 (where $p_2 > p_1$) above the break $\gamma_{\rm b}$:

$$N(\gamma) = \begin{cases} K\gamma^{-p_1} & \gamma_{\rm min} < \gamma \leq \gamma_{\rm b} \\ K\gamma_{\rm b}^{p_2-p_1}\gamma^{-p_2} & \gamma_{\rm b} < \gamma < \gamma_{\rm max} \\ 0 & \text{otherwise} \end{cases} \tag{4.4}$$

where $\gamma_{\rm max}$ is the maximum Lorentz factor of the distribution that depends on the cooling rate (see §4.32). For simplicity we omit hereafter the prime and the double prime for $N(\gamma)$ and γ. We can use the distribution $N(\gamma)$ to calculate the averages $\langle\gamma\rangle$ and $\langle\gamma^2\rangle$ as:

$$\begin{aligned} \langle\gamma\rangle &= \frac{\int N(\gamma)\gamma \mathrm{d}\gamma}{\int N(\gamma)\mathrm{d}\gamma} \\ \langle\gamma^2\rangle &= \frac{\int N(\gamma)\gamma^2 \mathrm{d}\gamma}{\int N(\gamma)\mathrm{d}\gamma} \end{aligned} \tag{4.5}$$

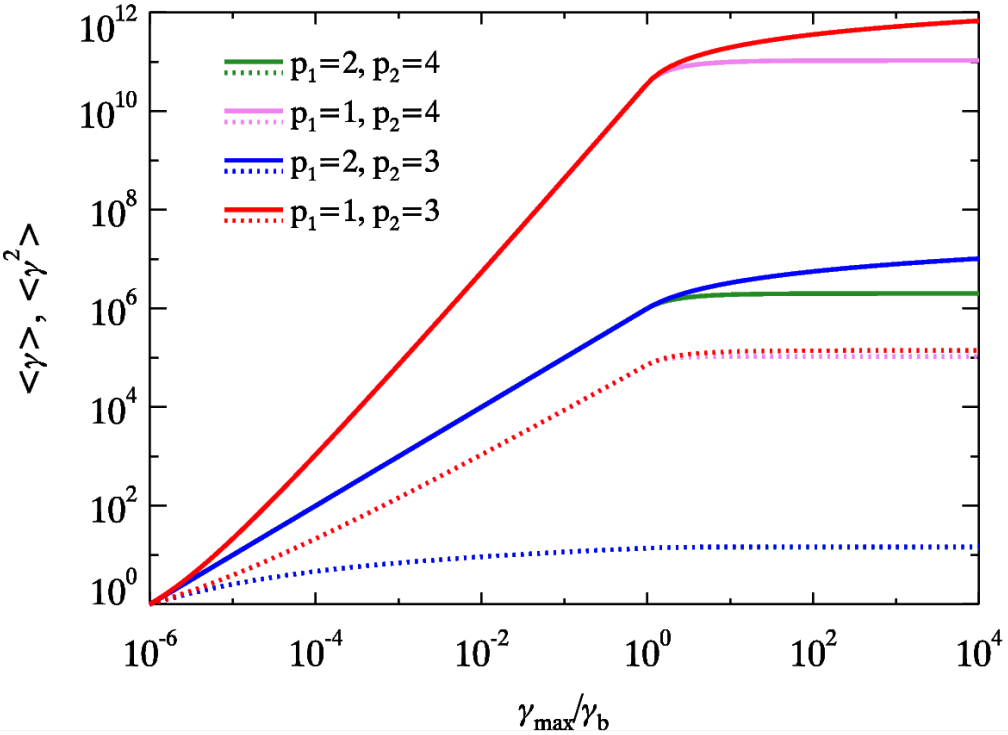

FIGURE 4.2: Evolution of $\langle\gamma\rangle$ (dotted lines) and $\langle\gamma^2\rangle$ (solid lines) as a function of the ratio $\gamma_{\rm max}/\gamma_{\rm b}$ for different values of p_1 and p_2. As the hottest particles cool faster, the radiative cooling reduces the maximum Lorentz factor of particles: $\gamma_{\rm max}$. For our case of interest $p_1 = 2$ and $p_2 = 4$ (denoted by the green curve), when $\gamma_{\rm max} > \gamma_{\rm b}$ we observe that both $\langle\gamma\rangle$ and $\langle\gamma^2\rangle$ are constant. The averages start decreasing only when $\gamma_{\rm max} < \gamma_{\rm b}$. A very similar behavior is observed for other power law indices that are shown in the figure for comparison.

In our work we fix $\gamma_{\rm min} = 1$, $p_1 = 2$ and $p_2 = 4$. A possible realisation of this case corresponds to continuous injection of electrons distributed as $Q(\gamma) \propto \gamma^{-s}$ above $\gamma_{\rm b}$, and $Q(\gamma) = 0$ below. If radiative cooling is fast (i.e., even particles with low Lorentz factors cool in a timescale shorter than the light crossing time), the stationary $N(\gamma)$ distribution will have a slope $p_2 = s + 1$ above $\gamma_{\rm b}$ and $p_1 = 2$ below. For $s = 3$ (i.e., $p_2 = 4$) Eq. 4.5 gives:

$$\begin{aligned}\langle\gamma\rangle &= \frac{3}{2}\,\frac{2\ln(\gamma_{\rm b}) + 1 - (\gamma_{\rm b}/\gamma_{\rm max})^2}{3 - 2/\gamma_{\rm b} - \gamma_{\rm b}^2/\gamma_{\rm max}^3} \\ \langle\gamma^2\rangle &= 3\,\frac{2\,\gamma_{\rm b} - 1 - \gamma_{\rm b}^2/\gamma_{\rm max}}{3 - 2/\gamma_{\rm b} - \gamma_{\rm b}^2/\gamma_{\rm max}^3}\end{aligned} \tag{4.6}$$

If the injection of particles is not continuous, the high energy particles are not replenished any longer, and the $N(\gamma)$ distribution cuts–off at the cooling energy $\gamma_{\rm c}$, which decreases

with time. The cooling of the plasma impacts the particle energy distribution which in turn affects the force that these particles experience (see Eq. 4.9). Therefore we have to account for radiative cooling of the sheath/spine plasma due to irradiation by the spine/sheath photons. The cooling rate is (e.g. Rybicki and Lightman 1986):

$$\dot{\gamma} = \frac{\mathrm{d}\gamma}{\mathrm{d}t'} = \frac{4}{3}\frac{\sigma_{\mathrm{T}} c U' \gamma_{\mathrm{max}}^2 \beta_{\mathrm{max}}^2}{m_{\mathrm{e}} c^2} \tag{4.7}$$

where U' is the integrated radiation energy density in the layer frame, γ_{max} and β_{max} are respectively the Lorentz factor and speed of the particle possessing the maximum internal energy (hence the subscript max) in a hot plasma. At each timestep $\Delta t'_i$ we calculate the cooling Lorentz factor of the leptons using Eq. 4.7:

$$\begin{aligned} \gamma_{\mathrm{c,i}} &= \gamma_{\mathrm{max,i-1}} - \dot{\gamma}_{i-1}\Delta t'_i \\ &= \gamma_{\mathrm{max,i-1}} - \frac{4}{3}\frac{\sigma_{\mathrm{T}} c U'_{\mathrm{i-1}} \gamma_{\mathrm{max,i-1}}^2 \beta_{\mathrm{max,i-1}}^2}{m_{\mathrm{e}} c^2}\Delta t'_i \end{aligned} \tag{4.8}$$

We assume that the particle distribution vanishes for $\gamma > \gamma_{\mathrm{c}}$: the cooling Lorentz factor γ_{c} becomes the new maximum Lorentz factor of the distribution, i.e., $\gamma_{\mathrm{max,i+1}} = \gamma_{\mathrm{c,i}}$. Since γ_{c} is time dependent, the averages $\langle\gamma\rangle$ and $\langle\gamma^2\rangle$ (see eqs. 4.6) also become time dependent. Graphically, the evolution of the averages as a function of the ratio $\gamma_{\mathrm{max}}/\gamma_{\mathrm{b}}$ (in other words, with time due to cooling) is depicted in the Fig. 4.2 for several power-law indices.

4.33 The equation of motion

In order to study the trajectory of the sheath or the layer, we require the equation of motion given as

$$\frac{\mathrm{d}p}{\mathrm{d}t} = F' \tag{4.9}$$

where $\mathrm{d}p$ and $\mathrm{d}t$ are calculated in the same frame (any frame), but F' is calculated in the frame *comoving with the particle* (see e.g., Weinberg 1972). Since we assume that the layer and the spine are optically thin, we can calculate the motion of a single particle due to Compton scattering. We define f as the ratio of number of leptons to protons and $f > 1$ indicates the presence of pairs in the plasma. This enables us to study the motion of an "effective particle" of inertial mass $m_{\mathrm{i}} = m_{\mathrm{p}}/f + \langle\gamma\rangle m_{\mathrm{e}}$, where the electron mass m_e is

multiplied by $\langle\gamma\rangle$ to account for the average internal energy of the leptons. Equation 4.9 can be written as:

$$m_{\rm i}c{\rm d}\frac{(\Gamma\beta)}{{\rm d}t} = F' \tag{4.10}$$

We begin by considering the motion of the layer due to the interaction with the radiation produced by the spine (moving with a constant bulk Lorentz factor $\Gamma_{\rm S}$). In this case, the driving force $F'_z(z)$ can be computed by considering the flux received by a particle in the layer located at a given z. This flux will be produced at different heights of the spine, seen under a different angle and with a different beaming. Therefore we will have to integrate over the entire length of the spine while accounting for the different degrees of relativistic effects.

From the detailed calculations as shown in the appendix, we write the equation of motion (Eq. 4.10) as:

$$\frac{{\rm d}(\Gamma_{\rm L}\beta_{\rm L})}{{\rm d}t} = \frac{16}{9}\frac{\sigma_{\rm T}}{m_{\rm i}bc^2}\langle\gamma^2\rangle\eta\int_{\theta_1}^{\theta_2}\lambda''_{\rm S}\frac{\delta_{\rm S}^4}{\delta_{\rm L}^2}\frac{\cos\theta-\beta_{\rm L}}{1-\beta_{\rm L}\cos\theta}{\rm d}\theta \tag{4.11}$$

where η is a factor of the order of unity that depends on the geometry of the system (in this case we used $\eta = 2/\pi$), $\lambda''_{\rm S} = \dfrac{{\rm d}L''_{\rm S}}{{\rm d}x''}$ is the spine comoving linear luminosity density which is connected to the spine isotropic luminosity $L_{\rm iso,S}$.

The drag Lorentz factor

This section introduces the physical meaning of drag Lorentz factor $\Gamma_{\rm L,drag}$ which we will frequently use to understand our results. $\Gamma_{\rm L,drag}$ is the value of $\Gamma_{\rm L}$ for which the z component of the force as measured in the comoving layer frame vanishes. The net force acting on the effective layer particle at a certain position is computed by accounting for photons that hit the effective particle both from above and below its position. As seen in the observer frame K, photons that hit the sheath "effective particle" with an incident angle less than $1/\Gamma_{\rm L}$ with respect to the sheath's direction of motion appear to arrive from above the effective particle's position in the sheath comoving frame. These photons decelerate the particle by imparting negative momentum (negative force). On the other hand, photons that are incident with an angle greater than $1/\Gamma_{\rm L}$ will accelerate the particle, generating a positive force. The value of the layer Lorentz factor for which these positive and negative forces are equal is called the *drag Lorentz factor*. Its value as a function of z

can be obtained by imposing the condition that $F'_z = 0$, and this simplifies Eq. 4.11 to:

$$\int_{\theta_1}^{\theta_2} \delta_{\rm S}^4 \Gamma_{\rm L,drag}^2 (1 - \beta_{\rm L,drag} \cos\theta)(\cos\theta - \beta_{\rm L,drag}) {\rm d}\theta = 0 \tag{4.12}$$

Since the sign of the total force F'_z depends only on the sign of the integral in Eq. 4.11 or Eq. 4.12, we will have:

$$\begin{cases} F'_z > 0 & \text{if} \quad \Gamma_{\rm L} < \Gamma_{\rm L,drag} \\ F'_z < 0 & \text{if} \quad \Gamma_{\rm L} > \Gamma_{\rm L,drag} \\ F'_z = 0 & \text{if} \quad \Gamma_{\rm L} = \Gamma_{\rm L,drag} \end{cases}$$

4.34 Feedback

The previous subsections describe the dynamical evolution of the sheath plasma interacting via Compton scattering with the spine photons. However, we ignored the effect of the sheath photons on the spine to simplify the analysis. In this section, we relax that assumption by accounting for the interaction of the layer photons with the spine and how this interaction modifies the spine Lorentz factor $\Gamma_{\rm S}(z)$. As a result, we can explore how the feedback between the spine–layer structure self regulates its very own dynamical evolution.

To study the spine–layer feedback, we need to modify some equations of the previous section according to the following considerations:

- As the bulk Lorentz factors for both the spine and the layer can be modified, we must compute two profiles $\Gamma_{\rm S}(z)$ and $\Gamma_{\rm L}(z)$ for the spine and the layer respectively.
- The linear luminosity density profiles of the spine and the layer ($\lambda_{\rm S}$ and $\lambda_{\rm L}$) can vary with position, but we assume that the comoving luminosity density profiles are proportional to the average square of the particle energies constituting the emitting plasma, i.e., $\lambda''_{\rm S} \propto \langle \gamma_{\rm S}^2 \rangle$ and $\lambda'_{\rm L} \propto \langle \gamma_{\rm L}^2 \rangle$. Thus, if the internal energy content of the plasma changes by radiative cooling, the comoving luminosity profile will no longer be independent of the position.
- We take advantage of the symmetry of the problem and suppose that the effect of the spine on the layer and the inverse effect, i.e., of the layer on the spine can be expressed by the same relations by simply switching the subscripts.

These considerations lead to the following system of differential equations describing the evolution of two "effective particles" that represent the spine and the layer (having masses $m_{\rm S} = m_{\rm p}/f_{\rm S} + \langle\gamma_{\rm S}\rangle m_{\rm e}$ and $m_{\rm L} = m_{\rm p}/f_{\rm L} + \langle\gamma_{\rm L}\rangle m_{\rm e}$ for the spine and the layer respectively):

$$\begin{cases} m_{\rm S} c \dfrac{{\rm d}(\Gamma_{\rm S}\beta_{\rm S})}{{\rm d}t} \;=\; \dfrac{16}{9}\dfrac{\sigma_{\rm T}}{bc}\langle\gamma_{\rm S}^2\rangle\eta \displaystyle\int_{\theta_1}^{\theta_2} \lambda'_{\rm L}(\theta)\frac{\delta_{\rm L}^4}{\delta_{\rm S}^2}\frac{\cos\theta - \beta_{\rm S}}{1-\beta_{\rm S}\cos\theta}{\rm d}\theta \\ m_{\rm L} c \dfrac{{\rm d}(\Gamma_{\rm L}\beta_{\rm L})}{{\rm d}t} \;=\; \dfrac{16}{9}\dfrac{\sigma_{\rm T}}{bc}\langle\gamma_{\rm L}^2\rangle\eta \displaystyle\int_{\theta_1}^{\theta_2} \lambda''_{\rm S}(\theta)\frac{\delta_{\rm S}^4}{\delta_{\rm L}^2}\frac{\cos\theta - \beta_{\rm L}}{1-\beta_{\rm L}\cos\theta}{\rm d}\theta \end{cases} \tag{4.13}$$

All the important steps leading to the above equations are fully described in the Appendix, along with the limits of integrations θ_1, θ_2 (which can be obtained using the Eqs. 6.55 and 6.56 respectively). We can compute the Lorentz factor profiles $\Gamma_{\rm S}(z)$ and $\Gamma_{\rm L}(z)$ by numerically solving this system. The reader should note that the acceleration of the layer (spine) depends linearly on the product of the isotropic luminosity of the spine (layer) and the average of the square of the leptonic Lorentz factor of the layer (spine). We call this product k:

$$k_{\rm S} \;=\; L_{\rm iso,L}\cdot\langle\gamma_{\rm S}^2\rangle; \quad k_{\rm L} \;=\; L_{\rm iso,S}\cdot\langle\gamma_{\rm L}^2\rangle \tag{4.14}$$

Hence we treat this product as a single parameter.

4.4 Results and Discussion

In this section we present and discuss the results of the numerical integration of the equations of motion considering different conditions:

- §4.41: Radiative acceleration of the layer: No cooling scenario
- §4.42: Radiative acceleration of the layer: Cooling scenario
  - §4.42: Single injection
  - §4.42: Continuous injection
- §4.43: The spine–layer feedback
  - §4.43: Continuous injection with feedback
- §4.44: The spine–layer feedback in e^+e^- pair loaded plasmas

4.41 Radiative acceleration of the layer: No cooling scenario

In this section we start with the simplest and somewhat unrealistic scenario where:

i) the spine moves with a constant bulk Lorentz factor $\Gamma_{\rm S}$ (not considering its deceleration due to layer photons);

ii) the sheath particle distribution does not change with time (i.e., the particles do not cool by radiative emission, or the cooling is exactly compensated by injection of new particles).

By switching 'off' the cooling we have made this scenario somewhat unrealistic, but this simplifies the problem at hand and in turn allows us to gain greater insight and develop intuition about the radiative acceleration phenomena. This will help to improve our understanding of more complex scenarios discussed later in the paper. We solve the equation of motion of the layer under different conditions (however we only vary a single parameter in each case to develop intuition) and we show the spatial profiles of $(\Gamma\beta)_{\rm L}$ and of the force perceived by the layer projected over the z–axis $F'_z(z)$.

Varying $k_{\rm L}$ — Fig. 4.3 shows the effects of varying $k_{\rm L}$ for a constant spine Lorentz factor $\Gamma_S = 15$ and an initial bulk Lorentz factor of the layer $\Gamma_{\rm L,0} = 3$. At the base of the structure, i.e., for small values of z, the forces are negative for all the curves irrespective of the $k_{\rm L}$ value (the yellow curve has the greatest magnitude and hence is clearly visible below the zero force mark, whereas the other curves experience comparatively much smaller forces which are difficult to resolve on the scale of Figure 4.3). This is due to the fact that at the start ($z = 0$) the layer particle sees a greater fraction of the radiation directed downward due to the entire spine–sheath structure located ahead. This decelerates the sheath thereby decreasing the $(\Gamma\beta)_{\rm L}$ as can be seen in the second panel, where the Lorentz factor profiles are compared with the drag Lorentz factor. We start the simulations with a value of $\Gamma_{\rm L,0} = 3$ which exceeds the drag Lorentz factor at that position. As a result negative forces arise from the drag effects to reduce Lorentz factor at (or below) the drag level (refer to § 4.33). We note that the force increases with the increasing values of $L_{\rm iso,S}\langle\gamma^2\rangle$ as seen from the force curves in the top panel of Fig. 4.3.

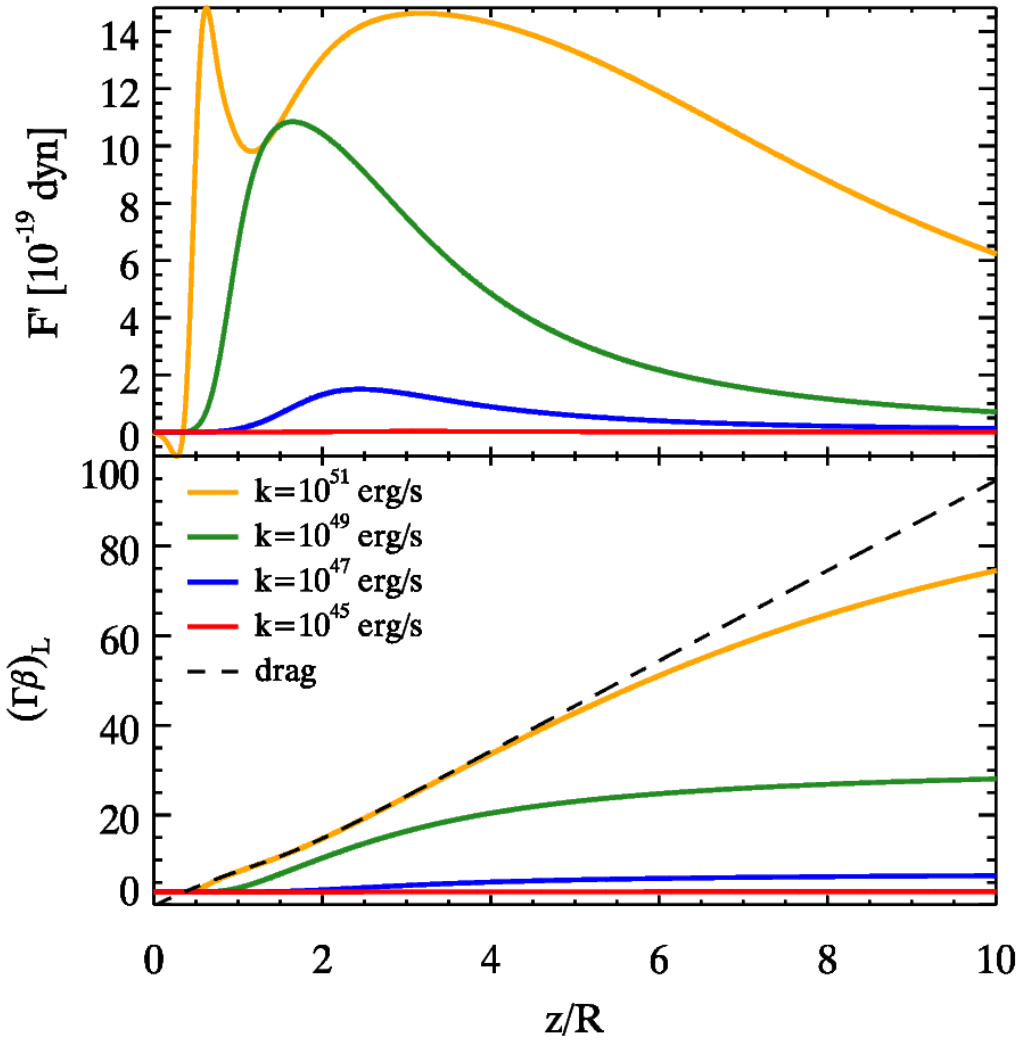

FIGURE 4.3: Radiative acceleration of the layer by varying $k_{\rm L} = L_{\rm iso,S} \cdot \langle \gamma_{\rm L}^2 \rangle$ (values from 10^{45} to 10^{51} erg s^{-1}). The spine Lorentz factor is constant $\Gamma_{\rm S} = 15$. The initial Lorentz factor of the layer is $\Gamma_{\rm L,0} = 3$. The x–axis is common for the two panels and depicts the position z normalized by the vertical structure dimension R. Top panel: radiative force F' as measured in the frame of the layer as a function of z/R. Bottom panel: layer Lorentz factor $(\Gamma\beta)_{\rm L}$ (solid lines) and the drag Lorentz factor $(\Gamma\beta)_{\rm L,drag}$ of the layer (dashed line) as a function of z/R.

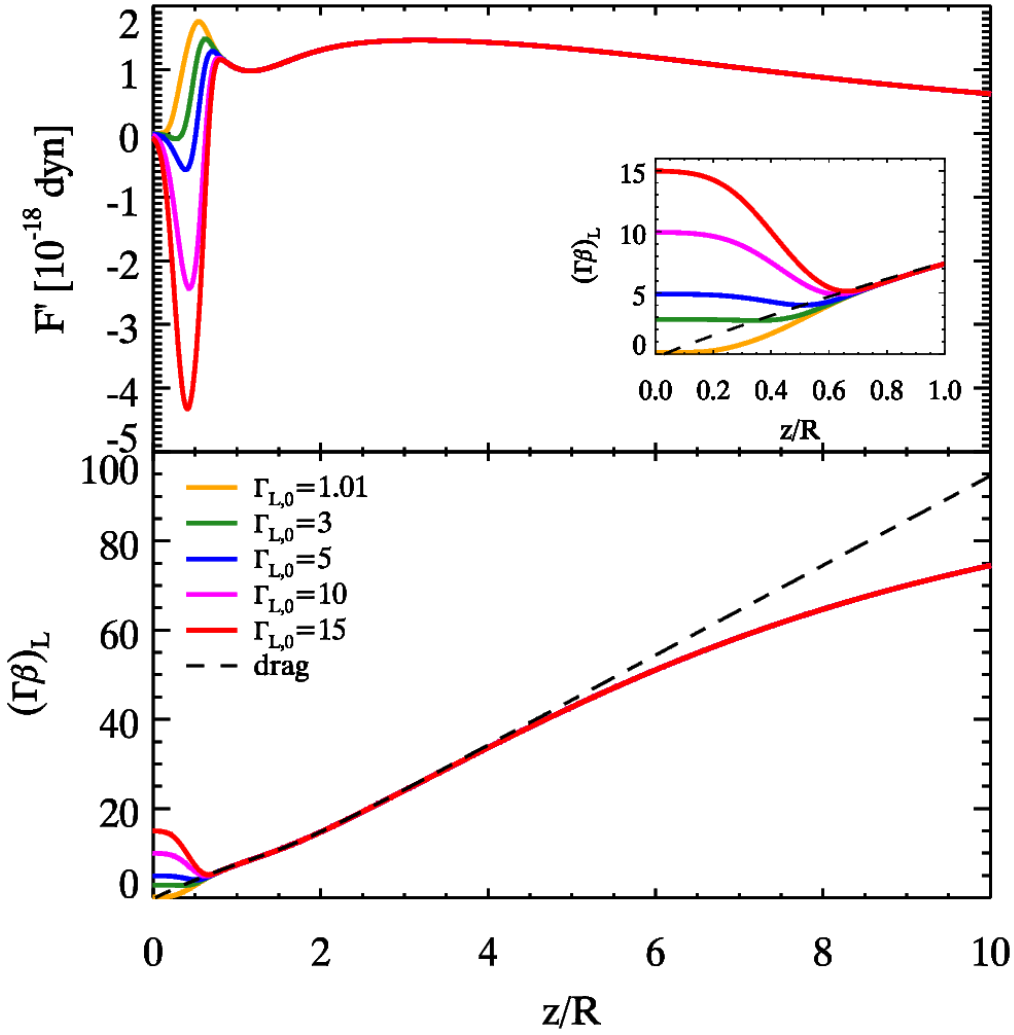

FIGURE 4.4: Radiative acceleration of the layer obtained by varying the initial layer Lorentz factor $\Gamma_{\rm L,0} = 1.01,\ 3,\ 5,\ 10,\ 15$. The spine isotropic luminosity is $L_{\rm iso,S} = 10^{45}$ erg/s and the leptons of the layer are hot ($\langle\gamma_{\rm L}^2\rangle = 10^6$) implying $k_L = 10^{51}$ erg/s. The spine Lorentz factor is constant $\Gamma_{\rm S} = 15$. Top panel: radiative force F' in layer frame as a function of z/R. Bottom panel: layer Lorentz factor $(\Gamma\beta)_{\rm L}$ (solid lines) and the drag Lorentz factor $(\Gamma\beta)_{\rm L,drag}$ of the layer (dashed line) as a function of z/R; Inset: a zoomed view of the behaviour of the layer Lorentz factor for $0 < z/R < 1$.

For low spine luminosities or if the sheath plasma has small internal energy (the case of a cold plasma with low value of $\langle\gamma_{\rm L}^2\rangle$) we find that the layer accelerates negligibly. Instead, significant acceleration is observed by increasing the spine luminosity or the mean squared energy of the particle in the layer. In such cases, the bulk Lorentz factor profile $(\Gamma\beta)_{\rm L}$ manifests an initial decrease due to the initial negative force and then a subsequent increase. This increase, at the beginning, follows the drag Lorentz factor profile but it flattens afterwards depending upon $k_{\rm L}$: the greater the value of $k_{\rm L}$, the greater the final value of $\Gamma_{\rm L}$ and the longer the time for which the bulk Lorentz factor profile follows the $\Gamma_{\rm L,drag}$ profile.

The curve with the highest $k_{\rm L}$ ($k_{\rm L} = 10^{51}$ erg s^{-1}) displays a peculiar force profile characterized by a double peak shape. This behavior is due to a confluence of two effects. Increasing the force increases $\Gamma_{\rm L}$ and if it approaches and attempts to surpass the drag limit, the force rapidly decreases (refer to § 4.33). Thus, the drag effect is responsible for producing the rapid drop and consequently, the first peak in the force profile. The second effect is due to the fact that when the layer effective particle surpasses the length–scale of the structure R, it receives most of the radiation produced by the entire spine length (pushing the effective particle along the positive z direction), which lies behind the particle. This produces the second maximum of the force profile. Note that the double peak is absent when the layer bulk Lorentz factor is nowhere near the drag limit.

Varying $\Gamma_{\rm L,0}$ — Fig. 4.4 shows the effects on radiative acceleration of the layer due to variation in the initial layer bulk Lorentz factor $\Gamma_{\rm L,0}$. The other quantities that remain fixed are the average internal energy content of the sheath leptons ($\langle\gamma_{\rm L}^2\rangle = 10^6$) and the isotropic spine luminosity $L_{\rm iso,S} = 10^{45}$ erg s^{-1}. In all cases, the force profile is characterized by the same features as observed in Fig. 4.3: initial negative force and double peak shape. However due to the different values of $\Gamma_{\rm L,0}$, the force magnitudes for the various curves are initially different, with the curves traveling at larger $\Gamma_{\rm L,0}$ experiencing initially a larger force which decelerates them below the drag limit. We also note an interesting merging feature of both the $\Gamma_{\rm L}$ and the force curves. With identical forces and Lorentz factor $\Gamma_{\rm L}$, we expect and observe the trajectories of the curves to remain merged. This feature

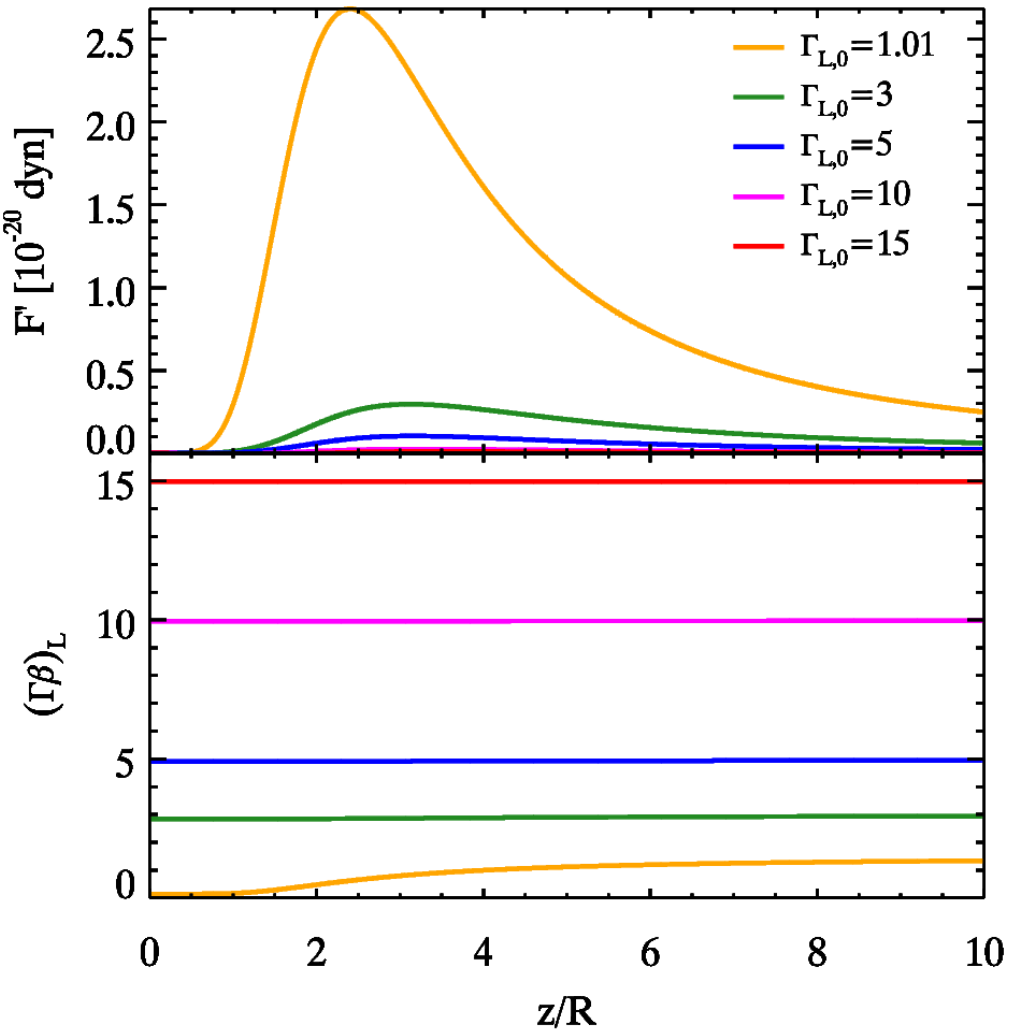

FIGURE 4.5: Radiative acceleration of the layer obtained by varying the initial layer Lorentz factor $\Gamma_{\rm L,0} = 1.01$, 3, 5, 10, 15. The spine isotropic luminosity is $L_{\rm iso,S} = 10^{45}$ erg s^{-1} and the leptons of the layer are cold ($\langle\gamma_{\rm L}^2\rangle = 1$). The spine Lorentz factor is constant $\Gamma_{\rm S} = 15$. Top panel: Radiative force F' in layer frame as a function of z/R. Bottom panel: Layer Lorentz factor $(\Gamma\beta)_{\rm L}$ (solid lines) as a function of z/R.

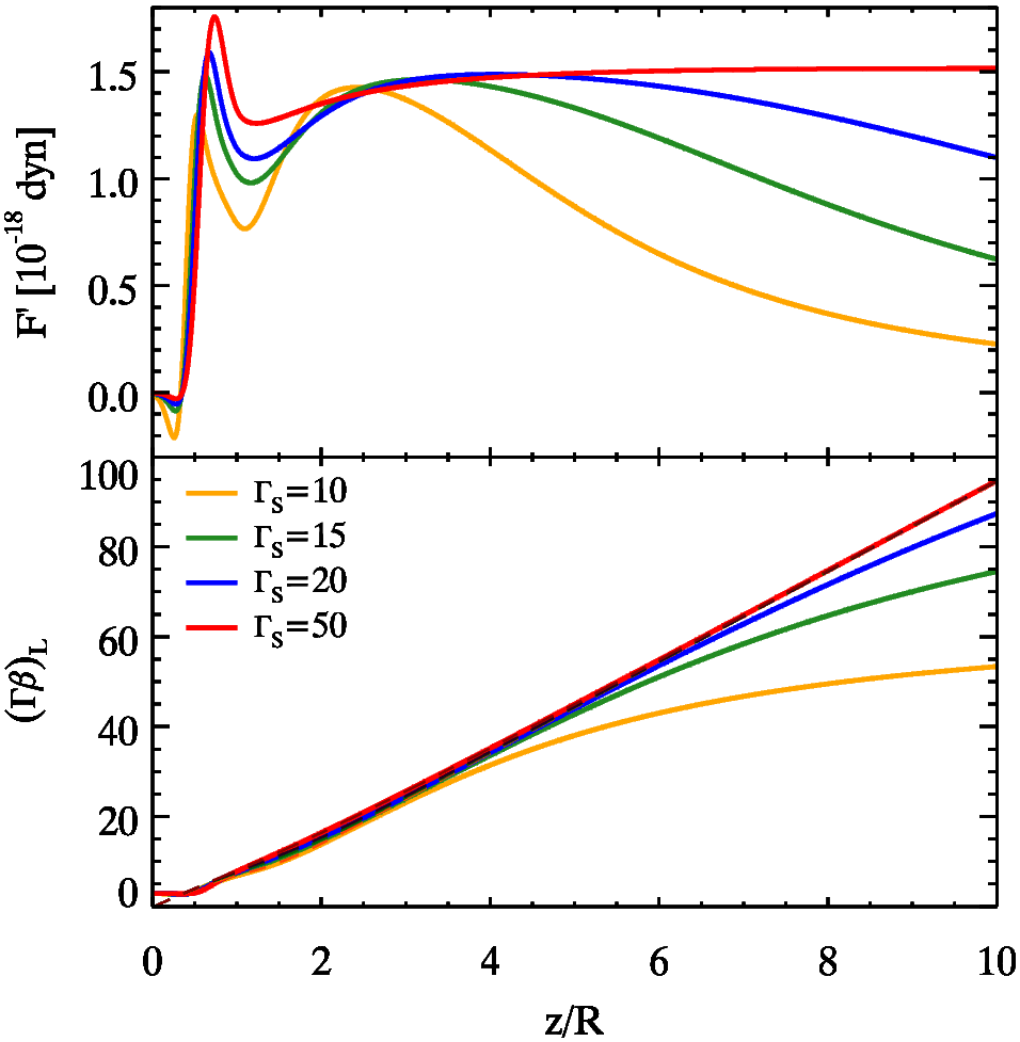

FIGURE 4.6: Radiative acceleration of the layer due to variation of the spine bulk Lorentz factor $\Gamma_{\rm S} = 10,\ 15,\ 20,\ 50$. The spine isotropic luminosity is $L_{\rm iso,S} = 10^{45}$ erg s^{-1} and the leptons of the layer are hot ($\langle\gamma_{\rm L}^2\rangle = 10^6$). The initial layer Lorentz factor is constant $\Gamma_{\rm L,0} = 3$. Top panel: radiative force F' in layer frame as a function of z/R. Bottom panel: Layer Lorentz factor $(\Gamma\beta)_{\rm L}$ (solid lines) and the drag Lorentz factor $(\Gamma\beta)_{\rm L,drag}$ of the layer (dashed line) as a function of z/R.

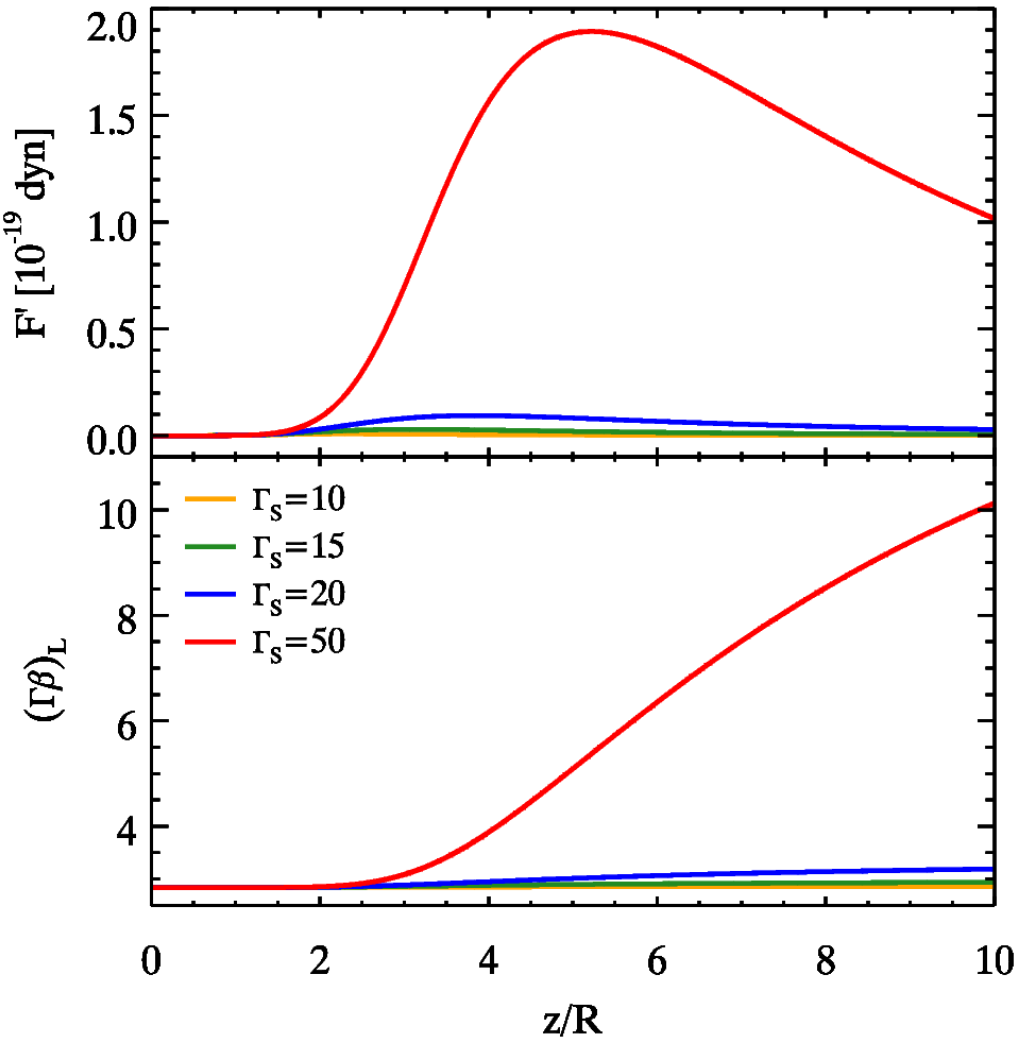

FIGURE 4.7: Radiative acceleration of the layer obtained by varying the spine bulk Lorentz factor $\Gamma_{\rm S} = 10,\ 15,\ 20,\ 50$. The spine isotropic luminosity is $L_{\rm iso,S} = 10^{45}$ erg s^{-1} and the leptons of the layer are cold ($\langle\gamma_{\rm L}^2\rangle = 1$). The initial layer Lorentz factor is constant $\Gamma_{\rm L,0} = 3$. Top panel: radiative force F' in layer frame as a function of z/R. Bottom panel: layer Lorentz factor $(\Gamma\beta)_{\rm L}$ (solid lines) as a function of z/R.

suggests that, in case of hot plasma and for $z > R$, the dynamical evolution of the layer does not depend on its initial Lorentz factor $\Gamma_{\rm L,0}$.

Fig. 4.5 depicts the radiative evolution of a cold plasma ($\langle\gamma_{\rm L}^2\rangle = 1$) for an isotropic spine luminosity ($L_{\rm iso,S} = 10^{45}$ erg s^{-1}) and a constant spine Lorentz factor of $\Gamma_{\rm S} = 15$. The value of $k_{\rm L}$ for Figs. 4.4 and 4.5 differs by 10^6 which is the average of the square of the leptonic Lorentz factor for the hotter plasma. We continue to vary $\Gamma_{\rm L,0}$ as our parameter and by comparing the two figures (Fig. 4.5 and Fig. 4.4) we note that the forces experienced by the colder leptons are smaller by two orders of magnitude. This strong reduction in the force results in negligible acceleration of the layer effective particle which maintains its initial Lorentz factor $\Gamma_{\rm L,0}$ except for the case $\Gamma_{\rm L,0} = 1.01$, where there is a weak increase of the bulk Lorentz factor to $\Gamma_{\rm L,fin} = 1.67$. We also note that as the forces involved are smaller than the previously considered cases, the drag force is not strong enough to create multiple force peaks. Thus the force profiles are characterized by single peaks which occur when the radiation from the entire spine irradiates the sheath particle.

Varying $\Gamma_{\rm S}$ — In the final case for this subsection, we explore the effects of varying $\Gamma_{\rm S}$ on the force and $(\Gamma\beta)_{\rm L}$ curves for $\Gamma_{\rm L,0} = 3$. If the sheath plasma is hot, we observe double peaked curves as shown in the top panel of Fig. 4.6. We also note that a faster spine produces a greater force on the sheath, resulting in a faster sheath. Fig. 4.7 shows the same physical quantities but for a cold sheath and we note that the forces involved are reduced by an order of magnitude. This does not result in a significant change of the layer Lorentz factors except for the case when $\Gamma_S = 50$, where a comparatively larger force leads to an accelerating sheath.

4.42 Radiative acceleration of the layer: cooling scenario

Single injection

In this subsection we explore a case where the particles of both the spine and the layer are energized only once before entering the active region and the particles in the layer can cool via radiative cooling. This implies that the layer leptonic energy distribution varies with time. For simplicity, we will assume here that the spine bulk Lorentz factor $\Gamma_{\rm S}$ is

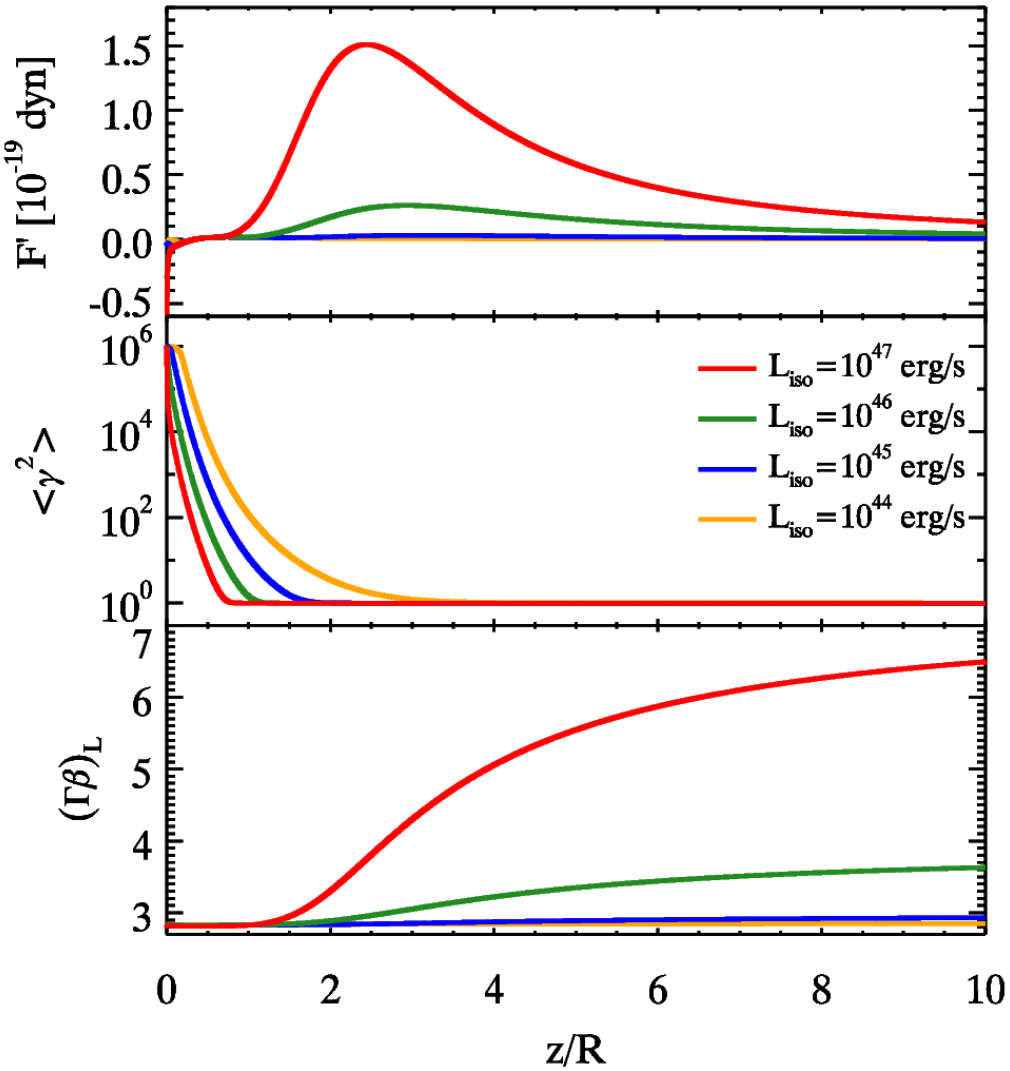

FIGURE 4.8: Radiative acceleration of the sheath obtained by varying the isotropic spine luminosity $L_{\rm iso,S}$ from 10^{44} to 10^{47} erg s^{-1} for sheath constituted by hot leptons ($\langle\gamma_{\rm L}^2\rangle = 10^6$), constant spine Lorentz factor of $\Gamma_S = 15$ and for an initial sheath Lorentz factor $\Gamma_L = 3$. The x–axis depicts the position z in units of the vertical structure dimension R. The top panel depicts the radiative force measured in the layer frame. Middle panel: the internal energy of the sheath denoted by $\langle\gamma_{\rm L}^2\rangle$. Bottom panel: Lorentz factor of the sheath $(\Gamma\beta)_{\rm L}$ measured in the observer frame.

constant, leaving the study of the possible change of $\Gamma_{\rm S}$ (caused by the interaction with the layer photons) to § 4.43.

We start by solving the equation of motion for the layer and we show the spatial profiles for $(\Gamma\beta)_{\rm L}$, the evolution of the average internal energy of the layer $\langle\gamma_{\rm L}^2\rangle$ and the profile of the force as perceived by the layer projected over the z-axis F'.

Varying $L_{\rm iso,S}$ — We begin by varying the intrinsic spine luminosity $L_{\rm iso,S}$, assuming that the population of the sheath is initially hot ($\langle\gamma_{\rm L}^2\rangle_{z=0} = 10^6$). The top panel of Fig. 4.8 depicts the force curves for different values of the spine luminosity. For small values of z, the force profiles are similar to the profiles in Fig. 4.3. All the curves show an initial negative force with magnitudes proportional to the spine luminosity (refer to § 4.41). The middle panel shows the variation of $\langle\gamma_{\rm L}^2\rangle$ and we note the difference in the cooling rates for the various curves, which arises because sheaths with more luminous spines cool faster. Note that the various curves in the second panel eventually merge due to continuous cooling. The third panel shows the variation of $(\Gamma\beta)_{\rm L}$. For $z < R$, all the layer curves show no acceleration. On the contrary, from the force curves one expects the layer to be decelerated due to the initial negative forces but these decelerations are small and hence difficult to resolve (and thus, see) in Fig. 4.8. However, the reader can observe the resolved deceleration for the blue curve in Fig. 4.8 through the red curve in the bottom panel of Fig. 4.9 because the product $k_L = 10^{51}$ erg/s is identical for these curves. When the effective sheath particle overtakes the scale–length R, the spine which lies behind it irradiates the particle from the rear. However, at these large values of z the sheath plasma is cold and only extremely large spine luminosities (e.g. $L_{\rm iso,S} \geq 10^{45}$ erg s^{-1}) are capable of significantly accelerating the layer particle and hence the layer, as shown in Fig. 4.8.

Varying $\langle\gamma_{\rm L}^2\rangle_{z=0}$ — We explore how the sheath evolves for different initial $\langle\gamma_{\rm L}^2\rangle_{z=0}$ (in short, $\langle\gamma_0^2\rangle$) values under the influence of radiative cooling with an initial sheath Lorentz factor $\Gamma_{\rm L,0} = 3$ and a constant spine luminosity $L_{\rm iso,S} = 10^{45}$ erg s^{-1}. Fig. 4.9 confirms that the force profile is characterized by negative values during the initial stages, with the hottest sheaths experiencing the greatest force magnitudes. The middle panel depicts the variation in $\langle\gamma_{\rm L}^2\rangle$ due to radiative cooling. The curves show an initial flat evolution and then a decreasing trend in such a manner that all the curves merge, irrespective of their $\langle\gamma_0^2\rangle$

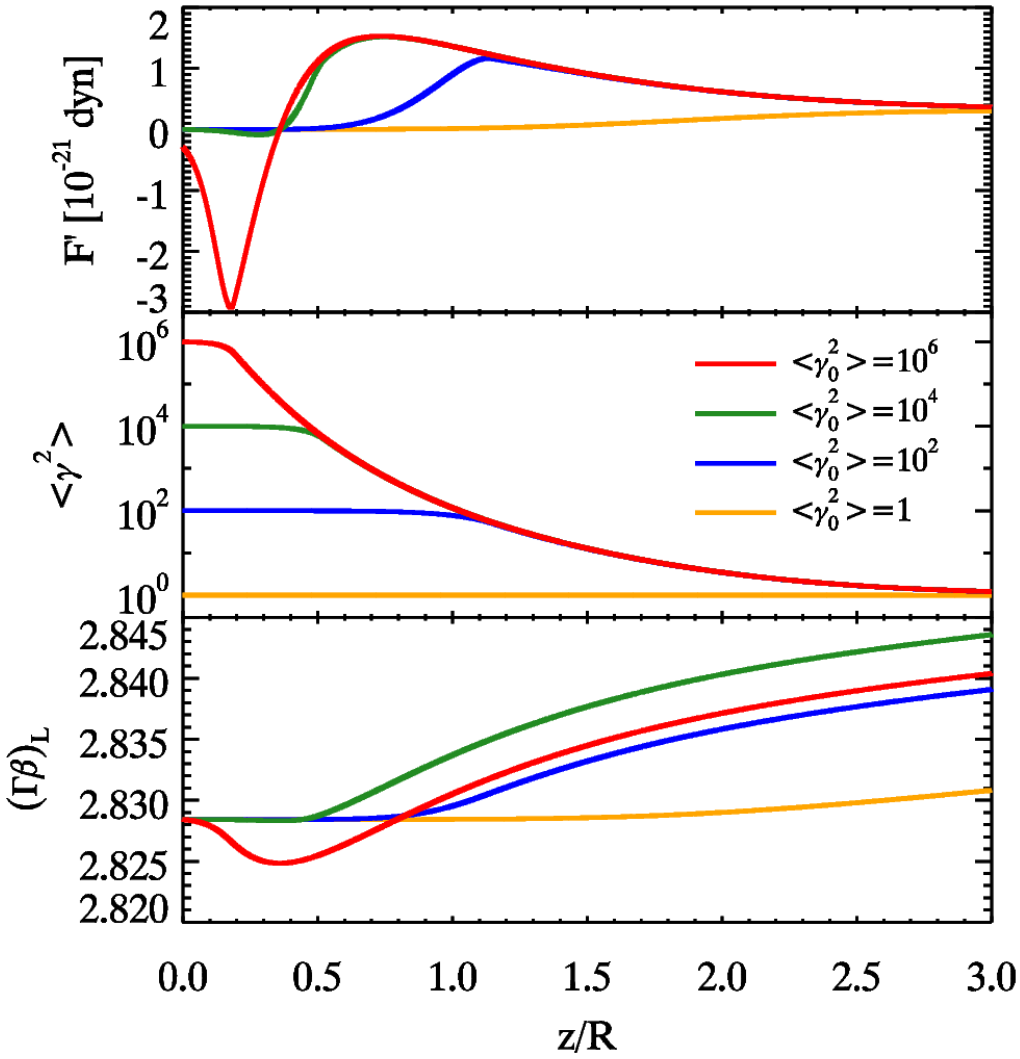

FIGURE 4.9: Radiative acceleration of the sheath due to variation of the average internal energy content of the sheath $\langle\gamma_{\rm L}^2\rangle$ from 1 to 10^6 for a constant isotropic spine luminosity $L_{\rm iso,S} = 10^{45}$ erg s^{-1}, a constant spine Lorentz factor $\Gamma_S = 15$ and for an initial sheath Lorentz factor $\Gamma_L = 3$. The x–axis depicts the position z normalized by the vertical structure dimension R. Top panel depicts the radiative force measured in the layer frame. Middle panel: the internal energy of the sheath denoted by $\langle\gamma^2\rangle$. Bottom panel: Lorentz factor of the sheath $(\Gamma\beta)_{\rm L}$ measured in the observer frame.

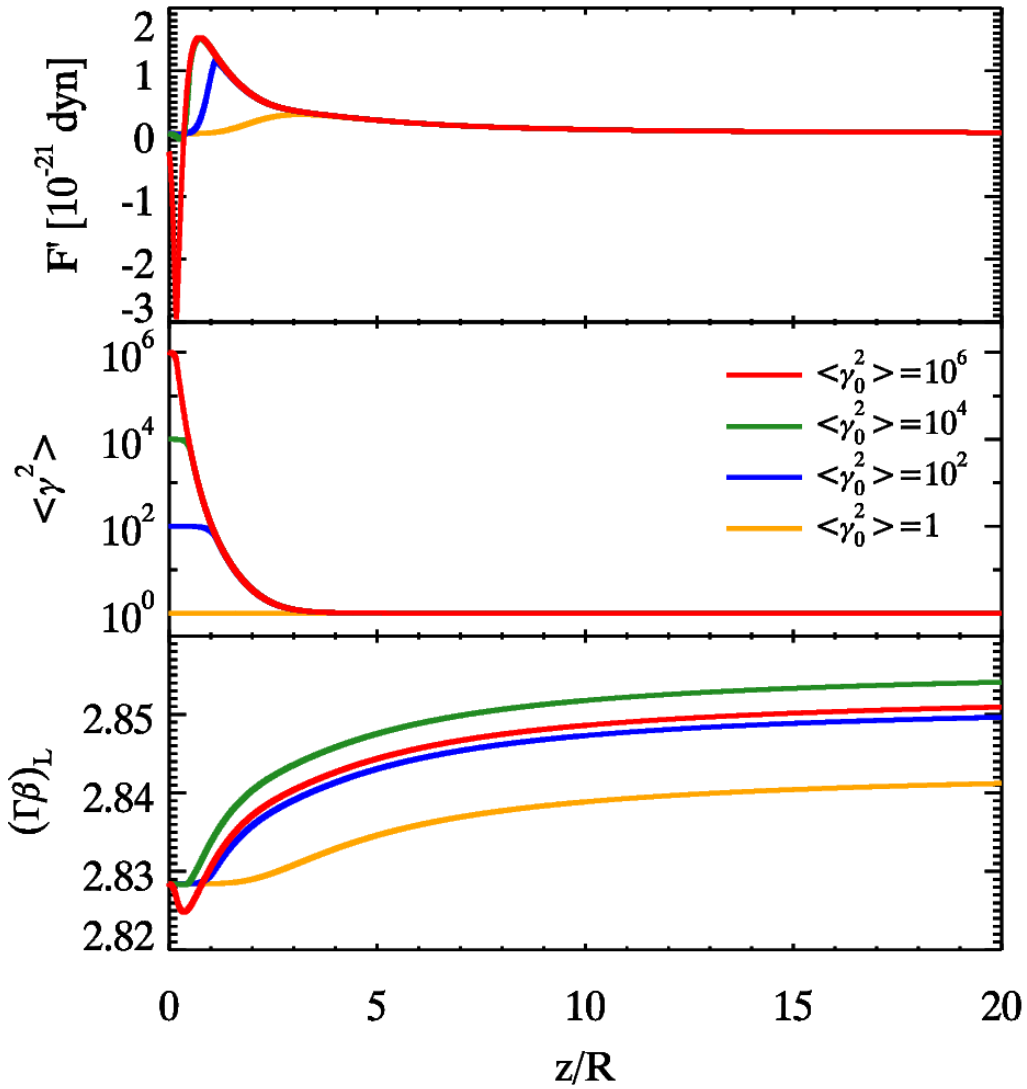

FIGURE 4.10: Same as Fig. 4.9, but zooming out to longer z/R to see the final values of $(\Gamma\beta)_{\rm L}$.

values. This behavior can be understood from Fig. 4.2 or from particle energy distribution $N(\gamma)$ of the layer (see Eq. 4.4): if the cooling energy γ_c is greater than the spectral break energy γ_b (i.e., $\gamma_{\rm c} > \gamma_{\rm b}$), then $\langle\gamma^2\rangle \sim \gamma_{\rm b}$ which implies that $\langle\gamma^2\rangle$ is almost constant (this corresponds to the initially flat evolutionary phase seen in the middle panel of Fig. 4.9). However, when $\gamma_{\rm c}$ crosses $\gamma_{\rm b}$, $\langle\gamma^2\rangle$ starts to decrease from its initial value and becomes comparable to $\gamma_{\rm c}$. Note that even though the force curves have merged (simultaneously with the merging of $\langle\gamma^2\rangle$ curves), the $(\Gamma\beta)_{\rm L}$ curves remain segregated due to the different initial decelerations resulting from the different initial behavior of $\langle\gamma^2\rangle$. This leads to the interesting result – the bulk Lorentz factor at saturation is maximum for an intermediate value of the initial $\langle\gamma_{\rm L}^2\rangle$ ($\langle\gamma_{\rm L}^2\rangle = 10^4$), instead of the curve with the initially hottest leptons ($\langle\gamma_{\rm L}^2\rangle = 10^6$), albeit by a small amount (see Fig. 4.10).

As a whole, we conclude from this section that the radiative cooling process causes the layer to lose internal energy rapidly and so it quenches the process of radiative acceleration. Except for cases with very high spine luminosity, we can affirm that the final bulk Lorentz factor of the layer $\Gamma_{\rm L}$ does not change significantly from its initial value $\Gamma_{\rm L,0}$ (see Fig. 4.10). This result is similar to those obtained by studying the radiative acceleration of a cold plasma in the no cooling scenario (cfr. §4.41).

Continuous injection

This scenario explores the situation where we have continuous energy injection inside the sheath region via, e.g., a standing shock, namely when the cooling is balanced by injection of fresh energetic particles that energize the plasma and the electron energy distribution is assumed to stay constant between $z = 0$ and $z = 10^{16}$ cm. There is no energy injection outside the active region. We assume that the injection rate within the active region is such that its effect is equivalent to making cooling ineffective. We still neglect here the radiative effects on the spine due to the layer and hence the bulk Lorentz factor of the spine $\Gamma_{\rm S}$ is assumed to be constant.

Differently from most of the other cases presented in this work, for this case we assume that the initial bulk Lorentz factor of the layer is close to unity. We intend to explore if the

layer can be accelerated radiatively and, achieve a bulk Lorentz factor $\Gamma_{\rm L} \sim 3$ as required by observations.

Fig. 4.11 depicts the evolution of the force, $\langle\gamma^2\rangle$ and $(\Gamma\beta)_{\rm L}$ curves. The continuous shocking re-energizes the particles within the standing shock region, and it is responsible for large forces proportional to the plasma's internal energy $\langle\gamma_{\rm L}^2\rangle$ content. Because there is continuous energy injection for $z \leq 10^{16}$ cm, we expect the physical quantities in this region to evolve in a fashion similar to the same quantities in § 4.41. Indeed, the evolution of the force curves in the standing shock region as depicted in Fig. 4.11 is very similar to Fig. 4.3 (the yellow curves are almost identical for $z < R$). The drop in the force is due to the bulk Lorentz factor of the layer approaching $\Gamma_{\rm L,drag}$ as explained earlier in § 4.41. All the three curves experience positive forces, leading to an accelerated layer as demonstrated by the $(\Gamma\beta)_{\rm L}$ plot in the bottom panel of Fig. 4.11. The cooling becomes effective for $z > 10^{16}$ cm ($z/R > 1$), resulting in a rapid decrease in the values of $\langle\gamma_{\rm L}^2\rangle$ for the various curves (middle panel of Fig. 4.11). A decrease in $\langle\gamma_{\rm L}^2\rangle$ correspondingly produces a rapid decrease in the force values also (top panel of Fig. 4.11). The role of radiative cooling in quenching the radiative force has been explored in detail in § 4.42. As the force values for $z > 10^{16}$ cm are quite small, we note that the layer Lorentz factors saturate close to the values attained at $z \sim R = 10^{16}$ cm.

Fig. 4.11 shows that if the layer is kept hot by a mechanism replenishing its energy losses, it can indeed be accelerated to "interesting" Lorentz factors (i.e., $\Gamma_{\rm L} \sim 3$). Of course, the hotter the layer, the stronger the Compton rocket effect and the larger the final Lorentz factor. We will see in the next subsection if this remains true when considering the feedback on the spine.

4.43 Spine–layer feedback

In §4.34, we described the feedback mechanism produced by relative interaction between the photons emitted by the layer and the spine particles and vice–versa, i.e., between spine photons and layer particles. In this section we aim to study the spine–layer feedback mechanism and how the mechanism modifies the Lorentz factor profiles for both the spine and the layer. First we will compute both the spine and the layer bulk Lorentz factor

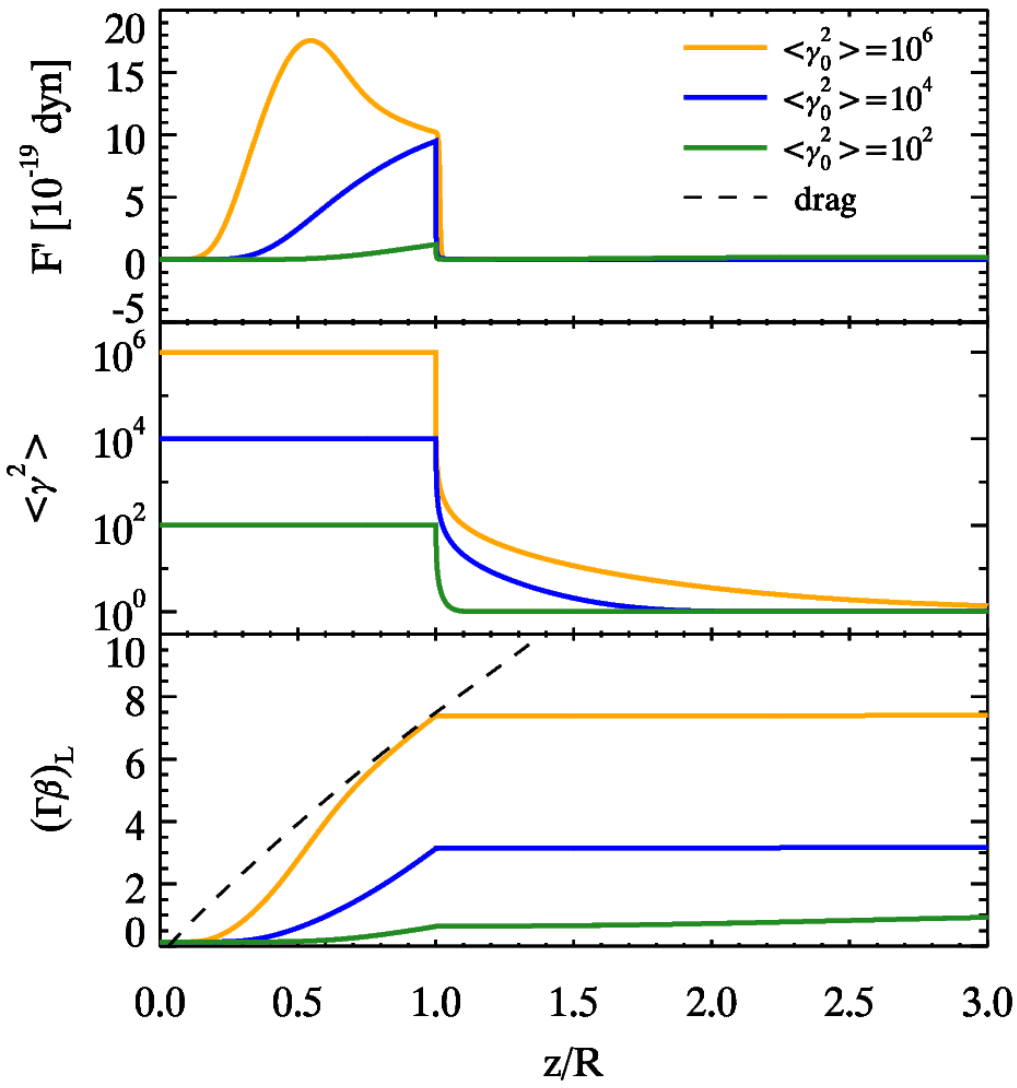

FIGURE 4.11: Radiative acceleration of the sheath obtained by varying the initial average internal energy content of the sheath $\langle\gamma_0^2\rangle$ from 10^2 to 10^6 for a constant isotropic spine luminosity $L_{\rm iso,S} = 10^{45}$ erg s^{-1}, a constant spine Lorentz factor $\Gamma_{\rm S} = 15$ and for an initial sheath Lorentz factor $\Gamma_{\rm L,0} = 1.01$. In this scenario, the plasma cools radiatively only for $z/R > 1$; for $0 < z/R < 1$ the plasma is continuously energized and maintains the average internal energy (thereby making cooling ineffective). The top panel depicts the radiative force measured in the layer frame. Middle panel: The variation in the internal energy of the sheath denoted by $\langle\gamma_{\rm L}^2\rangle$ as a function of the vertical position z. Bottom panel: $(\Gamma\beta)_{\rm L}$ profile of the sheath as measured in the observer frame.

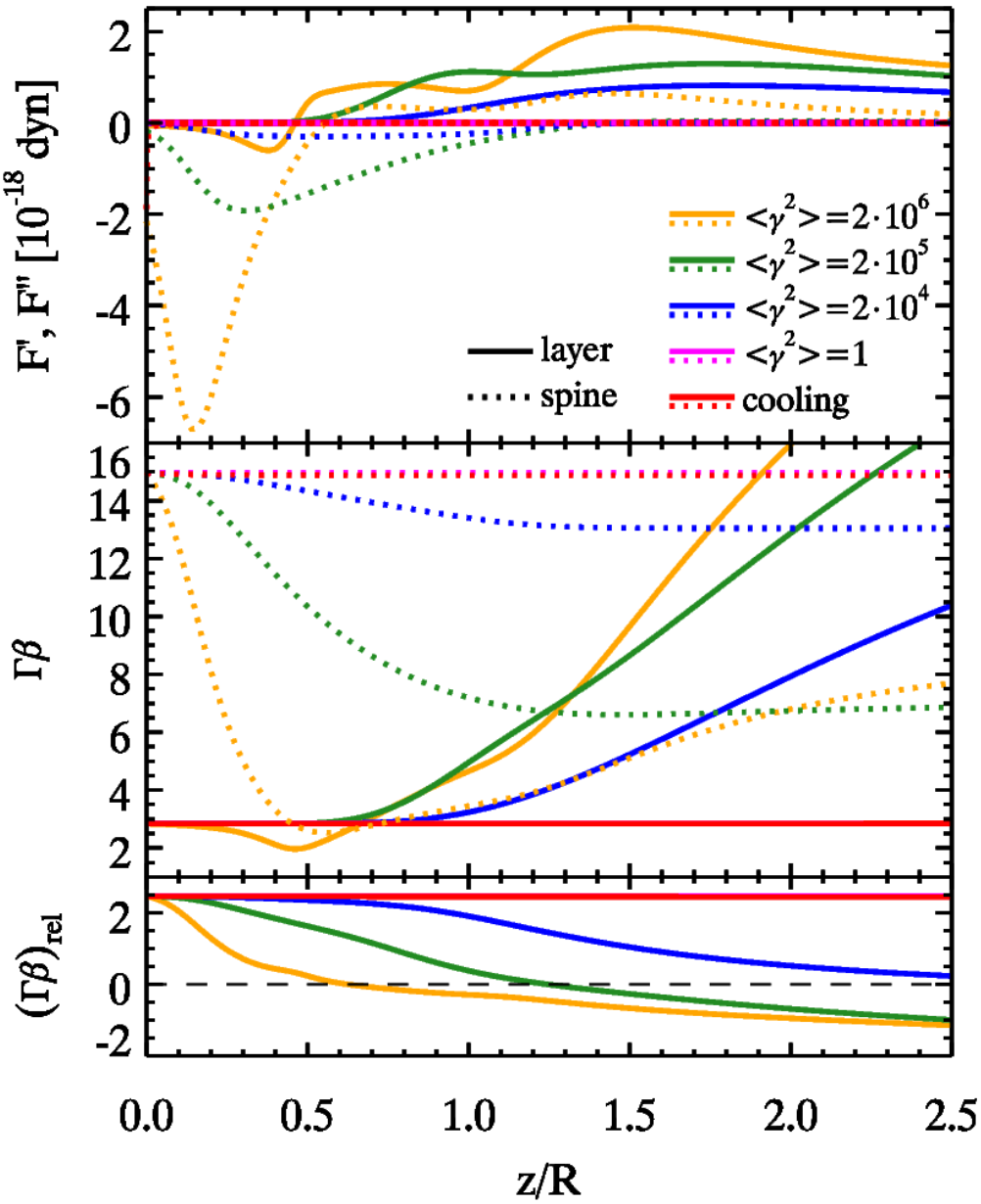

FIGURE 4.12: Radiative acceleration of spine and layer: the feedback. Comparison by varying $\langle\gamma^2\rangle = 2{\cdot}10^6, 2{\cdot}10^5, 2{\cdot}10^4, 1$ of both spine and layer in no cooling case and cooling case. Parameters used: $\Gamma_{\rm S,0} = 15$, $\Gamma_{\rm L,0} = 3$ and $L''_{\rm S} = 10 \cdot L'_{\rm L}$. Top panel: radiative force measured in spine (layer) frame in dotted (solid) lines as a function of z/R. Middle panel: Profile of $(\Gamma\beta)$ of the spine (layer) in dotted (solid) lines. Only for $\langle\gamma^2\rangle = 2 \cdot 10^6$ with no cooling, in the final stages the layer can travel faster than the spine. Bottom panel: The relative velocity profile of the spine with respect to the layer expressed in terms of $(\Gamma\beta)_{\rm rel}$.

profiles [$\Gamma_S(z)$ and $\Gamma_L(z)$] in a self–consistent manner. Second, we will study two cases with and without the presence of radiative cooling: in the first case the particle energy distribution is fixed for both the spine and the layer, which is equivalent to the no cooling scenario (however here feedback is active). In the other case, both the spine and layer particles cool radiatively (with feedback).

The spatial profiles of the rest frame forces and of the bulk Lorentz factors for spine and layer have been computed by numerically solving Eqs. 4.13. The results for the two cases (with cooling and without cooling), mentioned earlier are shown in Fig. 4.12 and are be summarized below:

(1) As expected, in all the explored cases the spine is decelerated by the Compton interaction with the layer photons. The force experienced by the spine is always negative (the only exception is the case with $\langle\gamma^2\rangle \sim 10^6$, where in the last stages the spine force turns positive);

(2) consistent with the results of previous sections, the layer is initially decelerated and later accelerated in all cases;

(3) the acceleration is stronger for greater values of $\langle\gamma^2\rangle$ and is negligible for cold plasmas;

(4) the cooling case reproduces the results of a cold spine and a cold layer, i.e., no significant change of bulk Lorentz factor;

(5) for high values of $\langle\gamma^2\rangle \sim 10^6$ the effect of deceleration of the spine and acceleration of the layer is so strong that the sheath can eventually travel faster than the spine. This occurs because the cooling has been switched off. We believe that this is rather unrealistic: to maintain such an energetic particle distribution a huge amount of energy must be supplied to the plasma.

Continuous injection with feedback

In this scenario we study the kinematic evolution of the plasma due to continuous injection (see §4.42) while taking into account the effects of spine–layer feedback. The initial internal energy content of the spine and the layer plasmas ($\langle\gamma_S^2\rangle$ and $\langle\gamma_L^2\rangle$ respectively) is maintained

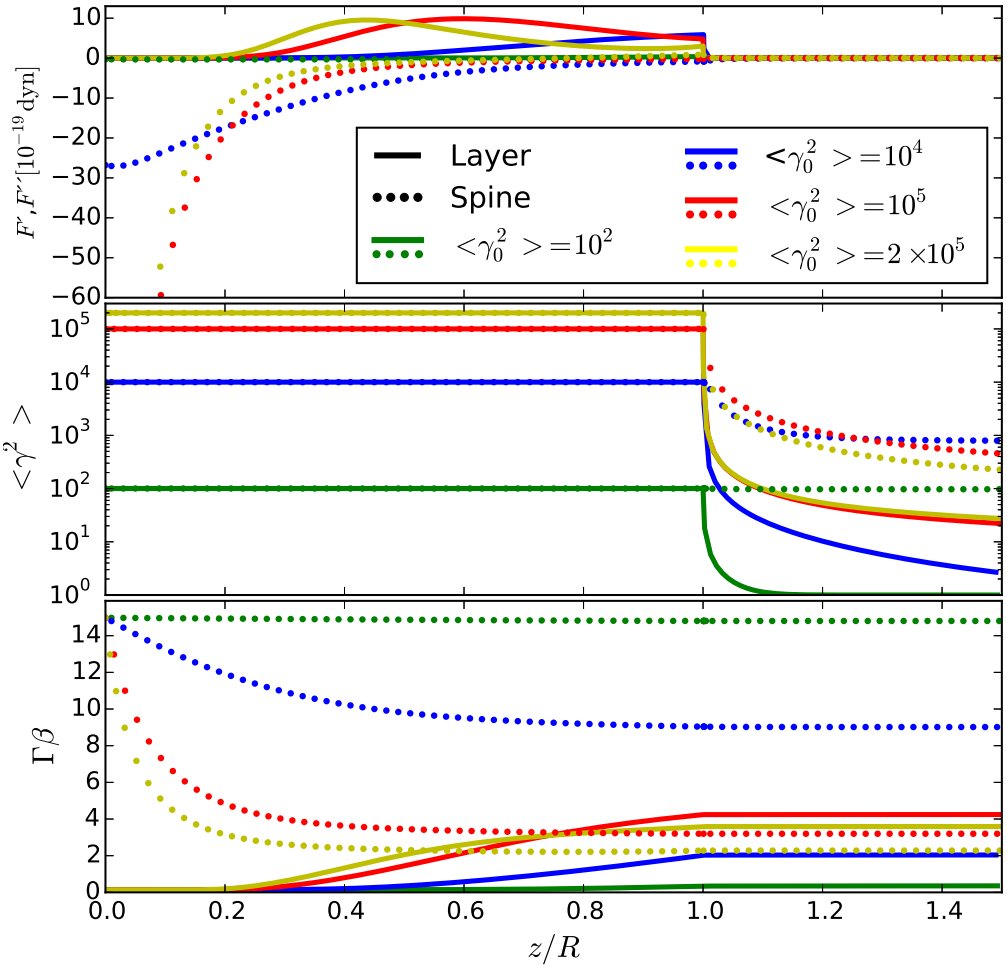

FIGURE 4.13: Radiative acceleration of spine and layer: the feedback with continuous injection. In this scenario, the plasma radiatively cools for z/R > 1 whereas for $0 < z/R < 1$ it is continuously energized thereby nullifying the radiative cooling (thus maintaining its internal energy content). The colored curves are obtained by varying $\langle\gamma^2\rangle = 2\times10^5$, 10^5, 10^4 and 10^2 for both the spine and the layer. Parameters used: $\Gamma_{\rm S,0} = 15$, $\Gamma_{\rm L,0} = 1.01$ and $L''_{\rm S} = 10\cdot L'_{\rm L}$. Top panel: radiative force measured in spine (layer) frame in dotted (solid) lines as a function of z/R. Middle panel: The variation in the internal energy of content of the spine and the layer denoted by $\langle\gamma^2_{\rm L}\rangle$ as a function of the vertical position z. Bottom panel: $(\Gamma\beta)$ profile measured in the observer frame.

by continuous injection of particles within the region $0 \leq z/R < 1$ thereby rendering radiative cooling ineffective. However, in the absence of particle injection, i.e., for $z/R > 1$ radiative cooling becomes important and impacts the evolution of the plasma by altering its internal energy content (see § 4.32). This scenario differs from § 4.42 because here we account for the radiative interplay between the spine and the layer and, as a result, the bulk Lorentz factor and the average internal energy content of the spine are no longer constants.

In order to study if the layer can accelerate from almost 'at rest' situation and achieve bulk motions required for explaining observations, we begin with the layer moving at a small initial bulk Lorentz factor $\Gamma_{\rm L,0} = 1.01$. The three panels, from top to bottom in Fig. 4.13 show how the forces, $\langle\gamma^2\rangle$, and, the velocity profile $\Gamma\beta$ for the spine and the layer evolve as a function of the normalized position z. We summarize the results of Fig. 4.13 below:

(1) For the cases with different initial $\langle\gamma_0^2\rangle$ values, the spine predominantly experiences a negative force with a magnitude proportional to the spine's internal energy content $\langle\gamma_S^2\rangle$. The forces are quite small for $\langle\gamma^2\rangle = 10^2$ and as a result negligible deceleration occurs in this case. The forces are significantly larger for cases with $\langle\gamma^2\rangle \geq 10^5$ which result in the decelerating spine traveling slower than the layer. With the layer now moving faster than the spine, this 'role reversal' causes the spine to experience a positive and accelerating force. However, the magnitude of this force is small due to the reduction in the relative bulk Lorentz factor between the spine and the layer;

(2) the layer is first decelerated and then accelerated (due to the system's geometry as explained in detail in § 4.41) as the top panel of Fig. 4.13 shows. However, for cases where $\langle\gamma^2\rangle \geq 10^5$ the top panel depicts formation of a peak, followed by a decline in the layer force curves within the region $0 \leq z/R < 1$. The peak's location coincides with the location where the decelerating spine slows down to speeds comparable to those of the layer (see bottom panel) - leading to reduced relative motion which suppresses Compton rocket acceleration. As a result, the force experienced by the layer peaks and declines;

(3) the net acceleration of the layer does not generally correlate with the average internal energy content of the layer. This is evident from the hotter plasma (yellow curve -

$\langle\gamma_0^2\rangle = 2\times10^5$) saturating at a lower speed than a cooler plasma (the red curve - $\langle\gamma_0^2\rangle = 10^5$) as depicted in the bottom panel of Fig. 4.13. This phenomenon can again be linked with a hotter spine being more quickly decelerated than a comparatively cooler spine. For sufficiently hot plasmas, the decelerating/slowing spine can end up traveling at comparable or slower speeds than the layer which leads to lesser relative motion and, thereby, suppression of the Compton rocket mechanism;

(4) in the $\langle\gamma^2\rangle = 10^4$ case (blue curve) the layer accelerates until $z/R = 1$, after which particle injection ceases, and radiative cooling rapidly decreases the layer's internal energy content. As a result the gradually increasing radiative force vanishes and the acceleration process is quenched. Rapid radiative cooling also occurs for plasmas with $\langle\gamma^2\rangle > 10^4$ (as shown by the red and yellow curves), and cools these plasmas faster than the $\langle\gamma^2\rangle = 10^4$ case (blue curve) as shown in the middle panel of Fig. 4.13. Again, this leads to the sudden drop in the force curves and quenches any further acceleration. The velocity saturation and force quenching phenomena observed here are identical to those observed in § 4.42.

As shown in the bottom panel of Fig. 4.13, by replenishing the energy lost radiatively by injecting particles continuously the layer can attain and maintain "interesting" Lorentz factors ($\Gamma_{\rm L}\sim 2-4.5$). Comparison between the results obtained here with those of § 4.42 shows that radiative feedback in hotter plasmas (both the spine and the layer are hot) reduces the relative bulk motion between the two components of the jet (i.e., the spine and the layer). This reduction in $\Gamma_{\rm rel}$ reduces the amount of boosted radiation thereby suppressing the Compton rocket effect. As a result, the layer does not accelerate and attain Lorentz factors beyond ~ 4.5. Thus in this particular scenario, acceleration/deceleration due to radiative feedback is responsible for regulating the bulk Lorentz factors of both the spine and the layer.

4.44 Spine–layer feedback in e^+e^- pair loaded plasmas

In this subsection we explore the impact of electron–positron pair loading on the radiative acceleration of the spine and the layer. While accounting for radiative feedback between the spine and the layer we explore the effects that different amounts of pair concentrations

can have on the spine–layer system. The main effect of pairs will be to make the plasma "lighter", in the sense that the radiative force will act on an increased number of leptons, while the inertia is still dominated by the same number of protons (except for the pair–dominated cases). Therefore the acceleration or the deceleration will be stronger. The amount of pairs in the plasma can be characterized by the lepton to proton ratio f (as defined in §4.33) as follows:

- Pair–free (PF) plasma ($f = 1$): there is one proton for every electron and no pairs are present.
- Pair enriched (PE) plasma ($f \sim 20$): this plasma is characterized by the presence of several electron–positron pairs. The value $f = 20$ is about the maximum allowed from considerations about the total power of relativistic jets (Ghisellini & Tavecchio 2010).
- Pair dominated (PD) plasma ($f \to \infty$): in this case leptons dominate the kinematics of the plasma. We show this case for illustration, even if it may not be realistic for AGN jets.

We will first study the case without feedback and with the spine moving with a constant bulk Lorenz factor $\Gamma_{\rm S} = 15$. Then we will study the feedback case, assuming that both the layer and the spine have the same number f of pairs. Within the case without feedback, we will study the extreme cases of a cold plasma ($\langle\gamma^2\rangle = 1$, Fig. 4.14) and a hot plasma ($\langle\gamma^2\rangle = 10^6$, Fig. 4.15). Finally, we study the feedback case (Fig. 4.16). The results of these cases are summarized as follows:

(1) *Cold plasma – No feedback* — Fig. 4.14 depicts the force experienced by the layer due to radiation from the spine in the upper panel. The lower panel depicts the radiative acceleration of the layer by plotting $(\Gamma\beta)_{\rm L}$ as a function of position z/R. We note that the force magnitudes are extremely small $\sim 10^{-21}$ dyn in comparison with forces observed in the earlier sections. The pair–free plasma case is identical to $\langle\gamma^2\rangle = 1$ in § 4.43. Even though the forces are small, the increased pair content decreases the mass of the effective particles. Thus the greater the amount of pairs, the greater the acceleration, as shown by the bottom panel in Fig. 4.14.

(2) *Hot cooling plasma – No feedback* — We consider a hot plasma with $\langle\gamma^2\rangle = 10^6$ with cooling enabled. Fig. 4.15 shows the force experienced by the layer (top panel), the variation of $\langle\gamma_{\rm L}^2\rangle$ (middle panel) and the evolution of $(\Gamma\beta)_{\rm L}$ (bottom panel) as a function of z/R. As expected, hotter plasmas experience a stronger and negative initial force which tends to decelerate them. The decelerations experienced depend upon the pair content, thereby the pair dominated plasma is decelerated more than the others. This slowing down of the plasma leads to a decrease of the (negative) force (due to the decrease of the received radiation energy density). This impacts the cooling rate as well as the force profile for the pair–dominated plasma. The lower cooling rate along with geometrical effect (entire spine irradiating the layer particle) is responsible for the burst in acceleration at large values of z.

(3) *Feedback* — Now we discuss the third case, where we compare hot and cold plasmas with *both cooling and feedback enabled.* Fig. 4.16 depicts the evolution of the forces F' and F" (upper panel) as measured in the frame of the layer and of the spine, respectively, and $(\Gamma\beta)_{\rm L}$. The forces $F'_{\rm S}$ experienced by the spine due to the radiative interaction with the layer are always negative leading to its deceleration. For cold plasmas (with initial $\langle\gamma^2\rangle = 1$) the deceleration, though small, is non–zero as compared to hot plasma with initial $\langle\gamma^2\rangle = 10^6$. We also note that with increasing f values, the deceleration becomes much stronger.

Similar to the results of previous sections the layer force $F'_{\rm L}$ (denoted by the solid curves in the upper panel of Fig. 4.16) starts off negative and turns positive (due to geometrical effects). The initial magnitudes are proportional to both $\langle\gamma^2\rangle$ and f. As a result the pair–dominated hot layer is initially significantly decelerated and then accelerates. At later times, because of cooling the acceleration is no longer a function of $\langle\gamma^2\rangle$ but still depends upon the particle ratio f. As a result, pair dominated $\Gamma_{\rm L,sat} \sim 6$ and enriched plasmas $\Gamma_{\rm L,sat} \sim 3.1$ accelerate even for $z/R > 5$ and much more than pair–free plasmas.

We can conclude that pair loading enables the plasma to accelerate significantly even when the plasmas are cold to begin with. Cold pair–enriched and the cold pair–dominated plasma exhibit significant acceleration, achieving layer Lorentz factors $\Gamma_{\rm L} \sim 4$ and $\Gamma_{\rm L} \sim 16$

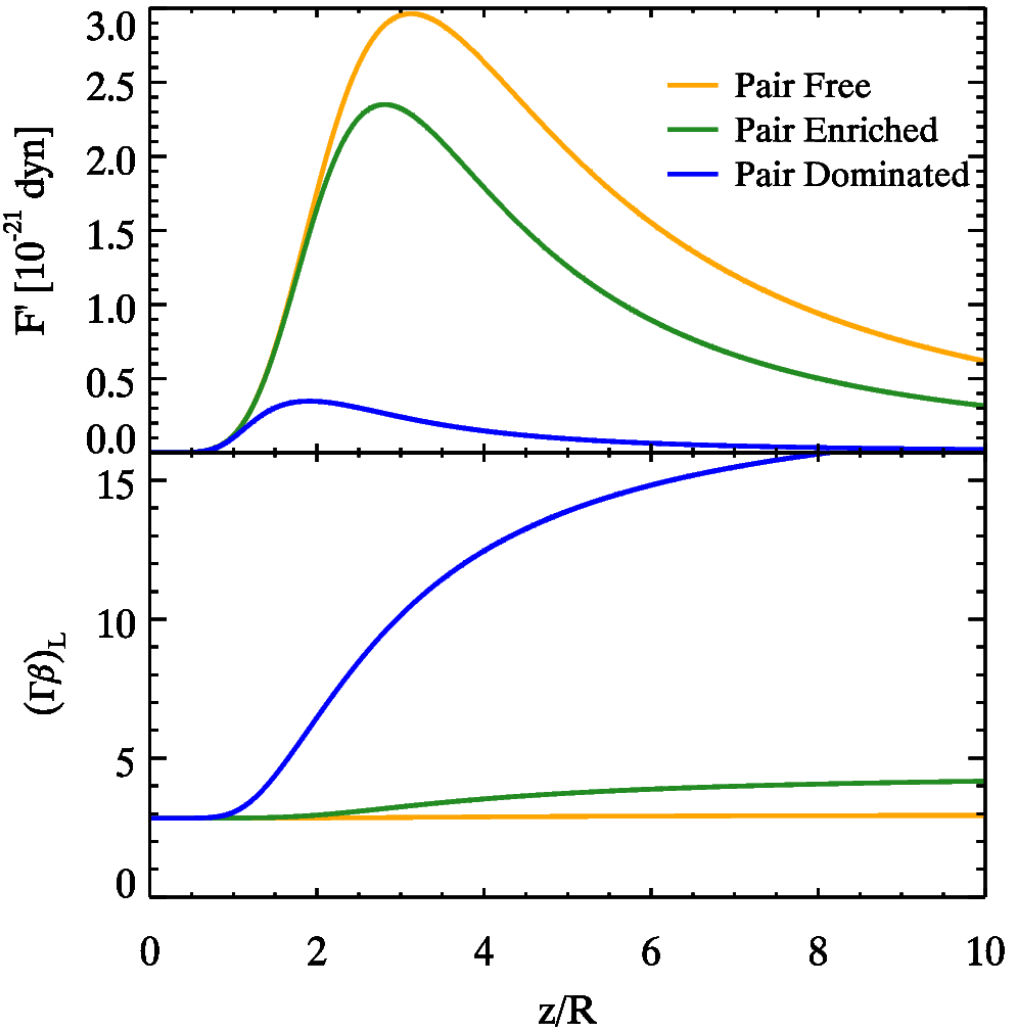

FIGURE 4.14: Radiative acceleration of a cold, pair–loaded layer plasma by varying lepton to proton ratio f; we analyze three cases with $\langle\gamma^2\rangle = 1$: no pairs in layer ($f = 1$); a plasma with $f = 20$ and the extreme case of a pair dominated plasma. Parameters used: $\Gamma_{\rm S} = 15$, $\Gamma_{\rm L,0} = 3$ and $L''_{\rm S} = 10 \cdot L'_{\rm L}$. Top panel: radiative force as measured in the layer frame. Bottom panel: profile of $(\Gamma\beta)_{\rm L}$ for the layer.

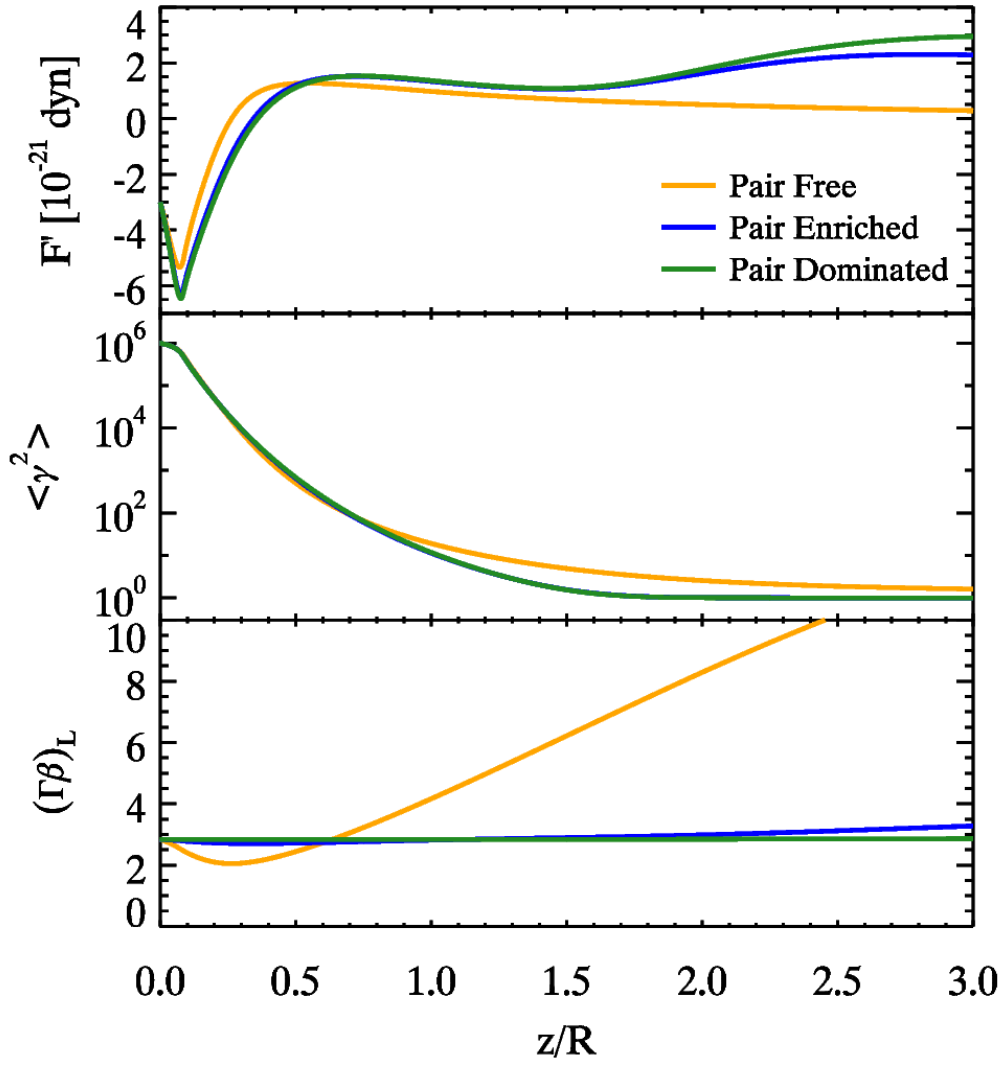

FIGURE 4.15: Radiative acceleration plot for a hot layer plasma having different lepton to proton ratios f; we analyze three distinct cases with an initial $\langle\gamma^2\rangle_{z=0} = 10^6$: no pairs in layer and spine plasma ($f = 1$); a pair–enriched $f = 20$ plasma, and the extreme case of a pair dominated plasma. Parameters used: $\Gamma_S = 15$, $\Gamma_{L,0} = 3$ and $L''_S = 10 \cdot L'_L$. Top panel: radiative force measured in layer frame as a function of z/R. Middle panel: the evolution of internal energy of the sheath denoted by $\langle\gamma^2_L\rangle$. Bottom panel: profile of $(\Gamma\beta)_L$ for the layer as a function of z.

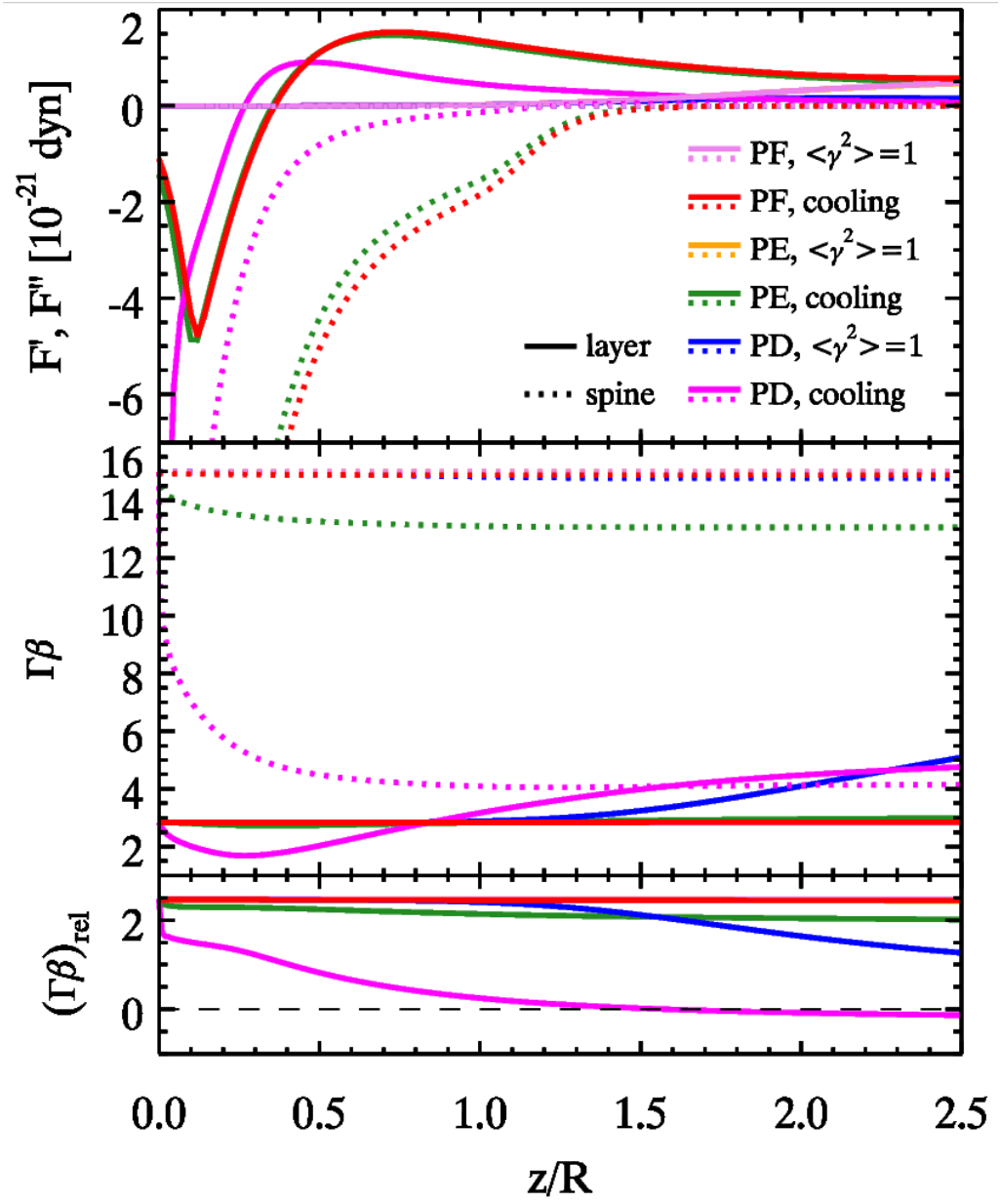

FIGURE 4.16: Radiative acceleration of the spine–layer pair loaded plasma with feedback; we compare and analyze three cases with different lepton to proton ratios: no pairs in the layer and spine plasmas (i.e. there is one lepton for each proton - PF); a plasma with $f = 20$ leptons for each proton (PE) and as the final case, a plasma dominated by pairs (PD). Parameters used: $\Gamma_{\rm S,0} = 15$, $\Gamma_{\rm L,0} = 3$ and $L''_{\rm S} = 10 \cdot L'_{\rm L}$. Top panel: Radiative force measured in spine (layer) frame in dotted (solid) lines as a function of z/R. Middle panel: Profile of $(\Gamma\beta)$ for the spine (layer) represented by dotted (solid) lines. Bottom panel: The relative velocity profile of the spine with respect to the layer expressed as $(\Gamma\beta)_{\rm rel}$.

respectively.

4.5 Conclusions

In this work we have investigated the effects of radiative acceleration through Compton scattering in a simple case of structured jet: the spine–layer scenario. We summarize here the several factors we have explored in our work that influence the dynamical evolution of a structured jet.

There are two main acceleration regimes:

- Compton Rocket Effect: For the Compton rocket to be effective the leptonic distribution must be hot ($\langle\gamma^2\rangle \gg 1$). The seed photons do not directly provide the driving force but act as a catalyst for the accelerated motion, in fact the bulk kinetic energy is supplied by the internal energy of the plasma.

- Radiatively Driven Motion/Normal Compton scattering: For this case the leptonic distribution of the plasma is cold ($\langle\gamma^2\rangle \sim 1$). The motion is driven solely by Compton scattering photons off cold electrons. The bulk kinetic energy of the plasma is supplied by the seed photon field due to momentum transfer to the plasma. The forces and hence the acceleration achieved in this case are small as compared to the Compton rocket effect.

Having identified the acceleration regimes, we will now summarize several factors important for acceleration:

- Radiative Cooling : Radiative cooling decreases the internal energy content ($\langle\gamma^2\rangle$) of the plasma quite rapidly which effectively kills the force – thereby quenching the acceleration process. Thus it plays an important role in determining whether the Compton rocket effect or the radiatively driven motion dominates the kinematics of the structured jet. In §4.41 we discussed how an initially hot plasma experiences a decelerating force for small values of z due to radiation directed along the negative

z direction or coming from spine regions located above the layer. As the plasma decelerates, it will simultaneously cool rapidly if radiative cooling is active. The magnitude of this decelerating force decreases due to two reasons – i) rapid cooling and ii) as the plasma travels further away from the base it receives some upward directed photons from the base (which is now to the rear of the layer plasma) pushing the layer plasma along the positive z direction. As a result, the magnitude of the decelerating force rapidly decreases and it does not produce a significant change in $\Gamma_{\rm L}$ values. As noted in § 4.42, the radiative cooling activated by low or moderate spine luminosities quenches the acceleration process – which effectively freezes the Lorentz factor of the layer at the value it had just before activation.

– Feedback: the feedback scenario enables us to study the self–consistent evolution of the spine and layer under the radiative influence of the layer and the spine respectively. Among the cases we studied, in the cooling regime neither the spine nor the layer shows any acceleration. In some cases, the layer accelerates and even overtakes the spine – but this requires a continuous injection of huge (and possibly unrealistic) amounts of energy. In the non–cooling or continuous energy injection regime, for $\langle\gamma^2\rangle > 2 \times 10^4$, significant accelerations can be seen for the layer and decelerations for the spine. Interestingly, by making the situation more realistic by limiting energy injection (having a energy injection limited to the active region as explored in § 4.42 and § 4.43) and by incorporating radiative cooling - the layer achieves Lorentz factors ~ 3 comparable to those required by observations. Thus radiative feedback induced acceleration plays in important role in regulating the bulk Lorentz factors of both the spine and the layer.

– Pair–loading: If electron positron pairs are present, they decrease the effective mass of the plasma. As a result, the same forces (for non pair loaded plasmas) can accelerate pair loaded plasmas to higher Lorentz factors. Furthermore, even cold pair–loaded plasmas can attain high $\Gamma_{\rm L}$ values as compared to non pair–loaded plasmas, as shown in Fig. 4.14.

– Factors influencing acceleration: the luminosity and the internal energy content of the plasma play a very important role in the acceleration process. In general, the greater

the luminosity the greater the observed acceleration. The same is true for the amount of the internal energy that can be converted into bulk motion by the Compton rocket effect. But this depends critically on the presence of same re–acceleration mechanism, able to maintain the plasma hot. In several scenarios explored, the maximum of the accelerating force occurs outside the active or the standing shock region – when the spine/layer particle observes the entire layer/spine irradiating it and thereby pushing it along the positive z direction. This effect was first noticed while investigating the (rather unrealistic) no cooling scenario (see § 4.41 where cooling was permanently switched off).

Regarding the possibility that the layer can be entirely accelerated by the radiative force, we can conclude that this is possible if the Compton rocket effect remains strong for a sufficiently long time, namely for the time needed to cross the active region $z \sim R$. This requires that $\langle\gamma^2\rangle$ remain large ($\gtrsim 10^4$) within the layer, and this in turn demands continuous injection of fresh energetic leptons throughout the layer length. Electrons–positron pairs can help, but are not crucial, since the maximum number of pairs per proton is limited.

If the magnetic field within the layer is B, we expect that its synchrotron emission peaks at $\nu_{\rm S,L} \sim 3.6\times10^6\gamma_{\rm b}^2 B\delta_{\rm L}$. According to Eq. 6 (with $\gamma_{\rm max} \gg \gamma_{\rm b}$) we have $\gamma_{\rm b}^2 \sim 10^8(\langle\gamma^2\rangle/10^4)^2$ leading to $\nu_{\rm S,L} \sim 3.6\times10^{14}(\langle\gamma^2\rangle/10^4)^2 B\delta_L$ Hz. For $B \sim$1 G, similar to the magnetic field of the spine of blazars in the γ–ray emitting zone (Tavecchio & Ghisellini 2015), we have that layers accelerated radiatively should peak in the optical–UV band, and there should be a relation between their synchrotron peak frequency and their bulk Lorentz factor. The higher $\nu_{\rm S,L}$ the larger $\Gamma_{\rm L}$, and the smaller the relative Γ between the spine and the layer.

On the contrary, if $\nu_{\rm S,L}$ is small, then $\langle\gamma^2\rangle$ is also small, suggesting $\Gamma_{\rm L} \sim 1$. Although the relative Γ approaches $\Gamma_{\rm S}$, the radiative interplay between the two structures should be weak, since the layer cannot produce many seed photons if its $\langle\gamma^2\rangle$ is small.

There is therefore a defined range of $\nu_{\rm S,L}$ where radiative acceleration of the layer can work. If $\nu_{\rm S,L}$ is in the far infrared and we have indications that $\Gamma_{\rm L} \sim 3$ or more, then it is very likely that the layer was not accelerated radiatively, but by the same process that accelerated the spine. The model can thus be tested studying the spectral energy

distribution of blazars and radio–galaxies. The blazars where we can reliably derive the spectral parameters of the layer are still too few to draw any strong conclusions. For radio–galaxies, we should be careful to select those whose observed emission is reliably associated to a layer located in the inner region of the relativistic jets, and not to more extended components. So, the selected sources should show rapid variability indicating a compact emitting region.

We have thus shown how structured spine–sheath jets are radiatively accelerated in the Compton rocket and radiatively driven motion regimes. We have considered different values of Lorentz factors, luminosities and internal energy contents to understand the details of the acceleration process and have been successful in developing some insight and intuition regarding the phenomena. We have also shown that by including radiative feedback (between the spine and the layer), radiative cooling and a realistic energy injection model (the continuous injection scheme within the active region) the observed Lorentz factor of the layer can be reproduced. We have also proposed tests for our model by utilizing layer associated emissions from inner parts of radio-galaxy jets. The range of our obtained Lorentz factors predict that radiatively accelerated layers' synchrotron peak values $\nu_{\rm S,L}$ occur in the IR-optical band.

Acknowledgments

GG and FT acknowledge contribution from a grant PRIN–INAF–2014. AC thanks and appreciates GG and INAF, Brera for their hospitality at Merate, IT.

---

5 GENERAL CONCLUSION

Jets are a commonly occurring astrophysical phenomenon. In my dissertation, I have explored through first principles how the coupling between photons and leptons is of fundamental importance in studying acceleration and emission from relativistic outflows in GRBs and AGNs.

The radiation mechanism responsible for producing the observed GRB prompt emission is still unknown. In Chapter 2, I have tackled the mystery of the unknown radiation mechanism lying at the heart of the GRB prompt emission by performing Monte Carlo simulations in a scattering dominated plasma. I use a self–developed code that incorporates the physical processes of Compton scattering, e^-e^+ production and annihilation, and tracks the energies of leptons and photons as they interact. An energy dissipation event (due to internal shocks or magnetic dissipation) is mimicked by energy injection into the lepton population which brings them out of equilibrium with the radiation. To study the effects of plasma composition I simulate both photon–rich and pair–enriched plasmas.

If the dissipation event occurs at low to moderate opacities (i.e., was sub–photospheric in nature), I find that the transient photon spectra display several non–thermal features, even if the interacting photon and lepton distributions were initially thermally distributed (as suggested by Lazzati and Begelman 2010), but, at different temperatures. In addition to thermal distributions, the study also includes the effect of non–thermal lepton populations on the photon spectra. By fitting the synthetic spectra obtained from the simulations to the empirical Band function (Band et al. 1993 and also see § 1.14), I find them to be in good agreement for 2-3 orders of magnitude of frequency. The simulated spectra can reproduce the Band parameters, i.e., the peak energy $E_{\rm peak}$, high energy spectral index β and especially the low energy spectral index $\alpha = -1$ which earlier works on sub–photospheric dissipation (Giannios 2006; Pe'er et al. 2006) were unable to reproduce. Earlier works (and codes) that modeled sub–photospheric dissipation assumed thermal lepton distributions throughout their modeling and did not account for impulsive or multiple discrete injections. In comparison with these earlier works, I performed simulations with impulsive or multiple discrete injection events. I also find that the pair–enriched simulations show

complex behavior, such as the presence of GeV photons and high–peak energies (higher than typical GRB energies) which offer a promising explanation of the diversity observed in GRBs having high–peak energies. The model shows that spectral correlations exist between the Band function parameters α and β, and between α and $E_{\rm peak}$. These correlations have been detected and discussed in the literature, with contradictory conclusions about their robustness (see Chapter 2). Robust future observations can test the model's validity by searching for these correlations. To summarize, my work shows that Comptonization of photons by sub–photospheric dissipation is a viable mechanism for generating prompt spectra from GRBs, particularly at low to moderate opacities.

The results of Chapter 2 show the importance of tracking lepton energies and that radiation–matter interactions can significantly modify the lepton energies (and also introduce non-thermal features). As the jet is composed of matter, I extend the arguments from Chapter 2 and infer that radiation–matter interactions can therefore influence the kinematic bulk motion of the jet. In Chapter 3, I explore radiative acceleration of jets (specifically GRB jets / fireballs) due to radiation–matter interactions, with the eventual goal of obtaining spectra from such accelerated jets. To quantitatively explore how these interactions accelerate jets and influence spectra, I have developed a time–dependent Monte Carlo code called the Dynamic Monte Carlo code or the *DynaMo* code. The *DynaMo* code simulates Compton scattering driven, radiative acceleration and expansion of plasma in a self–consistent manner. The code tracks the four–momenta of constituent particles (photons, leptons, and protons) and their positions as they interact via Compton scattering. By computing the dynamic time step after each scattering event, the code propagates the individual particles in the plasma and hence can study the bulk motion of the system of particles. The simulation ends when all the photons in the plasma have escaped.

As outlined in Chapter 3, I use the *DynaMo* code to study the evolution of dissipationless GRB fireballs of varying opacities and baryonic content. One of the strengths of my code is that it allows me to study unexplored regimes of fireball evolution that are difficult to study analytically. First and foremost, the simulation results show that embedded radiation can accelerate both baryon–devoid and baryon–loaded plasmas to relativistic speeds. Furthermore, the results (Lorentz factor and temperature evolution during the initial ac-

celeration stages) are in strong agreement with the theoretical proportionality relations of the fireball model. By varying the opacities of the simulated fireballs, I show that increasing the fireball opacity increases the number of photon–electron scatterings, which results in fireballs attaining higher Lorentz factors. This demonstrates how scatterings convert the internal energy in a fireball to kinematic bulk motion.

The most remarkable result that can be gleaned from my study is the discovery of new phases in the evolution of GRB fireballs. The fireball evolution shows a transition region (the region where the fireball's Lorentz factor begins to deviate from the radiation–dominated acceleration phase to the saturation phase where the Lorentz factor achieves a constant value), with an opacity dependent radial extent. In this region, more opaque fireballs transition gradually in comparison to less opaque / transparent ones.

Another significant result is the discovery of a post-photospheric acceleration phase in the previously unexplored region of $R_{\rm ph} < R_{\rm sat}$. In this phase, the terminal Lorentz factors of the simulated fireball are found to be higher than the theoretically computed values of the corresponding fireball. I find that this phase arises because instead of all photons escaping at the theoretical photospheric radius (i.e., when $\tau \sim 1$), only a fraction escape from the fireball. This occurs due to the probabilistic definition of opacity, which is accounted for in the *DynaMo* code. These trapped photons can still scatter and thus provide the extra acceleration leading to a higher than expected Lorentz factor. Intriguingly, I also find that the discrepancy between the theoretical and simulated values starts to decrease for more opaque fireballs. The reason behind this trend is that more opaque fireballs undergo more scatterings and by the time they become transparent the photons have lost more energy. As a result, the fraction that is still trapped is not as energetic as the fraction that was trapped in a less opaque fireball, which cannot provide significant additional acceleration.

The third and final remarkable result is the discovery of another phase of fireball acceleration occurring in the regime $R_{\rm ph} \geq R_{\rm sat}$. Contrary to the relation between the terminal Lorentz factors in the post–photospheric acceleration phase, in this new phase the theoretical terminal Lorentz factors are found to be larger than the simulated values. We attribute this to the fact that high opacity fireballs become matter–dominated while being optically thick, i.e., the energy content of matter exceeds that of radiation (which is still significant). This leads to low energy transfer per scattering between matter and radiation

as the scatterings now occur in the Thomson regime instead of the Compton regime. A large number of such low energy Thomson scatterings are required to transfer the remaining photon energy to further accelerate the fireball. Therefore, this phase is termed the Thomson–dominated phase and I also find that it is this phase that is responsible for the large extent of the transition region / gradual turnover of the Lorentz factor.

I also provide analytical estimates of the radial evolution of the Lorentz factor by curve–fitting the simulated data. This will enable other researchers to deduce jet parameters and provide observational tests for the model. To summarize, my first principles approach to investigate Compton scattering induced radiative acceleration has demonstrated that radiation can accelerate GRB fireballs to relativistic speeds. It provides new insight into GRB fireball evolution by unveiling new evolutionary phases. My results confirm that the radial evolution of the Lorentz factor is significantly different from earlier theoretical models and this opens up several interesting possibilities as to how the photon spectra and light curves will appear from such simulated fireballs.

Chapter 4 addresses the issue of how radiative acceleration can drive the kinematic evolution of individual structures within structured AGN jets. I utilize the resulting dynamics to resolve the puzzle of off–axis GeV emissions from radio galaxies. I consider radiative acceleration via Compton scattering in the simplest structured jet possible - the spine–layer structure. A spine–layer jet consists of an inner and faster moving part (called the spine) which is enveloped by a slower moving layer (or sheath). The goal of the study is to explore how the radiation produced by the spine (layer) can influence the physical properties (such as internal energy, bulk velocity) of the layer (spine). I have explored a comprehensive jet parameter space (jet luminosity, internal energy, initial bulk speed, pair–content) to evaluate their importance to radiative acceleration. I find two primary acceleration regimes - 1) Compton rocket driven: characterized by hotter leptons, extremely large accelerations with the seed photons catalyzing the conversion of internal energy into bulk motion (similar to GRB jets), 2) Radiatively driven / normal Compton scattering driven: characterized by significantly cooler plasmas with the seed photons driving the acceleration process by imparting momentum to the plasma.

My results indicate that the following factors significantly influence the radiative acceleration process -

- Radiative cooling: Radiative cooling decreases the available internal energy content of the leptons and hence determines if the acceleration regime is Compton rocket driven or normal Compton scattering driven. It plays an important role in quenching the acceleration process if the involved luminosities are low to moderate.

- Radiative Feedback: Incorporation of feedback between the spine and the layer has not been explored in any prior work. By incorporating the feedback process, I study self–consistently the evolution of both the spine and the sheath, due to the radiative influence of the sheath and the spine respectively. I find that by limiting the energy injection to active regions of the jets, the layer achieves Lorentz factors of around ~ 3, which is what is required to explain GeV emissions from radio galaxies.

- Pair–Loading: I explore how the presence of pairs can affect the evolution of the structured jet. The pairs lower the effective mass of the plasma and, as a result, the same radiative forces can accelerate the plasma to greater speeds (in comparison to pair devoid plasmas). In addition, I find that the presence of pairs can, to some extent, circumvent the effect of cooling as even cold pair–loaded plasmas can be accelerated to higher Lorentz factors in comparison to cold, pair devoid plasmas.

- The results also demonstrate that the intrinsic jet parameters such as luminosity and the internal energy content play a crucial role in the acceleration process.

I have also explored the possibility of a structured jet arising just by the effects of radiative acceleration, by considering if the layer can be radiatively accelerated from rest just due to the spine's luminosity. My findings indicate that this is possible if the layer plasma remains hot (for the Compton rocket effect to dominate) during the time taken to cross the active region $z \sim R$. This demands that the leptons must remain energized during the crossing period. I propose tests for my model by studying the SEDs of blazars and radio galaxies. My prediction is that the layers of structured jets would peak in the optical–UV band and there should exist a relation between the synchrotron peak frequency and bulk Lorentz factor . To summarize, I have shown that radiative feedback plays a crucial role in the kinematic evolution of structured jets. My results also indicate that by accounting for radiative feedback, energy injection and cooling mechanisms, the layer can be accelerated

from rest to $\Gamma \sim 3$, which is just what is required to explain GeV emissions from misaligned AGNs.

6 BIBLIOGRAPHY

A. A. Abdo, M. Ackermann, M. Ajello, W. B. Atwood, M. Axelsson, L. Baldini, J. Ballet, G. Barbiellini, M. G. Baring, D. Bastieri, K. Bechtol, R. Bellazzini, B. Berenji, E. D. Bloom, E. Bonamente, A. W. Borgland, J. Bregeon, A. Brez, M. Brigida, P. Bruel, T. H. Burnett, G. A. Caliandro, R. A. Cameron, P. A. Caraveo, J. M. Casandjian, E. Cavazzuti, C. Cecchi, Ö. Çelik, A. Chekhtman, C. C. Cheung, J. Chiang, S. Ciprini, R. Claus, J. Cohen-Tanugi, L. R. Cominsky, J. Conrad, S. Cutini, A. de Angelis, F. de Palma, G. Di Bernardo, E. d. C. e. Silva, P. S. Drell, A. Drlica-Wagner, R. Dubois, D. Dumora, C. Farnier, C. Favuzzi, S. J. Fegan, J. Finke, W. B. Focke, P. Fortin, L. Foschini, M. Frailis, Y. Fukazawa, S. Funk, P. Fusco, F. Gargano, D. Gasparrini, N. Gehrels, S. Germani, G. Giavitto, B. Giebels, N. Giglietto, P. Giommi, F. Giordano, T. Glanzman, G. Godfrey, I. A. Grenier, M.-H. Grondin, J. E. Grove, L. Guillemot, S. Guiriec, Y. Hanabata, M. Hayashida, E. Hays, D. Horan, R. E. Hughes, M. S. Jackson, G. Jóhannesson, A. S. Johnson, R. P. Johnson, W. N. Johnson, T. Kamae, H. Katagiri, J. Kataoka, N. Kawai, M. Kerr, J. Knödlseder, M. L. Kocian, M. Kuss, J. Lande, L. Latronico, M. Lemoine-Goumard, F. Longo, F. Loparco, B. Lott, M. N. Lovellette, P. Lubrano, G. M. Madejski, A. Makeev, M. N. Mazziotta, W. McConville, J. E. McEnery, C. Meurer, P. F. Michelson, W. Mitthumsiri, T. Mizuno, A. A. Moiseev, C. Monte, M. E. Monzani, A. Morselli, I. V. Moskalenko, S. Murgia, P. L. Nolan, J. P. Norris, E. Nuss, T. Ohsugi, N. Omodei, E. Orlando, J. F. Ormes, M. Ozaki, D. Paneque, J. H. Panetta, D. Parent, V. Pelassa, M. Pepe, M. Pesce-Rollins, F. Piron, T. A. Porter, S. Rainò, R. Rando, M. Razzano, A. Reimer, O. Reimer, T. Reposeur, L. C. Reyes, S. Ritz, L. S. Rochester, A. Y. Rodriguez, M. Roth, F. Ryde, H. F.-W. Sadrozinski, D. Sanchez, A. Sander, P. M. Saz Parkinson, J. D. Scargle, T. L. Schalk, A. Sellerholm, C. Sgrò, M. S. Shaw, E. J. Siskind, D. A. Smith, P. D. Smith, G. Spandre, P. Spinelli, M. S. Strickman, D. J. Suson, H. Tajima, H. Takahashi, T. Takahashi, T. Tanaka, Y. Tanaka, J. B. Thayer, J. G. Thayer, D. J. Thompson, L. Tibaldo, D. F. Torres, G. Tosti, A. Tramacere, Y. Uchiyama, T. L. Usher, V. Vasileiou, N. Vilchez, V. Vitale, A. P. Waite, P. Wang, B. L. Winer, K. S. Wood, T. Ylinen, and M. Ziegler. Fermi

observations of tev-selected active galactic nuclei. ApJ, 707:1310–1333, Dec. 2009a. doi: 10.1088/0004-637X/707/2/1310.

A. A. Abdo, M. Ackermann, M. Ajello, W. B. Atwood, M. Axelsson, L. Baldini, J. Ballet, G. Barbiellini, D. Bastieri, K. Bechtol, R. Bellazzini, B. Berenji, R. D. Blandford, E. D. Bloom, E. Bonamente, A. W. Borgland, J. Bregeon, A. Brez, M. Brigida, P. Bruel, T. H. Burnett, G. A. Caliandro, R. A. Cameron, A. Cannon, P. A. Caraveo, J. M. Casandjian, E. Cavazzuti, C. Cecchi, Ö. Çelik, E. Charles, C. C. Cheung, J. Chiang, S. Ciprini, R. Claus, J. Cohen-Tanugi, S. Colafrancesco, J. Conrad, L. Costamante, S. Cutini, D. S. Davis, C. D. Dermer, A. de Angelis, F. de Palma, S. W. Digel, D. Donato, E. d. C. e. Silva, P. S. Drell, R. Dubois, D. Dumora, Y. Edmonds, C. Farnier, C. Favuzzi, S. J. Fegan, J. Finke, W. B. Focke, P. Fortin, M. Frailis, Y. Fukazawa, S. Funk, P. Fusco, F. Gargano, D. Gasparrini, N. Gehrels, M. Georganopoulos, S. Germani, B. Giebels, N. Giglietto, P. Giommi, F. Giordano, M. Giroletti, T. Glanzman, G. Godfrey, I. A. Grenier, M.-H. Grondin, J. E. Grove, L. Guillemot, S. Guiriec, Y. Hanabata, A. K. Harding, M. Hayashida, E. Hays, D. Horan, G. Jóhannesson, A. S. Johnson, R. P. Johnson, T. J. Johnson, W. N. Johnson, T. Kamae, H. Katagiri, J. Kataoka, N. Kawai, M. Kerr, J. Knödlseder, M. L. Kocian, M. Kuss, J. Lande, L. Latronico, M. Lemoine-Goumard, F. Longo, F. Loparco, B. Lott, M. N. Lovellette, P. Lubrano, G. M. Madejski, A. Makeev, M. N. Mazziotta, W. McConville, J. E. McEnery, C. Meurer, P. F. Michelson, W. Mitthumsiri, T. Mizuno, A. A. Moiseev, C. Monte, M. E. Monzani, A. Morselli, I. V. Moskalenko, S. Murgia, P. L. Nolan, J. P. Norris, E. Nuss, T. Ohsugi, N. Omodei, E. Orlando, J. F. Ormes, M. Ozaki, D. Paneque, J. H. Panetta, D. Parent, V. Pelassa, M. Pepe, M. Pesce-Rollins, F. Piron, T. A. Porter, S. Rainò, R. Rando, M. Razzano, A. Reimer, O. Reimer, T. Reposeur, S. Ritz, L. S. Rochester, A. Y. Rodriguez, R. W. Romani, M. Roth, F. Ryde, H. F.-W. Sadrozinski, R. Sambruna, D. Sanchez, A. Sander, P. M. Saz Parkinson, J. D. Scargle, C. Sgrò, M. S. Shaw, D. A. Smith, P. D. Smith, G. Spandre, P. Spinelli, M. S. Strickman, D. J. Suson, H. Tajima, H. Takahashi, T. Tanaka, G. B. Taylor, J. B. Thayer, D. J. Thompson, L. Tibaldo, D. F. Torres, G. Tosti, A. Tramacere, Y. Uchiyama, T. L. Usher, V. Vasileiou, N. Vilchez, A. P. Waite, P. Wang, B. L. Winer, K. S. Wood, T. Ylinen, M. Ziegler, D. E. Harris, F. Massaro, and Ł. Stawarz. Fermi large area telescope gamma-ray detection of the radio galaxy m87. ApJ, 707:55–60, Dec.

2009b. doi: 10.1088/0004-637X/707/1/55.

A. A. Abdo, M. Ackermann, M. Ajello, L. Baldini, J. Ballet, G. Barbiellini, D. Bastieri, K. Bechtol, R. Bellazzini, B. Berenji, R. D. Blandford, E. D. Bloom, E. Bonamente, A. W. Borgland, A. Bouvier, T. J. Brandt, J. Bregeon, A. Brez, M. Brigida, P. Bruel, R. Buehler, T. H. Burnett, S. Buson, G. A. Caliandro, R. A. Cameron, A. Cannon, P. A. Caraveo, S. Carrigan, J. M. Casandjian, E. Cavazzuti, C. Cecchi, Ö. Çelik, A. Celotti, E. Charles, A. Chekhtman, A. W. Chen, C. C. Cheung, J. Chiang, S. Ciprini, R. Claus, J. Cohen-Tanugi, S. Colafrancesco, J. Conrad, D. S. Davis, C. D. Dermer, A. de Angelis, F. de Palma, E. d. C. e. Silva, P. S. Drell, R. Dubois, C. Favuzzi, S. J. Fegan, E. C. Ferrara, P. Fortin, M. Frailis, Y. Fukazawa, P. Fusco, F. Gargano, D. Gasparrini, N. Gehrels, S. Germani, N. Giglietto, P. Giommi, F. Giordano, M. Giroletti, T. Glanzman, G. Godfrey, P. Grandi, I. A. Grenier, J. E. Grove, L. Guillemot, S. Guiriec, D. Hadasch, M. Hayashida, E. Hays, D. Horan, R. E. Hughes, M. S. Jackson, G. Jóhannesson, A. S. Johnson, W. N. Johnson, T. Kamae, H. Katagiri, J. Kataoka, J. Knödlseder, M. Kuss, J. Lande, L. Latronico, S.-H. Lee, M. Lemoine-Goumard, M. Llena Garde, F. Longo, F. Loparco, B. Lott, M. N. Lovellette, P. Lubrano, G. M. Madejski, A. Makeev, G. Malaguti, M. N. Mazziotta, W. McConville, J. E. McEnery, P. F. Michelson, G. Migliori, W. Mitthumsiri, T. Mizuno, C. Monte, M. E. Monzani, A. Morselli, I. V. Moskalenko, S. Murgia, M. Naumann-Godo, I. Nestoras, P. L. Nolan, J. P. Norris, E. Nuss, T. Ohsugi, A. Okumura, N. Omodei, E. Orlando, J. F. Ormes, D. Paneque, J. H. Panetta, D. Parent, V. Pelassa, M. Pepe, M. Persic, M. Pesce-Rollins, F. Piron, T. A. Porter, S. Rainò, R. Rando, M. Razzano, S. Razzaque, A. Reimer, O. Reimer, L. C. Reyes, M. Roth, H. F.-W. Sadrozinski, D. Sanchez, A. Sander, J. D. Scargle, C. Sgrò, E. J. Siskind, P. D. Smith, G. Spandre, P. Spinelli, Ł. Stawarz, F. W. Stecker, M. S. Strickman, D. J. Suson, H. Takahashi, T. Tanaka, J. B. Thayer, J. G. Thayer, D. J. Thompson, L. Tibaldo, D. F. Torres, E. Torresi, G. Tosti, A. Tramacere, Y. Uchiyama, T. L. Usher, J. Vandenbroucke, V. Vasileiou, N. Vilchez, M. Villata, V. Vitale, A. P. Waite, P. Wang, B. L. Winer, K. S. Wood, Z. Yang, T. Ylinen, and M. Ziegler. Fermi large area telescope observations of misaligned active galactic nuclei. ApJ, 720:912–922, Sept. 2010. doi: 10.1088/0004-637X/720/1/912.

M. A. Abramowicz, I. D. Novikov, and B. Paczynski. The appearance of highly relativistic, spherically symmetric stellar winds. ApJ, 369:175–178, Mar. 1991. doi: 10.1086/169748.

L. Amati. The $e_{p,i}$-e_{iso} correlation in gamma-ray bursts: updated observational status, re-analysis and main implications. MNRAS, 372:233–245, Oct. 2006. doi: 10.1111/j.1365-2966.2006.10840.x.

Amati, L., Frontera, F., Tavani, M., in 't Zand, J. J. M., Antonelli, A., Costa, E., Feroci, M., Guidorzi, C., Heise, J., Masetti, N., Montanari, E., tnNicastro, L., Palazzi, E., Pian, E., Piro, L., and Soffitta, P. Intrinsic spectra and energetics of bepposax gammaâĂŞray bursts with known redshifts. *A&A*, 390(1):81–89, 2002. doi: 10.1051/0004-6361:20020722. URL https://doi.org/10.1051/0004-6361:20020722.

R. R. J. Antonucci and J. S. Miller. Spectropolarimetry and the nature of ngc 1068. ApJ, 297:621–632, Oct. 1985. doi: 10.1086/163559.

K. Asano, S. Inoue, and P. Mészáros. Prompt x-ray and optical excess emission due to hadronic cascades in gamma-ray bursts. ApJL, 725:L121–L125, Dec. 2010. doi: 10.1088/2041-8205/725/2/L121.

J. M. Attridge, D. H. Roberts, and J. F. C. Wardle. Radio jet-ambient medium interactions on parsec scales in the blazar 1055+018. ApJL, 518:L87–L90, June 1999. doi: 10.1086/312078.

M. Axelsson and L. Borgonovo. The width of gamma-ray burst spectra. MNRAS, 447: 3150–3154, Mar. 2015. doi: 10.1093/mnras/stu2675.

D. Band, J. Matteson, L. Ford, B. Schaefer, D. Palmer, B. Teegarden, T. Cline, M. Briggs, W. Paciesas, G. Pendleton, G. Fishman, C. Kouveliotou, C. Meegan, R. Wilson, and P. Lestrade. Batse observations of gamma-ray burst spectra. i - spectral diversity. ApJ, 413:281–292, Aug. 1993. doi: 10.1086/172995.

V. Beckmann and C. R. Shrader. *Active Galactic Nuclei*. Wiley-VCH Verlag GmbH, Aug. 2012.

A. M. Beloborodov. Collisional mechanism for gamma-ray burst emission. MNRAS, 407: 1033–1047, Sept. 2010. doi: 10.1111/j.1365-2966.2010.16770.x.

A. M. Beloborodov. Radiative transfer in ultrarelativistic outflows. ApJ, 737:68, Aug. 2011. doi: 10.1088/0004-637X/737/2/68.

A. M. Beloborodov. Regulation of the spectral peak in gamma-ray bursts. ApJ, 764:157, Feb. 2013. doi: 10.1088/0004-637X/764/2/157.

E. Berger. The environments of short-duration gamma-ray bursts and implications for their progenitors. New A Rev., 55:1–22, Jan. 2011. doi: 10.1016/j.newar.2010.10.001.

E. Berger. Short-duration gamma-ray bursts. *Annual Review of Astronomy and Astrophysics*, 52(1):43–105, aug 2014. doi: 10.1146/annurev-astro-081913-035926.

K. Beuermann, F. V. Hessman, K. Reinsch, H. Nicklas, P. M. Vreeswijk, T. J. Galama, E. Rol, J. van Paradijs, C. Kouveliotou, F. Frontera, N. Masetti, E. Palazzi, and E. Pian. VLT observations of GRB 990510 and its environment. A&A, 352:L26–L30, Dec. 1999.

R. D. Blandford and R. L. Znajek. Electromagnetic extraction of energy from kerr black holes. MNRAS, 179:433–456, May 1977. doi: 10.1093/mnras/179.3.433.

J. S. Bloom, D. A. Perley, W. Li, N. R. Butler, A. A. Miller, D. Kocevski, D. A. Kann, R. J. Foley, H.-W. Chen, A. V. Filippenko, D. L. Starr, B. Macomber, J. X. Prochaska, R. Chornock, D. Poznanski, S. Klose, M. F. Skrutskie, S. Lopez, P. Hall, K. Glazebrook, and C. H. Blake. Observations of the naked-eye grb 080319b: Implications of nature's brightest explosion. ApJ, 691:723–737, Jan. 2009. doi: 10.1088/0004-637X/691/1/723.

G. R. Blumenthal and R. J. Gould. Bremsstrahlung, synchrotron radiation, and compton scattering of high-energy electrons traversing dilute gases. *Reviews of Modern Physics*, 42:237–271, 1970. doi: 10.1103/RevModPhys.42.237.

G. Bodo, P. Rossi, A. Mignone, S. Massaglia, and A. Ferrari. Deceleration of relativistic jets. New A Rev., 47:557–559, Oct. 2003. doi: 10.1016/S1387-6473(03)00092-7.

Ž. Bošnjak, F. Daigne, and G. Dubus. Prompt high-energy emission from gamma-ray bursts in the internal shock model. A&A, 498:677–703, May 2009. doi: 10.1051/0004-6361/200811375.

J. J. Brainerd. Selection effects and the batse e-peak distribution. In J. Paul, T. Montmerle, and E. Aubourg, editors, *19th Texas Symposium on Relativistic Astrophysics and Cosmology*, Dec. 1998.

A. H. Bridle and R. A. Perley. Extragalactic radio jets. ARA&A, 22:319–358, 1984. doi: 10.1146/annurev.aa.22.090184.001535.

J. M. Burgess. Is spectral width a reliable measure of grb emission physics? *ArXiv e-prints*, May 2017.

J. M. Burgess, F. Ryde, and H.-F. Yu. Taking the band function too far: a tale of two α's. MNRAS, 451:1511–1521, Aug. 2015. doi: 10.1093/mnras/stv775.

J. I. Castor, D. C. Abbott, and R. I. Klein. Radiation-driven winds in of stars. ApJ, 195: 157–174, Jan. 1975. doi: 10.1086/153315.

G. Cavallo and M. J. Rees. A qualitative study of cosmic fireballs and gamma-ray bursts. MNRAS, 183:359–365, May 1978. doi: 10.1093/mnras/183.3.359.

A. Chhotray and D. Lazzati. Gamma-ray burst spectra and spectral correlations from sub-photospheric comptonization. ApJ, 802:132, Apr. 2015. doi: 10.1088/0004-637X/802/2/132.

E. Costa, F. Frontera, J. Heise, M. Feroci, J. in't Zand, F. Fiore, M. N. Cinti, D. Dal Fiume, L. Nicastro, M. Orlandini, E. Palazzi, M. Rapisarda#, G. Zavattini, R. Jager, A. Parmar, A. Owens, S. Molendi, G. Cusumano, M. C. Maccarone, S. Giarrusso, A. Coletta, L. A. Antonelli, P. Giommi, J. M. Muller, L. Piro, and R. C. Butler. Discovery of an x-ray afterglow associated with the γ-ray burst of 28 february 1997. Nature, 387:783–785, June 1997. doi: 10.1038/42885.

P. Crumley and P. Kumar. Hadronic models for large area telescope prompt emission observed in fermi gamma-ray bursts. MNRAS, 429:3238–3251, Mar. 2013. doi: 10.1093/mnras/sts581.

P. A. Curran, A. J. van der Horst, R. A. M. J. Wijers, R. L. C. Starling, A. J. Castro-Tirado, J. P. U. Fynbo, J. Gorosabel, A. S. Jarvinen, D. Malesani, E. Rol, N. R. Tanvir,

K. Wiersema, M. R. Burleigh, S. L. Casewell, P. D. Dobbie, S. Guziy, P. Jakobsson, M. Jelinek, P. Laursen, A. J. Levan, C. G. Mundell, J. Naranen, and S. Piranomonte. GRB 060206 and the quandary of achromatic breaks in afterglow light curves. *Monthly Notices of the Royal Astronomical Society: Letters*, 381(1):L65–L69, oct 2007. doi: 10.1111/j.1745-3933.2007.00368.x.

F. Daigne, Ž. Bošnjak, and G. Dubus. Reconciling observed gamma-ray burst prompt spectra with synchrotron radiation? A&A, 526:A110, Feb. 2011. doi: 10.1051/0004-6361/201015457.

F. D'Ammando, M. Orienti, F. Tavecchio, G. Ghisellini, E. Torresi, M. Giroletti, C. M. Raiteri, P. Grandi, M. Aller, H. Aller, M. A. Gurwell, G. Malaguti, E. Pian, and G. Tosti. Unveiling the nature of the γ-ray emitting active galactic nucleus pks 0521-36. MNRAS, 450:3975–3990, July 2015. doi: 10.1093/mnras/stv909.

W. Deng and B. Zhang. Low energy spectral index and e_p evolution of quasi-thermal photosphere emission of gamma-ray bursts. ApJ, 785:112, Apr. 2014. doi: 10.1088/0004-637X/785/2/112.

G. Drenkhahn and H. C. Spruit. Efficient acceleration and radiation in poynting flux powered GRB outflows. *Astronomy and Astrophysics*, 391(3):1141–1153, sep 2002. doi: 10.1051/0004-6361:20020839.

D. O. Edge, J. R. Shakeshaft, W. B. McAdam, J. E. Baldwin, and S. Archer. A survey of radio sources at a frequency of 159 mc/s. MmRAS, 68:37–60, 1959.

P. G. Edwards and B. G. Piner. The subluminal parsec-scale jet of markarian 501. ApJL, 579:L67–L70, Nov. 2002. doi: 10.1086/345290.

M. Elvis, T. Maccacaro, A. S. Wilson, M. J. Ward, M. V. Penston, R. A. E. Fosbury, and G. C. Perola. Seyfert galaxies as x-ray sources. MNRAS, 183:129–157, Apr. 1978. doi: 10.1093/mnras/183.2.129.

Y.-Z. Fan, D.-M. Wei, F.-W. Zhang, and B.-B. Zhang. The photospheric radiation model for the prompt emission of gamma-ray bursts: Interpreting four observed correlations. ApJL, 755:L6, Aug. 2012. doi: 10.1088/2041-8205/755/1/L6.

B. L. Fanaroff and J. M. Riley. The morphology of extragalactic radio sources of high and low luminosity. MNRAS, 167:31P–36P, May 1974. doi: 10.1093/mnras/167.1.31P.

A. Ferrari. Modeling extragalactic jets. ARA&A, 36:539–598, 1998. doi: 10.1146/annurev.astro.36.1.539.

G. J. Fishman, C. A. Meegan, R. B. Wilson, M. N. Brock, J. M. Horack, C. Kouveliotou, S. Howard, W. S. Paciesas, M. S. Briggs, G. N. Pendleton, T. M. Koshut, R. S. Mallozzi, M. Stollberg, and J. P. Lestrade. The first batse gamma-ray burst catalog. ApJS, 92: 229–283, May 1994. doi: 10.1086/191968.

D. A. Frail, S. R. Kulkarni, L. Nicastro, M. Feroci, and G. B. Taylor. The radio afterglow from the γ-ray burst of 8 may 1997. Nature, 389:261–263, Sept. 1997. doi: 10.1038/38451.

D. A. Frail, S. R. Kulkarni, R. Sari, S. G. Djorgovski, J. S. Bloom, T. J. Galama, D. E. Reichart, E. Berger, F. A. Harrison, P. A. Price, S. A. Yost, A. Diercks, R. W. Goodrich, and F. Chaffee. Beaming in gamma-ray bursts: Evidence for a standard energy reservoir. ApJL, 562:L55–L58, Nov. 2001. doi: 10.1086/338119.

J. Frank, A. King, and D. J. Raine. *Accretion Power in Astrophysics: Third Edition*. Cambridge University Press, Jan. 2002.

A. S. Fruchter, A. J. Levan, L. Strolger, P. M. Vreeswijk, S. E. Thorsett, D. Bersier, I. Burud, J. M. Castro Cerón, A. J. Castro-Tirado, C. Conselice, T. Dahlen, H. C. Ferguson, J. P. U. Fynbo, P. M. Garnavich, R. A. Gibbons, J. Gorosabel, T. R. Gull, J. Hjorth, S. T. Holland, C. Kouveliotou, Z. Levay, M. Livio, M. R. Metzger, P. E. Nugent, L. Petro, E. Pian, J. E. Rhoads, A. G. Riess, K. C. Sahu, A. Smette, N. R. Tanvir, R. A. M. J. Wijers, and S. E. Woosley. Long γ-ray bursts and core-collapse supernovae have different environments. Nature, 441:463–468, May 2006. doi: 10.1038/nature04787.

M. Georganopoulos and D. Kazanas. Relativistic and slowing down: The flow in the hot spots of powerful radio galaxies and quasars. ApJL, 589:L5–L8, May 2003a. doi: 10.1086/375796.

M. Georganopoulos and D. Kazanas. Decelerating flows in tev blazars: A resolution to the bl lacertae-fr i unification problem. ApJL, 594:L27–L30, Sept. 2003b. doi: 10.1086/378557.

G. Ghirlanda, L. Nava, G. Ghisellini, A. Celotti, D. Burlon, S. Covino, and A. Melandri. Gamma-ray bursts in the comoving frame. MNRAS, 420:483–494, Feb. 2012. doi: 10.1111/j.1365-2966.2011.20053.x.

G. Ghisellini. What is the radiative process of the prompt phase of gamma ray bursts? *X-ray Astronomy 2009; Present Status, Multi-Wavelength Approach and Future Perspectives*, 1248:45–48, July 2010. doi: 10.1063/1.3475299.

G. Ghisellini, editor. *Radiative Processes in High Energy Astrophysics*, volume 873 of *Lecture Notes in Physics, Berlin Springer Verlag*, 2013. doi: 10.1007/978-3-319-00612-3.

G. Ghisellini and F. Tavecchio. Compton rockets and the minimum power of relativistic jets. MNRAS, 409:L79–L83, Nov. 2010. doi: 10.1111/j.1745-3933.2010.00952.x.

G. Ghisellini, A. Celotti, and D. Lazzati. Constraints on the emission mechanisms of gamma-ray bursts. MNRAS, 313:L1–L5, Mar. 2000. doi: 10.1046/j.1365-8711.2000.03354.x.

G. Ghisellini, F. Tavecchio, and M. Chiaberge. Structured jets in tev bl lac objects and radiogalaxies. implications for the observed properties. A&A, 432:401–410, Mar. 2005. doi: 10.1051/0004-6361:20041404.

D. Giannios. Prompt emission spectra from the photosphere of a grb. A&A, 457:763–770, Oct. 2006. doi: 10.1051/0004-6361:20065000.

D. Giannios and H. C. Spruit. The role of kink instability in poynting-flux dominated jets. A&A, 450:887–898, May 2006. doi: 10.1051/0004-6361:20054107.

M. Giroletti, G. Giovannini, L. Feretti, W. D. Cotton, P. G. Edwards, L. Lara, A. P. Marscher, J. R. Mattox, B. G. Piner, and T. Venturi. Parsec-scale properties of markarian 501. ApJ, 600:127–140, Jan. 2004. doi: 10.1086/379663.

M. Giroletti, G. Giovannini, G. B. Taylor, and R. Falomo. A sample of low-redshift bl lacertae objects. ii. evn and merlin data and multiwavelength analysis. ApJ, 646:801–814, Aug. 2006. doi: 10.1086/504971.

A. Goldstein, J. M. Burgess, R. D. Preece, M. S. Briggs, S. Guiriec, A. J. van der Horst, V. Connaughton, C. A. Wilson-Hodge, W. S. Paciesas, C. A. Meegan, A. von Kienlin, P. N. Bhat, E. Bissaldi, V. Chaplin, R. Diehl, G. J. Fishman, G. Fitzpatrick, S. Foley, M. Gibby, M. Giles, J. Greiner, D. Gruber, R. M. Kippen, C. Kouveliotou, S. McBreen, S. McGlynn, A. Rau, and D. Tierney. The fermi gbm gamma-ray burst spectral catalog: The first two years. ApJS, 199:19, Mar. 2012. doi: 10.1088/0067-0049/199/1/19.

J. Goodman. Are gamma-ray bursts optically thick? ApJL, 308:L47–L50, Sept. 1986. doi: 10.1086/184741.

R. J. Gould and G. P. Schréder. Pair production in photon-photon collisions. *Physical Review*, 155:1404–1407, Mar. 1967. doi: 10.1103/PhysRev.155.1404.

P. Grandi. Gamma rays from radio galaxies: Fermi/lat observations. In *International Journal of Modern Physics Conference Series*, volume 8 of *International Journal of Modern Physics Conference Series*, pages 25–30, 2012. doi: 10.1142/S2010194512004370.

D. Guetta, M. Spada, and E. Waxman. Efficiency and spectrum of internal gamma-ray burst shocks. ApJ, 557:399–407, Aug. 2001. doi: 10.1086/321543.

S. Guiriec, V. Connaughton, M. S. Briggs, M. Burgess, F. Ryde, F. Daigne, P. Mészáros, A. Goldstein, J. McEnery, N. Omodei, P. N. Bhat, E. Bissaldi, A. Camero-Arranz, V. Chaplin, R. Diehl, G. Fishman, S. Foley, M. Gibby, M. M. Giles, J. Greiner, D. Gruber, A. von Kienlin, M. Kippen, C. Kouveliotou, S. McBreen, C. A. Meegan, W. Paciesas, R. Preece, A. Rau, D. Tierney, A. J. van der Horst, and C. Wilson-Hodge. Detection of a thermal spectral component in the prompt emission of grb 100724b. ApJL, 727:L33, Feb. 2011. doi: 10.1088/2041-8205/727/2/L33.

S. Guiriec, F. Daigne, R. Hascoët, G. Vianello, F. Ryde, R. Mochkovitch, C. Kouveliotou, S. Xiong, P. N. Bhat, S. Foley, D. Gruber, J. M. Burgess, S. McGlynn, J. McEnery, and N. Gehrels. Evidence for a photospheric component in the prompt emission of the short

grb 120323a and its effects on the grb hardness-luminosity relation. ApJ, 770:32, June 2013. doi: 10.1088/0004-637X/770/1/32.

R. Hascoët, F. Daigne, and R. Mochkovitch. Prompt thermal emission in gamma-ray bursts. A&A, 551:A124, Mar. 2013. doi: 10.1051/0004-6361/201220023.

T. M. Heckman. An optical and radio survey of the nuclei of bright galaxies - activity in normal galactic nuclei. A&A, 87:152–164, July 1980.

G. Henri and G. Pelletier. Relativistic electron-positron beam formation in the framework of the two-flow model for active galactic nuclei. ApJL, 383:L7–L10, Dec. 1991. doi: 10.1086/186228.

J. Hjorth and J. S. Bloom. The gamma-ray burst - supernova connection. *Gamma-Ray Bursts, Cambridge Astrophysics Series 51, pp. 169-190 (2012)*, 2011.

C. Hoffmeister. 354 neue veränderliche. *Astronomische Nachrichten*, 236:233, Sept. 1929. doi: 10.1002/asna.19292361502.

J. D. Hunter. Matplotlib: A 2d graphics environment. *Computing in Science & Engineering*, 9(3):90–95, 2007. doi: 10.1109/mcse.2007.55.

H. Ito, S. Nagataki, M. Ono, S.-H. Lee, J. Mao, S. Yamada, A. Pe'er, A. Mizuta, and S. Harikae. Photospheric emission from stratified jets. ApJ, 777:62, Nov. 2013. doi: 10.1088/0004-637X/777/1/62.

H. Ito, S. Nagataki, J. Matsumoto, S.-H. Lee, A. Tolstov, J. Mao, M. Dainotti, and A. Mizuta. Spectral and polarization properties of photospheric emission from stratified jets. ApJ, 789:159, July 2014. doi: 10.1088/0004-637X/789/2/159.

J. M. Jauch and F. Rohrlich. *The Theory of Photons and Electrons. The Relativistic Quantum Field Theory of Charged Particles with Spin One-half (Texts and Monographs in Physics)*. Springer-Verlag, 1980. ISBN 0387072950.

K. Katarzyński, H. Sol, and A. Kus. The multifrequency variability of mrk 421. A&A, 410:101–115, Oct. 2003. doi: 10.1051/0004-6361:20031245.

S. Keren and A. Levinson. Sub-photospheric, radiation-mediated shocks in gamma-ray bursts: Multiple shock emission and the band spectrum. ApJ, 789:128, July 2014. doi: 10.1088/0004-637X/789/2/128.

E. Y. Khachikian and D. W. Weedman. An atlas of seyfert galaxies. ApJ, 192:581–589, Sept. 1974. doi: 10.1086/153093.

M. Kino, F. Takahara, and M. Kusunose. Energetics of tev blazars and physical constraints on their emission regions. ApJ, 564:97–107, Jan. 2002. doi: 10.1086/323363.

R. W. Klebesadel, I. B. Strong, and R. A. Olson. Observations of gamma-ray bursts of cosmic origin. ApJL, 182:L85, June 1973. doi: 10.1086/181225.

S. S. Komissarov. Magnetic acceleration of relativistic jets. Mem. Soc. Astron. Italiana, 82:95, 2011.

A. Konopelko, A. Mastichiadis, J. Kirk, O. C. de Jager, and F. W. Stecker. Modeling the tev gamma-ray spectra of two low-redshift active galactic nuclei: Markarian 501 and markarian 421. ApJ, 597:851–859, Nov. 2003. doi: 10.1086/374593.

S. B. Kraemer, H. R. Schmitt, and D. M. Crenshaw. Probing the ionization structure of the narrow-line region in the seyfert 1 galaxy ngc 4151. ApJ, 679:1128-1143, June 2008. doi: 10.1086/587802.

H. Krawczynski, P. S. Coppi, and F. Aharonian. Time-dependent modelling of the markarian 501 x-ray and tev gamma-ray data taken during 1997 march and april. MNRAS, 336:721–735, Nov. 2002. doi: 10.1046/j.1365-8711.2002.05750.x.

P. Kumar and B. Zhang. The physics of gamma-ray bursts & relativistic jets. Phys. Rep., 561:1–109, Feb. 2015. doi: 10.1016/j.physrep.2014.09.008.

R. A. Laing. Brightness and polarization structure of decelerating relativistic jets. In P. E. Hardee, A. H. Bridle, and J. A. Zensus, editors, *Energy Transport in Radio Galaxies and Quasars*, volume 100 of *Astronomical Society of the Pacific Conference Series*, page 241, 1996.

D. V. Lal, P. Shastri, and D. C. Gabuzda. Seyfert galaxies: Nuclear radio structure and unification. ApJ, 731:68, Apr. 2011. doi: 10.1088/0004-637X/731/1/68.

D. Lazzati. Monte carlo radiation transfer simulations of photospheric emission in long-duration gamma-ray bursts. ApJ, 829:76, Oct. 2016. doi: 10.3847/0004-637X/829/2/76.

D. Lazzati and M. C. Begelman. Universal grb jets from jet-cocoon interaction in massive stars. ApJ, 629:903–907, Aug. 2005. doi: 10.1086/430877.

D. Lazzati and M. C. Begelman. Non-thermal emission from the photospheres of gamma-ray burst outflows. i. high-frequency tails. ApJ, 725:1137–1145, Dec. 2010. doi: 10.1088/0004-637X/725/1/1137.

D. Lazzati, B. J. Morsony, and M. C. Begelman. Very high efficiency photospheric emission in long-duration γ-ray bursts. ApJL, 700:L47–L50, July 2009. doi: 10.1088/0004-637X/700/1/L47.

D. Lazzati, B. J. Morsony, R. Margutti, and M. C. Begelman. Photospheric emission as the dominant radiation mechanism in long-duration gamma-ray bursts. ApJ, 765:103, Mar. 2013. doi: 10.1088/0004-637X/765/2/103.

E.-W. Liang, S.-X. Yi, J. Zhang, H.-J. Lü, B.-B. Zhang, and B. Zhang. Constraining gamma-ray burst initial lorentz factor with the afterglow onset feature and discovery of a tight Γ_0-e $_{gamma,iso}$ correlation. ApJ, 725:2209–2224, Dec. 2010. doi: 10.1088/0004-637X/725/2/2209.

K. R. Lind and R. D. Blandford. Semidynamical models of radio jets - relativistic beaming and source counts. ApJ, 295:358–367, Aug. 1985. doi: 10.1086/163380.

M. Livio. Astrophysical jets: a phenomenological examination of acceleration and collimation. Phys. Rep., 311:225–245, Apr. 1999. doi: 10.1016/S0370-1573(98)00102-1.

N. M. Lloyd and V. Petrosian. Synchrotron radiation as the source of gamma-ray burst spectra. ApJ, 543:722–732, Nov. 2000. doi: 10.1086/317125.

M. S. Longair. *High Energy Astrophysics*. Cambridge University Press, Feb. 2011.

D. López-Cámara, B. J. Morsony, M. C. Begelman, and D. Lazzati. Three-dimensional adaptive mesh refinement simulations of long-duration gamma-ray burst jets inside massive progenitor stars. ApJ, 767:19, Apr. 2013. doi: 10.1088/0004-637X/767/1/19.

D. López-Cámara, B. J. Morsony, and D. Lazzati. Photospheric emission from long-duration gamma-ray bursts powered by variable engines. MNRAS, 442:2202–2207, Aug. 2014. doi: 10.1093/mnras/stu1016.

C. Lundman, A. Pe'er, and F. Ryde. A theory of photospheric emission from relativistic, collimated outflows. MNRAS, 428:2430–2442, Jan. 2013. doi: 10.1093/mnras/sts219.

D. Lynden-Bell. Galactic nuclei as collapsed old quasars. Nature, 223:690–694, Aug. 1969. doi: 10.1038/223690a0.

M. Lyutikov, V. I. Pariev, and R. D. Blandford. Polarization of prompt gamma-ray burst emission: Evidence for electromagnetically dominated outflow. ApJ, 597:998–1009, Nov. 2003. doi: 10.1086/378497.

P. Madau and C. Thompson. Relativistic winds from compact gamma-ray sources. i. radiative acceleration in the klein-nishina regime. ApJ, 534:239–247, May 2000. doi: 10.1086/308738.

F. Massaro and J. E. Grindlay. Spectral evolution of long gamma-ray burst prompt emission: Electrostatic acceleration and adiabatic expansion. ApJL, 727:L1, Jan. 2011. doi: 10.1088/2041-8205/727/1/L1.

A. Mastichiadis and D. Kazanas. The supercritical pile gamma-ray burst model: The prompt to afterglow evolution. ApJL, 694:L54–L58, Mar. 2009. doi: 10.1088/0004-637X/694/1/L54.

J. C. McKinney. General relativistic magnetohydrodynamic simulations of the jet formation and large-scale propagation from black hole accretion systems. MNRAS, 368: 1561–1582, June 2006. doi: 10.1111/j.1365-2966.2006.10256.x.

J. C. McKinney and D. A. Uzdensky. A reconnection switch to trigger gamma-ray burst jet dissipation. MNRAS, 419:573–607, Jan. 2012. doi: 10.1111/j.1365-2966.2011.19721.x.

M. V. Medvedev, S. S. Pothapragada, and S. J. Reynolds. Modeling spectral variability of prompt gamma-ray burst emission within the jitter radiation paradigm. ApJL, 702: L91–L95, Sept. 2009. doi: 10.1088/0004-637X/702/1/L91.

P. Mészáros and M. J. Rees. Steep slopes and preferred breaks in gamma-ray burst spectra: The role of photospheres and comptonization. ApJ, 530:292–298, Feb. 2000. doi: 10.1086/308371.

P. Meszaros, P. Laguna, and M. J. Rees. Gasdynamics of relativistically expanding gamma-ray burst sources - kinematics, energetics, magnetic fields, and efficiency. ApJ, 415: 181–190, Sept. 1993. doi: 10.1086/173154.

P. Mészáros, E. Ramirez-Ruiz, M. J. Rees, and B. Zhang. X-ray-rich gamma-ray bursts, photospheres, and variability. ApJ, 578:812–817, Oct. 2002. doi: 10.1086/342611.

G. Migliori, P. Grandi, E. Torresi, C. Dermer, J. Finke, A. Celotti, R. Mukherjee, M. Errando, F. Gargano, F. Giordano, and M. Giroletti. Implications for the structure of the relativistic jet from multiwavelength observations of ngc 6251. A&A, 533:A72, Sept. 2011. doi: 10.1051/0004-6361/201116808.

A. Mizuta, S. Nagataki, and J. Aoi. Thermal radiation from gamma-ray burst jets. ApJ, 732:26, May 2011. doi: 10.1088/0004-637X/732/1/26.

H. Nagakura, H. Ito, K. Kiuchi, and S. Yamada. Jet propagations, breakouts, and photospheric emissions in collapsing massive progenitors of long-duration gamma-ray bursts. ApJ, 731:80, Apr. 2011. doi: 10.1088/0004-637X/731/2/80.

E. Nakar and T. Piran. Temporal properties of short gamma-ray bursts. MNRAS, 330: 920–926, Mar. 2002. doi: 10.1046/j.1365-8711.2002.05136.x.

L. Nava, G. Ghirlanda, G. Ghisellini, and A. Celotti. Spectral properties of 438 GRBs detected by Fermi/GBM. *Astronomy & Astrophysics*, 530:A21, apr 2011. doi: 10.1051/0004-6361/201016270.

A. Neronov, D. Semikoz, and I. Vovk. Very high-energy γ-ray emission from ic 310. A&A, 519:L6, Sept. 2010. doi: 10.1051/0004-6361/201014499.

S. L. Odell. Radiation force on a relativistic plasma and the eddington limit. ApJL, 243: L147–L149, Feb. 1981. doi: 10.1086/183462.

J. B. Oke and J. E. Gunn. The distance of bl lacertae. ApJL, 189:L5, Apr. 1974. doi: 10.1086/181450.

D. E. Osterbrock. Spectrophotometry of seyfert 1 galaxies. ApJ, 215:733–745, Aug. 1977. doi: 10.1086/155407.

D. E. Osterbrock. Seyfert galaxies with weak broad h alpha emission lines. ApJ, 249: 462–470, Oct. 1981. doi: 10.1086/159306.

B. Paczynski. Gamma-ray bursters at cosmological distances. ApJL, 308:L43–L46, Sept. 1986. doi: 10.1086/184740.

A. Pe'er. Temporal evolution of thermal emission from relativistically expanding plasma. ApJ, 682:463-473, July 2008. doi: 10.1086/588136.

A. Pe'er. Physics of gamma-ray bursts prompt emission. *Advances in Astronomy*, 2015: 907321, 2015. doi: 10.1155/2015/907321.

A. Pe'er and F. Ryde. A theory of multicolor blackbody emission from relativistically expanding plasmas. ApJ, 732:49, May 2011. doi: 10.1088/0004-637X/732/1/49.

A. Pe'er and F. Ryde. Photospheric emission in gamma-ray bursts. 2016.

A. Pe'er and E. Waxman. Prompt gamma-ray burst spectra: Detailed calculations and the effect of pair production. ApJ, 613:448–459, Sept. 2004. doi: 10.1086/422989.

A. Pe'er, P. Mészáros, and M. J. Rees. Peak energy clustering and efficiency in compact objects. ApJ, 635:476–480, Dec. 2005. doi: 10.1086/497360.

A. Pe'er, P. Mészáros, and M. J. Rees. The observable effects of a photospheric component on grb and xrf prompt emission spectrum. ApJ, 642:995–1003, May 2006. doi: 10.1086/501424.

A. Pe'er, H. Barlow, S. O'Mahony, R. Margutti, F. Ryde, J. Larsson, D. Lazzati, and M. Livio. Hydrodynamic properties of gamma-ray burst outflows deduced from the thermal component. ApJ, 813:127, Nov. 2015. doi: 10.1088/0004-637X/813/2/127.

B. M. Peterson. *An Introduction to Active Galactic Nuclei*. Cambridge University Press, Feb. 1997.

B. M. Peterson. Measuring the masses of supermassive black holes. Space Sci. Rev., 183: 253–275, Sept. 2014. doi: 10.1007/s11214-013-9987-4.

B. G. Piner and P. G. Edwards. The parsec-scale structure and jet motions of the tev blazars 1es 1959+650, pks 2155-304, and 1es 2344+514. ApJ, 600:115–126, Jan. 2004. doi: 10.1086/379769.

B. G. Piner and P. G. Edwards. First-epoch vlba imaging of 20 new tev blazars. ApJ, 797: 25, Dec. 2014. doi: 10.1088/0004-637X/797/1/25.

B. G. Piner, N. Pant, and P. G. Edwards. The parsec-scale jets of the tev blazars h1426+428, 1es 1959+650, and pks 2155-304: 2001-2004. ApJ, 678:64-77, May 2008. doi: 10.1086/533521.

B. G. Piner, N. Pant, and P. G. Edwards. The jets of tev blazars at higher resolution: 43 ghz and polarimetric vlba observations from 2005 to 2009. ApJ, 723:1150–1167, Nov. 2010. doi: 10.1088/0004-637X/723/2/1150.

T. Piran. Gamma-ray bursts and the fireball model. Phys. Rep., 314:575–667, June 1999. doi: 10.1016/S0370-1573(98)00127-6.

T. Piran. The physics of gamma-ray bursts. *Reviews of Modern Physics*, 76:1143–1210, Oct. 2004. doi: 10.1103/RevModPhys.76.1143.

R. D. Preece, M. S. Briggs, R. S. Mallozzi, G. N. Pendleton, W. S. Paciesas, and D. L. Band. The synchrotron shock model confronts a "line of death" in the batse gamma-ray burst data. ApJL, 506:L23–L26, Oct. 1998. doi: 10.1086/311644.

R. D. Preece, M. S. Briggs, R. S. Mallozzi, G. N. Pendleton, W. S. Paciesas, and D. L. Band. The batse gamma-ray burst spectral catalog. i. high time resolution spectroscopy of bright bursts using high energy resolution data. ApJS, 126:19–36, Jan. 2000. doi: 10.1086/313289.

Y. Qin, E.-W. Liang, Y.-F. Liang, S.-X. Yi, L. Lin, B.-B. Zhang, J. Zhang, H.-J. Lü, R.-J. Lu, L.-Z. Lü, and B. Zhang. A comprehensive analysis of fermi gamma-ray burst data. iii. energy-dependent t $_{90}$ distributions of gbm grbs and instrumental selection effect on duration classification. ApJ, 763:15, Jan. 2013. doi: 10.1088/0004-637X/763/1/15.

J. L. Racusin, S. V. Karpov, M. Sokolowski, J. Granot, X. F. Wu, V. Pal'shin, S. Covino, A. J. van der Horst, S. R. Oates, P. Schady, R. J. Smith, J. Cummings, R. L. C. Starling, L. W. Piotrowski, B. Zhang, P. A. Evans, S. T. Holland, K. Malek, M. T. Page, L. Vetere, R. Margutti, C. Guidorzi, A. P. Kamble, P. A. Curran, A. Beardmore, C. Kouveliotou, L. Mankiewicz, A. Melandri, P. T. O'Brien, K. L. Page, T. Piran, N. R. Tanvir, G. Wrochna, R. L. Aptekar, S. Barthelmy, C. Bartolini, G. M. Beskin, S. Bondar, M. Bremer, S. Campana, A. Castro-Tirado, A. Cucchiara, M. Cwiok, P. D'Avanzo, V. D'Elia, M. D. Valle, A. de Ugarte Postigo, W. Dominik, A. Falcone, F. Fiore, D. B. Fox, D. D. Frederiks, A. S. Fruchter, D. Fugazza, M. A. Garrett, N. Gehrels, S. Golenetskii, A. Gomboc, J. Gorosabel, G. Greco, A. Guarnieri, S. Immler, M. Jelinek, G. Kasprowicz, V. L. Parola, A. J. Levan, V. Mangano, E. P. Mazets, E. Molinari, A. Moretti, K. Nawrocki, P. P. Oleynik, J. P. Osborne, C. Pagani, S. B. Pandey, Z. Paragi, M. Perri, A. Piccioni, E. Ramirez-Ruiz, P. W. A. Roming, I. A. Steele, R. G. Strom, V. Testa, G. Tosti, M. V. Ulanov, K. Wiersema, R. A. M. J. Wijers, J. M. Winters, A. F. Zarnecki, F. Zerbi, P. Mészáros, G. Chincarini, and D. N. Burrows. Broadband observations of the naked-eye γ-ray burst GRB 080319b. *Nature*, 455(7210):183–188, sep 2008. doi: 10.1038/nature07270.

M. J. Rees and P. Meszaros. Unsteady outflow models for cosmological gamma-ray bursts. ApJL, 430:L93–L96, Aug. 1994. doi: 10.1086/187446.

M. J. Rees and P. Mészáros. Dissipative photosphere models of gamma-ray bursts and x-ray flashes. ApJ, 628:847–852, Aug. 2005. doi: 10.1086/430818.

B. Reipurth and J. Bally. Herbig-haro flows: Probes of early stellar evolution. *Annual Review of Astronomy and Astrophysics*, 39(1):403–455, sep 2001. doi: 10.1146/annurev.astro.39.1.403.

L. Resmi and B. Zhang. Gamma-ray burst prompt emission variability in synchrotron

and synchrotron self-compton light curves. MNRAS, 426:1385–1395, Oct. 2012. doi: 10.1111/j.1365-2966.2012.21531.x.

P. Rossi, A. Mignone, G. Bodo, S. Massaglia, and A. Ferrari. Formation of dynamical structures in relativistic jets: the fri case. A&A, 488:795–806, Sept. 2008. doi: 10.1051/0004-6361:200809687.

G. B. Rybicki and A. P. Lightman. *Radiative Processes in Astrophysics*. John Wiley & Sons Inc, June 1986.

F. Ryde and A. Pe'er. Quasi-blackbody component and radiative efficiency of the prompt emission of gamma-ray bursts. ApJ, 702:1211–1229, Sept. 2009. doi: 10.1088/0004-637X/702/2/1211.

E. E. Salpeter. Accretion of interstellar matter by massive objects. ApJ, 140:796–800, Aug. 1964. doi: 10.1086/147973.

M. Schmidt. 3c 273 : A star-like object with large red-shift. Nature, 197:1040, Mar. 1963. doi: 10.1038/1971040a0.

M. Schmidt. Quasistellar objects. ARA&A, 7:527, 1969. doi: 10.1146/annurev.aa.07.090169.002523.

M. Schmidt and R. F. Green. Quasar evolution derived from the palomar bright quasar survey and other complete quasar surveys. ApJ, 269:352–374, June 1983. doi: 10.1086/161048.

J. L. Schmitt. Bl lac identified as a radio source. Nature, 218:663, May 1968. doi: 10.1038/218663a0.

C. K. Seyfert. Nuclear emission in spiral nebulae. ApJ, 97:28, Jan. 1943. doi: 10.1086/144488.

M. Sikora, H. Sol, M. C. Begelman, and G. M. Madejski. Radiation drag in relativistic active galactic nucleus jets. MNRAS, 280:781–796, June 1996. doi: 10.1093/mnras/280.3.781.

N. Smith and S. P. Owocki. On the role of continuum-driven eruptions in the evolution of very massive stars and population iii stars. ApJL, 645:L45–L48, July 2006. doi: 10.1086/506523.

A. Spitkovsky. On the structure of relativistic collisionless shocks in electron-ion plasmas. ApJL, 673:L39, Jan. 2008. doi: 10.1086/527374.

J. T. Stocke, C. W. Danforth, and E. S. Perlman. Broad lyα emission from three nearby bl lacertae objects. ApJ, 732:113, May 2011. doi: 10.1088/0004-637X/732/2/113.

R. Svensson. Electron-positron pair equilibria in relativistic plasmas. ApJ, 258:335, July 1982. doi: 10.1086/160082.

M. R. Swain, A. H. Bridle, and S. A. Baum. Internal structure of the jets in 3c 353. ApJL, 507:L29–L33, Nov. 1998. doi: 10.1086/311663.

F. Tavecchio and G. Ghisellini. Spine-sheath layer radiative interplay in subparsec-scale jets and the tev emission from m87. MNRAS, 385:L98–L102, Mar. 2008. doi: 10.1111/j.1745-3933.2008.00441.x.

F. Tavecchio and G. Ghisellini. 3c 66b as a tev radio galaxy. MNRAS, 394:L131–L135, Mar. 2009. doi: 10.1111/j.1745-3933.2009.00629.x.

F. Tavecchio and G. Ghisellini. On the spine-layer scenario for the very high-energy emission of ngc 1275. MNRAS, 443:1224–1230, Sept. 2014. doi: 10.1093/mnras/stu1196.

F. Tavecchio, L. Maraschi, E. Pian, L. Chiappetti, A. Celotti, G. Fossati, G. Ghisellini, E. Palazzi, C. M. Raiteri, R. M. Sambruna, A. Treves, C. M. Urry, M. Villata, and A. Djannati-Ataï. Theoretical implications from the spectral evolution of markarian 501 observed with bepposax. ApJ, 554:725–733, June 2001. doi: 10.1086/321394.

F. Tavecchio, G. Ghisellini, G. Ghirlanda, L. Foschini, and L. Maraschi. Tev bl lac objects at the dawn of the fermi era. MNRAS, 401:1570–1586, Jan. 2010. doi: 10.1111/j.1365-2966.2009.15784.x.

F. Tavecchio, G. Ghisellini, and D. Guetta. Structured jets in bl lac objects: Efficient pev neutrino factories? ApJL, 793:L18, Sept. 2014. doi: 10.1088/2041-8205/793/1/L18.

A. Tchekhovskoy, R. Narayan, and J. C. McKinney. Efficient generation of jets from magnetically arrested accretion on a rapidly spinning black hole. MNRAS, 418:L79–L83, Nov. 2011. doi: 10.1111/j.1745-3933.2011.01147.x.

S. van der Walt, S. C. Colbert, and G. Varoquaux. The NumPy array: A structure for efficient numerical computation. *Computing in Science & Engineering*, 13(2):22–30, mar 2011. doi: 10.1109/mcse.2011.37.

D. E. Vanden Berk, G. T. Richards, A. Bauer, M. A. Strauss, D. P. Schneider, T. M. Heckman, D. G. York, P. B. Hall, X. Fan, G. R. Knapp, S. F. Anderson, J. Annis, N. A. Bahcall, M. Bernardi, J. W. Briggs, J. Brinkmann, R. Brunner, S. Burles, L. Carey, F. J. Castander, A. J. Connolly, J. H. Crocker, I. Csabai, M. Doi, D. Finkbeiner, S. Friedman, J. A. Frieman, M. Fukugita, J. E. Gunn, G. S. Hennessy, Ž. Ivezić, S. Kent, P. Z. Kunszt, D. Q. Lamb, R. F. Leger, D. C. Long, J. Loveday, R. H. Lupton, A. Meiksin, A. Merelli, J. A. Munn, H. J. Newberg, M. Newcomb, R. C. Nichol, R. Owen, J. R. Pier, A. Pope, C. M. Rockosi, D. J. Schlegel, W. A. Siegmund, S. Smee, Y. Snir, C. Stoughton, C. Stubbs, M. SubbaRao, A. S. Szalay, G. P. Szokoly, C. Tremonti, A. Uomoto, P. Waddell, B. Yanny, and W. Zheng. Composite quasar spectra from the sloan digital sky survey. AJ, 122:549–564, Aug. 2001. doi: 10.1086/321167.

T. Vuillaume, G. Henri, and P.-O. Petrucci. Variation of bulk lorentz factor in agn jets due to compton rocket in a complex photon field. A&A, 581:A18, Sept. 2015. doi: 10.1051/0004-6361/201525972.

S. J. Wagner and A. Witzel. Intraday variability in quasars and bl lac objects. ARA&A, 33:163–198, 1995. doi: 10.1146/annurev.aa.33.090195.001115.

S. Weinberg. *Gravitation and Cosmology: Principles and Applications of the General Theory of Relativity*. John Wiley & Sons Inc, July 1972.

S. Woosley and J. Bloom. The supernova–gamma-ray burst connection. *Annual Review of Astronomy and Astrophysics*, 44(1):507–556, sep 2006. doi: 10.1146/annurev.astro.43.072103.150558.

D. Yonetoku, T. Murakami, T. Nakamura, R. Yamazaki, A. K. Inoue, and K. Ioka. Gamma-

ray burst formation rate inferred from the spectral peak energy-peak luminosity relation. ApJ, 609:935–951, July 2004. doi: 10.1086/421285.

H.-F. Yu, R. D. Preece, J. Greiner, P. Narayana Bhat, E. Bissaldi, M. S. Briggs, W. H. Cleveland, V. Connaughton, A. Goldstein, A. von Kienlin, C. Kouveliotou, B. Mailyan, C. A. Meegan, W. S. Paciesas, A. Rau, O. J. Roberts, P. Veres, C. Wilson-Hodge, B.-B. Zhang, and H. J. van Eerten. The fermi gbm gamma-ray burst time-resolved spectral catalog: brightest bursts in the first four years. A&A, 588:A135, Apr. 2016. doi: 10.1051/0004-6361/201527509.

L. Zampieri, R. Turolla, L. Foschini, and A. Treves. Radiative acceleration and transient, radiation-induced electric fields. ApJ, 592:368–377, July 2003. doi: 10.1086/375702.

Y. B. Zel'dovich. The fate of a star and the evolution of gravitational energy upon accretion. *Soviet Physics Doklady*, 9:195, Sept. 1964.

B. Zhang and P. Mészáros. An analysis of gamma-ray burst spectral break models. ApJ, 581:1236–1247, Dec. 2002. doi: 10.1086/344338.

B. Zhang and H. Yan. The internal-collision-induced magnetic reconnection and turbulence (icmart) model of gamma-ray bursts. ApJ, 726:90, Jan. 2011. doi: 10.1088/0004-637X/726/2/90.

B.-B. Zhang, B. Zhang, E.-W. Liang, Y.-Z. Fan, X.-F. Wu, A. Pe'er, A. Maxham, H. Gao, and Y.-M. Dong. A comprehensive analysis of fermi gamma-ray burst data. i. spectral components and the possible physical origins of lat/gbm grbs. ApJ, 730:141, Apr. 2011. doi: 10.1088/0004-637X/730/2/141.

Appendices

A Time Step Calculation Details

In this section we detail our calculation of the DynaMo code's dynamic time step. We begin with a discussion of the opacity experienced by a photon immersed in a collection of scatterers at rest. We use this opacity to calculate the mean free path for a single photon. We then extend this analysis to calculate the opacity of a medium containing several photons and the mean free time of this population of photons.
We then detail how to incorporate the motion of scatterers into the opacity and mean free time calculations. As before, we derive the expression for mean free time for a single photon immersed among scatterers in motion. We use this result to find the mean free time for a population of photons in a moving medium.

A1 For scatterers at rest

Using eq. 3.8 (which is valid for scatterers at rest) as the defining equation of opacity, the mean free path ($l_{\rm mf}$) traversed by the photon can be computed to be –

$$l_{mf} = \frac{1}{n\sigma_T}. \tag{6.1}$$

We take advantage of the constancy of the speed of light to obtain the mean free time $t_{\rm mf}$ as –

$$t_{\rm mf} = \frac{1}{nc\sigma_T}. \tag{6.2}$$

The reader should note that this is the *mean* or *average* time that the photon travels between scatterings. For a medium containing $N_{\rm p}$ photons, the total infinitesimal opacity can be obtained by summing the individual contribution from each photon –

$$d\tau_{\rm Pop} = \sum_{i=1}^{N_{\rm p}} d\tau_i = \sum_{i=1}^{N_{\rm p}} n\sigma_T dl_i = n\sigma_T \sum_{i=1}^{N_{\rm p}} dl_i = n\sigma_T l_{\rm mf,Pop} N_{\rm p}, \tag{6.3}$$

where the subscript Pop is used for population and $l_{\rm mf,Pop}$ denotes the mean free path for the photon population. Similar to eq. 6.1, we can express the mean free path of the entire

population as –

$$l_{\rm mf,Pop} = \frac{1}{n\sigma_T N_{\rm p}} = \frac{l}{N_{\rm p}}. \tag{6.4}$$

The mean free time for this population can be computed to be –

$$t_{\rm Pop} = \frac{l_{\rm mf,Pop}}{c} = \frac{1}{N_{\rm p} cn\sigma_T} = \frac{t_{\rm mf}}{N_{\rm p}}. \tag{6.5}$$

A2 For scatterers in motion

In this section we derive the opacity and mean quantities when the scatterers in the medium are moving (i.e., the medium itself is moving) and compare them with the same quantities obtained when the scatterers are at rest. We begin with the case of just a single photon and then extend our calculation to a system containing multiple photons.

Consider the case where each of the scatterers travel at a unique velocity and hence contribute uniquely to the opacity. The differential opacity seen by a photon due to scatterers traveling at a distinct velocity given by $\vec{\beta_{\rm k}}$ is (see Abramowicz et al. 1991) –

$$d\tau_{\rm k} = n_{\rm k}\sigma_T(1 - \vec{\beta_{\rm k}}.\hat{r})dl \tag{6.6}$$

$$d\tau_{\rm k} = n_{\rm k}\sigma_T(1 - \beta_{\rm k}\cos\theta_{\rm k})dl \tag{6.7}$$

where $n_{\rm k}$ denotes the number density of scatterers traveling in the $k^{\rm th}$ direction with a speed $\beta_{\rm k}$, $\hat{r}$ is the unit vector along the direction of propagation of the photon and $\theta_{\rm k}$ is the angle between the photon's direction of propagation and $k^{\rm th}$ direction.

The total opacity as observed by the photon will be the sum of the opacities due to each individual scatterer and can be written as –

$$d\tau = \sum_k \tau_{\rm k} = \sum_k n_{\rm k}\sigma_T(1 - \vec{\beta_{\rm k}}.\hat{r})dl \tag{6.8}$$

$$d\tau = \sum_k \tau_{\rm k} = \sum_k n_{\rm k}\sigma_T(1 - \beta_{\rm k}\cos\theta_{\rm k})dl \tag{6.9}$$

where $\sum_k$ denotes the sum over the directions and speeds associated with the scatterers. These expressions can be used to write the mean free time experienced by a photon traveling through a moving medium as –

$$t_{mf} = \frac{1}{\sum_k n_{\rm k} c\sigma_T(1 - \beta_{\rm k}\cos\theta_{\rm k})}. \tag{6.10}$$

The reader should note that on comparison with a medium at rest, the photon observes a decrease in opacity (and an increase in the mean free time) if it moves along the direction of motion of the scatterer. For motion anti-parallel to the scatterer's motion, an increase in opacity is experienced and as a consequence, the mean free time is reduced.

If the total number of scatterers (say leptons) is fixed and denoted by the number N_e, we can re-write eq. 6.9 by eliminating n_k as –

$$d\tau = \frac{\sum_k^{N_e} \sigma_T(1-\beta_{\rm k}\cos\theta_{\rm k})}{V} dl, \tag{6.11}$$

where V denotes the volume occupied by the scatterers. Re-writing the mean free time obtained in eq. 6.10, we obtain –

$$t_{\rm mf} = \frac{l_{\rm mf}}{c} = \frac{V}{\sigma_T c \sum_{k=1}^{N_e}(1-\beta_{\rm k}\cos\theta_{\rm k})}. \tag{6.12}$$

Let us now extend the above analysis to the most general scenario – a plasma containing N_p photons and N_e leptons (which play the role of scatterers), and each lepton can be in motion. Similar to the calculation performed in Appendix A1, the opacity experienced by the $i^{\rm th}$ photon due to *any* lepton traveling along the $j^{\rm th}$ direction is –

$$d\tau_{\rm i,j} = \frac{\sigma_T(1-\beta_{\rm j}\cos\theta_{\rm ij})}{V} dl. \tag{6.13}$$

Using eqs. 6.12 and 6.13, the mean free time for the interaction between $i^{\rm th}$ photon – $j^{\rm th}$ lepton pair becomes –

$$t_{\rm i,j} = \frac{l_{\rm ij}}{c} = \frac{V}{\sigma_T c(1-\beta_{\rm j}\cos\theta_{\rm ij})}. \tag{6.14}$$

Using eq. 6.12 and 6.14, the mean free time experienced by the $i^{\rm th}$ photon as it interacts with all N_e leptons is –

$$t_{\rm i} = \frac{V}{\sum_{j=1}^{N_e}\sigma_T(1-\beta_{\rm j}\cos\theta_{\rm ij})c} = \frac{V}{\sigma_T c}\frac{1}{\sum_j(1-\beta_{\rm j}\cos\theta_{\rm ij})} = \frac{1}{\sum_j\left(\frac{1}{t_{\rm ij}}\right)}. \tag{6.15}$$

Most generally, the net infinitesimal opacity of the photon population can be written as –

$$d\tau_{\rm net} = \sum_{i=1}^{N_p} d\tau_{\rm i} = \sum_{i=1}^{N_p}\sum_{j=1}^{N_e}\frac{\sigma_T(1-\beta_{\rm j}\cos\theta_{\rm ij})dl}{V}. \tag{6.16}$$

The use of eqs. 6.12 and 6.16 provides us with the mean free time for the entire population, which is –

$$t_{\rm mf,Pop} = \frac{V}{\sigma_T c}\frac{1}{\sum_i\sum_j(1-\beta_{\rm j}\cos\theta_{\rm ij})} = \frac{1}{\sum_i\sum_j\left(\frac{1}{t_{\rm ij}}\right)} = \frac{1}{\sum_i\left(\frac{1}{t_{\rm i}}\right)}. \tag{6.17}$$

B Radius and Bulk Lorentz Factor Calculation

As stated in § 3.31, in order to characterize fireball evolution the bulk motion parameters are required. These parameters include the fireball's radius R, bulk Lorentz factor Γ and the temperature T' measured in the frame comoving with the fireball. In this section we illustrate how we compute the fireball's radius and bulk Lorentz factor from the individual positions and momenta of the matter particles (leptons). In other words, we show how to find the radius and velocity of the Center of Momentum (COM) frame associated with the system of particles.

As the simulated fireball is a thin–shell, its constituent particles are distributed within the shell's finite width. Let us denote the i^{th} particle's position as r_i and velocity v_i. Generally, the particles do not travel along the radial direction (which lies along the $\hat{z}$ direction as explained in § 3.3) because our simulation's origin is not coincident with each particle's position. As a consequence, we can resolve each particle's net velocity parallel and perpendicular to the radial vector at the particle's location. The radial components will contribute to the bulk motion whereas the non–radial components will provide us with a means to measure the temperature of the particles. The radial component of the velocity can be written as –

$$v_{\rm rad,i} = \vec{v_i}.\hat{z}. \tag{6.18}$$

In general, the radial direction at each particle's position $\vec{r_i}$ is different. However, if the angular size of the shell (in other words, the opening angle of our simulated fireball) is small then the positions of all particles lie within a narrow cone, and their radial vectors are approximately aligned. Using eq. 6.18, we can compute the radial Lorentz factor as –

$$\gamma_{\rm rad,i} = \frac{1}{\sqrt{1 - \frac{v^2_{\rm rad,i}}{c^2}}}. \tag{6.19}$$

The radius of the fireball R (or the radius of the COM) can be computed from the positions of the constituent particles as –

$$R = \frac{\sum_i \gamma_{\rm rad,i} \vec{r_i}.\hat{r_i}}{\sum_i \gamma_{\rm rad,i}}. \tag{6.20}$$

To calculate the bulk Lorentz factor Γ, we start with the equation for total momentum of the system which gives us –

$$\Gamma MV = \sum_i \gamma_{\rm rad,i} m_i v_{\rm rad,i} \tag{6.21}$$

where $V = c\sqrt{1 - 1/\Gamma^2}$. This equation can be simplified to –

$$\Gamma\beta = \frac{\sum_i \gamma_{\rm rad,i} m_i \beta_{\rm rad,i}}{M} = \frac{\sum_i \gamma_{\rm rad,i} \beta_{\rm rad,i}}{N}, \tag{6.22}$$

where we $\beta = V/c$, $\beta_{\rm rad,i} = v_{\rm rad,i}/c$ and $M = \sum_i^N m_i = Nm$. Using the relation $(\Gamma\beta)^2 = \Gamma^2 - 1$, we can find the bulk Lorentz factor from the radial Lorentz factors of individual particles as –

$$\Gamma = \sqrt{\left(\frac{\sum_i \gamma_{\rm rad,i}\beta_{\rm rad,i}}{N}\right)^2 + 1}. \tag{6.23}$$

C Comoving Temperature Calculation

As the fireball accelerates and expands, it uses internal energy to fuel its bulk kinetic motion. The temperature of an object is a measure of the internal energy (attributed to random kinetic energy) content of that object. The net motion of the particles forming the fireball, in particular, the matter (e.g., leptons) – is a composite of bulk motion (due to outward directed radiative acceleration) and random motion (due to temperature). Thus, determination of particles' temperature depends upon the particles' random speeds which can be correctly calculated only after accounting for their bulk velocity. As a result, we need to calculate the velocities of the particles as observed in the comoving frame and compute the temperature in that frame.

As discussed in section 3.32, the fireball is a thin spherical shell that is expanding radially outward. The constituent particles of this shell are distributed randomly within the shell and interact with other particles in the shell. The radial speed of the center of mass can be computed as –

$$V_{\rm COM} = \frac{\sum_i \gamma_i m_i v_{i,rad}}{\sum_i \gamma_i m_i}, \tag{6.24}$$

where $v_{\rm i,rad}$, γ_i and m_i are the radial speed, Lorentz factor, and mass respectively, of the i^{th} lepton and are defined in Appendix B. Due to the small opening angle of our simulated fireball, the COM velocity (bulk velocity) can be written as –

$$\vec{V}_{\rm COM} = V_{\rm COM}\hat{z}. \tag{6.25}$$

Using this bulk velocity, we can Lorentz transform the four–momenta of the particle to the COM frame. This transformation removes the radial–bulk motion component from the particle momentum, leaving behind the momentum only due to random motion. Let us denote the random velocity of the i^{th} lepton (as measured in the COM frame) by $v'_{\rm i/COM}$. The Lorentz factor associated with this random motion is –

$$\gamma'_{\rm i/COM} = \frac{1}{\sqrt{1-\frac{v'^2_{\rm i/COM}}{c^2}}}. \tag{6.26}$$

The average random kinetic energy or internal energy (denoted by $< KE' >$) of the system can be computed as –

$$< KE' >= \frac{\sum_{i=0}^{\rm N_e} KE'_i}{\rm N_e} = \sum_{i=0}^{\rm N_e} \frac{\left(< \gamma'_{\rm i/COM} > -1\right) mc^2}{N_{\rm e}}, \tag{6.27}$$

where KE'_i is the random kinetic energy of the i^{th} lepton and $\rm N_e$ denotes the total number of leptons present in the fireball. As the average kinetic energy and temperature are related by –

$$< KE' > \simeq 3k_B T', \tag{6.28}$$

the average temperature T' of the leptons can be computed as –

$$T' \simeq \frac{\sum_{i=0}^{\rm N_e} \left(< \gamma'_{\rm i/COM} > -1\right) mc^2}{3k_B N_{\rm e}}, \tag{6.29}$$

where k_B denotes the Boltzmann's constant.

D Code Tests

D1 Temperature Evolution

This section explores the evolution of comoving temperature T' (as measured in the jet frame) with the radius of the fireball. Figure 6.1 depicts the comoving temperature evolu-

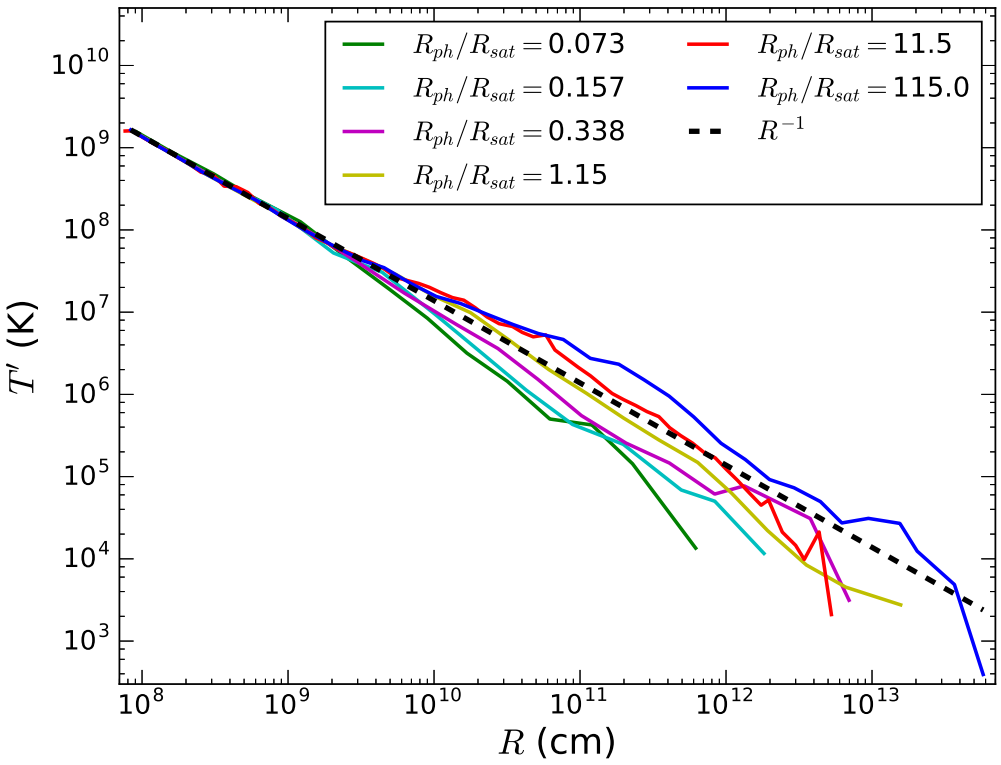

FIGURE 6.1: Evolution of the comoving temperature with the fireball radius. Each colored curve represents a fireball that begins evolution with a unique initial opacity. Also shown (by the dashed line) are the fireball model's theoretical predictions during the radiation–dominated acceleration phase.

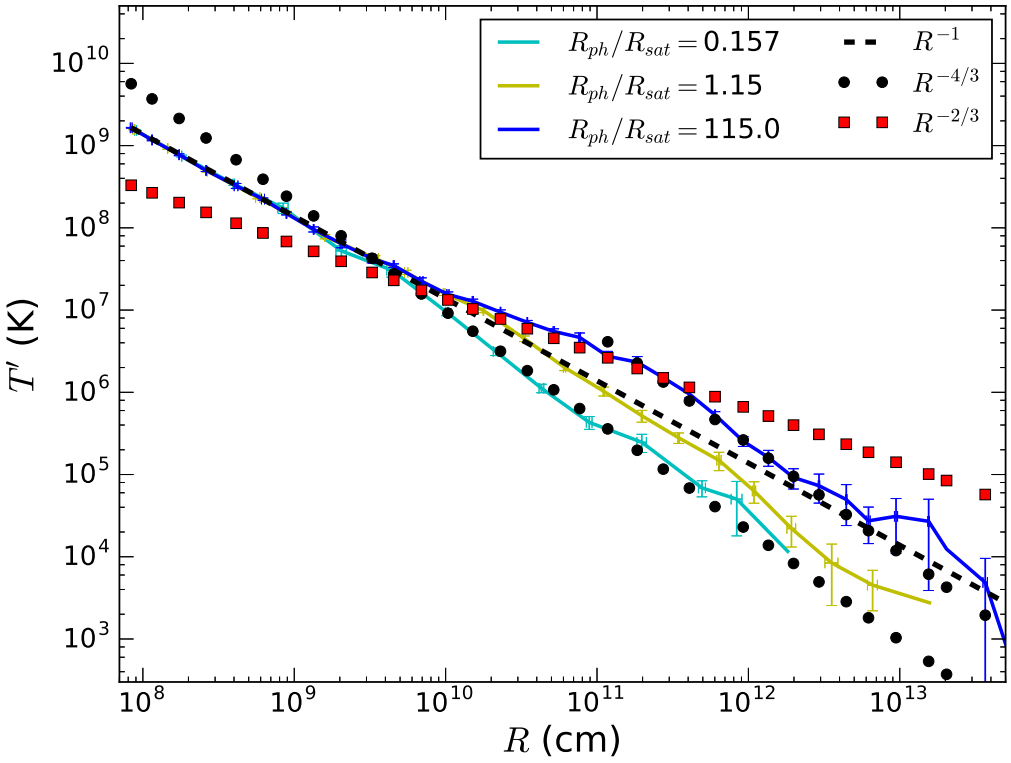

FIGURE 6.2: Comoving temperature evolution with radius for fireballs with $R_{\rm ph}/R_{\rm sat} = 0.157, 1.15$ & 115. The black circles depict a line that decays proportionally to $R^{-4/3}$, the red squares depict a decay proportional to $R^{-2/3}$, and the black dashed line represents a curve evolving proportionally to R^{-1}. The deviations of the evolutionary trajectories from the theoretical predictions are discussed in § D1. Also plotted are the error bars for the simulations computed from their standard deviation.

tion of baryon–free fireballs, parameterized by their different initial opacities (as discussed earlier in § 3.4, baryon–loaded fireball evolution is similar to the evolution of baryon–free fireballs, and hence the results of one hold true for the other). Fig. 6.1 shows that during the radiation–dominated acceleration phase the comoving temperature of all fireballs grows proportionally to R^{-1}, thus verifying the fireball model's proportionality relations (see eq. 3.2). The fireballs deviate from $T' \propto R^{-1}$ path when the radiation dominance ends (as discussed in § 3.4). However, from Fig. 6.1 we note that fireballs deviate differently depending upon their initial opacity.

Figure 6.2 investigates these deviations in greater detail. Similar to Fig. 6.1, Fig. 6.2 plots the comoving temperature with the fireball radius, but only for three fireballs (instead of six) characterized by $R_{\rm ph}/R_{\rm sat} = 0.157, 1.15$ & 115.0. Only three fireballs are plotted to improve clarity and develop a better understanding of the comoving temperature deviations. For each fireball displayed in Fig. 6.2, the transition from the radiation–dominated phase to the transient phase produces different evolutionary relationships between T' and R. If the fireball transitions from quadrant 1 to 3 via 2 (see Fig. 3.7, during the post–photospheric acceleration phase) the reduced optical depth causes radiation to decouple. As a result, the cyan curve (the least optically thick of the plotted fireballs) drops below the $T' \propto R^{-1}$ dashed line, and begins to evolve along the black dotted circles representing $T' \propto R^{-4/3}$ path.

The blue curve follows a different evolutionary path, a consequence of the blue fireball transitioning from quadrant 1 to 3 via quadrant 4 (see Fig. 3.7). The blue curve represents a highly opaque fireball that achieves matter domination before transparency, and as a result, undergoes the Thomson–dominated acceleration phase (see § 3.4). This results in the average lepton energy exceeding the photon energy and the fireball accelerates (as well as cools) gradually such that $T' \propto R^{-2/3}$. During the matter–dominated phase, the blue curve in Fig. 6.2 jumps above the $T' \propto R^{-1}$ dashed line, and follows the red squares. However, when the fireball eventually enters the optically thin regime (transitioning from quadrant 4 to 3) it begins following the black circles.

The yellow curve represents a fireball ($R_{\rm ph}/R_{\rm sat} = 1.15$) that is comparatively optically thick than the cyan one. As a result, its initial deviation (from the radiation–dominated phase) is similar to blue curve than the cyan curve. Fig. 3.7 shows that the yellow curve

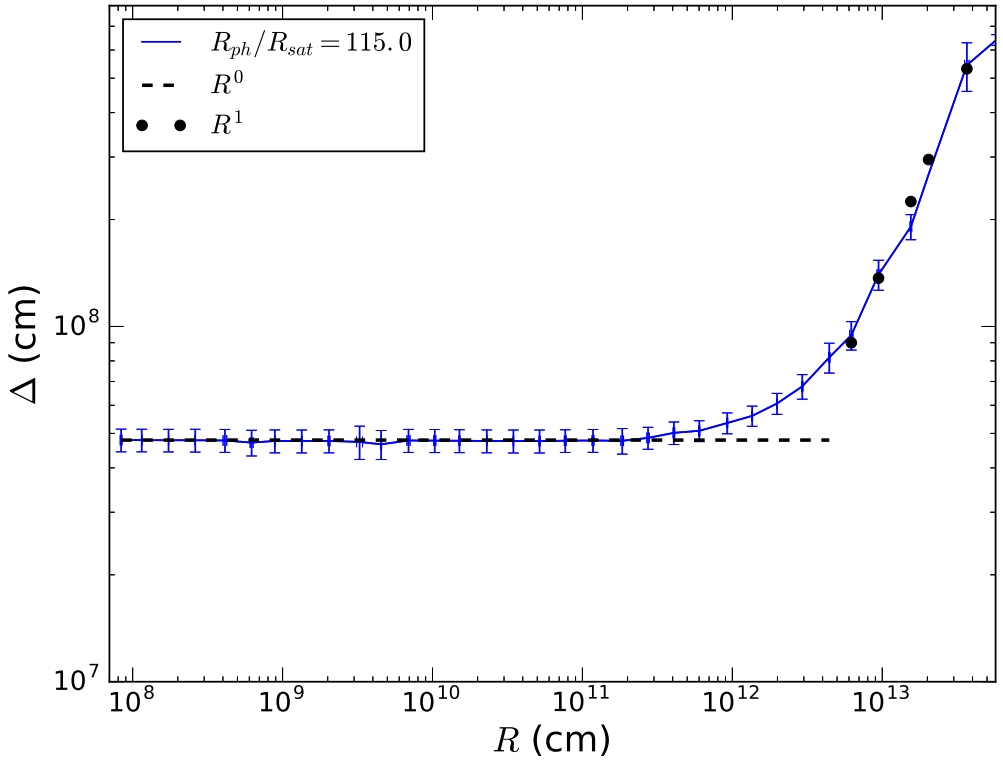

FIGURE 6.3: Evolution of the width of a fireball shell (for $R_{\rm ph}/R_{\rm sat} = 115$) as the fireball expands. As predicted by theory, the shell maintains a constant width during the acceleration phase.

becomes matter–dominated before becoming optically thin, and transitions from quadrant 1 to 3 via 4. As a result, the yellow curve jumps over the $T' \propto R^{-1}$ (dashed) line just like the blue curve, but only slightly. As the fireball represented by the yellow curve is not as optically thick as the one represented by the blue curve, the yellow curve becomes optically thin at a comparatively smaller radius. As a result, it drops below the $T' \propto R^{-1}$ line earlier than the blue fireball, and begins evolving along the black circles. Thus, we find that the fireball's transient phases can explain the temperature evolution and its deviation from $T' \propto R^{-1}$ proportionality relation.

D2 Shell Width Evolution

Meszaros et al. (1993) found that the width of a fireball shell in the lab–frame remains constant during the radiation–dominated acceleration phase. The shell starts expanding proportionally to R during the matter–dominated phase. Figure 6.3 depicts the evolution

of the width of the shell Δ in the lab frame and its evolution with the fireball radius, and it shows that the model is in agreement with the theory barring the transition phase.

D3 Restarted Simulations

As shown in § 3.4, the DynaMo code reproduces the proportionality relations of the fireball model (see eq. 3.2). A powerful feature of the code is the ability to start (or restart) the simulations at a specific point along the simulation (positions and four–momenta of particles are all that is required to initialize the simulation). In this section we discuss the results obtained by restarting a completed simulation at a specific point along its evolution and compare them with the results of the original simulation.
The simulations we are considering in this section are specified by $R_{\rm ph}/R_{\rm sat} = 0.157$ (see Fig. 3.3). The specific data point along the evolution which we use for the starting conditions for the 'restarted simulation' refers to the point when the bulk Lorentz factor of the original simulation equals 3. As shown in Figs. 6.4 and 6.5, the two simulations evolve consistently as expected, and both simulations are in agreement with the proportionality relations of the fireball model.

E Calculation of the R_{ph} and R_{sat}

A relativistically expanding fireball achieves saturation when all its internal energy is converted into bulk motion, and as a result its bulk Lorentz factor achieves the maximum possible value. Using the fireball initialization parameters defined in § 3.32, the maximum Lorentz factor achieved at saturation in our simulation is $\eta \sim 112.9$. In this section we calculate the photospheric radius $R_{\rm ph}$ in terms of the parameters defined in § 3.32. As the photospheric radius evolves differently during the acceleration and saturation phases of the fireball evolution, therefore we consider two cases: 1) the fireball attains the photospheric radius before saturation, i.e., $R_{\rm ph} < R_{\rm sat}$ and 2) when fireball achieves saturation before reaching the photospheric radius $R_{\rm ph} \geq R_{\rm sat}$.

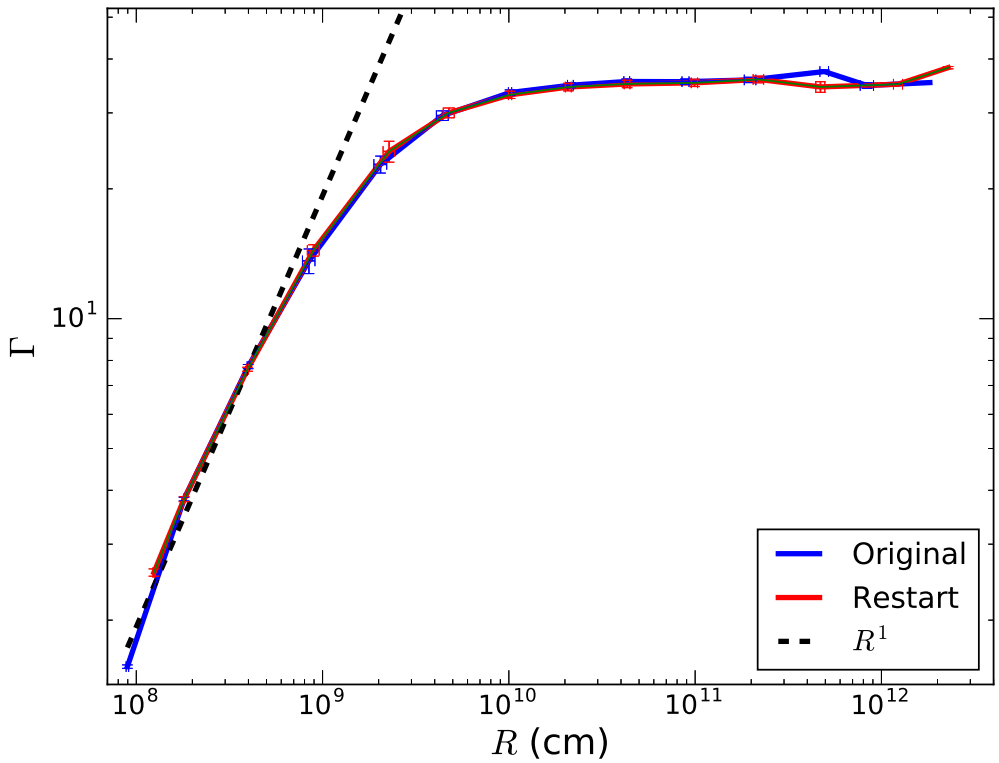

FIGURE 6.4: Evolution of Lorentz factor with radius for fireballs with $R_{\rm ph}/R_{\rm sat} = 0.157$. The blue curves represents the original simulation, which starts with no bulk motion. The red curve represents the simulation 'restarted' from the original simulation with initial conditions extracted at $\Gamma \sim 3$. Also plotted are the error bars for both the simulations computed from their standard deviation.

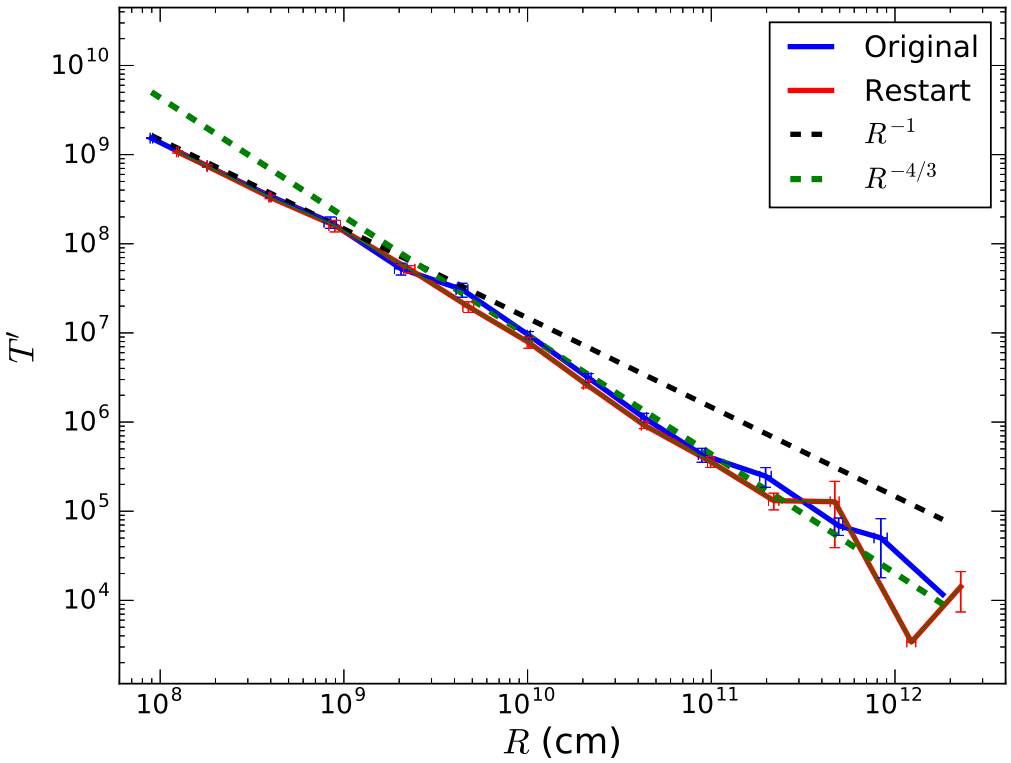

FIGURE 6.5: Evolution of comoving temperature with radius for fireballs with $R_{\rm ph}/R_{\rm sat} = 0.157$. The blue curves represents the original simulation which started with no bulk motion. The red curve is started with initial conditions extracted from the data of the original simulation (when $\Gamma \sim 3$). Also plotted are the error bars for the two simulations (computed from their standard deviation).

E1 Case I: $\frac{R_{\rm ph}}{R_{\rm sat}} < 1$

The first case considers the scenario that the photospheric radius is reached before the saturation radius, i.e., $R_{\rm ph} < R_{\rm sat}$. The saturation radius $R_{\rm sat}$ (the radius at which the fireball attains η) has already been obtained in eq. 3.7 as –

$$R_{\rm sat} = \eta \frac{R_0}{\Gamma_0} = \frac{E}{Mc^2} \frac{R_0}{\Gamma_0}. \tag{6.30}$$

The calculation of the photospheric radius $R_{\rm ph}$ begins with the calculation of opacity of the evolving fireball. As stated in Abramowicz et al. (1991), the lab frame opacity τ is given by –

$$\tau = \int_{R_{\rm ph}}^{\infty} n\sigma \left(1 - \beta \cos\theta\right) dR, \tag{6.31}$$

where n is the number density of scattering particles and the $(1 - \beta\cos\theta)$ term accounts for velocity dependence of opacity (β is the bulk speed of the outflow normalized by the speed of light). Assuming $nR^2 =$ constant, and for $\cos\theta \sim 1$ (small angle approximation), eq. 6.31 can be written as –

$$\tau = \int_{R_{\rm ph}}^{\infty} \frac{n_0 R_0^2 \sigma}{2R^2 \Gamma_{\rm ph}^2} dR. \tag{6.32}$$

If the fireball is within the acceleration regime (see eq. 3.2), we can write –

$$\frac{\Gamma_{\rm ph}}{R} = \frac{\Gamma_0}{R_0}. \tag{6.33}$$

Combining eqs. 6.32 and 6.33, the opacity equation becomes –

$$\tau = \frac{n_0 R_0^2 \sigma}{2} \int_{R_{\rm ph}}^{\infty} \frac{1}{R^4}. \tag{6.34}$$

The photospheric radius $R_{\rm ph}$ is attained when $\tau \sim 1$, which implies –

$$R_{\rm ph} = \left(\frac{n_0 R_0^4 \sigma}{6}\right)^{1/3}. \tag{6.35}$$

The ratio of the photospheric and the saturation radii can be written as –

$$\frac{R_{\rm ph}}{R_{\rm sat}} = \left(\frac{n_0 R_0^4 \sigma}{6}\right)^{1/3} \frac{1}{\eta R_0}. \tag{6.36}$$

To vary the results of eq. 6.36 we use the parameter σ as an effective cross–section. The connection between the effective cross–sectional parameter σ and the Thomson cross–section σ_T is –

$$\sigma_{\equiv}\frac{\sigma_T \sigma_{\rm coeff} V_0}{c} = \frac{\sigma_{\rm eff} V_0}{c}. \tag{6.37}$$

Re–writing eq. 6.36 using eq. 6.37 –

$$\frac{R_{\rm ph}}{R_{\rm sat}} = \left(\frac{n_0 R_0^4 \sigma}{6}\right)^{1/3} \frac{1}{\eta R_0} = \left(\frac{N R_0^4 \sigma_{\rm eff}}{6c}\right)^{1/3} \frac{1}{\eta R_0}. \tag{6.38}$$

Thus, by changing $\sigma_{\rm coeff}$ in eq. 6.37 for each simulation we can vary $\frac{R_{\rm ph}}{R_{\rm sat}}$, and as a consequence, the opacity of the plasma.

E2 Case II: $\frac{R_{\rm ph}}{R_{\rm sat}} \geq 1$

We now explore the case when the $R_{\rm ph} \geq R_{\rm sat}$. At the saturation radius, as all the internal energy has been converted into bulk kinetic energy, the acceleration of the fireball ceases and the fireball coasts beyond that radius at η. If the saturation radius is smaller than the photospheric radius, this implies radiation is still trapped within the fireball. As the fireball is no longer in the acceleration regime (see eq. 3.2), $\Gamma_{\rm ph} = \eta$, and the fireball opacity evolves differently from the case $R_{\rm ph} < R_{\rm sat}$. Using eq. 6.31, we can write –

$$\tau = 1 = \int_{R_{ph}}^{\infty} \frac{n_0 R_0^2 \sigma}{2R^2 \eta} dR. \tag{6.39}$$

The photospheric radius obtained by integration can be expressed as –

$$R_{\rm ph} = \frac{n_0 \sigma R_0^2}{2\eta^2}. \tag{6.40}$$

Therefore, the ratio of the photospheric to the saturation radii is –

$$\frac{R_{\rm ph}}{R_{\rm sat}} = \frac{n_0 \sigma R_0}{2\eta^3}. \tag{6.41}$$

Using eq. 6.37, we can rewrite eq. 6.41 as –

$$\frac{R_{\rm ph}}{R_{\rm sat}} = \frac{n_0 \sigma R_0}{2\eta^3} = \frac{N \sigma_{\rm eff} V_0 R_0}{2cV_0 \eta^3} = \frac{N \sigma_{\rm eff} R_0}{2c\eta^3}. \tag{6.42}$$

F Details of force calculation

Consider an element of the layer at position z; we call $\mathrm{d}U'$ the differential energy density of the spine radiation received from an angle between θ and $\theta + \mathrm{d}\theta$, measured in the frame of the layer. The contribution of this radiation energy density to the infinitesimal force $\mathrm{d}F'_{\mathrm{z}}$ parallel to the jet axis and acting on the layer particle is given by:

$$\mathrm{d}F'_{\mathrm{z}} \;=\; \frac{16}{9}\sigma_{\mathrm{T}}\langle\gamma^2\rangle\cos\theta'\mathrm{d}U' \tag{6.43}$$

where θ' is the angle of incoming photons with respect to the jet axis direction as seen by the layer. The total force exerted on the layer's effective particle can be computed by integrating the Eq. 6.43 over the incoming angles θ'. Since the spine is active between points that are fixed in the observer frame K, it is easier to compute the integral in that frame K. From the relations of aberration of the light (e.g. Weinberg, 1972) we have useful transformations:

$$\cos\theta' \;=\; \frac{\cos\theta - \beta_{\mathrm{L}}}{1 - \beta_{\mathrm{L}}\cos\theta} \tag{6.44}$$

$$\mathrm{d}\Omega' \;=\; \mathrm{d}\Omega \cdot \delta_{\mathrm{L}}^2 \tag{6.45}$$

The differential radiation energy density can be written as:

$$\frac{\mathrm{d}U'}{\mathrm{d}\Omega'} \;=\; \frac{I'}{c} \tag{6.46}$$

where I' is the bolometric radiation intensity as seen by the layer and it is related to the spine comoving radiation intensity I'' by:

$$I' \;=\; I'' \cdot \delta_{\mathrm{S,L}}^4 \tag{6.47}$$

Consider now that the uni–dimensional spine is actually an infinitesimal cylinder whose axis is coincident with the jet axis of height R and radius $r \to 0$. In this case we have:

$$I'' \;=\; j'' \cdot r \;=\; \lambda''_{\mathrm{S}}\frac{1}{\pi r} \tag{6.48}$$

where j'' is the comoving spine emissivity. $\lambda''_{\mathrm{S}} = \left[\dfrac{\mathrm{d}L''_{\mathrm{S}}}{\mathrm{d}x''}\right]$ is the comoving spine luminosity linear density profile; it is generally a function of the position z, but in case of uniform luminosity distribution we can write:

$$\lambda''_{\mathrm{S}} = \frac{\mathrm{d}L''_{\mathrm{S}}}{\mathrm{d}x''} \;=\; \frac{L''_{\mathrm{S}}}{R''} \;=\; \frac{L''_{\mathrm{S}}\Gamma_{\mathrm{S}}}{R} \tag{6.49}$$

where $R'' = R/\Gamma_{\rm S}$ is the length of the spine active region measured in the frame comoving to the spine. $L''_{\rm S}$ is the total comoving luminosity of the spine and it is related to the observed isotropic luminosity by (see Lind and Blandford 1985):

$$L_{\rm S,iso} \;=\; L''_{\rm S}\delta^3_{\rm S}(\theta_{\rm view}) \;=\; \frac{L''_{\rm S}}{\Gamma^3_{\rm S}(1-\beta_{\rm S}\cos\theta_{\rm view})^3} \tag{6.50}$$

where $\theta_{\rm view}$ is the angle between the jet axis and the line of sight. That relation is different from the usual one (that requires a factor δ^4 between the rest frame and the isotropic luminosity) because in this case there the rest frame emitting volume properly is ill-defined as the end points of the emitting region are moving with respect to the emitting fluid. We can relate the observed luminosity density $\lambda_{\rm S}$ with the comoving one through Eq. 6.51:

$$\lambda_{\rm S} \;=\; \frac{L_{\rm S,iso}}{R} \;=\; \lambda''_{\rm S}\frac{\delta^3_{\rm S}(\theta_{\rm view})}{\Gamma_{\rm S}} \tag{6.51}$$

Using the definition of solid angle $\mathrm{d}\Omega$ we can write:

$$\mathrm{d}\Omega \;=\; \frac{\mathrm{d}A}{D^2} \;=\; \frac{\mathrm{d}x\cdot 2r}{D^2} \;=\; \frac{\mathrm{d}\theta\cdot 2br}{D^2\sin^2\theta} \;=\; \frac{2r}{b}\mathrm{d}\theta \tag{6.52}$$

where $\mathrm{d}A = 2r\mathrm{d}x$ is the differential area of the spine seen under the angle $\mathrm{d}\Omega$, $D = b/\sin\theta$ is the distance between the emitting element of the spine and the layer, $x = -D\cos\theta = -b\cot\theta$ is the projection of D over the jet axis. Using eqs. 4.3, 6.45, 6.46, 6.47, 6.48, 6.52, we can write:

$$\frac{\mathrm{d}U'(\theta)}{\mathrm{d}\theta} \;=\; \lambda''_{\rm S}\eta\frac{\delta^4_{\rm S}}{\delta^2_{\rm L}}\frac{1}{bc} \tag{6.53}$$

that depends no more on $r \to 0$. In Eq. 6.53, η is a factor of the order of unity that depends on the geometry (in our case we use $\eta = 2/\pi$). The total force exerted on the layer test particle is obtained integrating Eq. 6.43:

$$F'_{\rm z} \;=\; \frac{16}{9}\frac{\sigma_{\rm T}}{bc}\langle\gamma^2\rangle\eta\int_{\theta_1}^{\theta_2}\lambda''_{\rm S}\frac{\delta^4_{\rm S}}{\delta^2_{\rm L}}\frac{\cos\theta-\beta_{\rm L}}{1-\beta_{\rm L}\cos\theta}\mathrm{d}\theta \tag{6.54}$$

The limits of integration θ_1 and θ_2 are measured in the central engine frame (comoving to the limits of the emitting volume) and depend only on the position of the layer z:

$$\cos\theta_1 \;=\; \frac{z}{(b^2+z^2)^{1/2}} \tag{6.55}$$

$$\cos\theta_2 \;=\; \frac{z-R}{(b^2+z^2+R^2-2Rz)^{1/2}} \tag{6.56}$$

Evaluating the force at each value of z we can obtain the layer Lorentz factor profile $\Gamma_{\rm L}(z)$ by numerically solving Eq. 4.10.